TAMPEREEN TEKNILLINEN YLIOPISTO
TAMPERE UNIVERSITY OF TECHNOLOGY

Jaakko Marttila

Quadrature Sigma-Delta Modulators for Reconfigurable A/D Interface and Dynamic Spectrum Access: Analysis, Design Principles and Digital Post-processing

Julkaisu 1265 • Publication 1265

Tampere 2014

Tampereen teknillinen yliopisto. Julkaisu 1265
Tampere University of Technology. Publication 1265

Jaakko Marttila

Quadrature Sigma-Delta Modulators for Reconfigurable A/D Interface and Dynamic Spectrum Access: Analysis, Design Principles and Digital Post-processing

Thesis for the degree of Doctor of Science in Technology to be presented with due permission for public examination and criticism in Tietotalo Building, Auditorium TB224, at Tampere University of Technology, on the 28th of November 2014, at 12 noon.

Tampereen teknillinen yliopisto - Tampere University of Technology
Tampere 2014

Supervisor
Mikko Valkama, Professor
Department of Electronics and Communications Engineering
Tampere University of Technology
Tampere, Finland

Pre-examiners
Timo Rahkonen, Professor
Department of Electrical Engineering
University of Oulu
Oulu, Finland

Ana Rusu, Professor
ICT School/Integrated Devices and Circuits
Royal Institute of Technology (KTH)
Stockholm, Sweden

Opponents
Timo Rahkonen, Professor
Department of Electrical Engineering
University of Oulu
Oulu, Finland

Håkan Johansson, Professor
Department of Electrical Engineering
Linköping University
Linköping, Sweden

ISBN 978-952-15-3408-9 (printed)
ISBN 978-952-15-3427-0 (PDF)
ISSN 1459-2045

ABSTRACT

In the course of development of wireless communications and its modern applications, such as cloud technologies and increased consumption and sharing of multimedia, the radio spectrum has become increasingly congested. However, temporarily and spatially underused spectrum exists at the same time. For increasing the efficiency of spectrum usage, the concept of dynamic spectrum access (DSA) has been proposed. Ultimately, the DSA principle should be exploited also in cognitive radio (CR) receivers. Herein, this paradigm is approached from the receiver architecture point-of-view, considering software-defined radio (SDR) as a platform for the future DSA and CR devices. Particularly, an analog-to-digital converter (ADC) architecture exploiting quadrature $\Sigma\Delta$ modulator (Q$\Sigma\Delta$M) is studied in detail and proposed as a solution for the A/D interface, being identified as a performance bottleneck in SDRs.

By exploiting a complex valued noise transfer function (NTF) enabled by the Q$\Sigma\Delta$M, the quantization precision of the ADC can be efficiently and flexibly focused on the frequency channels and the signals to be received and detected. At the same time, with a traditional non-noise-shaping ADC, the precision is distributed equally for the whole digitized frequency band containing also noninteresting signals. With a single Q$\Sigma\Delta$M, it is also possible to design a multiband NTF, allowing reception of multiple noncontiguous frequency channels without parallel receiver chains. Furthermore, with the help of digital control, the Q$\Sigma\Delta$M response can be reconfigured during operation. These capabilities fit in especially well with the above mentioned DSA and CR schemes, where the temporarily and spatially available channels might be scattered in frequency.

From the implementation point-of-view, the effects of inherent implementation inaccuracies in the Q$\Sigma\Delta$M design need to be thoroughly understood. In this thesis, novel closed-form matrix-algebraic expressions are presented for analyzing the transfer functions of a general multistage Q$\Sigma\Delta$M with arbitrary number of arbitrary-order stages. Altogether, the signal response of an I/Q mismatched Q$\Sigma\Delta$M has four components. These are the NTF, an image noise transfer function, a signal transfer function (STF) and an image signal transfer function. The image transfer functions are provoked by the I/Q mismatches and define the frequency profile of the generated mirror-frequency interference (MFI), potentially deteriorating the quality of the received signal. This contribution of the thesis increases the understanding of different QΣΔM structures and allows the designers to study the effects of the implementation inaccuracies in closed form.

In order to mitigate the MFI and improve the signal reception, a mirror-frequency rejecting STF design is proposed herein. This design is found to be effective against I/Q mismatches taking place in the feedback branches of the QΣΔM. This is shown with help of the closed-form analysis and confirmed with computer simulations on realistic reception scenarios.

When a mismatch location independent MFI suppression is the desired option, it is a logical choice to do this processing in a digital domain, after the whole analog receiver front-end. However, this sets demands for the information to be digitized, i.e., the source of the MFI should be available also in the digital domain. For this purpose, a novel multiband transfer function design is proposed herein. In addition, a QΣΔM specific digital MFI compensation algorithm is developed. The compensation performance is illustrated in practical single- and multiband reception scenarios, considering desired signal bandwidths up to 20 MHz. In the multiband scenario, allowing reception and detection of noncontiguous frequency channels with a single receiver chain, the digital compensation processing is done sub-bandwise, securing reliable functionality also under strongly frequency-selective interference. In the applied single- and multistage QΣΔM architectures, the I/Q mismatches are considered in all the QΣΔM branches as well as in the preceding receiver front-end, modeling the challenging and realistic scenario where the whole receiver chain includes cascaded in-phase/quadrature (I/Q) mismatch sources.

As a whole, developing digital MFI compensation is a significant step towards practical receiver implementations with QΣΔM ADCs. In consequence, this allows the exploitation of the multiband and reconfigurability properties. The proposed design can be implemented without additional analog components and is straightforwardly reconfigurable in dynamic signal conditions typical for DSA and CR systems, e.g., in case of frequency hand-off because of a primary user appearance. In addition, the digital post-compensation of the MFI eases the strict demands for the matching of the analog circuits in SDRs.

PREFACE

This thesis is based on research work carried out during the years 2008-2014 at the Department of Electronics and Communications Engineering (ELT), Tampere University of Technology (TUT), Tampere, Finland.

First and foremost I would like to thank my advisor, Professor Mikko Valkama for his invaluable guidance and motivation. His deep devotion to the field of science has also been of great inspiration for myself and helped me to proceed with the studies and the research. I am also grateful for the long-time Head of the former Department of Communications Engineering (DCE), Professor Markku Renfors for his support and sharing his wide knowledge on digital communications.

The research work for the thesis has been partially funded by the Academy of Finland (under the projects "251138 Digitally-enhanced RF for cognitive radio devices"), the Finnish Funding Agency for the Technology and Innovation (Tekes, under the projects "Advanced techniques for RF impairment mitigation in future wireless radio systems", "Enabling methods for dynamic spectrum access and cognitive radio"), the Austrian Center of Competence in Mechatronics (ACCM, under the project "Wireless communication technologies"). In addition, the personal financial support of HPY Research Foundation and Nokia Foundation is gratefully acknowledged.

My thanks go to my colleague and fellow post-graduate student M.Sc. Markus Allén who has been of great help in numerous research problems. We have been studying the wonderful world of analog-to-digital converters together and the discussions, on and off the topic, have been greatly fruitful. I am also grateful for D.Sc. Lauri Anttila and M.Sc. Vesa Lehtinen for sharing their experience on the related research topics and for our current and former office secretaries Heli Ahlfors, Soile Lönnquist, Tarja Erälaukko, M.Sc. Marianna Jokila and Kirsi Viitanen for their help with practical arrangements. I would like to thank my current and former room-mates Yaning Zou, Adnan Kiayani, Janis Werner, Mahmoud Abdelaziz and Paschalis Sofotasios, as well as Pedro Figueiredo e Silva across the corridor, for creating a pleasant place to work in. Furthermore, I am grateful for all the aforementioned and Toni Levanen, Jukka Talvitie, Tero Isotalo, Jussi Turkka, Ali Shahed hagh ghadam, Ville Syrjälä, Aki Hakkarainen, Jari Kangas and Joonas Säe for captivating and interesting discussion on a whole wide range of topics. In addition, I would like to extend my thanks to all my co-workers in the ELT and DCE at TUT for guaranteeing relaxed and productive atmosphere.

I am thankful for my friends for giving me also something else to think but the thesis. Many, profound, thanks for my parents Jukka and Merja for being there whenever needed and believing in me through all these years. And finally, for you Lumi, I would like to express my deepest gratitude, for being everything you are, may the paths chosen in future be whatever. I have learned from you so much more important lessons in life than I could ever imagine finding in a classroom.

Tampere, August 2014
Jaakko Marttila

CONTENTS

LIST OF PUBLICATIONS

This thesis is a compound thesis based on the following seven publications.

[P1] Jaakko Marttila, Markus Allén and Mikko Valkama, "Design and analysis of multi-stage quadrature sigma-delta A/D converter for cognitive radio receivers," in *Proceedings of the 16th IEEE International Workshop on Computer-Aided Modeling, Analysis and Design of Communication Links and Networks*, Kyoto, Japan, June 2011, 5 pages.

[P2] Jaakko Marttila, Markus Allén and Mikko Valkama, "Response analysis of second-order multi-band quadrature sigma-delta modulators with applications in cognitive radio devices," in *Proceedings of the 54th IEEE International Midwest Symposium on Circuits and Systems*, Seoul, South-Korea, August 2011, 4 pages.

[P3] Jaakko Marttila, Markus Allén and Mikko Valkama, "Quadrature sigma-delta modulators for cognitive radio - I/Q imbalance analysis and complex multiband principle," *Circuits, Systems and Signal Processing*, volume 30, number 4, pages 775–797, August 2011.

[P4] Jaakko Marttila, Markus Allén and Mikko Valkama, "Multi-stage quadrature sigma-delta modulators for reconfigurable multi-band analog-digital interface in cognitive radio devices," *EURASIP Journal on Wireless Communications and Networking*, volume 2011:130, October 2011, 23 pages.

[P5] Jaakko Marttila, Markus Allén and Mikko Valkama, "Digital mirror-frequency interference compensation for multiband quadrature sigma-delta ADC based cognitive radio receivers," in *Proceedigns of the 55th IEEE International Midwest Symposium on Circuits and Systems*, Boise, ID, August 2012, 4 pages.

[P6] Markus Allén, Jaakko Marttila and Mikko Valkama, “Wideband quadrature sigma-delta A/D conversion for cognitive radio - reconfigurable design and digital mirror-frequency suppression,” in *Proceedings of the 78th IEEE Vehicular Technology Conference*, Las Vegas, NV, September 2013, 5 pages.

[P7] Jaakko Marttila, Markus Allén and Mikko Valkama, “Frequency-agile multiband quadrature sigma-delta modulator for cognitive radio: analysis, design and digital post-processing,” *IEEE Journal on Selected Areas in Communications*, volume 31, number 11, pages 2222–2236, November 2013.

ABBREVIATIONS

3GPP	3rd Generation Partnership Project
A/D	analog-to-digital
ADC	analog-to-digital converter
AGC	automatic gain control
CIFB	cascade-of-integrators with distributed feedback
CR	cognitive radio
CT	continuous-time
D/A	digital-to-analog
DAC	digital-to-analog converter
DC	direct current
DCR	direct-conversion receiver
DSA	dynamic spectrum access
DSP	digital signal processing
FIR	finite impulse-response
FT	Fourier transform
I/Q	in-phase/quadrature
IF	intermediate frequency
IIR	infinite impulse-response
INTF	image noise transfer function
IRR	image rejection ratio
ISTF	image signal transfer function
LMS	least-mean-square
LTE	Long Term Evolution

LTE-A	Long Term Evolution Advanced
MFI	mirror-frequency interference
NTF	noise transfer function
PU	primary user
Q$\Sigma\Delta$M	quadrature $\Sigma\Delta$ modulator
RF	radio frequency
SC	switched-capacitor
SDR	software-defined radio
SINR	signal-to-interference-and-noise ratio
SNR	signal-to-noise ratio
SQNR	signal-to-quantization-noise ratio
STF	signal transfer function
SU	secondary user

CHAPTER 1

Introduction

1.1 Background and Research Motivation

With emerging cloud technologies and increasing amount of multimedia content sharing on wireless devices, available radio frequency (RF) spectrum is becoming increasingly crowded. Considerable share of this increased traffic is produced by mobile smartphones and tablets with audio and video streaming capabilities and, at the same time, having cloud storage available for data [8, 40]. These cloud services introduce also increasing amount of uplink traffic. This trend in the mobile industry calls for novel solutions to make usage of the spectrum as efficient as possible. For this purpose, concept of dynamic spectrum access (DSA) has been developed [107, 120]. In DSA, the goal is to assign temporally or spatially unused spectrum for active users in order to maximize the efficiency. A practical example of this is the introduction of so-called white space devices [88] taking advantage of vacant digital TV channels for other purposes, such as wireless broadband access [45].

The DSA is also considered as an integral part of a cognitive radio (CR) concept [7, 78]. A CR device should be able to sense its environment and make smart operation decisions based on the extracted data [84, 85]. Spectrum sensing for identification of transmission bands left unused by the primary users (PUs), known as spectrum holes, is a good example of this concept. This kind of tempo-spatial spectrum holes, exploited by secondary user (SU) signals, are illustrated in Figure 1.1.

From the hardware point-of-view, DSA, and ultimately CR, set novel challenges for the flexibility of the transceiver functionality [35, 98]. The device should be able to operate in dynamic radio conditions and access varying and possible scattered frequency channels. At the same time, the mobile industry demands set strict requirements for the power consumption, cost and size of the hardware. Especially the power consumption becomes a critical factor when considering a wideband receiver, digitizing, e.g., a whole cellular band for maximal flexibility implemented in digital domain. This kind of software-defined radio (SDR) receiver employing a single wideband receiver chain and pushing significant part of the signal processing into digital domain, instead of having multiple parallel analog receivers, has been identified as a fit platform for DSA

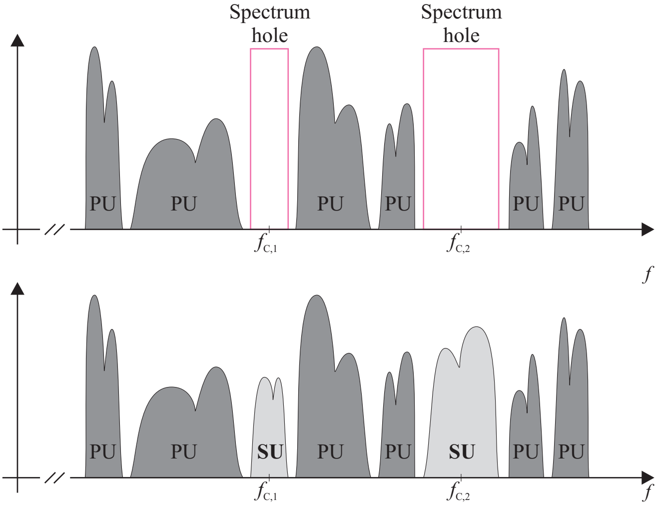

Figure 1.1: An example of spectrum holes being exploited by a secondary system. PUs have privilege for transmission on the depicted bands, while the SUs can use tempo-spatially available empty bands. The SU signals are depicted with light gray color.

and CR devices [4, 39]. However, an efficient implementation is an open research topic, gathering a lot of interest from both industry and academia. Especially, the analog-to-digital (A/D) conversion has been identified as a performance bottleneck [66, 69]. In the A/D conversion, there is inherent tradeoff between the resolution and speed, i.e., bandwidth of the analog-to-digital converter (ADC) and its power consumption. At the same time, when the bandwidth is increased, the resolution demand tends to increase because the reception band is more likely to include separate signals with highly varying power levels. Thus, even if the components would allow high resolution and speed, the ADC would become unsuitable for mobile battery operated devices because of the power consumption [20]. For this reason, it is essential to optimize the efficiency of the A/D interface. In this thesis, novel solutions to exactly this problem are proposed.

1.2 A/D Interface in Dynamic Spectrum Access and Cognitive Radio Receivers

The traditional idea for wideband A/D conversion in software-defined multistandard DSA or CR receivers is to use an oversampled Nyquist ADC [4]. In this scenario, the necessary resolution of the ADC is defined by the demanded resolution for the desired waveform to be received and signal dynamics inside the whole conversion band. Usually, this desired waveform is only a single sub-channel and rest of the signal content is filtered away in the digital domain. However, this signal content outside this sub-channel greatly affects the achieved resolution for the desired waveform. For example, if the desired waveform is transmitted over long distance and thus significantly attenuated, and there is another transmitter is the proximity of the receiver, the signal received from this latter transmitter might be tens of dBs stronger than the one from the far-away transmitter [91]. This strong blocking signal might be, e.g, from an extra-system user whose transmission power can not be tuned or an intra-system user being served with higher data rate and thus needing higher signal-to-noise ratio (SNR). At the same time, the ADC has a constant input voltage, controlled by an automatic gain control (AGC). When combined, these characteristics lead into effective downscaling of the desired waveform and increased resolution demand for the ADC if the resolution for this weak sub-channel is to be kept unaffected. Now, the situation is that the strong neighboring channel is converted into digital domain with comparatively high resolution, even though it is to be removed in digital filtering. The traditional way to cope with increased resolution demand are increasing sampling rate or number of quantization bits in the ADC. These options, however, increase the complexity and power consumption of the ADC [66, 69, 115, 116].

In contrast to the Nyquist ADCs, the main property of a $\Sigma\Delta$ ADC is shaping of the quantization error, or noise as it is often referred to [19]. This noise shaping allows pushing most of the quantization noise to those frequency channels which are not of interest for the receiver at hand. In this way, the quantization precision can be concentrated on the desired sub-channel, or generally sub-channels. This means that the above mentioned scenario, where the noninteresting neighboring signal is converted into digital domain with high resolution, can be avoided.

The $\Sigma\Delta$ ADC consists of a $\Sigma\Delta$ modulator, containing quantizer and in discrete-time implementations also sampler inside the modulator loop, followed by digital filtering. In this thesis, the main focus is on the $\Sigma\Delta$ modulator response characteristics and related digital signal processing. A basic lowpass $\Sigma\Delta$ modulator pushes the quantization noise towards higher frequencies, i.e., there is highpass filtering response for the quantization noise [19]. However, by using bandpass or quadrature bandpass $\Sigma\Delta$ modulators, it is possible to create the noise notch, meaning the frequency band form where the quantization noise is pushed away from, also on certain intermediate frequency (IF) [60, 98]. With these modulators, it is also possible to create multiple noise notches on noncontiguos frequency bands [P3]. Furthermore, the quadrature $\Sigma\Delta$ modulator (Q$\Sigma\Delta$M) allows frequency asymmetric design for the noise transfer function (NTF), which defines the quantization noise shaping response. This is a natural option for an I/Q receiver, having parallel I and Q signals on baseband already. A direct-conversion receiver (DCR), employing the I/Q principle is a popular choice for modern communications receivers [72, 81, 91], and has been considered a practical option for the SDR [22, 46]. At the same time, the SDR is considered as a promising physical layer solution for DSA and CR systems [83].

When using analog I/Q separation in the receiver, these rails should be perfectly matched for optimal performance [91]. However, this never happens in practice because the inherent implementation inaccuracies on the analog circuits. Nonideal matching of the rails induces mirror-frequency interference (MFI). This means that a copy of the signal is mirrored in frequency domain and then added on top of the original signal. This mirror-copy has certain attenuation which depends on the precision of the I/Q matching and is generally frequency-selective. In addition, the response for the original signal can be altered by the I/Q mismatches. This happens when the deviation from the ideal response has common part on both the rails [61]. Most important mismatch sources, e.g., in a DCR are down-converting I/Q mixer, the baseband filters and the ADCs [9,91]. This includes also QΣΔM based ADCs [59,60,62], in which the nature of the MFI depends on the exact location of the mismatches and, at the same time, on the designed quantization noise and signal responses [P3]. These are defined by the NTF and signal transfer function (STF), respectively.

The MFI can be reduced by improving the precision of the circuit design, but this has been considered unfeasible for demanding applications [92]. Without additional mitigation or suppression, a typical image rejection ratio (IRR) is around 30-40 dB for DCRs [9,27,38,42,91]. At the same time, in challenging applications, such as multiband reception or spectrum sensing in CR, the IRR demand might be as high as 80 dB [92]. One current research trend among the industry and academia is to use simple and cheap analog electronics, whose downfalls are thereafter mitigated or suppressed in digital domain by digital signal processing (DSP) algorithms. A number of digital MFI compensation algorithms have been proposed in current literature, most of them being targeted for traditional non-noise-shaping receivers [9–12,47,52,90]. Further references can be found, e.g., from [9].

When applying a QΣΔM for quantization noise shaping, the noise is pushed away from the desired frequency channel, and it might make the quantization noise level very high on the respective mirror-band [59, 60, 62]. This is especially the case when the noise shaping notch is designed for a higher IF. In this scenario, the mirror-band is further away from the desired band than with the close-to-zero IFs. From the digital MFI suppression point-of-view, this phenomenon is problematic, because most of the compensation algorithms demand knowledge of the mirror-band signal content, i.e., the mirror-band should have a reasonably good SNR [9]. This has made post-suppression of the MFI appearing earlier in the receiver chain, due to the I/Q mixer and the baseband filters, challenging, even if the QΣΔM itself would be perfectly I/Q matched.

In Figure 1.2, a reconfigurable multiband receiver structure employing a multiband QΣΔM is illustrated [P4]-[P7]. The operating band information for configuring the QΣΔM transfer functions can be obtained from spectrum sensing or from a specific control channel, depending on the application and system scenario at hand. This allows also efficient reception of noncontiguous frequency channels. A concrete example of this is kind of scenario in existing and emerging mobile cellular radio systems is intra-band carrier aggregation in 3rd Generation Partnership Project (3GPP) Long Term Evolution (LTE) [2,3] and Long Term Evolution Advanced (LTE-A) [1]. Thus, in dynamic operation conditions typical, e.g., for DSA and CR receivers, the operation band and the QΣΔM response can be reconfigured digitally with the help of straightforward parametrization of the STF and NTF. Thus, the bandwise signal-to-quantization-noise ratio (SQNR) can be optimized. The receiver principle illustrated in Figure 1.2 is the underlying main theme and basis of this thesis work.

1.3 Thesis Objectives

The objective of the thesis is to facilitate implementation of an I/Q mismatch robust multiband ADC using QΣΔM for quantization noise shaping. This kind of ADC is targeted for SDR receivers in the DSA and the CR context. Moreover, the thesis offers

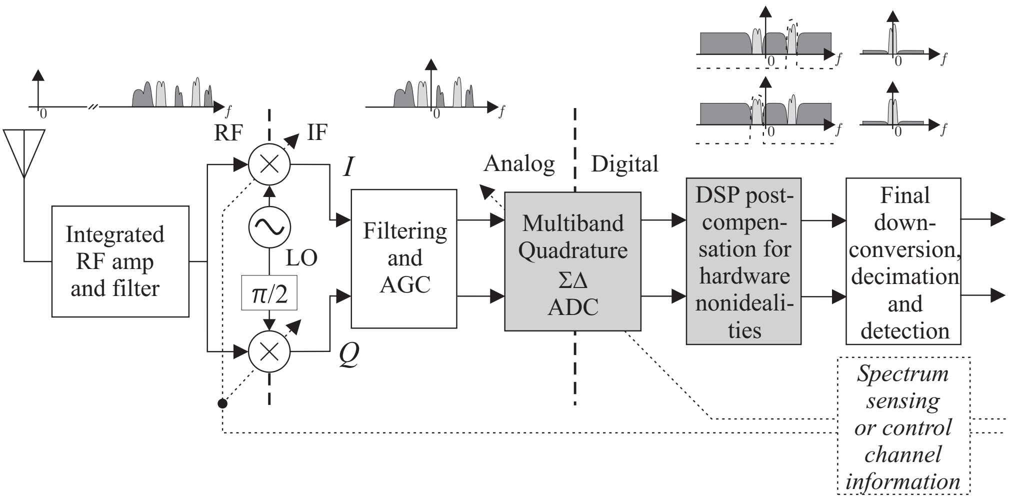

Figure 1.2: Block diagram of a *multiband* direct-conversion quadrature receiver, based on a frequency-agile QΣΔM. Principal spectra, where the two light gray signals are the desired ones, are illustrating the signal compositions at each stage.

design guidelines for a reconfigurable multiband QΣΔM employing multistage structures for increased flexibility. Both analog and digital approaches are developed for mitigating or suppressing the MFI induced by the I/Q mismatches between the receiver signal rails. The presented principles are applicable for both base station and mobile device receivers with proper adjustments. In addition, noncontiguous reception of multiple frequency channels, e.g., in carrier-aggregation scenarios of 3GPP mobile cellular radio systems, is in principle allowed by the multiband transfer function designs.

1.4 Main Results and Organization of the Thesis

The main results obtained in the thesis work are

- thorough analysis of separate I/Q mismatch sources inside single- [P2, P3] and multi-stage [P1, P4, P7] QΣΔMs and their respective MFI contributions, both from the input signal and quantization noise point-of-view

- developing a mirror-frequency rejecting STF design for the single- and multistage QΣΔMs, offering improved robustness against the I/Q mismatches in the feedback branch of the modulator, for which the generated interference is not shaped by the NTF [P1-P4]

- deriving a general closed-form formulation for analysis of the four transfer functions (STF, NTF, image signal transfer function (ISTF) and image noise transfer function (INTF)) of a QΣΔM having arbitrary number of arbitrary-order stages under implementation inaccuracies [P7]

- developing a reconfigurable multiband transfer function design with an aim for facilitating digital post-compensation of the MFI induced by the receiver implementation inaccuracies [P5-P7]

- developing digital post-compensation of the MFI independent of the original error source, being thus able to cover the MFI originating from the whole receiver chain including a cascade of I/Q mismatch sources, such as I/Q mixer, baseband filters and the QΣΔM itself [P5-P7]

- offering design guidelines for frequency-agile multiband QΣΔM as a part of a SDR receiver with straightforward parametrization and reconfiguration of the modulator stages [P4, P7].

In addition to the articles included in this thesis, a book chapter [112] giving an overview on advanced QΣΔM concepts has been published by the author and his colleagues. A conference paper [75] by the author has been left out of the thesis because the essential contributions have been included in [P3].

The thesis is organized as follows. Chapters 2 and 3 give an overview on I/Q signal processing techniques and ΣΔ modulators, respectively. The main contributions of the thesis are discussed in Chapters 4 and 5. Chapter 4 presents the analysis of the QΣΔM transfer functions under implementation inaccuracies. Chapter 5 gives the reconfigurable multiband transfer function concepts developed, namely I/Q mismatch robust mirror-frequency rejecting and digital MFI post-compensation facilitating designs. Furthermore, a digital circularity restoring MFI compensation approach fit for QΣΔM based receivers is presented in Chapter 5.

1.5 Author's Contributions to the Publications

The research work done for the thesis was carried out at the Department of Communications Engineering, and from beginning of 2013 at the Department of Electronics and Communications Engineering, Tampere University of Technology, Finland. The research was part of the projects *Advanced Techniques for RF Impairment Mitigation in Future Wireless Radio systems*, *Enabling Methods for Dynamic Spectrum Access and Cognitive Radio* (both funded by the Finnish Funding Agency for the Technology and Innovation), *Digitally-enhanced RF for cognitive radio devices* (funded by the Academy of Finland) and *Wireless Communication Technologies* (funded by the Austrian Center of Competence in Mechatronics) and is continuation for the authors Master's thesis finished in 2010. Originally, the topic was proposed by Prof. Mikko Valkama based on the extensive literature study covering the challenges of the A/D techniques in modern wireless communication, with emphasis on CR-like multistandard operation. This study was performed by the author and M.Sc Markus Allén. The thesis research is largely inspired by D.Sc. Stephen Jantzi's work in [59–64].

The research was performed in co-operation with the thesis supervisor Prof. Valkama and M.Sc. Allén. Prof. Valkama and M.Sc. Allén contributed to the final appearance of the publications [P1]-[P7] and gave their opinions during meetings and discussions.

In addition, D.Sc. Lauri Anttila participated the initial discussions on digital MFI post-compensation reported in [P5]-[P7] and M.Sc. Vesa Lehtinen, gave feedback on design and properties of infinite impulse-response (IIR) filters for [P3].

The signal models, mathematical derivations, computer simulations and performance analysis in [P1]-[P7] were performed by the author with Prof. Valkama's guidance. In addition, the author wrote the initial manuscripts for [P1]-[P7], which were finalized in co-operation with Prof. Valkama and M.Sc. Allén. The initial idea to use matrix format for general modeling of implementation inaccuracies in [P7] came from M.Sc. Allén. Although, the actual derivations, formulation and analysis were performed by the author.

CHAPTER 2

I/Q Signal Processing Basics and Dynamic Spectrum Access

Herein the I/Q signal processing principles and the DSA basics and requirements are presented. This forms a solid base for the discussion in the following chapters.

2.1 I/Q Signal Processing

Modern digital communication standards have widely employed complex signals, consisting of in-phase and quadrature components with 90° phase difference. Exploiting such signals is known as I/Q signal processing. The behavior of these signals can be modeled using complex-valued algebra, where imaginary unit j, defined as $j^2 = -1$, is used [5, 73].

2.1.1 Complex Signals, Filters and Systems

The complex numbers consist of a real and an imaginary part, i.e., $x = x_{\mathrm{re}} + jx_{\mathrm{im}}$, where x_{re} and x_{im} denote the real and imaginary parts. In complex-valued signal processing, two parallel real signals are used to carry the information of a complex number. Thus, an I/Q signal is written as $x(t) = x_{\mathrm{I}}(t) + jx_{\mathrm{Q}}(t)$. In this thesis, I/Q notation is used for transmitted/received signals, whereas real and imaginary parts of, e.g., complex filter impulse responses are denoted with the subscripts re and im, respectively.

One of the interesting properties of complex signals is that they are not limited to spectral symmetry, i.e., they are not conjugate symmetric, as opposed to the real-valued signals whose spectrum is always symmetric around the zero frequency. Thus, for real signals $X_{\mathrm{re}}(f) = X^*_{\mathrm{re}}(-f)$, where $X_{\mathrm{re}}(f)$ is a Fourier transform (FT) of $x_{\mathrm{re}}(t)$, denoted as $X_{\mathrm{re}}(f) = \mathscr{F}(x_{\mathrm{re}}(t))$.

In addition to the complex-valued signals, complex-valued filters are also not limited to the frequency-symmetry of their real-valued counterparts [73]. Herein, the impulse

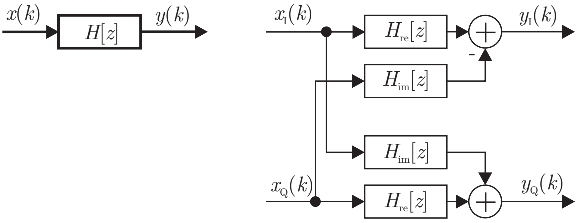

Figure 2.1: A complex-valued filter, shown with ideal complex-valued signals and parallel real I and Q signals having perfect matching between the rails.

response of a complex digital filter is denoted as $h(k) = h_{\mathrm{re}}(k) + jh_{\mathrm{im}}(k)$. Thus, the filter output is defined as

$$\begin{aligned} y(k) =& h(k) * x(k) \\ =& h_{\mathrm{re}}(k) * x_{\mathrm{I}}(k) - h_{\mathrm{im}}(k) * x_{\mathrm{Q}}(k) \\ &+ j(h_{\mathrm{re}}(k) * x_{\mathrm{Q}}(k) + h_{\mathrm{im}}(k) * x_{\mathrm{I}}(k)). \end{aligned} \tag{2.1}$$

From (2.1), it is clear that complex filtering can be realized with four real convolution operations as shown in Figure 2.1, where the z-domain transfer function of $h(k)$ is denoted as $H[z]$. A product of a complex signal and a complex-valued scalar multiplier is a special case of (2.1), having $h(k)$ as a scalar single-tap quantity $h = h_{\mathrm{re}} + h_{\mathrm{im}}$. For example, for a complex-valued integrator illustrated in Figure 2.2 with a single complex pole at M, the transfer function is

$$H[z] = \frac{1}{z - M} = \frac{z^{-1}}{1 - z^{-1}M}, \tag{2.2}$$

where the latter form nicely illustrates the delaying nature of the integrator [60]. At the same time, it should be noted that the real-valued implementation of a complex integrator, shown in Figure 2.2 is a second-order system while observing the I and Q responses separately. However, when combined into the complex form, the higher-order components cancel, giving the transfer function of (2.2).

Furthermore, a single-tap division of two complex-valued coefficients $a = a_{\mathrm{re}} + ja_{\mathrm{im}}$ and $b = b_{\mathrm{re}} + jb_{\mathrm{im}}$, is defined as

$$\frac{a}{b} = \frac{ab^*}{|b|^2} = \frac{a_{\mathrm{re}}b_{\mathrm{re}} + a_{\mathrm{im}}b_{\mathrm{im}} + j(a_{\mathrm{re}}b_{\mathrm{im}} - a_{\mathrm{im}}b_{\mathrm{re}})}{b_{\mathrm{re}}^2 + b_{\mathrm{im}}^2}. \tag{2.3}$$

Complex signal processing is utilized, e.g., in direct-conversion transmitters and receivers. In a direct-conversion transmitter a complex baseband waveform is multiplied with a complex exponential tone, consisting of cosine and sine as I and Q components, respectively, i.e., $e^{\pm j2\pi f_{\mathrm{C}}t} = \cos(2\pi f_{\mathrm{C}}t) \pm j\sin(2\pi f_{\mathrm{C}}t)$, oscillating at the RF carrier frequency f_{C}. Thereafter, the real part of this up-converted RF signal is used for actual transmission. This process is mathematically described as

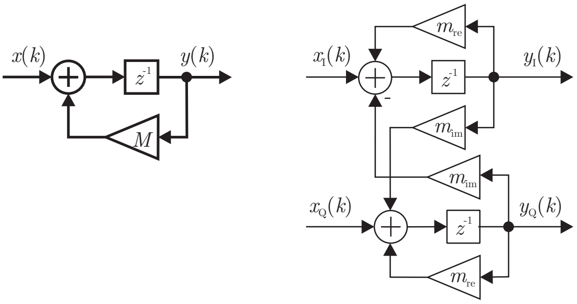

Figure 2.2: A complex-valued integrator, shown with ideal complex-valued signals and parallel real I and Q signals having perfect matching between the rails.

$$\begin{aligned} x_{\mathrm{RF}}(t) &= 2\mathrm{Re}[x(t)e^{j2\pi f_{\mathrm{C}}t}] \\ &= x(t)e^{j2\pi f_{\mathrm{C}}t} + x^*(t)e^{-j2\pi f_{\mathrm{C}}t} \\ &= 2x_{\mathrm{I}}(t)\cos(2\pi f_{\mathrm{C}}t) + 2x_{\mathrm{Q}}(t)\sin(2\pi f_{\mathrm{C}}t), \end{aligned} \tag{2.4}$$

where $x^*(t)$ denotes the complex conjugate of $x(t)$. The spectrum of $x^*(t)$ is a conjugate mirror image of the spectrum of $x(t)$, i.e., $\mathscr{F}(x^*(t)) = X^*(-f)$. Thus, the second line of (2.4) intuitively shows that the RF signal $x_{\mathrm{RF}}(t)$ is conjugate symmetric. It is exactly the $\mathrm{Re}[\cdot]$ operator that creates spectral symmetry to $x_{\mathrm{RF}}(t)$ by introducing the $x^*(t)e^{-j2\pi f_{\mathrm{C}}t}$ component.

Now, on the receiver side, this RF waveform $x_{\mathrm{RF}}(t)$ can be down-converted by first frequency-shifting it with a complex exponential tone of the opposite frequency. With real valued I/Q representation this corresponds to multiplying $x_{\mathrm{RF}}(t)$ with cosine and negative sine of the carrier frequency. The original baseband signal is thereafter recovered with lowpass filtering the frequency shifted signal. This is mathematically written as

$$\begin{aligned} x(t) &= h_{\mathrm{LP}}(t) * (x_{\mathrm{RF}}(t)e^{-j2\pi f_{\mathrm{C}}t}) \\ &= h_{\mathrm{LP}}(t) * (x_{\mathrm{RF}}(t)\cos(2\pi f_{\mathrm{C}}t)) - jh_{\mathrm{LP}}(t) * (x_{\mathrm{RF}}(t)\sin(2\pi f_{\mathrm{C}}t)), \end{aligned} \tag{2.5}$$

where $h_{\mathrm{LP}}(t)$ is the impulse response of the lowpass filter.

2.1.2 I/Q Mismatches in Complex Systems

Complex-valued linear signal processing discussed above can be extended to cover a concept of widely-linear systems [9, 73]. This means that in addition to the $x(t)$ itself, also its conjugate $x^*(t)$ is involved in the processing. In practice, this happens, for example, in complex filtering, defined in (2.1), implemented on a true circuit if the realizations of $h_{\mathrm{re}}(t)$ and $h_{\mathrm{im}}(t)$ operating on I and Q signals are not exactly equal. This phenomenon is known as I/Q mismatch or I/Q imbalance. Such a filter is illustrated in

Figure 2.3 with z-domain transfer functions. In this more general scenario, the output of the widely-linear, or I/Q mismatched, filter is

$$\begin{aligned} y(k) =& h_{\mathrm{re},1}(k) * x_{\mathrm{I}}(k) - h_{\mathrm{im},2}(k) * x_{\mathrm{Q}}(k) \\ &+ j(h_{\mathrm{re},2}(k) * x_{\mathrm{Q}}(k) + h_{\mathrm{im},1}(k) * x_{\mathrm{I}}(k)) \\ =& h_{\mathrm{nom}}(k) * x(k) + h_{\mathrm{cm}}(k) * x(k) + h_{\mathrm{diff}}(k) * x^*(k), \end{aligned} \tag{2.6}$$

where $h_{\mathrm{nom}}(k)$, $h_{\mathrm{cm}}(k)$ and $h_{\mathrm{diff}}(k)$ describe the nominal response, the common-mode error response and the differential error response, respectively [62]. The nominal response corresponds to the perfect matching scenario, the common-mode error results from a parallel error in the filters operating on the I and Q signals and the differential error is induced by opposite variations in the I and Q filters. Clearly, the common-mode error adds another component of nonconjugated $x(t)$. By combining the nominal and common-mode responses, the output of the widely-linear filter is $y(k) = h_{\mathrm{avg}}(k) * x(k) + h_{\mathrm{diff}}(k) * x^*(k)$, where

$$h_{\mathrm{avg}}(k) = \frac{h_{\mathrm{re},1}(k) + h_{\mathrm{re},2}(k)}{2} + j\frac{h_{\mathrm{im},1}(k) + h_{\mathrm{im},2}(k)}{2} \tag{2.7}$$

and

$$h_{\mathrm{diff}}(k) = \frac{h_{\mathrm{re},1}(k) - h_{\mathrm{re},2}(k)}{2} + j\frac{h_{\mathrm{im},1}(k) - h_{\mathrm{im},2}(k)}{2}. \tag{2.8}$$

At the same time, the corresponding z-domain transfer functions are obtained with z-transformations of (2.7) and (2.8) as

$$H_{\mathrm{avg}}[z] = \frac{H_{\mathrm{re},1}[z] + H_{\mathrm{re},2}[z]}{2} + j\frac{H_{\mathrm{im},1}[z] + H_{\mathrm{im},2}[z]}{2} \tag{2.9}$$

and

$$H_{\mathrm{diff}}[z] = \frac{H_{\mathrm{re},1}[z] - H_{\mathrm{re},2}[z]}{2} + j\frac{H_{\mathrm{im},1}[z] - H_{\mathrm{im},2}[z]}{2}. \tag{2.10}$$

The contribution of $h_{\mathrm{diff}}(k) * x^*(k)$ is known as MFI because of the spectral mirroring in the conjugation of $x(t)$ [9,62]. The severity of this interference is measured with IRR, being defined over the Nyquist frequency band as

$$IRR(e^{j2\pi f T_{\mathrm{S}}}) = 10\log_{10}\left|\frac{H_{\mathrm{avg}}(e^{j2\pi f T_{\mathrm{S}}})}{H_{\mathrm{diff}}(e^{j2\pi f T_{\mathrm{S}}})}\right|^2. \tag{2.11}$$

As a concrete example, the output of an I/Q mismatched complex integrator illustrated in Figure 2.4, given finally as $Y[z] = Y_{\mathrm{I}}[z] + jY_{\mathrm{Q}}[z]$, can be formed from the I and Q outputs

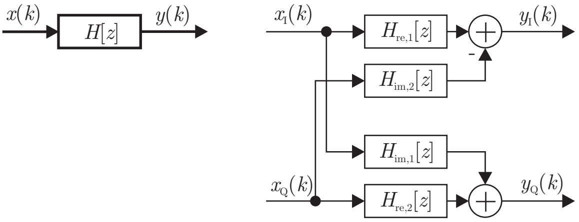

Figure 2.3: A complex-valued filter, shown with ideal complex-valued signals and parallel real I and Q signals having possible mismatch between the rails.

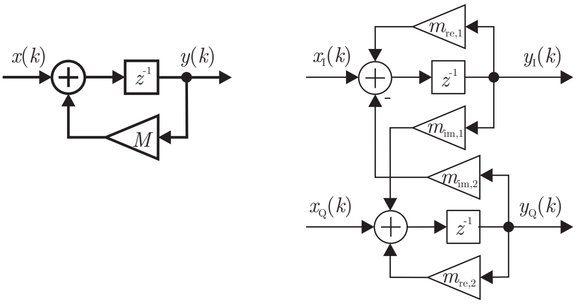

Figure 2.4: A complex-valued integrator, shown with ideal complex-valued signals and parallel real I and Q signals having possible mismatch between the rails.

$$Y_\mathrm{I}[z] = H_{\mathrm{re},1}[z]X_\mathrm{I}[z] - H_{\mathrm{im},2}[z]X_\mathrm{Q}[z], \tag{2.12}$$

$$Y_\mathrm{Q}[z] = H_{\mathrm{re},2}[z]X_\mathrm{Q}[z] + H_{\mathrm{im},1}[z]X_\mathrm{I}[z], \tag{2.13}$$

where

$$H_{\mathrm{re},1}[z] = \frac{z - m_{\mathrm{re},2}}{(z - m_{\mathrm{re},1})(z - m_{\mathrm{re},2}) + m_{\mathrm{im},1}m_{\mathrm{im},2}} \tag{2.14}$$

$$H_{\mathrm{re},2}[z] = \frac{z - m_{\mathrm{re},1}}{(z - m_{\mathrm{re},1})(z - m_{\mathrm{re},2}) + m_{\mathrm{im},1}m_{\mathrm{im},2}} \tag{2.15}$$

$$H_{\mathrm{im},1}[z] = \frac{m_{\mathrm{im},1}}{(z - m_{\mathrm{re},1})(z - m_{\mathrm{re},2}) + m_{\mathrm{im},1}m_{\mathrm{im},2}} \tag{2.16}$$

$$H_{\mathrm{im},2}[z] = -\frac{m_{\mathrm{im},2}}{(z - m_{\mathrm{re},1})(z - m_{\mathrm{re},2}) + m_{\mathrm{im},1}m_{\mathrm{im},2}}. \tag{2.17}$$

Now, the IRR of such integrator can be solved by applying (2.9)-(2.11).

2.1.3 Matrix Representation of Complex Numbers and Transfer Functions

Complex numbers and operations can also be represented in a matrix format [5,80]. To start with, a 1×2 vector contains the real and imaginary parts, or I and Q components, of a complex signal, i.e.,

$$\mathbf{x} = \left[\begin{array}{cc} x_{\mathrm{I}}(k) & x_{\mathrm{Q}}(k) \end{array} \right]. \tag{2.18}$$

Futhermore, widely linear operations can be written with the help of 2×2 matrices containing the four coefficients, i.e.,

$$\mathbf{A} = \left[\begin{array}{cc} a_{\mathrm{re},1} & a_{\mathrm{im},1} \\ -a_{\mathrm{im},2} & a_{\mathrm{re},2} \end{array} \right]. \tag{2.19}$$

Thus, the multiplication operation is written as

$$\begin{aligned} \mathbf{y} &= \mathbf{x}\mathbf{A} \\ &= \left[\begin{array}{cc} x_{\mathrm{I}}(k) & x_{\mathrm{Q}}(k) \end{array} \right] \left[\begin{array}{cc} a_{\mathrm{re},1} & a_{\mathrm{im},1} \\ -a_{\mathrm{im},2} & a_{\mathrm{re},2} \end{array} \right] \\ &= \left[\begin{array}{cc} a_{\mathrm{re},1} x_{\mathrm{I}}(k) - a_{\mathrm{im},2} x_{\mathrm{Q}}(k) & a_{\mathrm{im},1} x_{\mathrm{I}}(k) + a_{\mathrm{re},2} x_{\mathrm{Q}}(k) \end{array} \right], \end{aligned} \tag{2.20}$$

mathching with the single-tap special case of (2.6).

In similar manner, a widely-linear, or I/Q mismatched, version of the division of complex numbers presented in (2.3) can be written in matrix format by multiplying a matrix representing the numerator from right with an inverse of a matrix representing the denominator, i.e.,

$$\begin{aligned} \mathbf{A}\mathbf{B}^{-1} &= \left[\begin{array}{cc} a_{\mathrm{re},1} & a_{\mathrm{im},1} \\ -a_{\mathrm{im},2} & a_{\mathrm{re},2} \end{array} \right] \left[\begin{array}{cc} b_{\mathrm{re},1} & b_{\mathrm{im},1} \\ -b_{\mathrm{im},2} & b_{\mathrm{re},2} \end{array} \right]^{-1} \\ &= \frac{1}{b_{\mathrm{re},1} b_{\mathrm{re},2} + b_{\mathrm{im},1} b_{\mathrm{im},2}} \times \\ &\quad \left[\begin{array}{cc} a_{\mathrm{re},1} b_{\mathrm{re},2} + a_{\mathrm{im},1} b_{\mathrm{im},2} & -a_{\mathrm{re},1} b_{\mathrm{im},1} + a_{\mathrm{im},1} b_{\mathrm{re},1} \\ a_{\mathrm{re},2} b_{\mathrm{im},2} - a_{\mathrm{im},2} b_{\mathrm{re},2} & a_{\mathrm{re},2} b_{\mathrm{re},2} + a_{\mathrm{im},2} b_{\mathrm{im},1} \end{array} \right]. \end{aligned} \tag{2.21}$$

This is justified when the multiplying coefficient matrix is invertible, which holds in practical cases because of the 2×2 structure, where the real part (diagonal) elements share the same sign and the imaginary part (cross diagonal) elements have opposite signs, making the determinant nonzero.

Based on the matrix algebraic definitions for complex multiplication and division, it is also possible to write complex-valued, widely-linear, transfer function in matrix form. This, for example, allows studying I/Q mismatch effects in the transfer characteristics of complex filters. Gathering the transfer functions of (2.14)-(2.17) into a single widely-linear transfer function matrix allows presenting the total widely linear response with a simple matrix notation, given as

$$
\begin{aligned}
\mathbf{H} &= \begin{bmatrix} H_{\mathrm{re},1}[z] & H_{\mathrm{im},1}[z] \\ -H_{\mathrm{im},2}[z] & H_{\mathrm{re},2}[z] \end{bmatrix} \\
&= \begin{bmatrix} \frac{z-m_{\mathrm{re},2}}{(z-m_{\mathrm{re},1})(z-m_{\mathrm{re},2})+m_{\mathrm{im},1}m_{\mathrm{im},2}} & \frac{m_{\mathrm{im},1}}{(z-m_{\mathrm{re},1})(z-m_{\mathrm{re},2})+m_{\mathrm{im},1}m_{\mathrm{im},2}} \\ -\frac{m_{\mathrm{im},2}}{(z-m_{\mathrm{re},1})(z-m_{\mathrm{re},2})+m_{\mathrm{im},1}m_{\mathrm{im},2}} & \frac{z-m_{\mathrm{re},1}}{(z-m_{\mathrm{re},1})(z-m_{\mathrm{re},2})+m_{\mathrm{im},1}m_{\mathrm{im},2}} \end{bmatrix} \\
&= \frac{1}{(z-m_{\mathrm{re},1})(z-m_{\mathrm{re},2})+m_{\mathrm{im},1}m_{\mathrm{im},2}} \begin{bmatrix} z-m_{\mathrm{re},2} & m_{\mathrm{im},1} \\ -m_{\mathrm{im},2} & z-m_{\mathrm{re},1} \end{bmatrix} \\
&= \begin{bmatrix} z-m_{\mathrm{re},1} & -m_{\mathrm{im},1} \\ m_{\mathrm{im},2} & z-m_{\mathrm{re},2} \end{bmatrix}^{-1} \\
&= \left(\begin{bmatrix} z & 0 \\ 0 & z \end{bmatrix} - \begin{bmatrix} m_{\mathrm{re},1} & -m_{\mathrm{im},1} \\ m_{\mathrm{im},2} & m_{\mathrm{re},2} \end{bmatrix} \right)^{-1} \\
&= (\mathbf{I}z - \mathbf{M})^{-1}.
\end{aligned}
\tag{2.22}
$$

This approach is further utilized in Chapter 4 for analyzing the transfer functions of QΣΔMs.

2.2 Dynamic Spectrum Access Requirements for A/D Interface

Dynamic spectrum access aims for maximally efficient utilization of available RF spectrum [7,23,34,55,78,103]. However, in order to exploit locally or temporarily vacant frequency channels or bands, the transceiver hardware needs to be flexible [4,20,35,92,98]. In this section, these issues are discussed from the ADC point-of-view.

2.2.1 Dynamic Spectrum Access

The goal of the DSA is to find and utilize locally or temporarily unused parts of radio spectrum [7, 78]. The identification of such bands needs as accurate as possible information on the current spectrum usage, which can be obtained either from a central database or from ongoing spectrum sensing [45, 78, 79, 119]. In this thesis, the focus is on accessing the vacant operation bands in most efficient manner, assuming that information of such bands is available for the system.

2.2.2 Quadrature Sigma-Delta Modulator and Wideband Direct-Conversion Receiver

With a wideband DCR it is possible to access a number of transmission channels, i.e., frequency bands at once [72, 81, 91]. However, most of the channels might be occupied by someone else, being thus not of interest for the particular user. At the same time, converting these channels into digital information with high precision demands ADC resources, such as high sampling rate or number of quantization levels, draining the power of the device [66].

However, with a QΣΔM, it is possible to aim the available quantization and noise shaping resources on the bands of interest, while maintaining the ability to access multiple frequency channels, either at once or by reconfiguring the modulator response [P4]-[P7]. The first option is of interest when multiple noncontiguous bands are available at once, while the second case is realized when it is necessary, or beneficial, to change the operating band, e.g., in case of a frequency handoff. Such scenarios, where the transmission band needs to be changed are typical for DSA and CR receivers [7]. This combined with the wideband reception with reduced filtering makes the receiver signal conditions very dynamic and allows also high power level variations inside the reception band, creating possible blocker scenarios because of, e.g., MFI or nonlinear distortion originating from strong signals and falling on top of the weak ones [92].

2.2.3 Frequency Agile Operation

The QΣΔM response design allows noncontiguous multiband operation when the noise shaping notches are spread on separate bands. At the same time, the notch frequencies can be changed by tuning the modulator coefficients [P7]. In case of the transfer function design, multiband concept refers to designing multiple noncontiguous noise shaping notches, allowing reception of signals on noncontiguous frequency channels or slots. However, these signals can be located inside the same radio band or the same, e.g., cellular, transmission band.

The multiband reception allows increased robustness in frequency handoff scenarios were the transmission band needs to vacated. On one hand, the transmission can be continued on the remaining band(s) possibly still available if multiband transmission has been ongoing. On the other hand, the QΣΔM response can be reconfigured for new transmission band. These aspects are elaborated in more detail in Section 5.5 after discussing the transfer function design principles proposed in Chapter 5.

CHAPTER 3

Sigma-Delta Modulator Background and State-of-the-Art

Current technical literature contains a wealth of $\Sigma\Delta$ modulator variants, realizing different noise shaping effects and being impelemented with different techniques [102]. Regardless, all the architectures share common operation principle, having a STF shaping the input signal and a NTF shaping the quantization error. For discrete-time modulators, the ideal output of such general $\Sigma\Delta$ modulator can be expressed in z-domain as

$$V^{\mathrm{id}}[z] = STF[z]U[z] + NTF[z]E[z], \tag{3.1}$$

where $U[z]$ and $E[z]$ are the input signal and the quantization error, being shaped by the respective transfer function responses [19, 102]. While combined with high enough oversampling for the desired waveform to be converted, the NTF removes the quantization error efficiently from the band of this signal, allowing high SNRs even with only 1-bit quantization [19].

Later in this chapter, the most important characteristics of the common $\Sigma\Delta$ modulator variants are pointed out, having emphasis on the applicability to the DSA and CR. The discussion is divided into two parts; the Sections 3.2-3.4 discuss different noise shaping options, whereas Sections 3.5-3.8 concentrate on available implementation architectures.

3.1 Sigma-Delta Modulator History

The principle of $\Sigma\Delta$ modulation was first proposed in [56, 57]. Thereafter, the modulation technique was applied in A/D conversion in [28, 30, 31, 114] and the quantization noise structure was more thoroughly studied in [29, 30, 48, 50]. In [30], the linearized model for the modulator, introduced in [24], was found to predict the mean-squared quantizer error accurately. Although, the actual error is not uncorrelated with the input, as assumed in the linearized model [48, 51]. The effects of the nonlinear quantization were discussed in case of sinusoidal inputs in [13]. The exact structure of the quantization error is thoroughly discussed in [49, 51]. However, the linearized model has been applied widely for the purpose of transfer function analysis in more complex modulator structures [102].

Furthermore, higher order ΣΔ modulation with double integration was proposed in [29]. Later, in [100], the optimization of higher order modulator transfer functions was discussed in more detail. Multistage noise shaping A/D and digital-to-analog (D/A) converters were discussed originally in [37, 111]. At the same time, bandpass ΣΔ modulation was discussed in [63, 101] and developed further, e.g., in [64]. In parallel, also multiband noise shaping using parallel signal branches and ΣΔ modulators was proposed for the first time in [16–18]. Furthermore, complex bandpass ΣΔ modulator, i.e., a QΣΔM, in an ADC was discussed in [61] and implemented for the first time in [109]. Complex transfer function in case of bandpass and parallel multiband ΣΔ modulation are discussed also in [18]. In [19], different ΣΔ variants are explained in an overview manner.

3.2 Lowpass Modulator

A lowpass ΣΔ modulator is the traditional way of doing quantization noise shaping [19, 102]. A general Pth order modulator is illustrated in Figure 3.2. The ideal STF and NTF of such modulator are

$$STF[z] = z^{-P}, \tag{3.2}$$

$$NTF[z] = (1 - z^{-1})^{P}, \tag{3.3}$$

respectively. The NTF response is of highpass type, clearly pushing the quantization error toward higher frequencies. This is also illustrated in Figure 3.1 with simple first-order responses. In Figure 3.2, the STF is a pure delay, but generally it can have lowpass response, attenuating high-frequency input content. The lowpass ΣΔ modulators have been employed extensively, e.g., in audio applications, where high oversampling is easily attained [19]. In addition, they are suitable for narrowband direct-conversion radio receivers. For conversion of wideband waveforms, the NTF zeros can be spread around the zero frequency in order to obtain optimized SNR [100]. This kind of NTF is obtained by replacing one or more of the loop integrators with a resonator having a low-frequency pole, realizing thus a low-frequency NTF zero [19, 43]. The resonators are further exploited as loop filters in bandpass ΣΔ modulators, where the center of the noise shaping notch is placed on a nonzero frequency [19].

3.3 Bandpass Modulator

When the ΣΔ principle is extended to bandpass noise shaping, the poles and zeros of the transfer functions can be moved away from the zero frequency by using bandpass resonators instead of integrators as loop filters [19, 63, 87, 98, 99, 102]. This gives additional

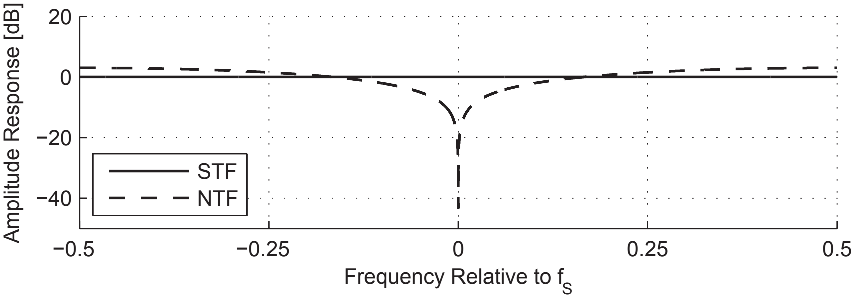

Figure 3.1: Example STF and NTF of a first-order ($P = 1$) lowpass $\Sigma\Delta$ modulator.

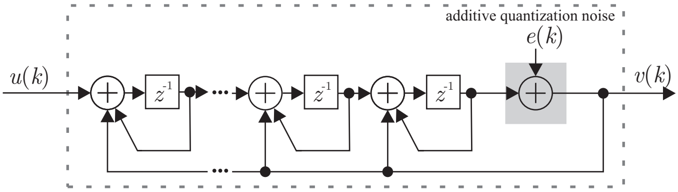

Figure 3.2: A Pth order lowpass $\Sigma\Delta$ modulator with delaying integrators placing the NTF zeros at the baseband.

degree-of-freedom for design of the responses. In practice, the NTF is of bandstop type, pushing quantization noise away from certain IF. At the same time, the STF can be designed to have bandpass response. In addition, the poles and zeros can be spread over the desired signal band in order to optimize the inband SNR [100]. However, because of the real valued resonators as loop filters, the transfer functions are limited to behave symmetrically around the zero frequency.

A simple example of bandpass $\Sigma\Delta$ modulator is shown in Figure 3.4. The ideal STF and NTF are given as

$$STF[z] = z^{-2P}, \tag{3.4}$$

$$NTF[z] = (1 + z^{-2})^{P}, \tag{3.5}$$

respectively. Thus, the modulator creates a symmetric noise shaping notch on the frequencies $\pm f_S/4$, pushing the noise towards low and high frequencies. This is illustrated with example transfer functions in Figure 3.3.

The bandpass $\Sigma\Delta$ modulation fits well in with IF receivers implementing the analog part with real valued signal processing [98, 99]. These include, e.g., superheterodyne receivers or real IF sampling receivers with digital quadrature down-conversion [99].

3.4 Quadrature Bandpass Modulator

Employing complex valued signal processing, the $\Sigma\Delta$ principle can be extended to quadrature bandpass modulation [19, 59–61, 102]. With the parallel I/Q rails and cross-

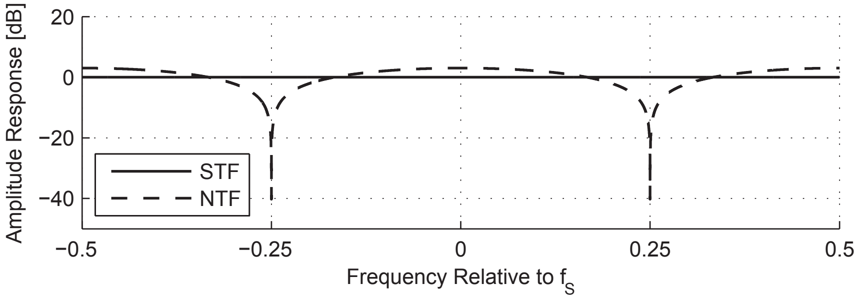

Figure 3.3: Example STF and NTF of a first-order ($P = 1$) real bandpass $\Sigma\Delta$ modulator. From the implementation point-of-view, the order is doubled for creating two poles and zeros for each transfer function.

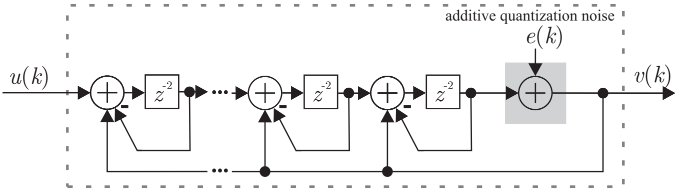

Figure 3.4: A Pth order real bandpass $\Sigma\Delta$ modulator with delaying bandpass resonators placing the NTF zeros at $\pm f_{\mathrm{S}}/4$.

connections between the rails, the NTF can have complex bandstop response, while the STF can be of complex bandpass type [61]. This allows frequency asymmetric responses for both the transfer functions.

The ideal STF and NTF of a general Nth-order Q$\Sigma\Delta$M, illustrated in Figure 3.6, are given by

$$STF[z] = \frac{A + \sum\limits_{p=1}^{P} B^{(p)} \prod\limits_{i=1}^{p} \frac{z^{-1}}{1-M^{(i)}z^{-1}}}{1 - \sum\limits_{p=1}^{P} R^{(p)} \prod\limits_{i=1}^{p} \frac{z^{-1}}{1-M^{(i)}z^{-1}}}, \tag{3.6}$$

$$NTF[z] = \frac{1}{1 - \sum\limits_{p=1}^{P} R^{(p)} \prod\limits_{i=1}^{p} \frac{z^{-1}}{1-M^{(i)}z^{-1}}}, \tag{3.7}$$

respectively, [P3]-[P7]. In simplified first-order scenario, employing only the rightmost complex integrator of Figure 3.6, the ideal ouput is given as

$$V^{\mathrm{id}}[z] = \frac{A + (B^{(1)} - M^{(1)}A)z^{-1}}{1 - (R^{(1)} + M^{(1)}1)z^{-1}} U[z] + \frac{1 - M^{(1)}z^{-1}}{1 - (R^{(1)} + M^{(1)})z^{-1}} E[z]. \tag{3.8}$$

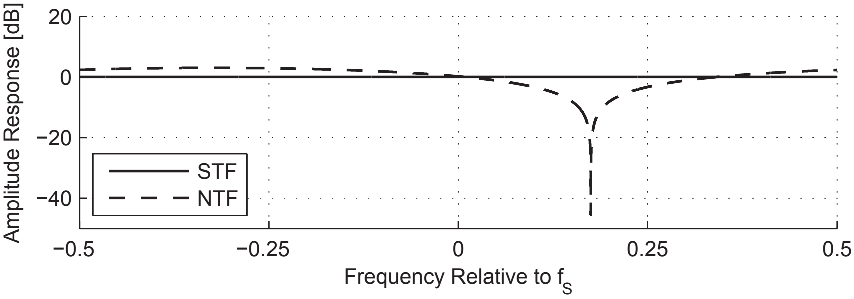

Figure 3.5: Example STF and NTF of a first-order ($P = 1$) quadrature bandpass ΣΔ modulator. From the real-valued implementation point-of-view, the order is doubled for creating two poles and zeros for each transfer function while the 90° phase shift between the I and Q rails actually cancels the other pole and zero.

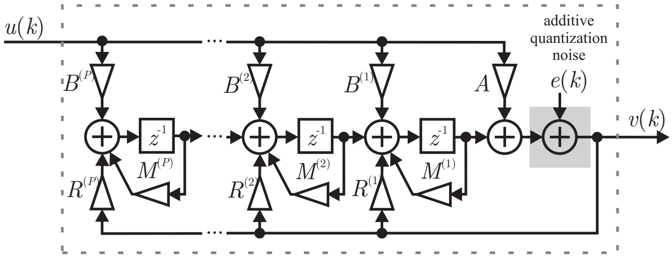

Figure 3.6: A Pth order quadrature ΣΔ modulator with delaying complex-valued integrators, where the integrator poles $M^{(1)} - M^{(P)}$ define the NTF zero positions.

From (3.8), it is visible that when the modulator coefficients A, $B^{(1)}$, $M^{(1)}$ and $R^{(1)}$ have specific values, the analysis can be simplified. Specifically, when $R^{(1)} = -M^{(1)}$, the denominator of the transfer functions goes to unity, meaning that the pole is set to the origin. At the same time, when $A = 0$ and $B^{(1)} = 1$, the numerator of the STF equals z^{-1}, i.e., also the STF zero is set to the origin. The numerator of the NTF sets the NTF zero to $M^{(1)}$, resulting in a noise shaping notch on the relative frequency defined by $\angle M^{(1)}$. This kind of first-order transfer functions are illustrated in Figure 3.5, having $\angle M^{(1)}$ equal to 0.175.

Generally, the loop filter feedback coefficients from $M^{(1)}$ to $M^{(P)}$ define the positions of the NTF zeros. This is considered as a starting point for the coefficient design and the NTF zeros are traditionally placed on the desired signal band [100]. However, it is possible to place certain amount of zeros, e.g., on the mirror band [60]. Second, the input coefficients A and $B^{(1)}$ to $B^{(P)}$ define the positions of the STF zeros [60]. These can be used to create frequency selectivity for the STF and include, e.g., part of the receiver selectivity inside the QΣΔM [60], [P3]. Finally, the feedback coefficients from $R^{(1)}$ to $R^{(P)}$ define the positions of the common poles for both of the transfer functions. The fact that the transfer functions share common poles is emphasized in (3.6)-(3.8) the STF and NTF having common denominators. If, e.g., a finite impulse-response

(FIR) transfer functions are desired, the common denominator can be set to unity, thus placing the poles into the origin.

Quadrature $\Sigma\Delta$ modulation is well-fitting solution for IF receivers employing analog I/Q down-conversion, or direct-conversion wideband receivers, where the desired signal lies on a nonzero IF frequency [59–61]. In wideband A/D conversion, where multiple signals are to be digitized with good resolution, Q$\Sigma\Delta$M allows also multiband noise shaping, creating noncontiguous NTF notches [P3]-[P6]. Furthermore, SNR optimization principles similar to lowpass $\Sigma\Delta$ modulators [100] can be used, having lowpass modulation as a special case with the NTF notch center frequency being exactly zero [P4, P7]. The analysis and design of such transfer functios are further discussed in Chapters 4 and 5.

3.5 Single-Stage vs. Multistage

The noise shaping capabilities of a $\Sigma\Delta$ modulator can be improved by increasing the order of a traditional single-stage modulator, as discussed earlier in this chapter. Concretely, this means, for example for a Q$\Sigma\Delta$M, that the NTF can contain higher number of notches, making the noise shaping more efficient. However, the order is limited by the modulator stability [19, 100, 102]. The stability characteristics are affected by the actual implemented NTF and the range of the applied input signal [100, 102]. In practice, robust modulators of higher order than four are rare in the current literature, and most of the designs implement orders even lower than that [102]. The stability analysis is highly tortuous because of nonlinear quantization inside the modulator loop [13, 96, 100, 102]. Multiple rule-of-thumb kind of approximate criteria exist, but, after all, thorough simulations are advised [102].

Because the stability limits the noise shaping performance of a single stage, a wide range of different multistage structures have been proposed for improving the resolution of a $\Sigma\Delta$ ADC [53, 70, 94, 95], [P4-P6]. When the overall noise shaping is implemented in, e.g., two cascaded stages, the individual stages can have lower order and thus be more easily designed stable. The order of the overall noise shaping equals the combined order of all the stages.

Originally, the multistage $\Sigma\Delta$ modulation was proposed to use output of the first stage as an input for the latter stage [37, 53, 94, 95]. However, more recent literature generally considers the quantization error of the first stage to be digitized by the following stage and then subtracted from the output of the first stage [19, 32, 67, 68, 70, 94, 102, 105, 106, 110]. A general L-stage Q$\Sigma\Delta$M using previous stage quantization error as an input for the following one is illustrated in Figure 3.7. The ideal output of such modulator is

$$V^{\mathrm{id}}[z] = \sum_{l=1}^{L} (-1)^{l+1} H_l^D[z] V_l^{\mathrm{id}}[z], \tag{3.9}$$

where $H_l^D[z]$ and $V_l^{\mathrm{id}}[z]$ are the digital matching filters and outputs of individual stages, respectively [P4, P7]. The digital matching filter transfer functions are

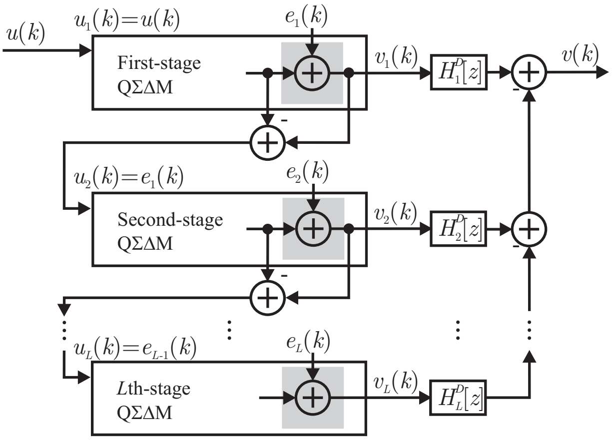

Figure 3.7: Multistage QΣΔM with arbitrary-order noise shaping in all the individual stages. Filters $H_1^D[z]$ to $H_L^D[z]$ are implemented digitally.

$$H_l^D[z] = \frac{H_1^D[z] \prod_{l=1}^{L-1} NTF_l^{\text{id}}[z]}{\prod_{l=2}^{L} STF_l^{\text{id}}[z]}, \; l \in \{1, 2, ..., L\}. \tag{3.10}$$

and the stage outputs are

$$V_l^{\text{id}}[z] = STF_l^{\text{id}}[z] U_l[z] + NTF_l^{\text{id}}[z] E_l[z], \; l \in \{1, 2, ..., L\}. \tag{3.11}$$

On the other hand, the output of an ideal general multistage ΣΔ modulator in (3.9) can be rewritten using a total STF and a total NTF for the last stage quantization error describing the transfer characteristics of the whole modulator for the respective components. In this way, the output becomes

$$\begin{aligned} V^{\text{id}}[z] =& STF_1^{\text{id}}[z] STF_2^D[z] U[z] + \frac{\prod_{l=1}^{L} NTF_l^{\text{id}}[z]}{\prod_{l=3}^{L} STF_l^{\text{id}}[z]} E_L[z] \\ =& STF_{\text{TOT}}^{\text{id}}[z] U[z] + NTF_{\text{TOT}}^{\text{id}}[z] E_L[z], \end{aligned} \tag{3.12}$$

from where you can easily see that the total STF consists of the STFs of the first two stages, having the contribution of the second-stage STF coming from the digital $H_1[z]$. The total NTF is defined by all the L stage NTFs and STFs also. Thus, the STFs of the latter stages do not affect the input signal itself, but only the noise shaping.

3.6 Discrete-Time vs. Continuous-Time

The $\Sigma\Delta$ modulators can be divided into two classes based on at which point inside the ADC the sampling process takes place. Depending on that, the $\Sigma\Delta$ loop processing is either discrete-time or continuous-time (CT) [29, 104]. In discrete-time modulators, the sampling is done before the $\Sigma\Delta$ loop, whereas in the CT variant the sampling takes place inside the loop, usually just before the quantization.

The discrete-time modulators are implemented with switched-capacitor (SC) technique. The SC implementation has certain limitations, for example, the settling time of the circuitry limits the frequency that the $\Sigma\Delta$ loop filter can be driven with [102]. However, the SC circuits have good accuracy and linearity, and their accurate analysis is more straightforward [102].

In CT $\Sigma\Delta$ modulators, the loop naturally operates in continuous-time. This allows driving the circuit with higher frequency, making it possible to obtain wider bandwidths for the whole modulator [102]. In addition, while the sampling is done inside the $\Sigma\Delta$ loop, the loop filter creates inherent anti-aliasing filtering [102]. Another clear benefit for the CT processing is that the sampling errors, like jitter, that happen inside the $\Sigma\Delta$ loop are shaped by the NTF in similar manner as the quantization error [102]. However, when the feedback branch digital-to-analog converter (DAC) needs to create a continuous-time waveform, the related jitter is acknowledged to degrade the modulator performance [41].

Generally, also the CT modulators are designed based on a discrete-time prototype [102]. First, a discrete-time modulator realizing the desired STF and NTF are designed and then the loop functionality is transformed into continuous-time. Thus, designing CT modulators has extra complexity compared to the discrete-time SC modulators.

3.7 Quadrature Bandpass Sigma-Delta Modulator State-of-the-Art

Until now, the most classical work in the field of Q$\Sigma\Delta$Ms is [60], proposing a fourth-order modulator implementation with STF selectivity and NTF design putting one of the zeros on the mirror-band in order to reduce mirrored noise on desired signal band. At the same time, [62] concentrates on discussing the I/Q mismatch effects on the Q$\Sigma\Delta$Ms, introducing the ISTF and INTF. Placing an NTF zero on the image band, in order to reduce the mirroring of the image band quantization noise to the desired signal band is first proposed in [62]. The main results of [60, 62] are used also in [59].

After the introduction, Q$\Sigma\Delta$Ms have gathered increasing attention and implemented modulators have been reported, e.g., in [14, 15, 21, 36, 54, 71]. Generally, reconfigurable and tunable $\Sigma\Delta$ modulators have been considered as a promising solution for SDR A/D interface [58, 65, 86, 98, 108, 115].

From the I/Q correction point-of-view, in [59], digital post-compensation of MFI, shortly mentioned also in [109], is noted as an interesting future work topic, in addition to doing capacitor swapping between the channels. The DSP compensation approach in [109] uses least-mean-square (LMS) adapted FIR filter for shaping the conjugated mirror-band signal content and then subtracts the filter output from the desired signal band. Herein, this idea is developed further and the LMS adaptation is replaced with circularity restoring algorithm published in [12]. Furthermore, a transfer function design dealing with this problem and facilitating digital MFI post-compensation is proposed in [P5-P7] and discussed in Chapter 5. In [109], it was speculated if the mirror-band notch in the NTF could be removed when using digital MFI compensation. This would, however, make compensation of the MFI originating from the mirror-band signal content a troublesome task, the signal being masked by significant amount of quantization noise. These problematics are elaborated in Chapter 5 and [P5-P7].

For the MFI mitigation or compensation, also multiple analog techniques have been proposed, including swapping between the I and Q rails [82, 89], element matching [6, 25, 26], double sampling [93] and STF modification without any additional circuitry [P3, P4]. At the same time, another digital MFI cancellation approach using inserted calibration signal is proposed in [117].

Generally, the mitigation and compensation approaches concentrating on mitigating the I/Q mismatches inside the QΣΔM itself [6, 25, 26, 89, 93, 118] do not consider other error sources, such as an I/Q mismatched quadrature mixer preceding the modulator. However, from the receiver performance point-of-view, this is a significant point of attention. Digital compensation methods for the mixer I/Q imbalance are proposed, e.g., in [9–12, 47, 52, 90]. However, in these works, it is assumed that the mirror band signal, acting as a MFI source, is available for the compensation processing in digital domain. Thus, exploiting these approaches in QΣΔM context needs certain modification for the STF and NTF, as well as for the filtering preceding the QΣΔM. These aspects are discussed in [P5]-[P7], proposing a transfer function design facilitating digital post-compensation for the MFI induced by the whole receiver chain. When this transfer function design is combined with, e.g., the circularity restoring approach in [9–12] the MFI compensation can be done without inserting additional calibration data.

3.8 Proposed Quadrature Bandpass Modulator Architectures

The analysis in this thesis concentrates on the discrete-time ΣΔ modulators but most of the concepts presented can potentially be extended to cover also CT implementations. This is interesting direction for the scientific research because recently the CT modulators have gained increasing interest, also in commercial use, especially in applications demanding large bandwidth. Wideband, or RF sampling, SDRs are a good example of such applications.

The ΣΔ modulators designs are usually separated into four different architectures based on how the feedback and feedforward branches are treated and if integrators or resonators are employed. The modulator structure studied in this thesis follows the QΣΔM structure originally presented in [60], being a recognized work in scientific literature. This structure is a complex variant of cascade-of-integrators with distributed feedback (CIFB) architecture. The structure is chosen because of its generality and flexiblity for both STF and NTF design. The zeros of the STF and NTF are controlled by the input coefficients and loop filter coefficients, respectively. The common poles for both the transfer functions are set by the feedback coefficients. For higher-order noise shaping in multiband receivers, also multistage noise shaping with cascaded QΣΔM stages is considered.

The general transfer function analysis presented in Chapter 4 covers arbitrary-order single-stage QΣΔMs, as well as multistage modulators with an arbitrary number of stages. Practical examples are given with second- and fourth-order QΣΔM stages, as a single-stage modulator or being combined to form a two- or three-stage modulator.

CHAPTER 4

Quadrature Modulator Transfer Function Analysis under Implementation Inaccuracies

THIS chapter presents a matrix algebraic analysis method for the four transfer functions (STF, ISTF, NTF and INTF) of a general multistage QΣΔM with arbitrary number of arbitrary-order stages under implementation inaccuracies. This gives designer a straightforward possibility to study the effects of, e.g., the inherent I/Q mismatches in more detail before implementing and measuring the actual device. This work was started in [74] and carried on in [P1-P4], resulting finally in the generalized matrix-algebraic analysis method presented in [P7].

Sections 4.1 and 4.2 present the derivation of the general QΣΔM mismatch model. Thereafter, in Sections 4.3 and 4.4, the insight obtained from the presented transfer function analysis is used to explain the roles of differing I/Q mismatch locations in a wideband DCR employing a QΣΔM for A/D conversion. Finally, Section 4.5 discusses the implementation inaccuracy effects on the QΣΔM stability.

4.1 Arbitrary-Order Single-Stage Modulator I/Q Mismatch Analysis

The matrix representation of complex numbers shown in Chapter 2 is used to derive the transfer functions and output of a single-stage QΣΔM used as a stand-alone modulator or as an individual stage of a multistage modulator. The single-stage modulator is a special case of the stage number L being one. The derivation is based on the ideal transfer functions presented in Chapter 3. Now, the scalar multiplications in (3.6) and (3.7) are replaced with matrix multiplications applying the inaccurately implemented QΣΔM coefficients. These coefficients are illustrated in Figure 4.1 for the lth stage of a multistage QΣΔM having order P. Therein, the complex-valued structure of Figure 3.6

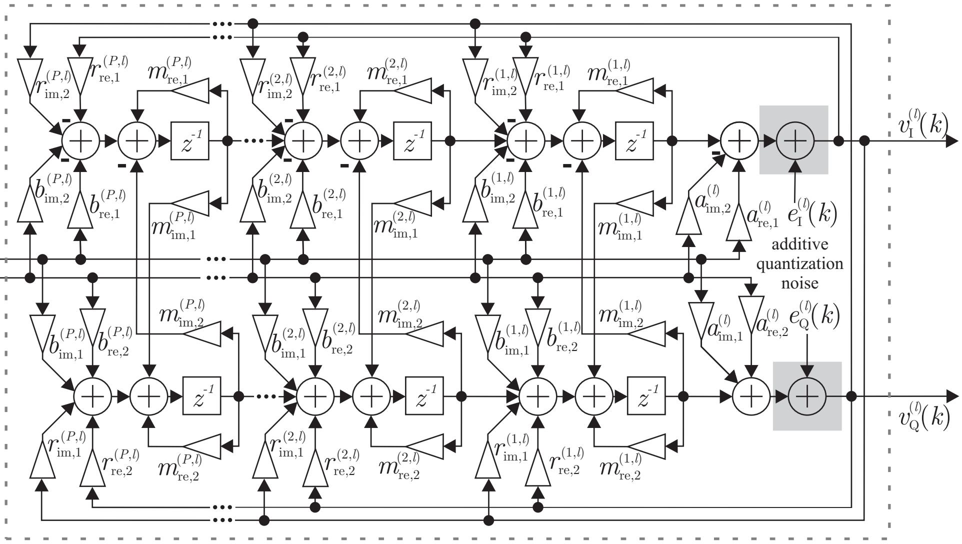

Figure 4.1: Principal implementation structure of the lth QΣΔM stage of order P in a multistage QΣΔM with parallel real signals and coefficients taking possible mismatches into account.

is drawn with parallel real-valued I/Q rails and coefficients. One of the benefits of this method is that analyzing all the separate signal paths of such a complicated structure can be avoided.

The input coefficients in the branch feeding the quantizer of the lth stage are defined by

$$\mathbf{A}^{(l)} = \begin{bmatrix} a^{(l)}_{\mathrm{re},1} & a^{(l)}_{\mathrm{im},1} \\ -a^{(l)}_{\mathrm{im},2} & a^{(l)}_{\mathrm{re},2} \end{bmatrix}. \tag{4.1}$$

In a similar manner, the rest of the input coefficients of the lth stage are defined by

$$\mathbf{B}^{(p,l)} = \begin{bmatrix} b^{(p,l)}_{\mathrm{re},1} & b^{(p,l)}_{\mathrm{im},1} \\ -b^{(p,l)}_{\mathrm{im},2} & b^{(p,l)}_{\mathrm{re},2} \end{bmatrix}, \tag{4.2}$$

where $p \in \{1, 2, ..., P\}$, going through the branches. Likewise, the loop filter and feedback coefficients are defined by

$$\mathbf{M}^{(p,l)} = \begin{bmatrix} m^{(p,l)}_{\mathrm{re},1} & m^{(p,l)}_{\mathrm{im},1} \\ -m^{(p,l)}_{\mathrm{im},2} & m^{(p,l)}_{\mathrm{re},2} \end{bmatrix} \tag{4.3}$$

and

$$\mathbf{R}^{(p,l)} = \begin{bmatrix} r_{\text{re},1}^{(p,l)} & r_{\text{im},1}^{(p,l)} \\ -r_{\text{im},2}^{(p,l)} & r_{\text{re},2}^{(p,l)} \end{bmatrix}, \tag{4.4}$$

having $p \in \{1, 2, ..., P\}$ again.

Now, the matrices can be inserted in (3.6) in place of the ideal scalar coefficients, resulting in

$$\begin{aligned} &\begin{bmatrix} STF_{\text{re},1}^{(l)}[z] & STF_{\text{im},1}^{(l)}[z] \\ -STF_{\text{im},2}^{(l)}[z] & STF_{\text{re},2}^{(l)}[z] \end{bmatrix} = \\ &\left(\mathbf{A}^{(l)} + \sum_{p=1}^{P} \mathbf{B}^{(p,l)} \prod_{i=1}^{p} \mathbf{I} z^{-1} \left(\mathbf{I} - \mathbf{M}^{(i,l)} z^{-1}\right)^{-1}\right) \times \\ &\left(\mathbf{I} - \sum_{p=1}^{P} \mathbf{R}^{(p,l)} \prod_{i=1}^{p} \mathbf{I} z^{-1} \left(\mathbf{I} - \mathbf{M}^{(i,l)} z^{-1}\right)^{-1}\right)^{-1}. \end{aligned} \tag{4.5}$$

where $STF_{\text{re},1}^{(l)}[z]$, $STF_{\text{im},1}^{(l)}[z]$, $STF_{\text{im},2}^{(l)}[z]$ and $STF_{\text{re},2}^{(l)}[z]$ are the parallel real components of the widely-linear I/Q mismatched lth stage STF denoted as $STF^{(l)}[z]$.

Similarly, the $NTF_{\text{re},1}^{(l)}[z]$, $NTF_{\text{im},1}^{(l)}[z]$, $NTF_{\text{im},2}^{(l)}[z]$ and $NTF_{\text{re},2}^{(l)}[z]$ can be solved by substituting the scalar coefficients of (3.7) with the matrices (4.1)-(4.4), giving

$$\begin{aligned} &\begin{bmatrix} NTF_{\text{re},1}^{(l)}[z] & NTF_{\text{im},1}^{(l)}[z] \\ -NTF_{\text{im},2}^{(l)}[z] & NTF_{\text{re},2}^{(l)}[z] \end{bmatrix} = \\ &\left(\mathbf{I} - \sum_{p=1}^{P} \mathbf{R}^{(p,l)} \prod_{i=1}^{p} \mathbf{I} z^{-1} \left(\mathbf{I} - \mathbf{M}^{(i,l)} z^{-1}\right)^{-1}\right)^{-1}. \end{aligned} \tag{4.6}$$

Now, The actual STF and the ISTF can be solved [62] by

$$STF_l[z] = \frac{STF_{\text{re},1}^{(l)}[z] + STF_{\text{re},2}^{(l)}[z]}{2} + j\frac{STF_{\text{im},1}^{(l)}[z] + STF_{\text{im},2}^{(l)}[z]}{2} \tag{4.7}$$

and

$$ISTF_l[z] = \frac{STF_{\text{re},1}^{(l)}[z] - STF_{\text{re},2}^{(l)}[z]}{2} + j\frac{STF_{\text{im},1}^{(l)}[z] - STF_{\text{im},2}^{(l)}[z]}{2}, \tag{4.8}$$

respectively. In parallel, the lth stage complex NTF and INTF can be solved by

$$NTF_l[z] = \frac{NTF_{\text{re},1}^{(l)}[z] + NTF_{\text{re},2}^{(l)}[z]}{2} + j\frac{NTF_{\text{im},1}^{(l)}[z] + NTF_{\text{im},2}^{(l)}[z]}{2} \tag{4.9}$$

and

$$INTF_l[z] = \frac{NTF_{\mathrm{re},1}^{(l)}[z] - NTF_{\mathrm{re},2}^{(l)}[z]}{2} + j\frac{NTF_{\mathrm{im},1}^{(l)}[z] - NTF_{\mathrm{im},2}^{(l)}[z]}{2}, \tag{4.10}$$

respectively [62]. Finally, the output of such QΣΔM stage is

$$V_l[z] = STF_l[z]U[z] + ISTF_l[z]U_l^*[z^*] + NTF_l[z]E_l[z] + INTF_l[z]E_l^*[z^*], \tag{4.11}$$

where $U_l[z]$ is the input signal and $U_l^*[z^*]$ is the complex conjugate of the input signal, $E_l[z]$ is the quantization noise and $E_l^*[z^*]$ is the complex conjugate of the quantization noise. This also illustrates how the individual signal components are shaped by the four transfer functions in (4.7)-(4.10).

4.2 Multistage Modulator I/Q Mismatch Analysis

Herein, the above results are utilized in deriving the behavior of a general multistage QΣΔM having arbitrary number of stages, as illustrated in Figure 3.7. In addition, a simplified two-stage QΣΔM, i.e., having $L = 2$, is shown in Figure 3 of [P1]. With the help of (4.11), the output of a general L-stage QΣΔM can be written as

$$V[z] = \sum_{l=1}^{L} (-1)^{l+1} H_l^D[z] V_l[z], \tag{4.12}$$

where $H_l^D[z]$ are the digital matching filters defined in (3.10). Assuming the quantization noise of a previous stage as input of the following one, (4.12) can be rewritten as

$$\begin{aligned} V[z] =& H_1^D[z]\Big(STF_1[z]U[z] + ISTF_1[z]U^*[z^*] \\ &+ NTF_1[z]E_1[z] + INTF_1[z]E_1^*[z^*]\Big) \\ &+ \sum_{l=2}^{L} (-1)^{l+1} H_l^D[z]\Big(STF_l[z]E_{l-1}[z] + ISTF_l[z]E_{l-1}^*[z^*] \\ &+ NTF_l[z]E_l[z] + INTF_l[z]E_l^*[z^*]\Big). \end{aligned} \tag{4.13}$$

Finally, from (4.13), it is possible to deduce the overall transfer functions for the input signal and the quantization noise of all L stages and respective conjugate components, given as

$$\begin{aligned}
STF_{\text{TOT}}[z] &= H_1^D[z]STF_1[z],\\
ISTF_{\text{TOT}}[z] &= H_1^D[z]ISTF_1[z],\\
NTF_{\text{TOT},l}[z] &= H_l^D[z]NTF_l[z] - H_{l+1}^D[z]STF_{l+1}[z], l \in \{1, 2, ..., L-1\},\\
INTF_{\text{TOT},l}[z] &= H_l^D[z]INTF_l[z] + H_{l+1}^D[z]ISTF_{l+1}[z], l \in \{1, 2, ..., L-1\},\\
NTF_{\text{TOT},L}[z] &= H_L^D[z]NTF_L[z],\\
INTF_{\text{TOT},L}[z] &= H_L^D[z]INTF_L[z].
\end{aligned} \tag{4.14}$$

With the definitions of (4.14), the overall output of an general multistage QΣΔM can be written as

$$\begin{aligned}
V[z] =& STF_{\text{TOT}}[z]U[z] + ISTF_{\text{TOT}}[z]U^*[z^*]\\
&+ \sum_{l=1}^{L} NTF_{\text{TOT},l}[z]E[z] + INTF_{\text{TOT}}E_l^*[z^*].
\end{aligned} \tag{4.15}$$

The behavior of the defined output signal and characteristics of the total transfer functions under implementation inaccuracies are illustrated in discussed further in Section 4.4 and illustrated with selected multistage designs in Chapter 5.

4.3 Observations on Separate I/Q Mismatch Locations in a Single-Stage Modulator

The effects of different I/Q mismatch sources inside a first-order single-stage QΣΔM are studied in [74] and [P3]. In addition, a DCR has additional MFI sources, when considering the whole receiver chain, namely a downconverting I/Q mixer and thereafter separate I and Q baseband rails with filters and amplifiers. Herein, the results presented in [P3] are complemented with examples using a 4th order single-stage QΣΔM for generality. The observations in this section are based on the derivations and analysis presented in Section 4.1 and [P7] and evaluation of (4.5)-(4.10) in the discussed scenarios. The z-domain transfer functions in presented scenarios are solved using Matlab [76] Symbolic Math toolbox [77], whereafter the frequency responses are evaluated with $z \leftarrow e^{j2\pi f}$ replacement.

4.3.1 Downconverting I/Q Mixer and Analog Baseband

From the signal response point-of-view, having I/Q mismatch in the receiver chain preceding the QΣΔM has similar nature as the I/Q mismatches in the modulator input coefficients discussed in detail in the following sub-section 4.3.2. Therein, the MFI is generated because of the spectral mirroring of the QΣΔM input. Generally, without extra calibration, the DCR IRR is considered to be between 30 and 40 dB and can be frequency selective [9, 27, 38, 42, 91]. Further details can be found, e.g., from [9].

Considering the I/Q calibration and MFI suppression schemes it should kept in mind that even if the QΣΔM would be ideal, the preceding components are creating MFI. Furthermore, several digital MFI suppression methods proposed in the literature, considering the analog receiver front-end and baseband, assume that also the mirror-band MFI source signal is available in digital domain [9–12, 47, 52, 90]. Thus, if such post-suppression is to be deployed, it should be kept in mind while designing the QΣΔM that also the mirror-band should have reasonable SQNR.

4.3.2 Modulator Input Coefficients

In [P3], it is found out that having I/Q mismatch in the QΣΔM input coefficients introduces an ISTF response for the modulator. This means that the input signal for the modulator is creating MFI, i.e., the conjugate of the original input is added to the output of the modulator shaped only by the modulator ISTF. The input I/Q mismatches do not give rise to an INTF, meaning that they do not produce mirroring effect for the quantization noise. This is also confirmed herein by the general analysis presented in Section 4.1 and [P7]. This is very intuitive because the quantization error is not yet present in the signal processed in the modulator input.

It should also be noted that the exact ISTF characteristics depend on the amount and location of the I/Q mismatch. Two separate exemplary mismatch scenarios and the related transfer functions are illustrated in Figure 4.2. The transfer functions are obtained using (4.5)-(4.10). A fourth-order single-stage QΣΔM with five input branches following the structure of Figure 3.6 is considered herein for illustration purposes. The STF is designed to have two separate passbands for multiband reception of two signal channels and exemplary sampling frequency of 128 MHz is assumed. In first scenario, the solid cyan line of the top plot shows the total ISTF when all the input branches have the same 3 % I/Q mismatch. The shape of this ISTF follows the shape of the STF and has constant IRR around 30 dB. The dashed cyan line shows ISTF induced by the I/Q mismathces of 1 %, 2 %, 3 %, 4 % and 5 % for the input branch coefficients A and $B^{(1)} - B^{(4)}$ or in opposite order (dotted line). Thus, the average mismatch equals 3 % of the previous scenario. However, it is now seen that the shape of the ISTF differs clearly from the STF and the IRR is no more constant. The same applies while having the mismatches in reversed order, changing, however, the exact frequency behavior of the ISTF.

This shows that having unequal or differing mismatches in the branches introduces additional frequency selectivity to the ISTF. It is again also intuitive when the I/Q mismatches create the z-domain transfer function for the input signal conjugate and the branches correspond to different delays therein, having unequal mismatch contribution.

At the same time, the bottom plot of Figure 4.2 confirms that no INTF response is present in either of the analyzed scenarios. This also matches the findings in [P3].

4.3.3 Modulator Loop-Filter Coefficients

Generally, the interference, distortion and noise added to the signal inside the ΣΔ modulator loop experience shaping by the NTF, alleviating the contribution of these error sources [25].

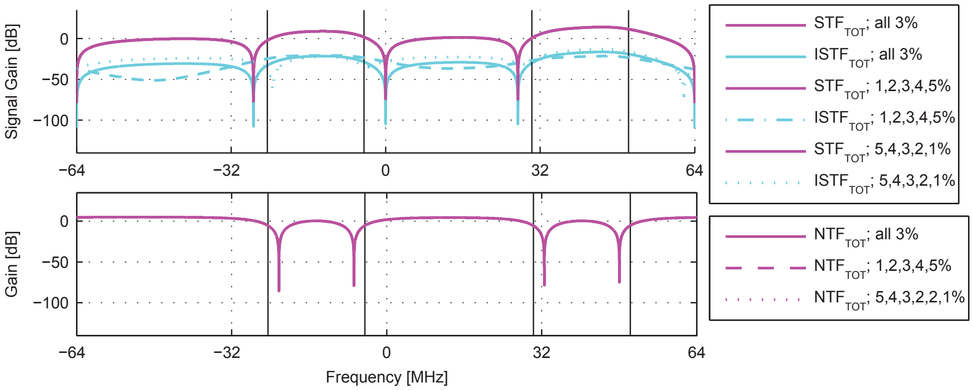

Figure 4.2: 4th order two-band QΣΔM transfer functions in the input mismatch scenarios having either constant or varying I/Q mismatches in the input branch coefficients A and $B^{(1)} - B^{(4)}$.

In case of I/Q mismatch only in the QΣΔM loop filter, there exists a special case, where only mirroring of the quantization error is induced [P3]. This happens when the STF is designed to have unity response and the input signal is entering only the quantizer, not the modulator loop. This, however, needs the input and feedback coefficients to be ideal, otherwise also the input signal leaks to the loop filters. Anyway, this leakage has in practical cases significant attenuation, thus diminishing the amount of MFI resulting from the mirroring of the input signal because of the loop filter I/Q mismatches in case of the unity STF design.

On the other hand, if the STF is designed to have nonunity response, also the input signal is entering the loop filters and experiences spectral mirroring. The IRRs for the input signal and the quantization error in the exemplary scenario described in Sub-Section 4.3.2 are plotted in Figure 4.3. Herein, the transfer function components are first solved using (4.5)-(4.10) and the IRRs are evaluated with the help of (2.11). Again, three scenarios with equal and unequal I/Q mismatches are shown, having either constant 2.5 % mismatches or 1 %, 2 %, 3 % and 4 % mismatches for each of the loop filter feedback coefficients from $M^{(1)}$ to $M^{(4)}$ or in opposite order. It is again visible that having differing mismatches affects the frequency charasteristics of the QΣΔM image rejection, even though the average levels of the mismatches and IRRs remain the same. From the reversed order I/Q mismatch scenario, it is visible that the noise IRR is mostly affected around the NTF notches realized by the integrators having the highest I/Q mismatches. For example, the noise notches on the desired signal band around +40 MHz is realized by $M^{(1)}$ and $M^{(2)}$, having the highest mismatches in the latter scenario and resulting in lower IRR on that band.

4.3.4 Modulator Feedback Coefficients

When there is I/Q mismatch in the QΣΔM feedback coefficients, both the input signal and the quantization error experience spectral mirroring [P3]. The MFI induced by the

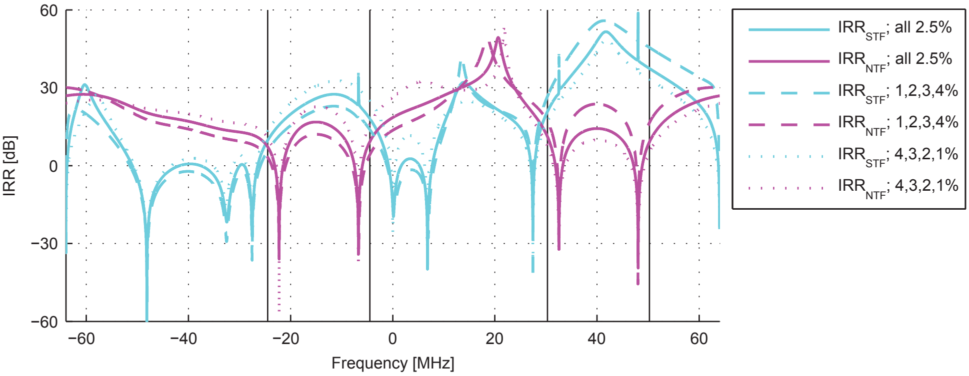

Figure 4.3: 4th order two-band QΣΔM IRRs in the loop filter mismatch scenarios havingh either constant or varying I/Q mismatches in the loop filter feedback branch coefficients $M^{(1)} - M^{(4)}$.

I/Q mismatches in the feedback branch is considered challenging because it appears directly at the modulator output, without NTF shaping [25]. However, the MFI originating from the input signal because of the feedback mismatches can be suppressed by designing the STF to reject the mirror band signal content, i.e., by placing the STF zeros on the mirror frequencies of the desired signal band. This method is called *mirror-frequency-rejecting STF design* in [P1-P4] and is one of the main contributions of this thesis. The design is discussed in further detail in Chapter 5.

With the general transfer function analysis presented in Section 4.1, it can be shown that similar to the input and the loop filter I/Q mismatches, the relative locations of the mismatches affect the resulting IRR frequency characteristics. This is shown in an exemplary scenario, discussed already in sub-sections 4.3.2 and 4.3.3, in Figure 4.4. Again, the mismatches in the studied scenarios are constant 2.5 % and 1 %, 2 %, 3 % and 4 % for the feedback coefficients from $R^{(1)}$ to $R^{(4)}$ or in opposite order. Also in here, the transfer function components are derived using (4.5)-(4.10), allowing evaluation of the IRRs.

4.4 Observations on Separate I/Q Mismatch Locations in a Multi-Stage Modulator

Herein, the I/Q mismatch effects in a multistage QΣΔM are illustrated using a three-stage modulator as a concrete example. The base for the analysis is formed by evaluating (4.13), including the matching filters $H_l^D[z]$ of (3.10), when the number of stages is three, i.e., $L = 3$. This gives

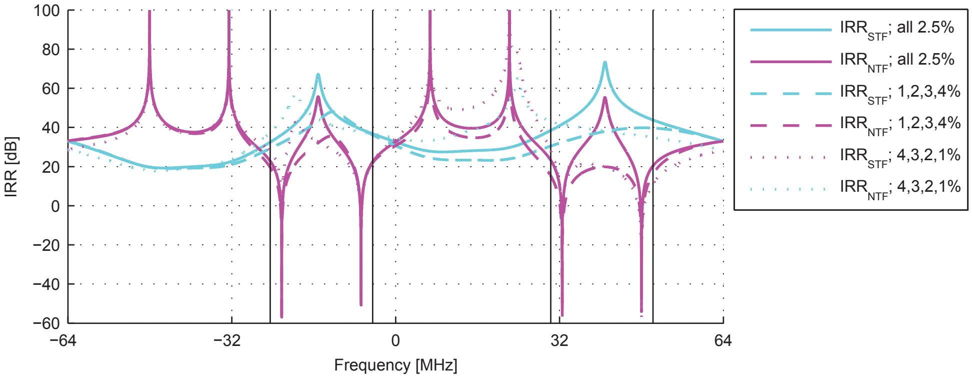

Figure 4.4: 4th order two-band QΣΔM IRRs in the feedback mismatch scenarios having either constant or varying I/Q mismatches in the modulator feedback branch coefficients $R^{(1)} - R^{(4)}$.

$$
\begin{aligned}
V[z] =& H_1^D[z]\big(STF_1[z]U[z] + ISTF_1[z]U^*[z^*] + NTF_1[z]E_1[z] + INTF_1[z]E_1^*[z^*]\big) \\
&- H_2^D[z]\big(STF_2[z]E_1[z] + ISTF_2[z]E_1^*[z^*] + NTF_2[z]E_2[z] + INTF_2[z]E_2^*[z^*]\big) \\
&+ H_3^D[z]\big(STF_3[z]E_2[z] + ISTF_3[z]E_2[z] + NTF_3[z]E_3[z] + INTF_3[z]E_3[z]\big) \\
=& STF_2^D[z]STF_1[z]U[z] + STF_2^D[z]ISTF_1[z]U^*[z^*] \\
&+ \big(STF_2^D[z]NTF_1[z] - NTF_1^D[z]STF_2[z]\big)E_1[z] \\
&+ \big(STF_2^D[z]INTF_1[z] + NTF_1^D[z]ISTF_2[z]\big)E_1^*[z^*] \\
&+ \big(- NTF_1^D[z]NTF_2[z] + NTF_1^D[z]NTF_2^D[z]/STF_3^D[z]STF_3[z]\big)E_2[z] \\
&+ \big(- NTF_1^D[z]INTF_2[z] + NTF_1^D[z]NTF_2^D[z]/STF_3^D[z]ISTF_3[z]\big)E_2^*[z^*] \\
&+ NTF_1^D[z]NTF_2^D[z]/STF_3^D[z]NTF_3[z]E_3[z] \\
&+ NTF_1^D[z]NTF_2^D[z]/STF_3^D[z]INTF_3[z]E_3^*[z^*],
\end{aligned}
\tag{4.16}
$$

from where the total transfer functions for the eight signal components can be extracted. Thus, these are given as

$$\begin{aligned}
STF_{\mathrm{TOT}}[z] &= STF_2^D[z]STF_1[z] \\
ISTF_{\mathrm{TOT}}[z] &= STF_2^D[z]ISTF_1[z] \\
NTF_{\mathrm{TOT},1}[z] &= STF_2^D[z]NTF_1[z] - NTF_1^D[z]STF_2[z] \\
INTF_{\mathrm{TOT},1}[z] &= STF_2^D[z]INTF_1[z] + NTF_1^D[z]ISTF_2[z] \\
NTF_{\mathrm{TOT},2}[z] &= -NTF_1^D[z]NTF_2[z] + NTF_1^D[z]NTF_2^D[z]/STF_3^D[z]STF_3[z] \\
INTF_{\mathrm{TOT},2}[z] &= -NTF_1^D[z]INTF_2[z] + NTF_1^D[z]NTF_2^D[z]/STF_3^D[z]ISTF_3[z] \\
NTF_{\mathrm{TOT},3}[z] &= NTF_1^D[z]NTF_2^D[z]/STF_3^D[z]NTF_3[z] \\
INTF_{\mathrm{TOT},3}[z] &= NTF_1^D[z]NTF_2^D[z]/STF_3^D[z]INTF_3[z].
\end{aligned} \tag{4.17}$$

The total transfer function equations show that in case of perfect I/Q matching, meaning zero response for the image transfer functions, and perfect matching between the analog and the digital transfer functions, only $STF_{\mathrm{TOT}}[z]$ and $NTF_{\mathrm{TOT},3}[z]$ remain nonzero.

The responses for each of the total transfer functions are also illustrated in Figure 4.5 in case of second-order stages, making the overall noise shaping order six, and incorporating feedback branch I/Q mismatches. Therein, reception of two noncontiguous frequency channels is assumed, dividing the NTF zeros on those bands and using simple frequency-flat STF design for all the stages. The sampling frequency is assumed to be 128 MHz and the received signal bandwidths to be 10 MHz each. These channels to be received are marked with gray solid lines in Figure 4.5. This simplified design is used herein to illustrate the I/Q mismatch effects. Further aspects of the transfer function design in a multistage QΣΔM are discussed in Chapter 5.

From the signal response point-of-view, it is clear from $STF_{\mathrm{TOT}}[z]$ and $ISTF_{\mathrm{TOT}}[z]$ that only the characteristics of the first-stage affect that. Both responses contain the digital copy of $STF_2^D[z]$, which in the designs discussed in this thesis is a pure delay. Furthermore, $ISTF_2[z]$ and $ISTF_3[z]$ do not affect the signal response, because only quantization error components are processed in the respective modulator stages.

As mentioned earlier, in case of perfect matching the first-stage quantization error does not appear at the modulator output due to the zero response of $NTF_{\mathrm{TOT},1}[z]$ and $INTF_{\mathrm{TOT},1}[z]$. However, under I/Q mismatches in the stages, both direct and image components do appear. The $NTF_{\mathrm{TOT},1}[z]$ has nonzero response even if the matching of the digital transfer functions $STF_2^D[z]$ and $NTF_1^D[z]$ would be perfect. This is because complex transfer functions are no more commutative under I/Q imbalance [110]. Furthermore, introduction of $INTF_1[z]$ and $ISTF_2[z]$ induce also image response for the first-stage quantization error.

With perfect matching, also the response for the second-stage quantization error components go to zero and only the shaped third-stage quantization error appears at the output. From the total transfer functions of (4.17), it is clear that the two terms in the second-stage noise total responses cancel each other in perfect conditions. However, with the I/Q mismatches, and thus the image transfer function components included, the conjugate of the second-stage quantization error is leaking to the output. The direct quantization error component is still canceled, assuming that the digital

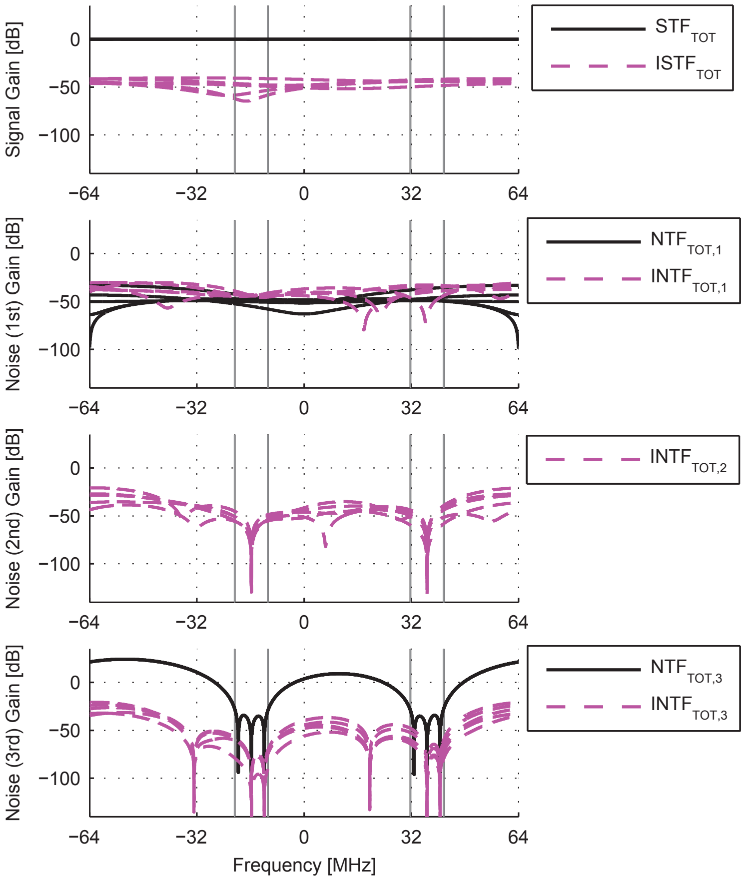

Figure 4.5: Three-stage QΣΔM STF and ISTF (top) together with NTF and INTF for first-, second- and third-stage quantization errors. Five independent realizations in real gain values of the feedback branches of all the stages are drawn from a uniform distribution between ±1% around the ideal value. Multiband reception of two information signals with center frequencies of 36.74 and -15.74 MHz is assumed. These bands are marked with gray solid lines in the plots.

transfer function components are matched to the analog ones. In both $NTF_{\mathrm{TOT},2}[z]$ and $INTF_{\mathrm{TOT},2}[z]$ the latter term describes contribution appearing through the third-stage. In case of $NTF_{\mathrm{TOT},2}[z]$, this is the part designed to cancel the original second-stage quantization error.

As a final component generated by the I/Q mismatches in a three-stage QΣΔM, the image response for the third-stage quantization error is induced by the I/Q mismatches in the third stage. This is illustrated by the $INTF_3[z]$ in $INTF_{\mathrm{TOT},3}[z]$.

The discussion for separate I/Q mismatch locations in a single-stage QΣΔM in Section 4.3 applies for all the stages in a multi-stage QΣΔM. For example, if the third stage has mismatches only in the input branch coefficient(s), no image response is induced for the third-stage quantization error. This is because this mismatch affects only response of the third-stage input, which is the second-stage quantization error. This is included in $INTF_{\mathrm{TOT},2}[z]$ latter term, having contribution from $ISTF_3[z]$.

4.5 Modulator Stability Under Implementation Inaccuracies

The ΣΔ modulator stability is mainly defined by the NTF response and the input signal level and behavior. The linear model predicts the effect of the NTF [102]. The role of the input signal is highlighted because of the nonlinear quantizer taking place in an actual ΣΔ ADC. For example, if the input signal is large enough direct current (DC), exceeding the highest quantization level, the input for the first integrator will be always positive and the loop will be unstable [102]. The modulator input is not affected by the possible I/Q mismatches inside the modulator. However, the exact NTF characteristics and the signal entering the quantizer can be altered because of the implementation inaccuracies, such as I/Q mismatches.

For the NTF, there are certain approximate criteria, while the exact and general conditions are not known [102]. For example, Lee's Criterion [33, 102] states that the amplitude response of the NTF should be less than 1.5. At the same time, to guarantee stable operation from input signal level point-of-view, the loop components, i.e., the op amps and the quantizer, are not heavily overloaded. Furthermore, this depends also on the STF response prior each of the components [102].

Thus, the modulator stability is prone for increased amplitude response in both the STF and NTF. However, when implementing random inaccuracies for all the QΣΔM coefficients for the exemplary modulator case discussed in Section 4.3, the STF and ISTF show significant peaking, illustrated in Figure 4.6. The coefficient values are drawn from a uniform distribution between ± 1 % around the ideal value and ten responses are plotted for all the four transfer functions. From Figure 4.6 it is visible that the NTF remains practically unchanged. Consequently, the designer should pay attention for the STF behavior under implementation inaccuracies by avoiding the peaking, or limiting the applied input to stable range. The stable range in design at hand should be confirmed by simulations [102].

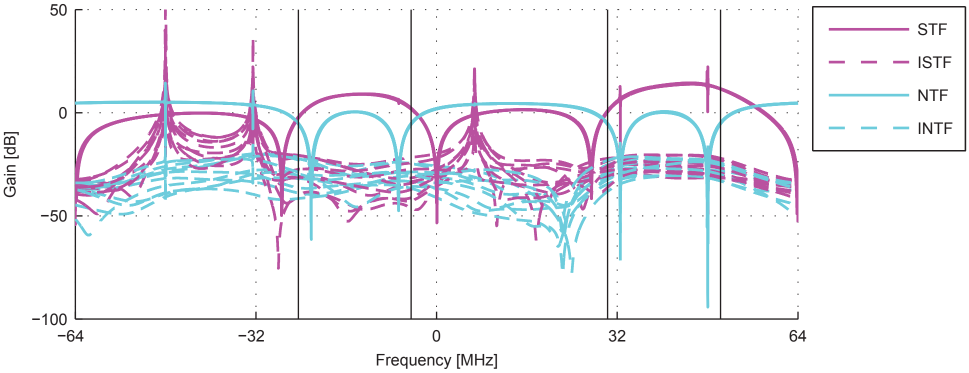

Figure 4.6: Ten realizations of the 4th order two-band QΣΔM transfer functions with random I/Q mismatches in all the modulator coefficients drawn from a uniform distribution between ± 1 % around the ideal value.

CHAPTER 5

Multiband Transfer Function Designs and Digital Post-Processing for Improved Image Rejection

This chapter proposes a complex-valued multiband designs for QΣΔM transfer functions, allowing reception of multiple waveforms of interest on noncontiguos frequency bands in parallel [P3]. This can be done with a single QΣΔM without implementation of parallel ADC branches.

First, target values for maximum tolerable interference, because of the implementation inaccuracies, is studied with receiver system level calculations and targeted interference rejection ratio is defined. Thereafter, two methods for improving the QΣΔM image rejection are discussed. These are mirror-frequency rejecting STF design [P1]-[P4] and digital MFI suppression facilitated by appropriate QΣΔM transfer function design [P5]-[P6]. The first one is effective against MFI induced in the QΣΔM feedback branches and the latter one allows suppression of the MFI generated by the whole receiver chain in DCRs. Furthermore, a digital circularity restoring MFI suppression is proposed in QΣΔM context. The QΣΔM specific signal modeling is introduced bringing insight into the contribution of separate transfer components. Finally, reconfigurability of the multiband transfer function is considered. At the same time, role of the DSA, contributing to the operation conditions, is discussed.

5.1 Receiver System Level Considerations

The performance of the transfer function designs, combined with digital post-processing in Section 5.4, is measured with interference rejection ratio, Γ, as a figure-of-merit. This is defined as the ratio of the output power of an ideal QΣΔM on certain band and the power increase because of the nonidealities on the same band, i.e.,

$$\Gamma_1 = \frac{\int\limits_{f \in \Omega_{\mathrm{C},1}} G_\sigma(e^{j2\pi f T_\mathrm{S}})df}{\int\limits_{f \in \Omega_{\mathrm{C},1}} G_\tau(e^{j2\pi f T_\mathrm{S}})df}, \tag{5.1}$$

where the integration is done over the desired signal band to be received, defined as $\Omega_{\mathrm{C},1} = \{f_{\mathrm{C},1} - W_1/2, ..., f_{\mathrm{C},1} + W_1/2\}$. Herein, $f_{\mathrm{C},1}$ and W_1 are the center frequency and bandwidth of the signal to be received, respectively. In addition, $G_\sigma(e^{j2\pi f T_\mathrm{S}})$ and $G_\tau(e^{j2\pi f T_\mathrm{S}})$ are the spectral densities of the ideal modulator output and the additional interference generated by the nonidealities, respectively.

The target value for this measure in certain reception scenario can be obtained with system calculations, considering, for example, the receiver SNR, the ADC SQNR and the targeted signal-to-interference-and-noise ratio (SINR) on the reception band at hand. Herein, an exemplary scenario is used to derive a rule-of-thumb value, against which the results in the following sections are compared. The parameters applied in this scenario are summarized in Table 5.1. The detection of a 16-QAM waveform with bandwidth of $W_{\text{16-QAM}}$=10 MHz is assumed as a part of a multiband reception scenario, having sampling frequency of f_C=128 MHz. The received desired signal power is assumed to be -84 dBm (sensitivity level), remaining 20 dB above the thermal noise floor at -104 dBm. Taking a typical receiver overall noise figure of 7 dB into account, this gives a SNR of 13 dB at the input of the ADC (SNR_PRE= 13 dB). Thus, with a digital SINR target of, say, 10 dB ($SINR_\mathrm{target}$=10 dB) for detection, implementation margin of 3 dB is allowed.

For the QΣΔM, different combinations of noise shaping and quantization are studied, considering first, third and sixth order noise shaping for the band at hand ($P_{16-\mathrm{QAM}} = \{1, 3, 6\}$) combined with 1- and 3-bit quantization ($b_\mathrm{Q} = \{1, 3\}$). For the noise shaping, the zero-optimization gains of $ZOG_\mathrm{dB} = \{0, 8, 23\}$ are found from [100] for the three chosen noise shaping orders.

Based on these parameters, the SQNR of a QΣΔM is defined as

Table 5.1: A summary of receiver system level and A/D interface properties used in the interference rejection example

Property	Value
Desired signal waveform	16-QAM
Desired signal bandwidth $W_{\text{16-QAM}}$	10 MHz
Thermal noise $kTW_{\text{16-QAM}}$	-104 dBm
Receiver overall noise figure	7 dB
Implementation margin	3 dB
$SINR_\mathrm{target}$ for detection	10 dB
Received desired signal power	-84 dBm
Sampling frequency f_C	128 MHz
Number of quantization bits b_Q	{1,3}
Noise-shaping order $P_{\text{16-QAM}}$	{1,3,6}
Zero-optimization gain	{0,8,23} dB
SNR_PRE at the ADC input	13 dB
Full-band Crest-factor CF_dB	5 dB
Full-band signal power relative to the desired signal power	0...140 dB

$$
\begin{aligned}
SQNR = 6.02b_{\mathrm{Q}} + 4.76 - CF_{\mathrm{dB}} - 10\log_{10}\left(\frac{\pi^{2P_{16-\mathrm{QAM}}}}{2P_{16-\mathrm{QAM}}+1}\right) \\
+ (20P_{16-\mathrm{QAM}}+10)\log_{10}\left(\frac{f_S}{W_{16-\mathrm{QAM}}}\right) + ZOG_{\mathrm{dB}} - 10\log_{10}\left(\frac{S_{\mathrm{full-band}}}{S_{16-\mathrm{QAM}}}\right),
\end{aligned}
\tag{5.2}
$$

where, in addition to the values in Table 5.1, $S_{\text{full-band}}$ is the power of the whole ADC input containing also possible blockers and $S_{16-\mathrm{QAM}}$ is the desired signal power. Thus, the total SNR after the ADC, considering the thermal noise N_{PRE} and the quantization error N_{Q} ($N_{\mathrm{TOT}} = N_{\mathrm{PRE}} + N_{\mathrm{Q}}$) on the desired signal band, is given as

$$
\begin{aligned}
SNR_{\mathrm{TOT}} &= 10\log_{10}\left(\frac{S_{16-\mathrm{QAM}}}{N_{\mathrm{TOT}}}\right) \\
&= 10\log_{10}\left(\frac{S_{16-\mathrm{QAM}}}{N_{\mathrm{PRE}}+N_{\mathrm{Q}}}\right) \\
&= 10\log_{10}\left(\frac{1}{10^{-SNR_{\mathrm{PRE}}/10}+10^{-SQNR/10}}\right).
\end{aligned}
\tag{5.3}
$$

Now, the maximum amount of tolerable interference, still allowing $SINR_{\text{target}}$ set for the detection, is defined as I_{MAX}. With the help of this, also the needed interference rejection ratio can be solved as a ratio of the outputs of an ideal QΣΔM ($S_{16-\mathrm{QAM}} + N_{\mathrm{TOT}}$) to the I_{MAX}, i.e.,

$$
\begin{aligned}
\Gamma_{\text{demand}} &= 10\log_{10}\left(\frac{S_{16-\mathrm{QAM}}+N_{\mathrm{TOT}}}{I_{\mathrm{MAX}}}\right) \\
&= 10\log_{10}\left(\frac{1+10^{-SNR_{\mathrm{TOT}}/10}}{10^{-SINR_{\text{target}}/10}-10^{-SNR_{\mathrm{TOT}}/10}}\right), SNR_{\mathrm{TOT}} > SINR_{\text{target}}.
\end{aligned}
\tag{5.4}
$$

In Figure 5.1, the interference rejection ratio is plotted as a function of full-band signal power relative to the desired signal power, implicating relative power level of the possible blocking signals. Different quantization and noise shaping combinations denoted in Table 5.1 are depicted. It is clearly visible that different noise shaping orders give differing tolerance against the interference because of the varying amount of quantization noise appearing inside the desired signal band. However, as a main conclusion herein, it should be noted that 14 dB interference rejection ratio can be considered as a rule-of-thumb. In certain scenarios higher values give additional performance benefit, but with each noise-shaping order, the demand starts to climb towards infinity withing close vicinity of the 14 dB limit. This difference is less than 10 dB change in the full-band signal power relative to the desired signal power. Thus, 14 dB is considered as a target value in the following studies in this chapter. More detailed system level analysis can be found in [P4].

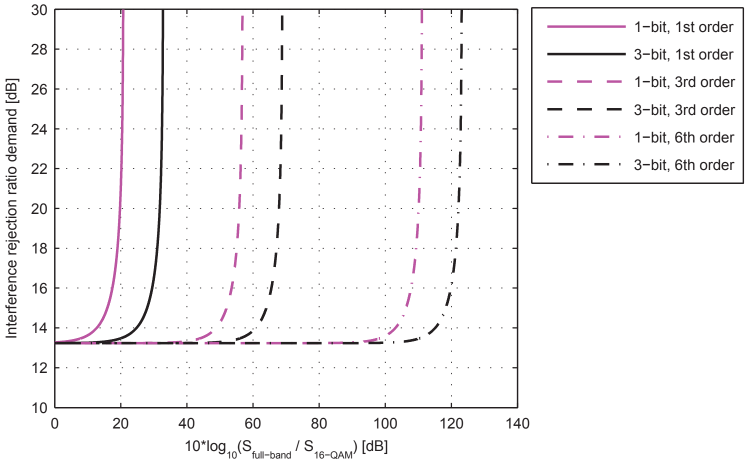

Figure 5.1: Required interference rejection ratio with different QΣΔM setups as a function of full-band signal power relative to the desired signal power. SNR_{PRE} at the ADC input and $SINR_{\mathrm{target}}$ for detection are assumed 13 dB and 10 dB, respectively, giving implementation margin of 3 dB.

5.2 Mirror-frequency Rejecting Signal Transfer Function Design

The MFI induced by the I/Q mismatches in the QΣΔM feedback branches can be alleviated by designing the STF to reject the mirror-band of the information signal(s) of interest. The details and effects of this design are discussed in the following sub-sections in case of two different QΣΔM architectures. These are examples of architectures where the design principle can be applied. The same mirror-frequency rejecting principle can be followed with other designs also.

5.2.1 Single-Stage Second-Order Modulator

First, the mirror-frequency rejecting STF design is demonstrated with a second-order QΣΔM having a single conversion stage. Furthermore, the multiband transfer function design is illustrated by assuming reception of two noncontiguous frequency channels around center frequencies of f_1=48 MHz and f_2=19 MHz, resulting in relative frequencies $\bar{f}_1 = 0.38$ and $\bar{f}_2 = -0.15$ with sampling frequency of f_S=128 MHz [P2].

For a second-order QΣΔM following the architecture presented in Section 3.4 and in Figure 3.6, the transfer functions are defined as

$$STF[z] = \frac{A + (B^{(1)} - M^{(1)}A - M^{(2)}A)z^{-1} + (B^{(2)} - M^{(1)}B^{(1)} + M^{(1)}M^{(2)}A)z^{-2}}{1 - (M^{(1)} + M^{(2)} + R^{(1)})z^{-1} + (M^{(1)}M^{(2)} + M^{(1)}R^{(1)} - R^{(2)})z^{-2}} \tag{5.5}$$

$$NTF[z] = \frac{1 - (M^{(1)} + M^{(2)})z^{-1} + (M^{(1)}M^{(2)})z^{-2}}{1 - (M^{(1)} + M^{(2)} + R^{(1)})z^{-1} + (M^{(1)}M^{(2)} + M^{(1)}R^{(1)} - R^{(2)})z^{-2}}. \tag{5.6}$$

Therein, the loop filter feedback coefficients $M^{(1)}$ and $M^{(2)}$ define the positions of the NTF poles. In case of two-band reception, these are set to the desired band center frequencies on unit-circle. Thus, $M^{(1)} = e^{j2\pi\bar{f}_1}$ and $M^{(1)} = e^{j2\pi\bar{f}_2}$.

Furthermore, if frequency-flat STF design is desired, the STF zeros should be placed in the origin, by setting the STF numerator to unity. This actualizes when $A = 1$, $B^{(1)} = M^{(1)}A + M^{(2)}A$ and $B^{(2)} = M^{(1)}B^{(1)} - M^{(1)}M^{(2)}A$. On the other hand, in case of mirror-frequency rejecting STF design, the STF zeros should be placed on the unit-circle at the mirror-frequencies $-\bar{f}_1$ and $-\bar{f}_2$. For this, $A = 1$, $B^{(1)} = M^{(1)}A + M^{(2)}A - e^{-j2\pi\bar{f}_1} - e^{-j2\pi\bar{f}_2}$ and $B^{(2)} = M^{(2)}B^{(1)} - M^{(2)}M^{(1)}A + e^{-j2\pi\bar{f}_1}e^{-j2\pi\bar{f}_2}$, setting the numerator to $1 + (e^{-j2\pi\bar{f}_1} + e^{-j2\pi\bar{f}_1})z^{-1} - (e^{-j2\pi\bar{f}_1}e^{-j2\pi\bar{f}_2})z^{-2}$, whose roots, and thus the zero placements, are the two given exponents.

Finally, if FIR transfer functions are desired, the common denominator should be set to unity. For this, $R^{(1)} = M^{(1)} + M^{(2)}$ and $R^{(2)} = M^{(1)}M^{(2)} + M^{(1)}R^{(1)}$.

In Figure 5.2, both the flat and the mirror-frequency rejecting STF frequency responses are illustrated together with the NTF which remains the same in both scenarios. Furthermore, five independent I/Q mismatched realizations of feedback coefficients $R^{(1)}$ and $R^{(2)}$ are drawn from a uniform distribution between $\pm 1\%$ around the ideal value. This results in the ISTF and INTF responses shown in Figure 5.2. Therein, it is clearly visible that the mirror-frequency rejecting STF design attenuates the ISTF response around the desired signal bands denoted with the vertical lines. The additional attenuation allowed by this design is in the order of 20 dB. In the following sub-section, the performance of the mirror-frequency rejecting STF design is further illustrated in a multistage QΣΔM, using also computer simulations of a realistic reception scenario.

5.2.2 Three-Stage Modulator with Second-Order Stages

Herein, a three-stage QΣΔM is used to illustrate the mirror-frequency rejecting STF design in case of a multistage modulator. Furthermore, the additional degrees-of-freedom for the NTF design allowed by the multistage architecture are highlighted.

Using three second-order stages allows the overall NTF to have an order of six, being generally the combined order of all the stages. When considering, e.g., two-band reception, this configuration allows placing three NTF zeros on both the bands to be received and detected. The zero locations inside the band can be optimized according to [100]. Furthermore, realization of the overall NTF zeros needs to be divided between the three stage NTFs. Ideally, it would not make any difference in which order the zeros would be created. However, having I/Q mismatches included, the designer should pay

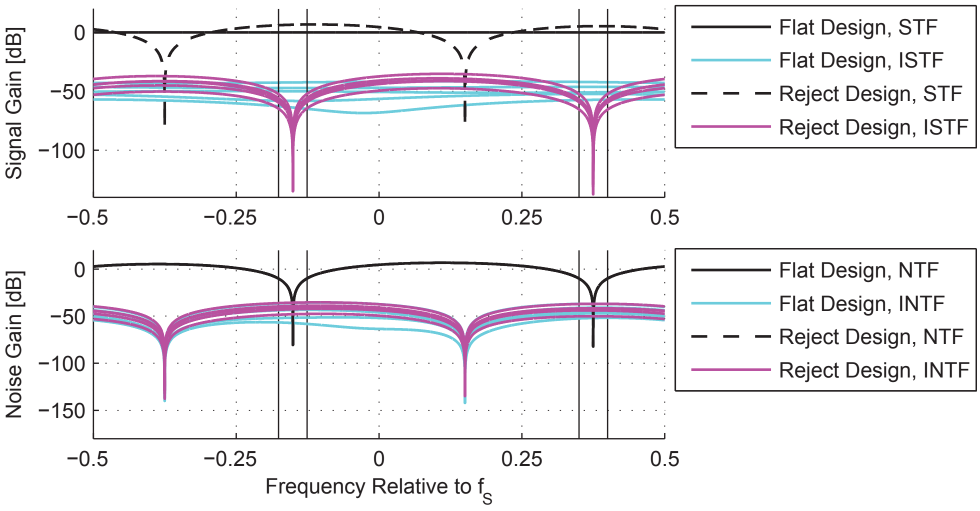

Figure 5.2: Second-order single-stage QΣΔM STF, ISTF (above) and NTF and INTF (below). Five independent random variations in real gain values of both modulator feedback branches with frequency-flat STF design ("Flat Design") and *mirror-frequency rejecting* STF design ("Reject Design").

attention to the INTF responses also. For example, in a three-stage QΣΔM the mirror version, i.e., the conjugate, of the first-stage quantization error $E_1^*[z^*]$ is shaped by $ISTF_{\mathrm{TOT},1}[z] = NTF_1^D[z]ISTF_2[z]$ and the conjugate of the second-stage quantization error $E_2^*[z^*]$ is shaped by $ISTF_{\mathrm{TOT},2}[z] = -NTF_1^D[z]INTF_2[z]$ [P4]. Thus, having the digital copy $NTF_1^D[z]$ of the first-stage NTF present in both the conjugate error responses, the first-stage NTF is proposed to have the zeros in the centers of both the reception bands, in order to attenuate also the conjugate error therein [P4]. Thereafter, the latter stages are used to widen the noise shaping notches around the first-stage zeros.

From the STF design point-of-view, in case of I/Q mismatches present, the most attention should be paid to the ISTF of the first stage, where it is possible to have stronger blocking signals present on the mirror bands. The latter stages process the quantization error of the previous stage as inputs and are thus less likely to have high dynamics in the input power levels with realistic, rich enough, inputs. In addition, the latter stage STFs do not contribute to the overall STF, which is defined solely by the first-stage STF and the digital copy of the second-stage STF. Furthermore, the latter one being implemented in the digital domain, its response can not be used to alleviate the I/Q mismatch problem in the analog components. Thus, the mirror-frequency rejecting STF design is applied in the first stage, the second and third stage STFs being designed as frequency-flat. The design flow is summarized in Table 5.2. The detailed equations for solving the coefficient values in this design can be found from [P4].

The performance of this design is illustrated with computer simulations assuming two-band reception of 16-QAM and QPSK waveforms with 10 MHz bandwidths while

Table 5.2: Overall design flow of a three stage two-band QΣΔM [P4]

Preliminary Reception and Spectrum Sensing Information

1. Obtain the desired signal center frequencies ($f_{\mathrm{C},1}$ and $f_{\mathrm{C},2}$)
2. Obtain the desired signal bandwidths
3. Find the optimal frequency offsets ($f_{\mathrm{offset},1}$ and $f_{\mathrm{offset},2}$) for the NTF zero placements inside the desired signal bands, e.g., from [96]
4. Based on the spectrum sensing information, find the most harmful blockers ($f_{\mathrm{int},1}$ and $f_{\mathrm{int},2}$)
    - In case of mirror-frequency rejecting STF design $f_{\mathrm{int},1} = -f_{\mathrm{C},1}$ and $f_{\mathrm{int},2} = -f_{\mathrm{C},2}$

Design of a Three-Stage Two-Band QΣΔM with Mirror-Frequency Rejecting First-Stage STF

Transfer function design for the first-stage (two-band NTF and mirror-frequency rejecting STF)

1. Place the NTF zeros: $\varphi^{(1)}_{\mathrm{NTF},1} = e^{j2\pi f_{\mathrm{C},1}T_{\mathrm{S}}}$, $\varphi^{(1)}_{\mathrm{NTF},2} = e^{j2\pi f_{\mathrm{C},2}T_{\mathrm{S}}}$
2. Place the STF zeros: $\varphi^{(1)}_{\mathrm{STF},1} = e^{j2\pi f_{\mathrm{int},1}T_{\mathrm{S}}}$, $\varphi^{(1)}_{\mathrm{NTF},2} = e^{j2\pi f_{\mathrm{int},2}T_{\mathrm{S}}}$
3. Place the common poles: $\psi^{(1)}_{\mathrm{common},1} = 0.5e^{j2\pi f_{\mathrm{C},1}T_{\mathrm{S}}}$ and $\psi^{(1)}_{\mathrm{common},2} = 0.5e^{j2\pi f_{\mathrm{C},2}T_{\mathrm{S}}}$
4. Solve the modulator loop filter coefficients $M^{(1)}_1$ and $M^{(2)}_1$; input coefficients A_1, $B^{(1)}_1$ and $B^{(2)}_1$; and feedback coefficients $R^{(1)}_1$ and $R^{(2)}_1$.

Transfer function design for the second-stage (two-band NTF and frequency-flat STF)

5. Place the NTF zeros: $\varphi^{(2)}_{\mathrm{NTF},1} = e^{j2\pi(f_{\mathrm{C},1}+f_{\mathrm{offset},1})T_{\mathrm{S}}}$, $\varphi^{(2)}_{\mathrm{NTF},2} = e^{j2\pi(f_{\mathrm{C},2}+f_{\mathrm{offset},2})T_{\mathrm{S}}}$
6. Place the STF zeros: $\varphi^{(2)}_{\mathrm{STF},1} = 0$, $\varphi^{(2)}_{\mathrm{NTF},2} = 0$
7. Place the common poles: $\psi^{(2)}_{\mathrm{common},1} = 0$ and $\psi^{(2)}_{\mathrm{common},2} = 0$
8. Solve the modulator loop filter coefficients $M^{(1)}_2$ and $M^{(2)}_2$; input coefficients A_2, $B^{(1)}_2$ and $B^{(2)}_2$; and feedback coefficients $R^{(1)}_2$ and $R^{(2)}_2$.

Transfer function design for the third-stage (two-band NTF and frequency-flat STF)

9. Place the NTF zeros: $\varphi^{(3)}_{\mathrm{NTF},1} = e^{j2\pi(f_{\mathrm{C},1}-f_{\mathrm{offset},1})T_{\mathrm{S}}}$, $\varphi^{(3)}_{\mathrm{NTF},1} = e^{j2\pi(f_{\mathrm{C},2}-f_{\mathrm{offset},2})T_{\mathrm{S}}}$
10. Place the STF zeros: $\varphi^{(3)}_{\mathrm{STF},1} = 0$, $\varphi^{(3)}_{\mathrm{NTF},2} = 0$
11. Place the common poles: $\psi^{(3)}_{\mathrm{common},1} = 0$ and $\psi^{(3)}_{\mathrm{common},2} = 0$
12. Solve the modulator loop filter coefficients $M^{(1)}_3$ and $M^{(2)}_3$; input coefficients A_3, $B^{(1)}_3$ and $B^{(2)}_3$; and feedback coefficients $R^{(1)}_3$ and $R^{(2)}_3$.

mirror-band blockers are also present. In the simulations, the real valued I/Q model shown in Figure 4.1 is employed, having true quantizers on both the signal branches. The output spectrum of the QΣΔM illustrating the signal scenario and the STF effects is shown in Figure 5.3. In all the stages, 3-bit I and Q quantizers are used and the sampling frequencies are 128 MHz. The performance is measured with interference rejection ratio Γ_1 and Γ_2 for the 16-QAM and QPSK signal bands, respectively.

Finally, the simulation results while having random I/Q mismatches in the feedback coefficients of all the stages are shown in Figure 5.4. The mismatched coefficient values

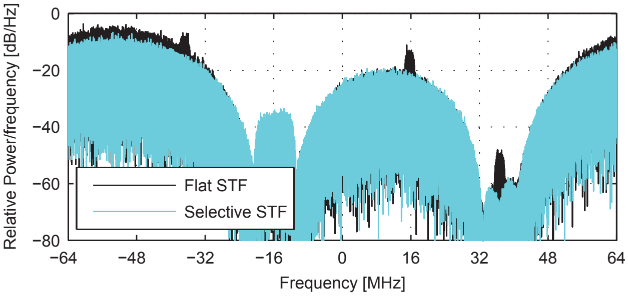

Figure 5.3: Example power spectral densities of output signals used in simulations with frequency-flat and mirror-frequency-rejecting STF designs with 16-QAM information signal around center frequency of 36.74 MHz disabled to highlight image rejection properties. 3-bit quantizers are used in all the three stages.

are drawn from a uniform distribution ranging ±1% around the ideal coefficient values. The interference rejection ratios are averaged over 25 independent realizations. From Figure 5.4 it is clear the mirror-frequency rejecting STF design improves the interference rejection ratios compared to the frequency-flat STF design. The gains are around 15 dB and 10 dB for the 16-QAM and QPSK waveforms, respectively, with the relative mirror-band blocker powers between +10 and +60 dB. This is the practical range where heavy MFI is falling on top of the desired waveforms if no means are taken to prevent that. At the same, e.g., for the 16-QAM carrier the range where interference rejection ratio stays above 14 dB is extended from +22 dB relative blocker power to +40 dB, denoting significant increase in the blocker tolerance. In Section 5.1, this 14 dB level was indeed found to be valid rule-of-thumb for interference rejection ratio demand by receiver system calculations in a practical reception scenario like the one simulated herein.

As a summary, the mirror-frequency rejecting STF design is efficient in mitigating the I/Q mismatch effects of the QΣΔM feedback branch coefficients and suppressing the induced MFI, as shown with further examples in [P1]-[P4]. However, it does not alleviate the MFI problem, if there are I/Q mismatches in the QΣΔM input or loop-filter coefficients or in the preceding receiver front-end.

5.3 Facilitating Digital Mirror-Frequency Interference Suppression

The QΣΔM transfer functions have traditionally been designed to shape the quantization noise away from the desired signal band and to have the signal response as close to the unity as possible or to filter the out-of-band signal content away [60]. This is an efficient design when the quantization error is considered as the main error source. However, when taking other receiver nonidealities and implementation inaccuracies into account, the distortion and interference generated at the preceding receiver analog front-end and the QΣΔM itself need to be considered also. Exactly this is done in [P5-P7].

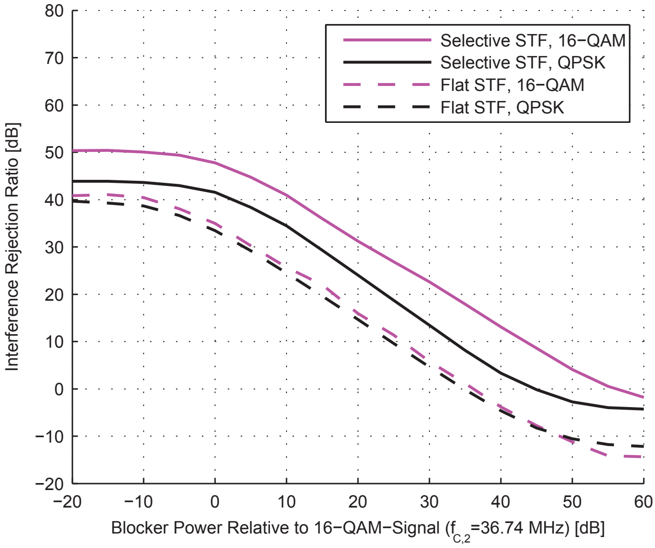

Figure 5.4: Interference rejection ratios for the desired signals with three-stage QΣΔM using 3-bit quantizers at each stage, as a function of blocker signal power. Frequency-flat (“Flat STF”) and mirror-frequency-rejecting STF (“Selective STF”) designs are simulated

In recent past, there has been significant advances in digital compensation of these so-called dirty-RF impairments, such as the MFI originating from the mismatches of I/Q circuits [44, 92, 97, 113]. This kind of compensation algorithms typically need digitized information of the original sources of the interference. Thus, in the case of I/Q mismatches and MFI considered herein, the mirror-band signal should be converted into the digital domain with reasonable resolution. This is where the above-described traditional NTF design (possibly combined with the STF filtering) becomes unsuitable. If all the NTF zeros are placed on the desired signal band, the noise load of the mirror-band is potentially very high, resulting in a very low SQNR. This is, of course, even more emphasized if the STF is attenuating the mirror-band decreasing the signal power. In [60], a mirror-band NTF notch was proposed to avoid mirroring of the quantization noise pushed on the mirror-band. However, the STF was used to attenuate the mirror-band signal content, impeding the actual post-compensation of MFI originating from the possible mirror-band blocker signal.

The MFI inside the QΣΔM can be controlled partly by mirror-frequency rejecting STF design [P3, P4] or other analog techniques [6, 25, 89, 93]. However, problems arise when the I/Q mismatches of the preceding receiver components are taken into account. For example, when the I/Q mixer, used to bring the desired signal down to the IF, creates MFI and the original mirror-band blocker is filtered out before or inside the QΣΔM. The interference remains on top of the desired signal but the information of the interference source is removed, making post-compensation a troublesome task.

The STF and NTF designs solving this problem are based on the single-band NTF design with one mirror-band zero of [60], being extended to complex multiband concept of [P3]. The main idea is to preserve the possible mirror-band blockers by creating STF passbands on those bands. While the mirror-band NTF zero helps in decreasing the MFI from the conjugated quantization error [60], it is used herein also in purpose of increasing the SQNR on the mirror-band. This is done in order to use the mirror-band signal content thereafter in digital MFI suppression. Without this information the compensation task would become very challenging or even impossible. There is also a clear benefit doing the MFI suppression in digital domain, namely this processing considering the MFI induced by the whole receiver, independent of exact locations of the I/Q mismatches. For example, even if the QΣΔM would be ideal, the downconverting I/Q mixer and the analog baseband I and Q components create MFI in a DCR anyway. Generally, similar design flow as described in Table 5.2 can be followed also in this scenario. However, it should be taken into account that the STF zeros are not used to block the mirror-bands, but to attenuate other possible blocking or noninteresting signals.

5.3.1 Two-Stage Modulator with Fourth-Order Stages

Herein, a concrete design example is given for the digital MFI suppression facilitating transfer function principle described above. The design is concretized with a two-stage QΣΔM with fourth-order stages, having thus an overall noise shaping order of eight. Multiband reception and detection of two noncontiguous information signals of interest is assumed.

For both the desired signal bands, three NTF zeros are used for the noise shaping and the remaining two zeros are placed on the mirror-bands in order to keep the SQNR reasonable also therein. In simplest, the STF could have unity response, the main point being that neither the desired bands nor the mirror-bands are attenuated. However, the STF zeros can utilized in attenuating other noninteresting signal content and thus limiting overall signal dynamics. As in Sub-Section 5.2.2 for the latter stages of a three-stage QΣΔM, the second stage STF is designed frequency-flat. This is because of the minimized delay and the input, being the quantization error of the first-stage, is less likely to have high dynamics. Further discussion on the general transfer function design principles for a two-stage QΣΔM can be found in [P1, P7].

It should be noticed that the transfer functions can be straightforwardly reconfigured using information available about the center frequencies, bandwidths, resolution demands and spectrum sensing information about the strongest blocking signals possibly present within the overall conversion band. The last one can be used to place the first-stage STF zeros on those frequencies while the other information is used to optimize the NTF responses with help of, e.g., [100].

For concisety of presentation, the mathematical details of solving the QΣΔM coefficients is omitted herein. However, this information can be found in [P7], where equations are given for straightforwardly deriving the QΣΔM coefficients when having knowledge of the frequency bands to be received. The total transfer functions describing the response for an ideal modulator, where the shaped versions of the input signal and the second-stage quantization error are present at the output, are shown in Figure 5.5 together with an exemplary input spectrum. The sampling frequency is assumed to be 128 MHz. The desired information signal are 16-QAM and QPSK waveforms around

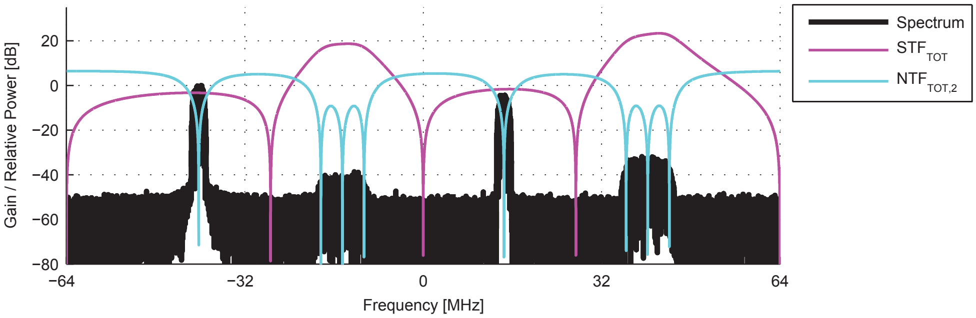

Figure 5.5: The ideal designed transfer functions (overall response) together with an example spectrum of input signal used in the simulations. The desired information signals are located around center frequencies of 40 MHz and -15 MHz with 16-QAM and QPSK waveforms, respectively. The blocking signals are located on the mirror frequencies of the desired signals.

40 MHz and -15 MHz center frequencies, respectively, both having 10 MHz bandwidth. The blocking signals are located on the respective mirror-frequencies. It should be noted that the NTF notches and STF passbands are designed exactly on those bands.

For reception of a single wider-bandwidth information signal, the QΣΔM responses can also be reconfigured, following the design guidelines discussed above. An example of this kind of design, with 20 MHz desired 16-QAM waveform, is illustrated in Figure 5.6. Therein, six NTF zeros are placed on the desired signal band and two on the mirror-band. The STF passbands are designed on both these bands and the STF zeros are used to attenuate noninteresting signal content.

Examples of the compensation performance in these two scenarios are given in the following sub-section, after describing the digital MFI suppression algorithm applied. Furthermore, the exact transfer functions and image transfer function characteristics under implementation inaccuracies are illustrated and analyzed in [P7].

5.4 Digital Post-Processing for Mirror-frequency Interference Suppression

In this section, the actual MFI suppression algorithm is described, the digital post-compensation being facilitated by the transfer function design discussed above. The QΣΔM specific sub-bandwise frequency-selective algorithm is developed herein based on [12]. This blind block-based algorithm was chosen because of its simplicity and independency of any calibration signals.

Herein, the digital compensator coefficients applied for MFI suppression are derived in a multiband reception case, where S noncontiguous signal bands are received and detected, for generality. Thereafter, in the computer simulations two-band [P7] and single-wideband cases [P6] (having $S = 2$ and $S = 1$, respectively) are applied. This

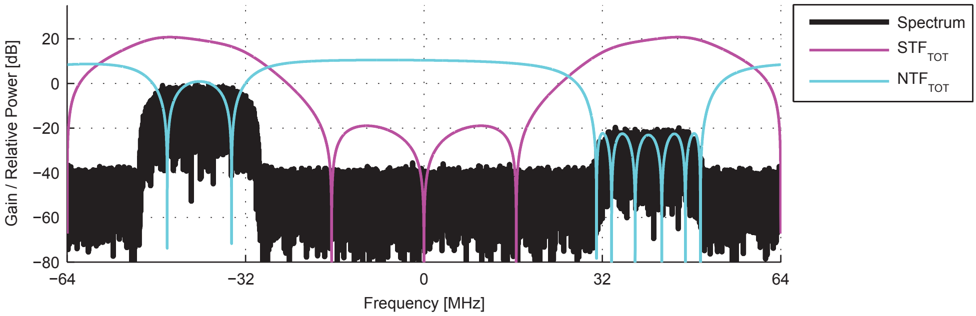

Figure 5.6: The ideal designed transfer functions for single-band reception (overall response) together with an example spectrum of input signal used in the simulations. The desired information signal is located around center frequency of 40 MHz with 16-QAM waveform. The blocking signal is located on the mirror frequency of the desired signal.

also highlights the reconfigurability and degrees-of-freedom allowed by the two-stage QΣΔM transfer function design discussed in Sub-Section 5.3.1.

Now, the QΣΔM input, including the MFI created by the receiver front-end, e.g., because of the nonideal I/Q mixer is written in z-domain as

$$U[z] = STF_{\mathrm{FE}}[z]X[z] + ISTF_{\mathrm{FE}}[z]X^*[z^*], \tag{5.7}$$

where $STF_{\mathrm{FE}}[z]$ and $ISTF_{\mathrm{FE}}[z]$ denote the STF and ISTF of the receiver front-end, being unknown. When this nonideal signal as a whole is fed into an I/Q mismatched QΣΔM, the digitized signal is given by

$$\begin{aligned} V[z] &= STF_{\mathrm{SD}}[z]U[z] + ISTF_{\mathrm{SD}}[z]U^*[z^*] + NTF[z]E[z] + INTF[z]E^*[z^*] \\ &= STF_{\mathrm{TOT}}[z]X[z] + ISTF_{\mathrm{TOT}}[z]X^*[z^*] + NTF[z]E[z] + INTF[z]E^*[z^*], \end{aligned} \tag{5.8}$$

where $STF_{\mathrm{SD}}[z]$ and $ISTF_{\mathrm{SD}}[z]$ describe the QΣΔM signal and image signal responses and $STF_{\mathrm{TOT}}[z]$ and $ISTF_{\mathrm{TOT}}[z]$ include the total contribution of both the front-end and the QΣΔM. It should be noted that these are frequency-selective functions, having notable dynamics over frequency when a wide signal band is considered. In addition, $X[z]$ is the ideally down-converted MFI-free baseband signal.

From the digitized waveform $v(k)$, the desired signal bands and the respective mirror bands are picked with the filters $\mathbf{n}_1$ to $\mathbf{n}_S$ and $\mathbf{n}_1^*$ to $\mathbf{n}_S^*$ as shown in Figure 5.7. The desired band filter coefficients are given as $\mathbf{n}_s = [n_{s,1}, n_{s,2}, ..., n_{s,M+1}]^T$, where $s \in \{1, 2, ..., S\}$ and M equals the filter order and the mirror-band filters are their complex-conjugates, having conjugation performed elementwise.

Now, the inband responses of the transfer functions are denoted with impulse-responses. Thus, $\mathbf{h}^{\mathrm{TOT}}_{\mathrm{STF},\bar{x}_s}$ and $\mathbf{h}^{\mathrm{TOT}}_{\mathrm{ISTF},\bar{x}_s}$ contain the total STF and ISTF responses on the sub-band s. By assuming practical (clearly above 0 dB) inband SNR and thus neglecting the lower power noise components, the compensated bandwise output signals $y_s(k)$ are given in time-domain by

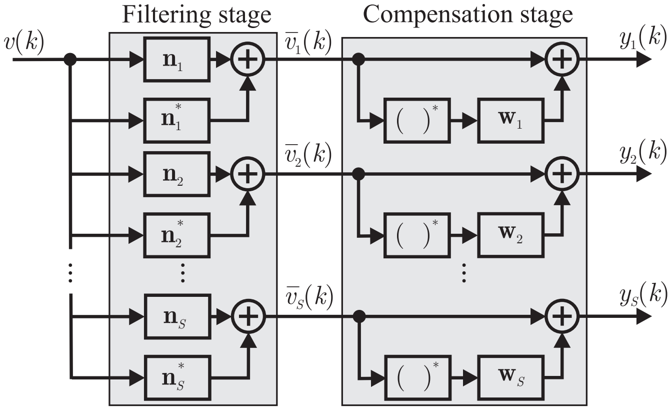

Figure 5.7: Digital frequency-selective MFI post-compensation structure for general multiband reception, processing S parallel information signals to be received and detected. The filters $\mathbf{n}_1$ to $\mathbf{n}_S$ and $\mathbf{n}_1^*$ to $\mathbf{n}_S^*$ are used to pick the desired signals and the related mirror-bands, respectively.

$$\begin{aligned} y_s(k) \approx & \mathbf{h}_{\mathrm{STF},\bar{x}_s}^{\mathrm{TOT}} * \bar{x}_s(k) + \mathbf{h}_{\mathrm{ISTF},\bar{x}_s}^{\mathrm{TOT}} * \bar{x}_s^*(k) \\ & + \mathbf{w}_s * [\mathbf{h}_{\mathrm{ISTF},\bar{x}_s}^{\mathrm{TOT}} * \bar{x}_s^*(k) + \mathbf{h}_{\mathrm{STF},\bar{x}_s}^{\mathrm{TOT}} * \bar{x}_s(k)]. \end{aligned} \tag{5.9}$$

Herein, the aim is in minimizing the MFI originaring from the mirror-band blocker(s) because of the receiver front-end and the QΣΔM I/Q mismatches.

The bandwise N-tap compensation vectors $\mathbf{w}_s = [w_{s,1}, w_{s,2}, ..., n_{s,N}]^T$ are estimated for band s using the frequency-selective circularity restoring MFI compensation algorithm published in [12]. Therein, the circularity is defined as the complementary autocorrelation function c_{y_s} of $y_s(k)$ being zero, i.e., $c_{y_s}(\tau) = \mathrm{E}\,[y_s(k)y_s(k-\tau)] = 0$, meaning that real and imaginary parts of the compensated outputs are equally powerful and instantaneously mutually uncorrelated. Similarly, the traditional autocorrelation function γ_{y_s} is given by $\gamma_{y_s} = \mathrm{E}[y_s(k)y_s^*(k-\tau)]$. Now, the compensator coefficients $\mathbf{w}_s$, restoring the circularity of the compensated signal, can be solved by using the observed subband signal second-order statistics $c_{\bar{v}_s}(\tau) = \mathrm{E}\,[\bar{v}_s(k)\bar{v}_s(k-\tau)]$ and $\gamma_{\bar{v}_s}(\tau) = \mathrm{E}[\bar{v}_s(k)\bar{v}_s^*(k-\tau)]$. The complementary autocorrelation values are placed in a column-vector

$$\mathbf{c}_{\bar{v}_s} = \mathrm{E}\,[\bar{\mathbf{v}}_s(k)\bar{v}_s(k)] = [c_{\bar{v}_s}(0), c_{\bar{v}_s}(1), ..., c_{\bar{v}_s}(N-1)]^T, \tag{5.10}$$

where

$$\bar{\mathbf{v}}_s(k) = [\bar{v}_s(k), \bar{v}_s(k-1), ..., \bar{v}_s(k-N+1)]^T, \tag{5.11}$$

having the length of N. In parallel, the autocorrelation function values are used to create the matrices

$$\mathbf{\Gamma}_{\bar{v}_s} = \begin{bmatrix} \gamma_{\bar{v}_s}(0) & \gamma_{\bar{v}_s}(1) & \cdots & \gamma_{\bar{v}_s}\bar{v}_s(N-1) \\ \gamma^*_{\bar{v}_s}(1) & \gamma_{\bar{v}_s}(0) & \cdots & \gamma_{\bar{v}_s}(N-2) \\ \vdots & \vdots & \ddots & \vdots \\ \gamma^*_{\bar{v}_s}(N-1) & \gamma^*_{\bar{v}_s}(N-2) & \cdots & \gamma_{\bar{v}_s}(0) \end{bmatrix}, \tag{5.12}$$

and

$$\mathbf{\Gamma}'_{\bar{v}_s} = \begin{bmatrix} \gamma_{\bar{v}_s}(0) & \gamma_{\bar{v}_s}(1) & \cdots & \gamma_{\bar{v}_s}(N-1) \\ \gamma_{\bar{v}_s}(1) & \gamma_{\bar{v}_s}(0) & \cdots & \gamma_{\bar{v}_s}(N-2) \\ \vdots & \vdots & \ddots & \vdots \\ \gamma_{\bar{v}_s}(N-1) & \gamma_{\bar{v}_s}(N-2) & \cdots & \gamma_{\bar{v}_s}(0) \end{bmatrix}. \tag{5.13}$$

Finally, the approximately optimal compensator coefficients are given by

$$\mathbf{w}_s = -(\mathbf{\Gamma}_{\bar{v}_s} + \mathbf{\Gamma'}_{\bar{v}_s})^{-1}\mathbf{c}_{\bar{v}_s}. \tag{5.14}$$

In a simplified single-tap, frequency-independent, compensation scenario, this results in

$$w_s = -\frac{c_{\bar{v}_s}(0)}{\gamma_{\bar{v}_s}(0) + \sqrt{\gamma_{\bar{v}_s}(0)^2 - |c_{\bar{v}_s}(0)^2|}}. \tag{5.15}$$

In above, $s = 1$ for single-band reception and generally $s \in \{1, ..., S\}$ for reception of S signal bands. In practice, sample estimates of the second-order statistics $c_{\bar{v}_s}(\tau)$ and $\gamma_{\bar{v}_s}(\tau)$ are used and calculated over a block of received data samples.

The gains achieved with the proposed transfer function design combined with digital compensation described above are illustrated in Figure 5.8, when single-tap compensation is used in two-band reception scenario illustrated in Figure 5.5 and described in detail in [P7]. Therein, I/Q mismatches are assumed in all the coefficients of a two-stage QΣΔM described in Section 5.3.1. The coefficient values are again drawn from a uniform distribution ranging ±1% around the ideal values. In addition, the preceding analog front-end is assumed to have 30 dB IRR. The interference rejection ratio (defined in (5.1)) results are averaged over 150 independent realizations. The real valued I/Q signal modeling is again employed in the simulations together with true 3-bit I and Q quantizers for both the stages.

This scenario is realistic and challenging, considering multiple sources of MFI in a practical reception scenario. Figure 5.8 shows the post-processing based MFI suppression outperforming the mirror-frequency rejecting STF design in this scenario, while having even more significant gain over the noncompensated scenario. The achieved gains are between 6 dB and 14 dB when the relative blocker powers are from +20 dB to +50 dB. Furthermore, the interference rejection ratio of 14 dB, found to be practical in Section 5.1, can be maintained up to the relative blocker levels close to +25 dB while with other approaches the corresponding number is +15 dB.

The mirror-frequency rejecting STF design does not gain from the digital processing, because it is removing exactly the information that would be needed by the STF filtering. On the very highest blocker powers, the interference rejection ratio becomes limited by the quantization errors of the stages and their conjugate terms, which are not suppressed by the post-processing as efficiently as the input signal originating MFI.

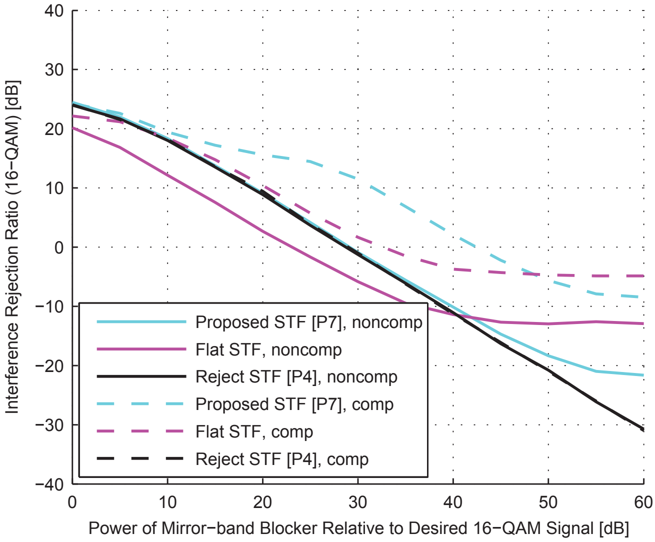

Figure 5.8: Interference rejection ratios for a 16-QAM signal with two-stage QΣΔM, in a two-band reception scenario, as a function of blocker signal power. The proposed STF, frequency-flat ("Flat STF") and mirror-frequency rejecting STF [P4] ("Reject STF") designs are simulated. I/Q mismatches are considered in all the coefficients of both stages together with image rejection ratio of 30 dB for the preceding receiver chain. [P7]

Furthermore, in a single-band reception scenario, illustrated in Figure 5.6, multi-tap frequency-selective compensation is applied. The interference rejection ratio results are shown in Figure 5.9. Therein, 200 independent random realizations of I/Q mismatched QΣΔM coefficients are used. From the results, it is clearly visible that in this wideband reception scenario, adding another tap for the compensation benefits the performance. For example, the 14 dB interference rejection ratio can be maintained up to +20 dB relative blocker power with the two-tap compensation while the corresponding numbers are +10 dB and +5 dB with the single-tap compensation and without compensation, respectively. These results also show that improved blocker tolerance can be obtained by suppressing MFI with the digital processing, which is facilitated by the transfer function design proposed herein. This is a significant benefit in dynamic signal conditions typical for DSA and CR receivers.

5.5 Transfer Function Reconfigurability in Dynamic Operation Conditions

With straightforward parametrization of the QΣΔM coefficients as function of the desired waveform center frequencies and bandwidths, the transfer functions can be easily reconfigured for varying reception scenarios. For example, in Table 5.2, a step-by-step design guide is given for a three-stage two-band QΣΔM. With this procedure, the

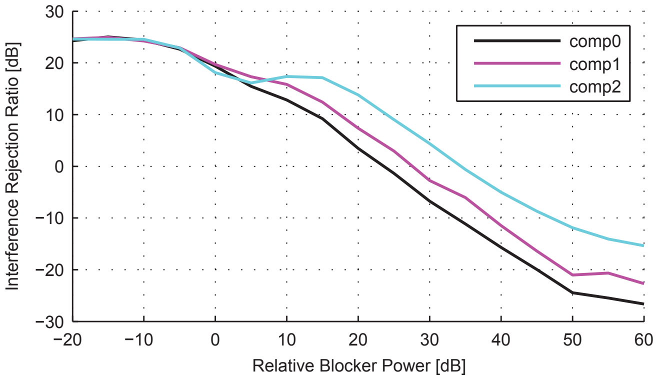

Figure 5.9: Interference rejection ratios for a 16-QAM signal with two-stage QΣΔM, in a single band reception scenario, as a function of blocker signal power. No compensation ("comp0"), single-tap compensation ("comp1") [P7] and two-tap compensation ("comp2") cases are simulated. I/Q mismatches are considered in all the coefficients of both the stages together with image rejection ratio of 30 dB for the preceding receiver chain. [P6]

transfer functions can be adapted in case of, e.g., a frequency handoff, being a typical scenario for the DSA and CR receivers, when the user is operating on unlicensed spectrum. There, the transmission should be moved to another band if the current band needs to be vacated for the PU. At the same time, the multiband reception allowed by the multiband transfer functions in the QΣΔM bring additional robustness for the SUs when the transmission can be continued on another band even if the other one needs to be vacated.

The transfer functions can also be reconfigured for reception of different number of information signals. For example, for a single wideband carrier with 20 MHz bandwidth, the NTF zeros can be placed contiguously inside this band, as discussed in [P7] in case of two-stage QΣΔM with overall noise-shaping order of eight, allowing efficient noise shaping even with lower oversampling ratios. On the other hand, noncontiguous NTF design allows reception of multiple distinct information signals on separate frequency bands. With the QΣΔM of [P7] theoretically eight separate narrowband waveforms could be received when having a single noise shaping notch for each band.

From practical point-of-view, tuning of the QΣΔM coefficients is implemented with digital control, having 6-8 bit resolution, resulting in sufficient dynamics and coefficient accuracy when operating on, for example, TV white spaces, where the channel spacing and the center frequency resolution is 8 MHz while the ADC sampling frequency being in the order of 100 MHz [P7]. The actual implementation of this control is an interesting future work topic.

With these reconfiguration options, a multistage QΣΔM is a potential option for DSA and CR receivers operating in dynamic signal conditions. At the same time, the power dissipation of the quantization process can be directed to the desired signal band.

CHAPTER 6

Conclusion

6.1 Main Results

This thesis discussed frequency-agile multiband transfer function designs for single- and multistage QΣΔMs intended for DSA and CR receivers. Employing a complex-valued NTF for quantization noise shaping allows more efficient utilization of receiver resources, such as battery power, through optimization of quantization precision and sampling frequency. The multiband quantization noise shaping allows also use of a number of noncontiguous frequency channels that are available, e.g., at a certain moment in a certain location in a DSA system. This kind of frequency agile spectrum access helps in improving efficiency of the spectrum usage, which is gathering a lot of academic and industrial attention at the moment. In parallel, the effects of I/Q mismatches because of unavoidable implementation inaccuracies were analyzed in detail, taking into account the QΣΔM itself as well as the preceding radio front-end. These components produce the combined MFI observed in digital domain. This was done with the help of a general closed-form transfer function analysis method which uses matrix-representation of I/Q mismatched QΣΔM coefficients. Furthermore, the transfer functions were designed with an aim of minimizing the MFI on desired signal bands to be received and detected. For this, two approaches were proposed. These are mirror-frequency rejecting STF design and transfer function design facilitating digital MFI post-compensation.

With the help of the closed-form expressions presented in this thesis, the four transfer functions (NTF, STF, INTF and ISTF) of the QΣΔM can be solved for any modulator order or number of stages. Furthermore, a closed-form equation for the output of such a modulator under coefficient mismatches was given. The transfer function analysis showed that the characteristics of the induced MFI depends significantly on the exact location of the I/Q mismatches inside a QΣΔM, or an analog radio front-end. The I/Q mismatches in the radio front-end or input branches of the QΣΔM create a mirror response only for the QΣΔM input signal, not for the quantization error. At the same time, mismatches in the loop filters and the modulator feedbacks generally cause also mirroring of the quantization error. Furthermore, the roles of the I/Q errors in the different stages of a multistage QΣΔM were analyzed. It was found that only the transfer characteristics of the two first stages affect the signal response while the errors in the latter stages modify only the quantization error response.

From the MFI mitigation point-of-view, the mirror-frequency rejecting STF design was found to be effective against the interference induced by the I/Q mismatches in the QΣΔM feedback branches. This was initially shown with the closed-form transfer function analysis illustrating the ISTF notch on the desired signal band indicating attenuated MFI and confirmed with simulations in realistic reception scenarios. The advantages of this approach include the fact that no changes to the circuitry or additional processing is needed. However, the MFI generated by other error sources are not mitigated.

In order to mitigate the MFI independent of the I/Q mismatch location, digital interference suppression is a logical choice. For application of this kind of algorithms in a receiver employing a QΣΔM for efficient signal digitization, a specific transfer function design scheme was proposed in this thesis work. With the design, the mirror-band signal acting as an interference source was used to digitally remove the MFI falling on top of the desired information signal because of the multiple I/Q mismatches included in a complete receiver chain. The analysis and simulations showed significant interference suppression, achieved by straightforwardly implementable blind post-compensation algorithm developed for QΣΔMs. Earlier digital MFI suppression approaches in QΣΔM receivers have relied on injected calibration signals or other non-blind approaches.

Overall, the transfer function analysis deepens the understanding of the behavior of different QΣΔM structures under I/Q mismatch and allows the designers to examine the effects of the inherent implementation inaccuracies in more detail already before measuring the actual implementation. In addition, facilitating digital compensation of MFI is an important step towards robust receiver implementations using quadrature QΣΔM ADCs, allowing the promising multiband and reconfigurability properties to be exploited in practice. The proposed design can be implemented without additional analog components and is straightforwardly reconfigurable in dynamic signal conditions typical for DSA and CR systems, e.g., in case of frequency hand-off because of a PU appearance. In addition, facilitating the digital post-compensation of the receiver front-end originating interference eases the demands for the matching of these circuits.

6.2 Future Work

The research work done for this thesis points towards several future research topics. The digital control for the transfer function reconfiguration should be studied in further detail in order to secure robust operation. This, of course, includes also analog circuit design with tunable modulator coefficients. Related to the actual circuit implementation of the modulator, there are multiple items that need to be studied in further detail. These include, e.g., amplitude scaling depending on the applied supply voltage, effects of the circuit settling times, use of non-delaying integrators and possible need for dynamic element matching in multibit feedback DACs.

Another concrete work item is the extension of the reported analysis to cover continuous-time QΣΔM variants, which have gathered increasing interest recently, allowing driving the feedback loop with higher frequencies and thus using also higher sampling rates.

This brings potential for even wider bandwidth operation and when combined with reconfigurable multiband transfer function designs has significant potential for frequency-agile wideband spectrum access.

Furthermore, research on time-interleaved ADCs and their unique characteristics and nonidealities has increased lately and extending the QΣΔM concept into that direction is a very interesting topic for the future research. As a matter of fact, an I/Q system is inherently time-interleaved but interleaving number of QΣΔM branches has potential for increasing the processing bandwidth even further. With all the cross-connections between the signal rails and different implementation options this is a cumbersome analysis but would bring valuable insight into the available potential.

Altogether, designing and implementing a viable and efficient A/D interface for SDRs and DSA or CR systems pose a research challenge valid for a great deal of future research. Especially when considering mobile devices and increasing number of cellular base stations, setting stringent requirements for power consumption, size and price of the devices.

REFERENCES

[1] *LTE; Feasibility study for Further Advancements for E-UTRA (LTE-Advanced)*, 3GPP TR 36.912 version 11.0.0 Release 11, Oct. 2012.

[2] *LTE; Evolved Universal Terrestrial Radio Access (E-UTRA); Base Station (BS) radio transmission and reception*, 3GPP TS 36.104 version 11.9.0 Release 11, Aug. 2014.

[3] *LTE; Evolved Universal Terrestrial Radio Access (E-UTRA); User Equipment (UE) radio transmission and reception*, 3GPP TS 36.101 version 11.9.0 Release 11, Jul. 2014.

[4] A. Abidi, “The path to the software-defined radio receiver,” *IEEE Journal of Solid-State Circuits*, vol. 42, no. 5, pp. 954–966, May 2007.

[5] T. Adali, P. Schreier, and L. Scharf, “Complex-valued signal processing: The proper way to deal with impropriety,” *IEEE Transactions on Signal Processing*, vol. 59, no. 11, pp. 5101–5125, Nov 2011.

[6] W. Akram and E. Swartzlander, “Tunable mismatch shaping for quadrature bandpass delta-sigma data converters,” in *Proc. IEEE Workshop on Signal Processing Systems*, Oct 2010, pp. 198–203.

[7] I. F. Akyildiz, W.-Y. L. Lee, M. C. Vuran, and S. Mohanty, “NeXt generation/dynamic spectrum access/cognitive radio wireless networks: a survey,” *Computer Networks*, vol. 50, pp. 2127–2159, 2006.

[8] A. Alexiou, “Wireless world 2020: Radio interface challenges and technology enablers,” *IEEE Vehicular Technology Magazine*, vol. 9, no. 1, pp. 46–53, March 2014.

[9] L. Anttila, “Digital front-end signal processing with widely-linear signal models in radio devices,” Ph.D. dissertation, Tampere University of Technology, Finland, 2011.

[10] L. Anttila, M. Valkama, and M. Renfors, "Blind moment estimation techniques for I/Q imbalance compensation in quadrature receivers," in *Proc. 17th Annual IEEE International Symposium on Personal, Indoor and Mobile Radio Communications*, Helsinki, Finland, 11-14 Sept. 2006.

[11] ——, "Blind compensation of frequency-selective I/Q imbalances in quadrature radio receivers: Circularity -based approach," in *Proc. IEEE International Conference Acoustics, Speech and Signal Processing*, vol. 3, April 2007, pp. III–245–III–248.

[12] ——, "Circularity based I/Q imbalance compensation in wideband direct-conversion receivers," *IEEE Transactions on Vehicular Technology*, vol. 57, no. 3, pp. 2099–2113, July 2008.

[13] S. Ardalan and J. Paulos, "An analysis of sinusoidally excited delta-sigma modulators," in *Proc. IEEE International Conference on Acoustics, Speech, and Signal Processing*, vol. 12, Apr 1987, pp. 2129–2132.

[14] J. Arias, P. Kiss, V. Prodanov, V. Boccuzzi, M. Banu, D. Bisbal, J. Pablo, L. Quintanilla, and J. Barbolla, "A 32-mW 320-MHz continuous-time complex delta-sigma ADC for multi-mode wireless-LAN receivers," *IEEE Journal of Solid-State Circuits*, vol. 41, no. 2, pp. 339–351, Feb 2006.

[15] A. Atac, L. Liao, Y. Wang, M. Schleyer, Y. Zhang, R. Wunderlich, and S. Heinen, "A 1.7mw quadrature bandpass $\Delta\Sigma$ ADC with 1MHz BW and 60dB DR at 1MHz IF," in *Proc. IEEE International Symposium on Circuits and Systems*, May 2013, pp. 1039–1042.

[16] P. Aziz, "Multi-band oversampled noise shaping analog to digital conversion," Ph.D. dissertation, University of Pennsylvania, Philadelphia, 1996.

[17] P. Aziz, H. Sorensen, and J. Van der Spiegel, "Multi band sigma delta analog to digital conversion," in *Proc. IEEE International Conference on Acoustics, Speech, and Signal Processing*, vol. iii, Apr 1994, pp. III/249–III/252 vol.3.

[18] ——, "Performance of complex noise transfer functions in bandpass and multi band sigma delta systems," in *Proc. IEEE International Symposium on Circuits and Systems*, vol. 1, 30 Apr-3 May 1995, pp. 641–644 vol.1.

[19] P. Aziz, H. Sorensen, and J. van der Spiegel, "An overview of sigma-delta converters," *IEEE Signal Processing Magazine*, vol. 13, no. 1, pp. 61–84, Jan 1996.

[20] R. Bagheri, A. Mirzaei, M. Heidari, S. Chehrazi, M. Lee, M. Mikhemar, W. Tang, and A. Abidi, "Software-defined radio receiver: dream to reality," *IEEE Communications Magazine*, vol. 44, no. 8, pp. 111–118, Aug 2006.

[21] H. Berndt, R. Richter, and H.-J. Jentschel, "A 100 MS/sec, 8th-order quadrature sigma-delta ADC for complex-IF signal digitization in a wideband-IF sampling receiver," in *Proc. 5th International Conference on ASIC*, vol. 1, Oct 2003, pp. 669–672 Vol.1.

[22] A. Bourdoux, J. Craninckx, A. Dejonghe, and L. Van der Perre, “Receiver architectures for software-defined radios in mobile terminals: the path to cognitive radios,” in *Proc. IEEE Radio and Wireless Symposium*, Jan 2007, pp. 535–538.

[23] S. Boyd, J. Frye, M. Pursley, and T. Royster, “Spectrum monitoring during reception in dynamic spectrum access cognitive radio networks,” *IEEE Transactions on Communications*, vol. 60, no. 2, pp. 547–558, February 2012.

[24] R. Brainard and J. Candy, “Direct-feedback coders: design and performance with television signals,” *Proceedings of the IEEE*, vol. 57, no. 5, pp. 776–786, May 1969.

[25] L. Breems, E. Dijkmans, and J. Huijsing, “A quadrature data-dependent DEM algorithm to improve image rejection of a complex modulator,” *IEEE Journal of Solid-State Circuits*, vol. 36, no. 12, pp. 1879–1886, Dec. 2001.

[26] ——, “A quadrature data-dependent DEM algorithm to improve image rejection of a complex $\Sigma\Delta$ modulator,” in *Digest of Technical Papers, IEEE International Solid-State Circuits Conference*, Feb 2001, pp. 48–49.

[27] M. Camus, B. Butaye, L. Garcia, M. Sie, B. Pellat, and T. Parra, “A 5.4 mW/0.07 mm^2 2.4 GHz front-end receiver in 90 nm CMOS for IEEE 802.15.4 WPAN standard,” *IEEE Journal of Solid-State Circuits*, vol. 43, no. 6, pp. 1372–1383, June 2008.

[28] J. Candy, “A use of limit cycle oscillations to obtain robust analog-to-digital converters,” *IEEE Transactions on Communications*, vol. 22, no. 3, pp. 298–305, Mar 1974.

[29] ——, “A use of double integration in sigma delta modulation,” *IEEE Transactions on Communications*, vol. 33, no. 3, pp. 249–258, Mar 1985.

[30] J. Candy and O. Benjamin, “The structure of quantization noise from sigma-delta modulation,” *IEEE Transactions on Communications*, vol. 29, no. 9, pp. 1316–1323, Sep 1981.

[31] J. Candy, B. Wooley, and O. Benjamin, “A voiceband codec with digital filtering,” *IEEE Transactions on Communications*, vol. 29, no. 6, pp. 815–830, Jun 1981.

[32] G. Cauwenberghs and G. Temes, “Adaptive digital correction of analog errors in MASH ADCs. I. off-line and blind on-line calibration,” *IEEE Transactions on Circuits and Systems II, Analog and Digital Signal Processing*, vol. 47, no. 7, pp. 621–628, Jul 2000.

[33] K.-H. Chao, S. Nadeem, W. Lee, and C. Sodini, “A higher order topology for interpolative modulators for oversampling A/D converters,” *IEEE Transactions on Circuits and Systems*, vol. 37, no. 3, pp. 309–318, Mar 1990.

[34] J. Chapin and W. Lehr, “Cognitive radios for dynamic spectrum access - the path to market success for dynamic spectrum access technology,” *IEEE Communications Magazine*, vol. 45, no. 5, pp. 96–103, May 2007.

[35] W. Chappell, E. Naglich, C. Maxey, and A. Guyette, “Putting the radio in ’software-defined radio’: hardware developments for adaptable RF systems,” *Proceedings of the IEEE*, vol. 102, no. 3, pp. 307–320, March 2014.

[36] W. Cheng, K. P. Pun, C. Chan, and C. Choy, “An IF-sampling SC complex lowpass $\Sigma\Delta$ modulator with high image rejection by capacitor sharing,” in *Proc. IEEE International Symposium on Circuits and Systems*, vol. 1, May 2004, pp. I–1140–3 Vol.1.

[37] W. Chou, P. Wong, and R. Gray, “Multistage sigma-delta modulation,” *IEEE Transactions on Information Theory*, vol. 35, no. 4, pp. 784–796, Jul 1989.

[38] J. Crols and M. Steyaert, “Low-IF topologies for high-performance analog front ends of fully integrated receivers,” *IEEE Transactions on Circuits and Systems II, Analog and Digital Signal Processing*, vol. 45, no. 3, pp. 269–282, Mar 1998.

[39] P. Cruz, N. Carvalho, and K. Remley, “Designing and testing software-defined radios,” *IEEE Microwave Magazine*, vol. 11, no. 4, pp. 83–94, June 2010.

[40] K. David, S. Dixit, and N. Jefferies, “2020 vision - the wireless world research forum looks to the future,” *IEEE Vehicular Technology Magazine*, vol. 5, no. 3, pp. 22–29, Sept 2010.

[41] A. Edward and J. Silva-Martinez, “General analysis of feedback DAC’s clock jitter in continuous-time sigma-delta modulators,” *IEEE Transactions on Circuits and Systems II, Express Briefs*, vol. 61, no. 5, May 2014.

[42] I. Elahi, K. Muhammad, and P. Balsara, “Parallel correction and adaptation engines for I/Q mismatch compensation,” *IEEE Transactions on Circuits and Systems II, Express Briefs*, vol. 56, no. 1, pp. 86–90, Jan 2009.

[43] J. Ferguson, P.F., A. Ganesan, and R. Adams, “One bit higher order sigma-delta A/D converters,” in *IEEE International Symposium on Circuits and Systems*, May 1990, pp. 890–893 vol.2.

[44] G. Fettweis, M. Lohning, D. Petrovic, M. Windisch, P. Zillmann, and W. Rave, “Dirty RF: a new paradigm,” in *Proc. 16th Annual IEEE International Symposium on Personal, Indoor and Mobile Radio Communications*, Berlin, Germany, 11-14 Sept. 2005.

[45] A. Flores, R. Guerra, E. Knightly, P. Ecclesine, and S. Pandey, “IEEE 802.11af: a standard for TV white space spectrum sharing,” *IEEE Communications Magazine*, vol. 51, no. 10, pp. 92–100, October 2013.

[46] V. Giannini, J. Craninckx, S. D’Amico, and A. Baschirotto, “Flexible baseband analog circuits for software-defined radio front-ends,” *IEEE Journal of Solid-State Circuits*, vol. 42, no. 7, pp. 1501–1512, July 2007.

[47] G.-T. Gil, “Nondata-aided I/Q mismatch and DC offset compensation for direct conversion receivers,” *IEEE Transactions on Signal Processing*, vol. 56, no. 7, pp. 2662–2668, July 2008.

[48] R. Gray, “Oversampled sigma-delta modulation,” *IEEE Transactions on Communications*, vol. 35, no. 5, pp. 481–489, May 1987.

[49] ——, “Quantization noise spectra,” *IEEE Transactions on Information Theory*, vol. 36, no. 6, pp. 1220–1244, Nov 1990.

[50] R. Gray, W. Chou, and P. Wong, “Quantization noise in single-loop sigma-delta modulation with sinusoidal inputs,” *IEEE Transactions on Communications*, vol. 37, no. 9, pp. 956–968, Sep 1989.

[51] R. Gray and D. Neuhoff, “Quantization,” *IEEE Transactions on Information Theory*, vol. 44, no. 6, pp. 2325–2383, Oct 1998.

[52] F. Harris, “Digital filter equalization of analog gain and phase mismatch in I-Q receivers,” in *Proc. 5th IEEE International Conference on Universal Personal Communications*, vol. 2, Sep 1996, pp. 793–796 vol.2.

[53] T. Hayashi, Y. Inabe, K. Uchimura, and T. Kimura, “A multistage delta-sigma modulator without double integration loop,” in *Digest of Technical Papers IEEE International Solid-State Circuits Conference*, vol. XXIX, Feb 1986, pp. 182–183.

[54] C.-Y. Ho, W.-S. Chan, Y.-Y. Lin, and T.-H. Lin, “A quadrature bandpass continuous-time delta-sigma modulator for a tri-mode GSM-EDGE/UMTS/DVB-T receiver,” *IEEE Journal of Solid-State Circuits*, vol. 46, no. 11, pp. 2571–2582, Nov 2011.

[55] O. Ileri and N. B. Mandayam, “Dynamic spectrum access models: toward an engineering perspective in the spectrum debate,” *IEEE Communications Magazine*, vol. 46, no. 1, pp. 153–160, January 2008.

[56] H. Inose and Y. Yasuda, “A unity bit coding method by negative feedback,” *Proceedings of the IEEE*, vol. 51, no. 11, pp. 1524–1535, Nov 1963.

[57] H. Inose, Y. Yasuda, and J. Murakami, “A telemetering system by code modulation - $\Delta - \Sigma$ modulation,” *IRE Transactions on Space Electronics and Telemetry*, vol. SET-8, no. 3, pp. 204–209, Sept 1962.

[58] M. Ismail and D. Rodríguez de Llera González, Eds., *Radio Design in Nano-meter Technologies.* Dordrecht, Netherlands: Springer, 2006.

[59] S. Jantzi, “Quadrature bandpass delta-sigma modulation for digital radio,” Ph.D. dissertation, University of Toronto, Toronto, Canada, 1997.

[60] S. Jantzi, K. Martin, and A. Sedra, “A quadrature bandpass delta-sigma modulator for digital radio,” *IEEE Journal of Solid-State Circuits*, vol. 32, no. 12, pp. 1935–1950, Dec. 1997.

[61] S. Jantzi, K. W. Martin, M. Snelgrove, and A. Sedra, “A complex bandpass $\Sigma\Delta$ converter for digital radio,” in *Proc. IEEE International Symposium on Circuits and Systems*, London, UK, 30 May-2 Jun 1994, pp. 453–456.

[62] S. Jantzi, K. Martin, and A. Sedra, “The effects of mismatch in complex bandpass ΔΣ modulators,” in *Proc. IEEE International Symposium on Circuits and Systems*, Atlanta, GA, 12-15 May 1996, pp. 227–230.

[63] S. Jantzi, R. Schreier, and M. Snelgrove, “Bandpass sigma-delta analog-to-digital conversion,” *IEEE Transactions on Circuits and Systems*, vol. 38, no. 11, pp. 1406–1409, Nov 1991.

[64] S. Jantzi, M. Snelgrove, and J. Ferguson, P.F., “A fourth-order bandpass sigma-delta modulator,” *IEEE Journal of Solid-State Circuits*, vol. 28, no. 3, pp. 282–291, Mar 1993.

[65] K. Karthikeyan and N. Vasudevan, “Analysis of performance of sigma delta architecture in software defined radio,” in *Proc. Recent Advances in Space Technology Services and Climate Change*, Nov 2010, pp. 164–166.

[66] P. Kenington and L. Astier, “Power consumption of A/D converters for software radio applications,” *IEEE Transactions on Vehicular Technology*, vol. 49, no. 2, pp. 643–650, Mar 2000.

[67] P. Kiss, “Adaptive digital compensation of analog circuit imperfections for cascaded delta-sigma analog-to-digital converters,” Ph.D. dissertation, ”Politehnica” University, Timisoara, Romania, 1999.

[68] P. Kiss, J. Silva, A. Wiesbauer, T. Sun, U.-K. Moon, J. Stonick, and G. Temes, “Adaptive digital correction of analog errors in MASH ADCs. II. correction using test-signal injection,” *IEEE Transactions on Circuits and Systems II, Analog and Digital Signal Processing*, vol. 47, no. 7, pp. 629–638, Jul 2000.

[69] B. Le, T. Rondeau, J. Reed, and C. Bostian, “Analog-to-digital converters,” *IEEE Signal Processing Magazine*, vol. 22, no. 6, pp. 69–77, Nov 2005.

[70] T. Leslie and B. Singh, “An improved sigma-delta modulator architecture,” in *IEEE International Symposium on Circuits and Systems*, May 1990, pp. 372–375 vol.1.

[71] B. Li and K.-P. Pun, “A high image-rejection SC quadrature bandpass DSM for low-if receivers,” *IEEE Transactions on Circuits and Systems I, Regular Papers*, vol. 61, no. 1, pp. 92–105, Jan 2014.

[72] P.-I. Mak, S.-P. U, and R. Martins, “Transceiver architecture selection: Review, state-of-the-art survey and case study,” *IEEE Circuits and Systems Magazine*, vol. 7, no. 2, pp. 6–25, Second 2007.

[73] K. Martin, “Complex signal processing is not complex,” *IEEE Transactions on Circuits and Systems I, Regular Papers*, vol. 51, no. 9, pp. 1823–1836, Sept 2004.

[74] J. Marttila, “Quadrature sigma-delta ADCs: Modeling and signal processing,” Master’s thesis, Tampere University of Technology, Finland, 2010.

[75] J. Marttila, M. Allen, and M. Valkama, "I/Q imbalance effects in quadrature $\Sigma\Delta$ modulators - analysis and signal processing," in *Proc. IEEE International Microwave Workshop Series on RF Front-ends for Software Defined and Cognitive Radio Solutions*, Feb 2010, pp. 1–4.

[76] Mathworks. Matlab. [Online]. Available: http://www.mathworks.com/products/matlab/

[77] ——. Symbolic math toolbox. [Online]. Available: http://www.mathworks.com/products/symbolic/

[78] M. Matinmikko, "Spectrum sharing using cognitive radio system capabilities," Ph.D. dissertation, University of Oulu, Finland, 2012.

[79] M. Matinmikko, H. Okkonen, M. Palola, S. Yrjölä, P. Ahokangas, and M. Mustonen, "Spectrum sharing using licensed shared access: the concept and its workflow for LTE-advanced networks," *IEEE Wireless Communications*, vol. 21, no. 2, pp. 72–79, April 2014.

[80] K. Matthews, *Elementary Linear Algebra.* Brisbane, Australia: Univ. Queensland, 2012, [E-book]. Available: http://www.numbertheory.org/ [Accessed: 11 Apr. 2012].

[81] L. Maurer, R. Stuhlberger, C. Wicpalek, G. Haberpeuntner, and G. Hueber, "Be flexible," *IEEE Microwave Magazine*, vol. 9, no. 2, pp. 83–95, April 2008.

[82] R. Maurino and C. Papavassiliou, "Quadrature sigma; delta; modulators with a dynamic element matching scheme," *IEEE Transactions on Circuits and Systems II, Express Briefs*, vol. 52, no. 11, pp. 771–775, Nov 2005.

[83] J. Mitola, "Cognitive radio architecture evolution," *Proceedings of the IEEE*, vol. 97, no. 4, pp. 626–641, April 2009.

[84] J. Mitola and J. Maguire, G.Q., "Cognitive radio: making software radios more personal," *IEEE Personal Communications*, vol. 6, no. 4, pp. 13–18, Aug 1999.

[85] J. Mitola III, "Cognitive radio - an integrated agent architecture for software defined radio," Ph.D. dissertation, Royal Institute of Technology, Stockholm, Sweden, 2000.

[86] A. Morgado, R. del Rio, and J. dela Rosa, "High-efficiency cascade $\Sigma\Delta$ modulators for the next generation software-defined-radio mobile systems," *IEEE Transactions on Instrumentation and Measurement*, vol. 61, no. 11, pp. 2860–2869, Nov 2012.

[87] T. Pearce and A. Baker, "Analogue to digital conversion requirements for HF radio receivers," in *Proc. IEE colloquium on system aspects and applications of ADCs for radar, sonar and communications*, Nov 1987.

[88] A. Prata, A. Oliveira, and N. Carvalho, "An agile digital radio system for UHF white spaces," *IEEE Microwave Magazine*, vol. 15, no. 1, pp. 92–97, Jan 2014.

[89] K.-P. Pun, C.-S. Choy, C.-F. Chan, and J. da Franca, “An I/Q mismatch-free switched-capacitor complex sigma-delta modulator,” *IEEE Transactions on Circuits and Systems I, Express Briefs*, vol. 51, no. 5, pp. 254–256, May 2004.

[90] K. Pun, J. Franca, C. Azeredo-Leme, C. Chan, and C. Choy, “Correction of frequency dependent I/Q mismatches in quadrature receivers,” *Electronics Letters*, vol. 37, no. 23, pp. 1415–1417, Nov. 2001.

[91] B. Razavi, “Design considerations for direct-conversion receivers,” *IEEE Transactions on Circuits and Systems II: Analog and Digital Signal Processing*, vol. 44, no. 6, pp. 428–435, Jun 1997.

[92] ——, “Cognitive radio design challenges and techniques,” *IEEE Journal of Solid-State Circuits*, vol. 45, no. 8, pp. 1542–1553, Aug 2010.

[93] S. Reekmans, P. Rombouts, and L. Weyten, “Mismatch insensitive double-sampling quadrature bandpass ΣΔ modulation,” *IEEE Transactions on Circuits and Systems I, Regular Papers*, vol. 54, no. 12, pp. 2599–2607, Dec. 2007.

[94] D. Ribner, “Multistage bandpass delta sigma modulators,” *IEEE Transactions on Circuits and Systems II, Analog and Digital Signal Processing*, vol. 41, no. 6, pp. 402–405, Jun 1994.

[95] D. Ribner, R. Baertsch, S. Garverick, D. McGrath, J. Krisciunas, and T. Fujii, “A third-order multistage sigma-delta modulator with reduced sensitivity to nonidealities,” *IEEE Journal of Solid-State Circuits*, vol. 26, no. 12, pp. 1764–1774, Dec 1991.

[96] L. Risbo, “Σ-Δ modulators - stability analysis and optimization,” Ph.D. dissertation, Technical University of Denmark, Copenhagen, Denmark, 1994.

[97] Z. Ru, N. Moseley, E. Klumperink, and B. Nauta, “Digitally enhanced software-defined radio receiver robust to out-of-band interference,” *IEEE Journal of Solid-State Circuits*, vol. 44, no. 12, pp. 3359–3375, Dec. 2009.

[98] A. Rusu, B. Dong, and M. Ismail, “Putting the ’flex’ in flexible mobile wireless radios,” *IEEE Circuits and Devices Magazine*, vol. 22, no. 6, pp. 24–30, Nov.-Dec. 2006.

[99] T. Salo, “Bandpass delta-sigma modulators for radio receivers,” Ph.D. dissertation, Helsinki University of Technology, Finland, 2003.

[100] R. Schreier, “An empirical study of high-order single-bit delta-sigma modulators,” *IEEE Transactions on Circuits and Systems II, Analog and Digital Signal Processing*, vol. 40, no. 8, pp. 461–466, Aug 1993.

[101] R. Schreier and M. Snelgrove, “Bandpass sigma-delta modulation,” *Electronics Letters*, vol. 25, no. 23, pp. 1560–1561, Nov 1989.

[102] R. Schreier and G. Temes, *Understanding Delta-Sigma Data Converters*. Hoboken, NJ: Wiley, 2005.

[103] K. Shin, H. Kim, A. Min, and A. Kumar, “Cognitive radios for dynamic spectrum access: from concept to reality,” *IEEE Wireless Communications*, vol. 17, no. 6, pp. 64–74, December 2010.

[104] O. Shoaei and M. Snelgrove, “Optimal (bandpass) continuous-time $\Sigma\Delta$,” in *IEEE International Symposium on Circuits and Systems*, vol. 5, May 1994, pp. 489–492 vol.5.

[105] A. Silva, J. Guilherme, and N. Horta, “Reconfigurable multi-mode sigma-delta modulator for 4G mobile terminals,” *The VLSI Journal of Integration*, vol. 42, no. 1, pp. 34–46, Jan. 2009.

[106] J. Silva, “High performance delta-sigma analog-to-digital converters,” Ph.D. dissertation, Oregon State University, Corvallis, 2005.

[107] M. Song, C. Xin, Y. Zhao, and X. Cheng, “Dynamic spectrum access: from cognitive radio to network radio,” *IEEE Wireless Communications*, vol. 19, no. 1, pp. 23–29, February 2012.

[108] M. Sosio, A. Liscidini, and R. Castello, “A 2G/3G cellular analog baseband based on a filtering ADC,” *IEEE Transactions on Circuits and Systems II, Express Briefs*, vol. 59, no. 4, pp. 214–218, April 2012.

[109] A. Swaminathan, M. Snelgrove, S. Jantzi, and S. Bazarjani, “A monolithic complex sigma-delta modulator for digital radio,” in *IEEE-CAS Region 8 Workshop on Analog and Mixed IC Design*, Sept 1996, pp. 83–86.

[110] Y. Tang, K.-W. Cheng, S. Gupta, J. Paramesh, and D. Allstot, “Cascaded complex ADCs with adaptive digital calibration for I/Q mismatch,” *IEEE Transactions on Circuits and Systems I, Regular Papers*, vol. 55, no. 3, pp. 817–827, April 2008.

[111] K. Uchimura, T. Hayashi, T. Kimura, and A. Iwata, “Oversampling A-to-D and D-to-A converters with multistage noise shaping modulators,” *IEEE Transactions on Acoustics, Speech and Signal Processing*, vol. 36, no. 12, pp. 1899–1905, Dec 1988.

[112] M. Valkama, J. Marttila, and M. Allén, *Digital Processing for Front End in Wireless Communication and Broadcasting.* Cambridge University Press, 2011, ch. Advanced quadrature sigma-delta modulators for A/D interface.

[113] M. Valkama, J. Pirskanen, and M. Renfors, “Signal processing challenges for applying software radio principles in future wireless terminals: an overview,” *International Journal of Communications Systems*, vol. 15, pp. 741–769, 2002.

[114] R. van de Plassche, “A sigma-delta modulator as an A/D converter,” *IEEE Transactions on Circuits and Systems*, vol. 25, no. 7, pp. 510–514, Jul 1978.

[115] N. Vun and A. Prenkumar, “ADC systems for SDR digital front-end,” in *Proc. 9th International Symposium on Consumer Electronics*, Macau, Hong Kong, 14-16 June 2005.

[116] R. Walden, “Analog-to-digital converter survey and analysis,” *IEEE Journal on Selected Areas in Communications*, vol. 17, no. 4, pp. 539–550, Apr 1999.

[117] L. Yu and M. Snelgrove, “A novel adaptive mismatch cancellation system for quadrature IF radio receivers,” *IEEE Transactions on Circuits and Systems II, Analog and Digital Signal Processing*, vol. 46, no. 6, pp. 789–801, June 1999.

[118] ——, “Mismatch cancellation for complex bandpass sigma-delta modulators,” in *Proc. 40th IEEE International Midwest Symposium on Circuits and Systems*, vol. 2, Aug 1997, pp. 814–817.

[119] T. Yucek and H. Arslan, “A survey of spectrum sensing algorithms for cognitive radio applications,” *IEEE Communications Surveys & Tutorials*, vol. 11, no. 1, pp. 116–130, First 2009.

[120] Q. Zhao and B. Sadler, “A survey of dynamic spectrum access,” *IEEE Signal Processing Magazine*, vol. 24, no. 3, pp. 79–89, May 2007.

PUBLICATION 1

Jaakko Marttila, Markus Allén and Mikko Valkama, “Design and analysis of multi-stage quadrature sigma-delta A/D converter for cognitive radio receivers,” in *Proceedings of the 16th IEEE International Workshop on Computeter-Aided Modeling, Analysis and Design of Communonication Links and Networks*, Kyoto, Japan, June 2011.

Design and Analysis of Multi-Stage Quadrature Sigma-Delta A/D Converter for Cognitive Radio Receivers

Jaakko Marttila, Markus Allén and Mikko Valkama
Department of Communications Engineering
Tampere University of Technology
P.O. Box 553, FI-33101, Tampere, Finland
jaakko.marttila@tut.fi, markus.allen@tut.fi, mikko.e.valkama@tut.fi

Abstract* — In this article, the design and analysis of sophisticated multi-band quadrature ΣΔ modulators (QΣΔM) are addressed, offering a high-performance and easily-reconfigurable solution for the analog-to-digital (A/D) interface of cognitive radio receivers. Based on spectrum sensing information, the multi-band principle stemming from multi-stage converter implementation enables multiple reconfigurable noise transfer function (NTF) notches for efficient quantization noise shaping. Also mirror-frequency-rejecting signal transfer function (STF) design is proposed for multi-stage QΣΔM, which implements part of the receiver selectivity and offers also robustness against certain circuit implementation nonidealities. More specifically, we concentrate here on the so-called in-phase / quadrature (I/Q) imbalance problem, being an unavoidable problem in quadrature circuits and thus also in QΣΔMs. An analytical closed-form model is derived for a two-stage QΣΔM under implementation nonidealities, realizing multi-band noise shaping with first-order building blocks. Stemming from this analysis, it is shown that clever design of the NTF and the STF of the multi-stage QΣΔM offers both straightforward reconfigurability and robustness against converter implementation mismatches.

***Index Terms* — Analog-digital conversion, bandpass filters, complex filters, cognitive radio, digital radio, I/Q imbalance, mirror-frequency interference, radio receivers, sigma-delta modulation**

I. INTRODUCTION

Nowadays, growing number of parallel wireless communication standards, together with ever-increasing traffic amounts, create a widely acknowledged need for novel radio solutions, such as emerging cognitive radio paradigm [1]. On the other hand, transceiver implementations should be small-sized, power efficient, highly integrable and cheap [2], [3]. At the same time, operating band should be extremely wide (even gigahertz range), dynamic range of the wideband receiver should be high (tens of dBs) and the transceiver should be able to adapt to numerous different transmission schemes and waveforms [3], [4]. These demands create a big challenge particularly for the mobile receiver design. Therein, especially the analog-to-digital interface has been identified as a key performance limiting bottleneck [2], [3].

A promising solution for the receiver design in this kind of scenario is low-IF architecture with a quadrature ΣΔ analog-to-digital (A/D) converter [5]. Furthermore, a multiband modulator aimed to cognitive radio receivers is proposed in [6] and illustrated with receiver block diagram and principal spectra in Fig. 1. This kind of multi-band design for quadrature ΣΔ modulator (QΣΔM) offers frequency agile flexibility and reconfigurability together with capability of receiving multiple parallel frequency bands [6], which are considered essential when realizing A/D interface for cognitive radio solutions [1]. The characteristics of such QΣΔM can be directly adapted to different reception scenarios based on spectrum sensing information.

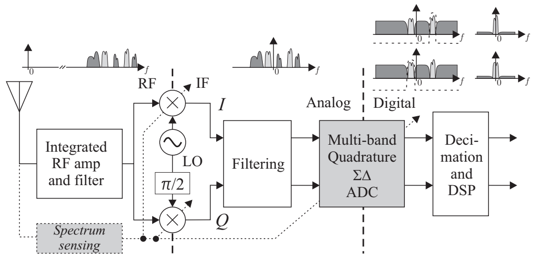

Fig. 1. Block diagram of *multi-band* low-IF quadrature receiver, based on QΣΔM together with principal spectra, where two light grey signals are the desired ones, illustrating the signal composition at each stage.

However, implementing quadrature circuits brings always a challenge of matching the I and Q rails and controlling mismatch induced mirror-frequency interference (MFI) [5]. In QΣΔM, the mismatch generates image response for both the input signal and the quantization error [5], [6], [7]. From the noise point of view, placing a noise transfer function (NTF) notch also on the mirror-frequency to cancel MFI is proposed in [5]. This however wastes shaping performance from the desired signal point of view and restricts design freedom, especially in multi-band scenarios. In addition, this does not take mirroring of the input signal into account. Furthermore, modifications to analog circuitry have been proposed in [8]–[10] to minimize the interference. However, additional components add to the circuit area and power dissipation of the modulator [8]. On the other hand, sharing the components between the branches [9], [10] degrades sampling properties of the modulator. In [6] and [7], the authors found that mirror-frequency-rejecting signal transfer function (STF) design can mitigate the input signal originating MFI in case of mismatch in the feedback branch of a first-order QΣΔM. In this article, the idea is extended to cover multiband designs realized with multi-stage QΣΔM, which offer valuable degrees of freedom and flexibility for the response design. The feedback I/Q imbalance effects and related digital calibration in multi-stage QΣΔM are addressed also in [11]. However, therein main emphasis is on noise originating MFI and only a frequency-flat STF is considered.

The rest of the article is organized as follows. In Section II basics of quadrature ΣΔ modulation are reviewed. Section III proposes a new closed-form transfer function model for I/Q imbalance effects in a two-stage QΣΔM. Design of the modulator transfer functions in presence of I/Q mismatches is discussed in Section IV. Finally, Section V presents the results of the designs and Section VI concludes the article.

This work was supported by the Academy of Finland, the Finnish Funding Agency for Technology and Innovation (Tekes), HPY Research Foundation and Nokia Foundation.

II. QUADRATURE ΣΔ MODULATION

Quadrature variant of the ΣΔ modulator is presented in [5]. The concept is based on the modulator structure similar to the one used in real lowpass and bandpass modulators, but employing complex-valued input and output signals together with complex loop filters (integrators). This complex signal processing gives additional degree of freedom to response design, allowing frequency-asymmetric noise and signal transfer functions. For analysis purposes, a linear model of the modulator can be used. In other words, this means that quantization error is assumed to be additive and having no correlation with the input signal. Although not being exactly true, this allows analytical derivation of the transfer functions and has thus been applied widely, e.g. in [5] and [12]. Now, the output of ordinary quadrature ΣΔ modulator is defined as

$$V[z] = STF[z]U[z] + NTF[z]E[z] \tag{1}$$

where $STF[z]$ and $NTF[z]$ are generally complex-valued functions. To further illustrate the composition, a block diagram of a general N'th order QΣΔM is given in Fig. 2.

In the following subsections, multi-stage and multi-band principles will be presented. These are important concepts, considering reconfigurability in the A/D interface and frequency agile conversion with high-enough resolution.

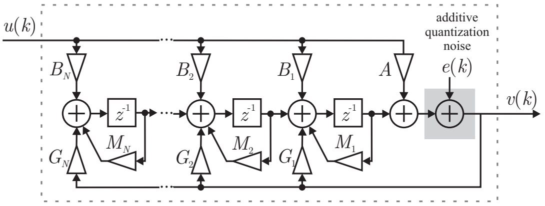

Fig. 2. Discrete-time linearized model of an N'th-order QΣΔM with complex-valued signals and coefficients.

A. *Multi-Stage Quadrature ΣΔ Modulator*

Multi-stage ΣΔ modulators have been introduced to improve resolution, e.g., in case of wideband information signal, when attainable oversampling is limited. This principle was first proposed with lowpass modulator [12], but has thereafter been extended to QΣΔMs [8], [11]. The block diagram of two-stage QΣΔM is given in Fig. 3, where both individual stages are of arbitrary order.

The main goal in multi-stage QΣΔM is to digitize quantization error of the first stage with the second stage and thereafter subtract it from the original output. Due to the noise shaping in the first stage, the digitized error estimate must be filtered in the same way to achieve effective cancellation. Similarly, the output of the first stage must be filtered with digital equivalent of the second-stage signal transfer function. These filters are depicted in Fig. 3 with $H_1^D[z]$ and $H_2^D[z]$. Now, the final output becomes

$$\begin{aligned} V[z] &= H_1^D[z]STF_1[z]U[z] + H_1^D[z]NTF_1[z]E_1[z] \\ &-H_2^D STF_2 E_1[z] - H_2^D[z]NTF_2[z]E_2[z]. \end{aligned} \tag{2}$$

Assuming ideal matching of the digital filters, i.e., $H_1^D[z] = STF_2^D[z]$ and $H_2^D[z] = NTF_1^D[z]$, the first-stage noise components are reduced, giving

$$V_{ideal}[z] = STF_2^D[z]STF_1[z]U[z] - NTF_1^D[z]NTF_2[z]E_2[z]. \tag{3}$$

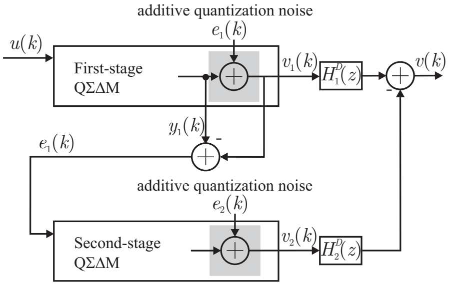

Fig. 3. Two-stage QΣΔM with arbitrary-order noise shaping on both individual stages. Filters $H_1^D[z]$ and $H_2^D[z]$ are implemented digitally.

From (3) it can be seen that the overall shaping for the signal and second-stage noise components are the products of the transfer functions of the individual stages and thus of the combined order.

B. *Multi-Band Principle for Cognitive Radio*

With QΣΔM transfer functions of higher than the first order, it is possible to place multiple NTF zeros on the conversion band [5]. Traditional way of exploiting this property has been making the noise shaping notch wider, thus improving the resolution of the interesting wideband information signal [5]. However, in cognitive radio based systems, it is desirable to be able to receive more than one detached frequency bands – and signals – in parallel [1].

Complex multi-band noise shaping without restriction to frequency-symmetry is able to respond to this need with noncontiguous NTF notches. This is the central theme of this article. In addition, the frequencies of the notches can be tuned straightforwardly and independently, e.g., in case of frequency handoff. The frequency bands of the desired signals and the most harmful blockers are obtained with spectrum sensing. Thereafter, the modulator coefficients (see Fig. 2) are tuned in order to realize as efficient NTF and STF as possible. The zeros and the poles of the transfer functions are straightforwardly defined by the coefficients. Further details on parametrization of multi-band transfer functions can be found in [6].

III. I/Q IMBALANCE IN MULTI-STAGE QΣΔM

Ideally, the I and Q rails of a QΣΔM are matched perfectly. With this ideal matching, (1)–(3) are valid. However, in true circuit implementation, coefficient values are never exact. In this section, a novel analytical closed-form model for modeling I/Q imbalance in multi-stage QΣΔM is derived. First, mismatch effects in individual stage are reviewed based on previous analyses on single-stage modulators [6], [7]. Thereafter, the model is extended to cover the whole multi-stage structure, assuming a QΣΔM with two stages. Such analysis is missing from the existing literature.

A. *I/Q Imbalance Effects on Individual QΣΔM Stage*

Quadrature signal processing is implemented with parallel real signals and coefficients. In Fig. 4, this is demonstrated in case of a single first-order QΣΔM stage (parallel real signal I and Q rails) and taking mismatches in the coefficients into account. Deviation between coefficient-values of the rails, which should ideally be the same, results in MFI. This interference can be presented mathematically with conjugate response of the signal and the noise components. Thus, image signal transfer function (ISTF) and image noise transfer function (INTF) are introduced to describe the output under

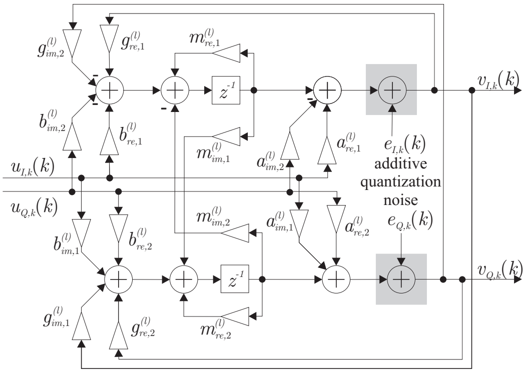

Fig. 4. Implementation structure of a single QΣΔM stage with parallel real signals and coefficients, taking possible coefficient mismatches into account.

I/Q imbalance. In the following, an analytical model is presented, first for individual stages of a two-stage QΣΔM. For simplicity of notation, first-order stages are assumed in this section. With help of this analysis, a closed-form model is then developed for an I/Q mismatched two-stage QΣΔM as a whole.

The I/Q imbalance analysis for a single stage is based on the block diagram given in Fig. 4. There, real and imaginary parts of the coefficients of Fig. 3 (for $N = 1$) are marked with subscripts *re* and *im*, whereas nonideal implementation values of the signal rails are separated with subscripts 1 and 2. The independent coefficients of the stages are denoted with superscript l. Thus, in order to obtain the complex outputs $V_l[z] = V_{I,l}[z] + jV_{Q,l}[z]$ of the stages (assuming two stages, i.e., $l \in \{1,2\}$), the I branch outputs are given by

$$\begin{aligned} V_{I,l}[z] = {} & \frac{\alpha_I^{(l)}[z]}{\gamma_I^{(l)}[z]} U_{I,l}[z] - \frac{\beta_I^{(l)}[z]}{\gamma_I^{(l)}[z]} U_{Q,l}[z] + \\ & \frac{\varepsilon_I^{(l)}[z]}{\gamma_I^{(l)}[z]} E_{I,l}[z] + \frac{\eta_I^{(l)}[z]}{\gamma_I^{(l)}[z]} E_{Q,l}[z] - \frac{\rho_I^{(l)}[z]}{\gamma_I^{(l)}[z]} V_{Q,l}[z], \end{aligned} \tag{4}$$

where the auxiliary variables multiplying the signal components are defined by the coefficients (see Fig. 4) in the following manner:

$$\alpha_I^{(l)}[z] = a^{(l)}_{re,1} + (b^{(l)}_{re,1} - m^{(l)}_{re,1} a^{(l)}_{re,1} + m^{(l)}_{im,2} a^{(l)}_{im,1}) z^{-1}, \tag{5}$$

$$\beta_I^{(l)}[z] = a^{(l)}_{im,2} + (b^{(l)}_{im,1} - m^{(l)}_{re,1} a^{(l)}_{im,2} - m^{(l)}_{im,2} a^{(l)}_{re,2}) z^{-1}, \tag{6}$$

$$\varepsilon_I^{(l)}[z] = 1 - m^{(l)}_{re,1} z^{-1}, \tag{7}$$

$$\eta_I^{(l)}[z] = m^{(l)}_{im,2} z^{-1}, \tag{8}$$

$$\rho_I^{(l)}[z] = (g^{(l)}_{im,2} + m^{(l)}_{im,2}) z^{-1}, \tag{9}$$

$$\gamma_I^{(l)}[z] = 1 - (g^{(l)}_{re,1} + m^{(l)}_{re,1}) z^{-1}. \tag{10}$$

This follows directly from a step-by-step signal analysis of the implementation structure in Fig. 4. Similarly, the real-valued Q branch outputs are given by

$$\begin{aligned} V_{Q,l}[z] = {} & \frac{\beta_Q^{(l)}[z]}{\gamma_Q^{(l)}[z]} U_{I,l}[z] + \frac{\alpha_Q^{(l)}[z]}{\gamma_Q^{(l)}[z]} U_{Q,l}[z] + \\ & \frac{\varepsilon_Q^{(l)}[z]}{\gamma_Q^{(l)}[z]} E_{Q,l}[z] - \frac{\eta_Q^{(l)}[z]}{\gamma_Q^{(l)}[z]} E_{I,l}[z] + \frac{\rho_Q^{(l)}[z]}{\gamma_Q^{(l)}[z]} V_{I,l}[z] \end{aligned} \tag{11}$$

where

$$\alpha_Q^{(l)}[z] = a^{(l)}_{re,2} + (b^{(l)}_{re,2} - m^{(l)}_{re,2} a^{(l)}_{re,2} + p^{(l)}_{im,1} a^{(l)}_{im,2}) z^{-1}, \tag{12}$$

$$\beta_Q^{(l)}[z] = a^{(l)}_{im,1} + (b^{(l)}_{im,1} - m^{(l)}_{re,2} a^{(l)}_{im,1} - m^{(l)}_{im,1} a^{(l)}_{re,1}) z^{-1}, \tag{13}$$

$$\varepsilon_Q^{(l)}[z] = 1 - m^{(l)}_{re,2} z^{-1}, \tag{14}$$

$$\eta_Q^{(l)}[z] = m^{(l)}_{im,1} z^{-1}, \tag{15}$$

$$\rho_Q^{(l)}[z] = (g^{(l)}_{im,1} + m^{(l)}_{im,1}) z^{-1}, \tag{16}$$

$$\gamma_Q^{(l)}[z] = 1 - (g^{(l)}_{re,2} + m^{(l)}_{re,2}) z^{-1}. \tag{17}$$

In this way, the complex-valued output and the exact behavior of each transfer function can be solved analytically in different I/Q mismatch scenarios. As a result, the output of an individual stage with nonideal matching of the I and Q branches becomes

$$\begin{aligned} V_l[z] = V_{I,l}[z] + jV_{Q,l}[z] = STF_l[z] U_l[z] + ISTF_l[z] U_l^*[z^*] \\ + NTF_l[z] E_l[z] + INTF_l[z] E_l^*[z^*] \end{aligned} \tag{18}$$

where superscript asterisk ($*$) denotes complex conjugation and the transfer functions are, based on (4) and (11) (omitting $[z]$ from the modulator coefficient variables of (5)–(10) and (12)–(17) for notational convenience), given by

$$\begin{aligned} STF_l[z] = {} & \frac{\gamma_Q^{(l)}\alpha_I^{(l)} + \gamma_I^{(l)}\alpha_Q^{(l)} - \rho_Q^{(l)}\beta_I^{(l)} - \rho_I^{(l)}\beta_Q^{(l)}}{2(\gamma_I^{(l)}\gamma_Q^{(l)} + \rho_I^{(l)}\rho_Q^{(l)})} \\ & + j\frac{\rho_I^{(l)}\alpha_Q^{(l)} + \rho_Q^{(l)}\alpha_I^{(l)} + \gamma_Q^{(l)}\beta_I^{(l)} + \gamma_I^{(l)}\beta_Q^{(l)}}{2(\gamma_I^{(l)}\gamma_Q^{(l)} + \rho_I^{(l)}\rho_Q^{(l)})}, \end{aligned} \tag{19}$$

$$\begin{aligned} ISTF_l[z] = {} & \frac{\gamma_Q^{(l)}\alpha_I^{(l)} - \gamma_I^{(l)}\alpha_Q^{(l)} + \rho_Q^{(l)}\beta_I^{(l)} - \rho_I^{(l)}\beta_Q^{(l)}}{2(\gamma_I^{(l)}\gamma_Q^{(l)} + \rho_I^{(l)}\rho_Q^{(l)})} \\ & + j\frac{\rho_Q^{(l)}\alpha_I^{(l)} - \rho_I^{(l)}\alpha_Q^{(l)} + \gamma_I^{(l)}\beta_Q^{(l)} - \gamma_Q^{(l)}\beta_I^{(l)}}{2(\gamma_I^{(l)}\gamma_Q^{(l)} + \rho_I^{(l)}\rho_Q^{(l)})}, \end{aligned} \tag{20}$$

$$\begin{aligned} NTF_l[z] = {} & \frac{\gamma_Q^{(l)}\varepsilon_I^{(l)} + \gamma_I^{(l)}\varepsilon_Q^{(l)} + \rho_I^{(l)}\eta_Q^{(l)} + \rho_Q^{(l)}\eta_I^{(l)}}{2(\gamma_I^{(l)}\gamma_Q^{(l)} + \rho_I^{(l)}\rho_Q^{(l)})} \\ & + j\frac{\rho_I^{(l)}\varepsilon_Q^{(l)} + \rho_Q^{(l)}\varepsilon_I^{(l)} - \gamma_Q^{(l)}\eta_I^{(l)} - \gamma_I^{(l)}\eta_Q^{(l)}}{2(\gamma_I^{(l)}\gamma_Q^{(l)} + \rho_I^{(l)}\rho_Q^{(l)})}, \end{aligned} \tag{21}$$

$$\begin{aligned} INTF_l[z] = {} & \frac{\gamma_Q^{(l)}\varepsilon_I^{(l)} - \gamma_I^{(l)}\varepsilon_Q^{(l)} + \rho_I^{(l)}\eta_Q^{(l)} - \rho_Q^{(l)}\eta_I^{(l)}}{2(\gamma_I^{(l)}\gamma_Q^{(l)} + \rho_I^{(l)}\rho_Q^{(l)})} \\ & + j\frac{\gamma_Q^{(l)}\eta_I^{(l)} - \gamma_I^{(l)}\eta_Q^{(l)} + \rho_Q^{(l)}\varepsilon_I^{(l)} - \rho_I^{(l)}\varepsilon_Q^{(l)}}{2(\gamma_I^{(l)}\gamma_Q^{(l)} + \rho_I^{(l)}\rho_Q^{(l)})}. \end{aligned} \tag{22}$$

For the latter stage ($l = 2$), the quantization error of the previous stage is used as an input, meaning that $U_2[z] = E_1[z]$. In the following, the above analysis for the individual stages $l \in \{1,2\}$ is combined in order to complete the closed form overall model for the two-stage QΣΔM.

B. I/Q Imbalance Model for Two-Stage QΣΔM

For multi-stage QΣΔM, the final output signal is defined as a difference of digitally filtered output signals of the stages [12]. In two-stage structure (ideal modulator graphically illustrated in Fig. 3) the output of the first stage, given by (18) with $l = 1$, is filtered with digital filter $H_1^D[z]$ (usually matched to the STF of the second stage) and the output of the second stage, similarly given by (18) with $l = 2$, is filtered with $H_2^D[z]$ (usually matched to the NTF of the first stage). Thus, the final output can now be expressed as

$$V[z] = H_1^D[z]V_1[z] - H_2^D[z]V_2[z] \tag{23}$$

in case of I/Q mismatches in both the stages. Replacing $V_1[z]$ and $V_2[z]$ in (23) with (18) for $l \in \{1,2\}$ gives now an expression for the output as

$$\begin{aligned} V[z] = {} & STF_2^D[z]STF_1[z]U[z] + STF_2^D[z]ISTF_1[z]U^*[z^*] \\ & + STF_2^D[z]NTF_1[z]E_1[z] + STF_2^D[z]INTF_1[z]E_1^*[z^*] \\ & - NTF_1^D[z]STF_2[z]E_1[z] - NTF_1^D[z]ISTF_2[z]E_1^*[z^*] \\ & - NTF_1^D[z]NTF_2[z]E_2[z] - NTF_1^D[z]INTF_2[z]E_2^*[z^*], \end{aligned} \tag{24}$$

where the transfer functions are as defined in (19)–(22). Again, the digital filters are assumed matched to the analog transfer functions with $H_1^D[z] = STF_2^D[z]$ and $H_2^D[z] = NTF_1^D[z]$. It should be noticed that the first-stage quantization noise terms $STF_2^D[z]NTF_1[z]E_1[z]$ and $NTF_1^D[z]STF_2[z]E_1[z]$ do not reduce to zero due to noncommutativity of the complex transfer functions under I/Q imbalance [11]. Now, it is clear that filtered versions of the original and conjugate components of the input, the first-stage quantization error and the second-stage quantization error are all present at the output. The roles of the separate signal components are further illustrated with numerical results in Section V.

IV. QΣΔM TRANSFER FUNCTION DESIGN FOR COGNITIVE RADIO UNDER I/Q IMBALANCE

In cognitive radio type receiver, signal dynamics can be tens of (even 50–60) dBs [4]. With such signal composition, controlling, e.g., image rejection of the receiver components is essential. Herein, we concentrate on QΣΔM transfer function design under I/Q imbalance, having minimization of input signal oriented MFI as the goal.

The NTF and the STF of a QΣΔM can be designed by placing transfer function zeros and poles, parameterized and tuned (allowing reconfigurability) by the QΣΔM coefficients, inside the unit circle [5]. In cognitive radio receiver, this is assumed to be done based on the spectrum sensing information as illustrated in Fig. 1. With this information about frequency bands of the desired and blocking signals, the modulator coefficients can be reconfigured to give the best achievable noise and signal responses (NTF and STF). An example of this parametrization and design of the coefficient values are further illustrated for a single-stage QΣΔM in [6]. The design is constrained because the transfer functions share common poles due to the modulator structure, but the zeros can be placed independent of each other [6]. It is exactly the zeros, which define the notches of the transfer functions. Thus, a common choice is to place NTF zeros on the desired signal band(s), generating the desired noise shaping effect. In [5], the STF design, for one, is used to attenuate out-of-band frequencies of the input signal uniformly. Multi-stage and higher-order QΣΔMs also allow multi-band noise shaping, which means that the NTF zeros are placed on noncontiguous frequencies [6]. Consequently, such multi-band capability offers, e.g., additional capacity and robustness in cognitive radio transmission scheme [1].

In QΣΔMs, the modulator feedback branch mismatches have been considered most crucial [8], [9], [11]. Exactly this problem can be fought against with clever transfer function design, which is proposed herein for multi-stage QΣΔMs. The signal fed to the feedback branch of the modulator is the same as in the output, so the STF and NTF effect is seen therein in full extent. Taking this into account, together with potential blocking signal energy on the mirror band, mirror-frequency-rejecting STF design is a recommended choice for single-stage QΣΔMs based on the analysis in [6], [7]. The main difference in this design compared to the one proposed in [5] is deeper notching of the mirror-band(s) in order to attenuate possible input blocker(s) as effectively as possible.

In addition to the previous studies [6], [7], the analysis in this article shows that *the first stage of a multi-stage modulator* benefits substantially from the mirror-frequency-rejecting STF design proposed herein. This will be further illustrated with numerical examples in Section V. The role of the first-stage is emphasized because of the possible blocking signals. The input of the latter stage(s) is the error of the previous stage(s) and thus likely having less power variations along frequency axis. Albeit the overall STF is a product of the stage STFs, only the first-stage STF can offer robustness against input signal originating MFI stemming from the mismatches in the feedback branch of that stage. Thus, design of the first-stage STF should be considered carefully in presence of I/Q mismatches.

V. RESULTS ON TRANSFER FUNCTION ANALYSIS

Herein, the model derived in Section III is used to analytically calculate the transfer functions for two-stage QΣΔMs under I/Q imbalance, having both stages of order two. Thus, the overall STF and NTF orders are four. The transfer functions are analyzed with randomly deviated modulator feedback gain values ($G_1^{(l)}$ and $G_2^{(l)}$ for $l \in \{1,2\}$) to model implementation inaccuracies. The deviation values are drawn from uniform distribution with maximum of ±1% relative to the ideal value. Thus, for example one realization of the real part of the mismatched modulator feedback gain becomes $g_{re,1}^{(1)} = (1 + \Delta_{g^{(1)}})g_{re}^{(1)}$, where $g_{re,1}^{(1)}$ is the implementation value and $g_{re}^{(1)}$ the ideal value. Five independent mismatched realizations of each transfer function are plotted to demonstrate the effects of inaccuracies on the responses. Multi-band reception [6] of two parallel information signals around relative center frequencies of 0.38 and 0.15 is assumed as an example. These bands (relative bandwidth of 0.05) are marked in the following figures with black solid lines.

With ordinary *frequency-flat STF design for both stages*, the transfer functions are plotted in Fig. 5. The three plots present the responses for the input signal, first-stage quantization error and second-stage quantization error, respectively. The ISTF response

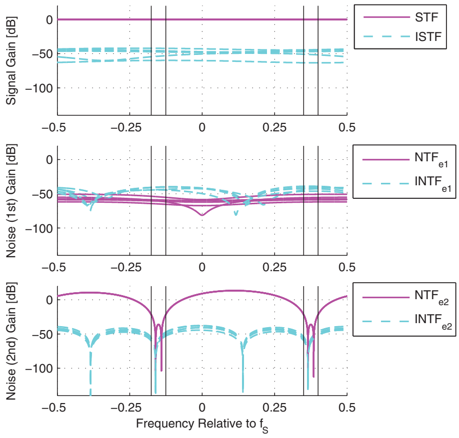

Fig. 5. Two-stage QΣΔM STF and ISTF (top) together with NTF and INTF for first- (middle) and second-stage quantization noise (bottom). Five independent random realizations in real gain values of feedback branches of both stages and *frequency flat STF designs*.

averages at -50 dB level, varying between -40 dB and -60 dB over the desired signal bands. Noise responses in middle and bottom plots show that second-stage error is well shaped, but first-stage error is leaking to the output due to noncommutativity of mismatched complex transfer functions. However, attenuation is still at the level of -40 dB, image response exceeding the original one with approximately 15 dB. The second-stage noise is shown to be shaped effectively, the four noise notches being visible. The noise attenuation is at the level of -40 dB.

In Fig. 6, *the proposed mirror-frequency-rejecting STF of the first-stage* improves image rejection from the input signal point of view, showing on average 30 dB increase in image rejection over the desired bands. The noise shaping results remain essentially similar compared to the previous case. If the *second stage STF is also designed to reject mirror frequencies*, as in Fig. 7, image rejection of the mirror bands is clearly improved (ISTF notches on the mirror bands). However, no significant image rejection improvements are achieved from the desired band point of view compared to the case with mirror-frequency-rejecting STF design only on the first stage. However, the STF notches in the mirror bands are widened because of digital filter $H_1^D[z]$ is matched to the mirror-frequency-rejecting STF of the second stage. This result highlights the importance of the first-stage STF design, as discussed above in Section IV. The noise shaping results are again very similar to the previous cases.

VI. CONCLUSIONS

This paper provided an analytical transfer function model for I/Q imbalance effects in a two-stage QΣΔM. Based on the derived model, it was concluded that the proposed mirror-frequency-rejecting STF design applied in the first stage of a two-stage QΣΔM was able to improve the image rejection of the input signal component in the modulator by 30 dB when considering feedback branch I/Q mismatches. This technique improves the image rejection of a multistage QΣΔM without additional electronics, enabling more robust operation under challenging signal dynamics typical for cognitive radio receivers.

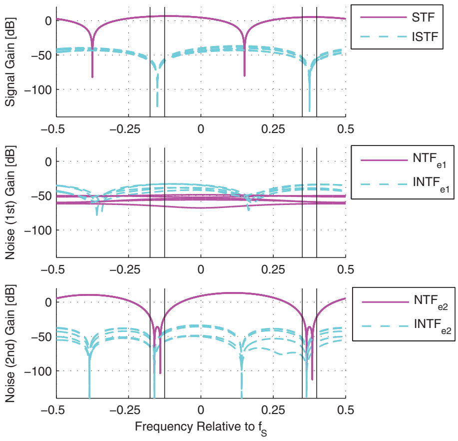

Fig. 6. Two-stage QΣΔM STF and ISTF (top) together with NTF and INTF for first- (middle) and second-stage quantization noise (bottom). Five independent random realizations in real gain values of feedback branches of both stages and *proposed mirror-frequency-rejecting STF design in first stage*.

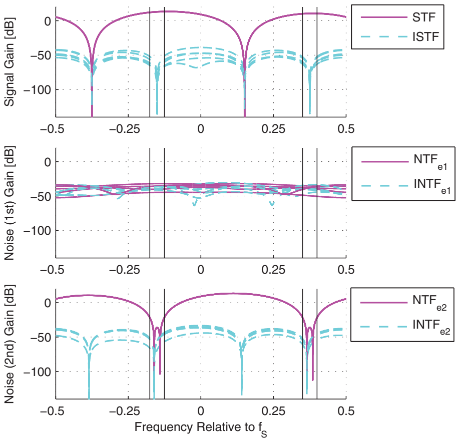

Fig. 7. Two-stage QΣΔM STF and ISTF (top) together with NTF and INTF for first- (middle) and second-stage quantization noise (bottom). Five independent random realizations in real gain values of feedback branches of both stages and *mirror-frequency-rejecting STF designs in both stages*.

REFERENCES

[1] I. F. Akyildiz, W.-Y. Lee, M. C. Vuran and S. Mohanty, “NeXt generation/dynamic spectrum access/cognitive radio wireless networks: a survey,” *Computer Networks*, vol. 50, no. 13, pp. 2127–2159, Sep. 2006.

[2] P.-I. Mak, S.-P. U and R. P. Martins, “Transceiver architecture selection: review, state-of-the-art survey and case study,” *IEEE Circuits Syst. Mag.*, vol. 7, no. 2, pp. 6–25, 2007.

[3] R. Bagheri, A. Mirzaei, M. E. Heidari, S. Chehrazi, M. Lee, M. Mikhemar, W. K. Tang and A. A. Abidi, “Software-defined radio receiver: dream to reality,” *IEEE Commun. Mag.*, vol. 44, no. 8, pp. 111–118, Aug. 2006.

[4] B. Razavi, “Cognitive radio design challenges and techniques,” *IEEE J. Solid-State Circuits*, vol. 45, no. 8, pp. 1542–1553, Aug. 2010.

[5] S. Jantzi, K. Martin, and A. Sedra, “A quadrature bandpass delta-sigma modulator for digital radio,” *IEEE J. Solid-State Circuits*, vol. 32, no. 12, pp. 1935–1950, Dec. 1997.

[6] J. Marttila, M. Allén and M. Valkama, “Quadrature ΣΔ modulation for cognitive radio – I/Q imbalance analysis and complex multiband principle,” *Circuits, Syst. and Signal Process.: Special Issue Embedded Signal Process. Circuits and Syst. Cognitive Radio-based Wireless Comm. Devices*, in press.

[7] J. Marttila, M. Allén and M. Valkama, “I/Q imbalance effects in quadrature ΣΔ modulators – analysis and signal processing,” in *Proc. IEEE Int. Microwave Workshop Series RF Front-ends for Software Defined and Cognitive Radio Solutions*, Aveiro, Portugal, Feb. 2010.

[8] L. J. Breems, E. C. Dijkmans and J. H. Huijsing, “A quadrature data-dependent DEM algorithm to improve image rejection of a complex modulator,” *IEEE J. Solid-State Circuits*, vol. 36, no. 12, pp. 1879–1886, Dec. 2001.

[9] K.-P. Pun, W.-T. Cheng, C.-S. Choy and C.-F. Chan, “A 75-dB image rejection IF-input quadrature-sampling ΣΔ modulator,” *IEEE J. Solid State Circ.*, vol. 41, no. 6, June 2006.

[10] S. Reekmans, P. Rombouts and L. Weyten, “Mismatch insensitive double-sampling quadrature bandpass ΣΔ modulation,” *IEEE Trans. Circuits and Syst. I: Regular Papers*, vol. 54, no. 12, Dec. 2007.

[11] Y. Tang, K.-W. Cheng, S. Gupta, J. Paramesh and D. J. Allstot, “Cascaded complex ADCs with adaptive digital calibration for I/Q mismatch,” *IEEE Trans. Circuits Syst. I, Reg. Papers*, vol. 55, no. 3, pp. 817–827, Apr. 2008.

[12] R. Schreier and G. C. Temes, *Understanding Delta-Sigma Data Converters*. Hoboken, NJ: Wiley, 2005.

PUBLICATION 2

Jaakko Marttila, Markus Allén and Mikko Valkama, “Response analysis of second-order multi-band quadrature sigma-delta modulators with applications in cognitive radio devices,” in *Proceedings of the 54th IEEE International Midwest Symposium on Circuits and Systems*, Seoul, South-Korea, August 2011.

Response Analysis of Second-Order Multi-Band Quadrature ΣΔ Modulators with Applications in Cognitive Radio Devices

Jaakko Marttila, Markus Allén and Mikko Valkama
Department of Communications Engineering
Tampere University of Technology
P.O. Box 553, FI-33101, Tampere, Finland
jaakko.marttila@tut.fi, markus.allen@tut.fi, mikko.e.valkama@tut.fi

***Abstract* — In this article, a novel analytical closed-form model is derived for second-order quadrature ΣΔ modulators (QΣΔM) taking implementation inaccuracies of QΣΔM coefficients into account. The model enables analytical examination of the modulator I/Q imbalance effects on input-output relation as well as signal and noise transfer functions (STF and NTF) independently. Thus, the image rejection of the QΣΔM can be evaluated both from the input signal and quantization error point-of-view. With the help of the model, it is shown analytically that a mirror-frequency rejecting STF design is an efficient way to mitigate mirror-frequency interference originating from blocking signals at the input of the modulator because of the QΣΔM feedback branch I/Q mismatches. The straightforward parametrization allows reconfigurability of the transfer functions which can be exploited, e.g., together with multi-band noise shaping capabilities. These concepts are valuable in A/D converters aimed to cognitive radio (CR) solutions. In CR receivers, A/D interface has been considered as a major bottleneck and QΣΔM offers frequency agile performance well fit for the purpose.**

***Index Terms* — Analog-to-digital conversion, complex filters, cognitive radio, digital radio, I/Q imbalance, mirror-frequency interference, radio receivers, sigma-delta modulation**

I. INTRODUCTION

Lately, increased traffic amounts in wireless networks have generated a widely acknowledged need for more efficient utilization of the limited accessible frequency spectrum. This is the goal, to which the emerging cognitive radio paradigm is aiming [1]. However, numerous technical challenges lie in the way to this target. Transceiver electronics should be small-sized, cheap and power efficient, especially in mass-market mobile devices [2]. However, ideally the same transceiver should be able to operate on gigahertz range bandwidth and receiver dynamic range of several tens of dBs, with altering transmission schemes and waveforms [3]. These demands become most evident when concerning analog-to-digital conversion, which has been identified as a performance-limiting bottleneck in mobile receivers [2].

A potential solution for this problem in the A/D interface is quadrature ΣΔ modulator (QΣΔM) based low-IF receiver [4]. Furthermore, a multi-band extension of this reception scheme aimed to the cognitive radio devices is proposed in [5] and illustrated with receiver block diagram and principal spectra of the stages in Fig. 1. The multi-band scheme for QΣΔM offers frequency agile flexibility and reconfigurability together with the capability of receiving multiple parallel frequency-slices [5]. These are considered as essential characteristics when realizing an A/D interface for the cognitive radio [1].

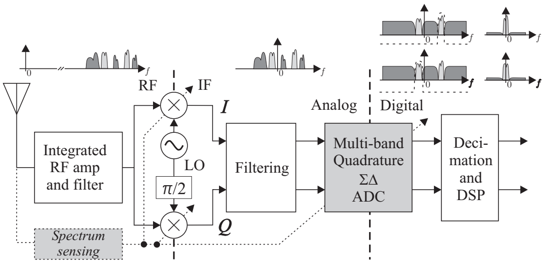

Fig. 1. Block diagram of *multi-band* low-IF quadrature receiver using QΣΔM, together with principal spectra, where the two light grey signals are the desired ones, illustrating the signal composition at each stage.

The quadrature circuit implementation has, however, an inherent problem of matching the I and Q rails. These mismatches induce mirror-frequency interference (MFI), which is thus a problem also in QΣΔM-based receivers [4]. In QΣΔMs generally, both the input signal and quantization error have mirror-responses [4], [5], [6]. The MFI originating from the quantization error due to the I/Q mismatches can be mitigated by placing noise transfer function (NTF) notch on the mirror-frequency of the desired signal band [4]. However, this wastes noise shaping capabilities on noninteresting frequency band and restricts the design freedom, particularly if combined with the multi-band reception. At the same time, input signal originating MFI remains unmitigated. In addition, analog circuit modifications have been proposed to reduce the MFI [7], [8], [9]. However, additional components add to the circuit area and power dissipation of the modulator [7]. On the other hand, sharing the components between the rails degrades sampling properties of the modulator [8], [9]. In [5] and [6], the authors initially showed that mirror-frequency-rejecting signal transfer function (STF) design can mitigate the input signal originating MFI in case of mismatch in the feedback branch of a first-order QΣΔM. In this article the idea is extended to cover the multi-band design of [5] with a second-order QΣΔM. A novel closed-form model is proposed for the output of the modulator, taking implementation inaccuracies into account.

This work was supported by the Academy of Finland, the Finnish Funding Agency for Technology and Innovation (Tekes), Austrian Center of Competence in Mechatronics (ACCM), HPY Research Foundation and Nokia Foundation.

The rest of the article is organized as follows. In Section II, basics of quadrature ΣΔ modulation are reviewed. Section III proposes a new closed-form model for I/Q imbalance effects in a second-order QΣΔM. Finally, Section IV presents the results of the transfer function analysis and Section V concludes the article.

II. QUADRATURE ΣΔ MODULATION AND MULTI-BAND PRINCIPLE

The main QΣΔM principle is presented in [4]. This concept is based on the modulator structure similar to the one used in real lowpass and bandpass modulators, but employing complex-valued input and output signals together with complex integrators as loop filters. This complex signal processing gives an additional degree of freedom to the response design, allowing frequency-asymmetric NTF and STF. For analysis purposes, a linear model of the modulator can be used. This means that quantization error is assumed to be additive and having no correlation with the input signal. Although not being exactly true, this allows analytical derivation of the transfer functions and has thus been applied widely, e.g., in [4] and [10]. In this way, the output of the QΣΔM is defined as

$$V[z] = STF[z]U[z] + NTF[z]E[z] \tag{1}$$

where $STF[z]$ and $NTF[z]$ are generally complex-valued transfer functions. To further illustrate the composition, a block diagram of a second-order QΣΔM is given in Fig. 2.

The complex NTF allows also frequency-asymmetric multi-band noise shaping. This is an important concept, considering the reconfigurability of the A/D interface and frequency agile conversion with high enough resolution. With QΣΔM of higher than first order, it is possible to place multiple NTF zeros on the conversion band. Traditional way of exploiting this property has been making the noise shaping notch wider, thus improving the resolution of the interesting information signal [4]. However, in cognitive radio based systems, it is desirable to be able to receive multiple detached frequency bands – and signals – in parallel [1]. The possible number of these notches is defined by the overall order of the QΣΔM. In addition, the frequencies of the notches can be tuned straightforwardly, e.g., in case of frequency handoff. Further details on design and parametrization of multi-band transfer functions can be found in [5].

III. I/Q IMBALANCE IN QUADRATURE ΣΔ MODULATORS

Ideally, I and Q rails of a QΣΔM are matched perfectly. With this perfect matching, (1) is valid. However, in true circuit implementation, coefficient values are never exact. In Fig. 3, this is demonstrated with a second-order QΣΔM having parallel real signal rails (I and Q) and taking mismatches in the coefficients into account. Deviation between coefficient values of the rails, which ideally should be the same, results in MFI. This interference can be presented mathematically with the conjugate response of the signal and the noise components. Thus, image signal transfer function (ISTF) and image noise transfer function (INTF) are introduced to describe the output under I/Q imbalance. In the following, a novel analytical model is presented for the second-order QΣΔM.

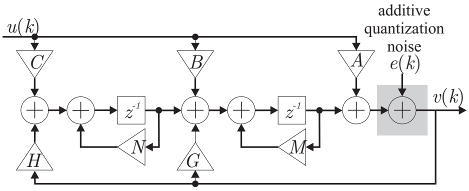

Fig. 2. Discrete-time linearized model of a second-order QΣΔM with complex-valued signals and coefficients.

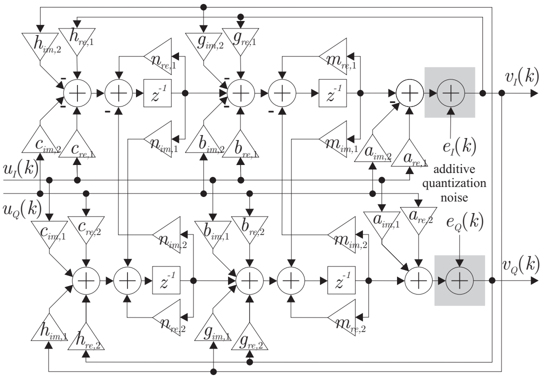

Fig. 3. Discrete-time linearized model of a second-order QΣΔM with parallel real signals and coefficients taking possible mismatches into account.

The output of a QΣΔM with nonideal matching of the I and Q rails (assuming linearized model) becomes

$$\begin{aligned} V[z] &= STF[z]U[z] + ISTF[z]U^*[z^*] \\ &+ NTF[z]E[z] + INTF[z]E^*[z^*] \end{aligned} \tag{2}$$

where superscript asterisk denotes complex conjugation. The image rejection of a first-order QΣΔM was analyzed based on the transfer functions in [5], [6]. Now, we present the novel analytical model for second-order QΣΔMs based on the block diagram of a mismatched second-order QΣΔM given in Fig. 3. Therein, real and imaginary parts of the coefficients of Fig. 2 are marked with subscripts *re* and *im* respectively whereas nonideal implementation values of the signal rails are separated with subscripts 1 and 2. Thus, in order to obtain the final complex-valued output $V[z] = V_I[z] + jV_Q[z]$ of the modulator, the I rail output is given as (with the help of auxiliary variables)

$$\begin{aligned} V_I[z] = &\frac{\alpha_I[z]}{\gamma_I[z]}U_I[z] - \frac{\beta_I[z]}{\gamma_I[z]}U_Q[z] + \\ &\frac{\varepsilon_I[z]}{\gamma_I[z]}E_I[z] + \frac{\eta_I[z]}{\gamma_I[z]}E_Q[z] - \frac{\rho_I[z]}{\gamma_I[z]}V_Q[z], \end{aligned} \tag{3}$$

where the variables multiplying the signal components are defined by the modulator coefficients (see Fig. 3) in the following manner:

$$\begin{aligned} \alpha_I[z] = a_{re,1} &+ [b_{re,1} - m_{re,1}a_{re,1} - n_{re,1}a_{re,1} \\ &+ n_{im,2}a_{im,1} + m_{im,2}a_{im,1}]z^{-1} + [c_{re,1} - n_{re,1}b_{re,1} \\ &+ n_{re,1}m_{re,1}a_{re,1} - n_{re,1}m_{im,2}a_{im,1} + n_{im,2}b_{im,1} \\ &- n_{im,2}m_{im,1}a_{re,1} - n_{im,2}m_{re,2}a_{im,1}]z^{-2}, \end{aligned} \tag{4}$$

$$\begin{aligned}\beta_I[z] = a_{im,2} &+ [b_{im,2} - n_{re,1}a_{im,2} - n_{im,2}a_{re,2} \\ &- m_{re,1}a_{im,2} - m_{im,2}a_{re,2}]z^{-1} + [c_{im,2} - n_{re,1}b_{im,2} \\ &+ n_{re,1}m_{re,1}a_{im,2} + n_{re,1}m_{im,2}a_{re,2} - n_{im,2}b_{re,2} \\ &- n_{im,2}m_{im,1}a_{im,2} + n_{im,2}m_{re,2}a_{re,2}]z^{-2},\end{aligned} \tag{5}$$

$$\begin{aligned}\varepsilon_I[z] = 1 &- [n_{re,1} + m_{re,1}]z^{-1} + [n_{re,1}m_{re,1} \\ &- n_{im,2}m_{im,1}]z^{-2},\end{aligned} \tag{6}$$

$$\begin{aligned}\eta_I[z] = [n_{im,2} &+ m_{im,2}]z^{-1} - [n_{re,1}m_{im,2} \\ &+ n_{im,2}m_{re,2}]z^{-2},\end{aligned} \tag{7}$$

$$\begin{aligned}\rho_I[z] = [n_{im,2} &+ g_{im,2} + m_{im,2}]z^{-1} - [h_{im,2} - n_{re,1}g_{im,2} \\ &- n_{re,1}m_{im,2} - n_{im,2}g_{re,2} - n_{im,2}m_{re,2}]z^{-2},\end{aligned} \tag{8}$$

$$\begin{aligned}\gamma_I[z] = 1 &- [n_{re,1} + g_{re,1} + m_{re,1}]z^{-1} + [h_{re,1} - n_{re,1}g_{re,1} \\ &- n_{re,1}m_{re,1} + n_{im,2}g_{im,1} + n_{im,2}m_{im,1}]z^{-2}.\end{aligned} \tag{9}$$

Similarly, the real-valued Q rail output is given by

$$\begin{aligned}V_Q[z] = \frac{\beta_Q[z]}{\gamma_Q[z]}U_I[z] &+ \frac{\alpha_Q[z]}{\gamma_Q[z]}U_Q[z] + \\ \frac{\varepsilon_Q[z]}{\gamma_Q[z]}E_Q[z] &- \frac{\eta_Q[z]}{\gamma_Q[z]}E_I[z] + \frac{\rho_Q[z]}{\gamma_Q[z]}V_I[z]\end{aligned} \tag{10}$$

where

$$\begin{aligned}\alpha_Q[z] = a_{re,2} &+ [b_{re,2} + n_{im,1}a_{im,2} - n_{re,2}a_{re,2} \\ &+ m_{im,1}a_{im,2} - m_{re,2}a_{re,2}]z^{-1} + [c_{re,2} - n_{re,2}b_{re,2} \\ &- n_{im,1}m_{im,2}a_{re,2} + n_{im,1}b_{im,2} - n_{im,1}m_{re,1}a_{im,2} \\ &- n_{re,2}m_{im,1}a_{im,2} + n_{re,2}m_{re,2}a_{re,2}]z^{-2},\end{aligned} \tag{11}$$

$$\begin{aligned}\beta_Q[z] = a_{im,1} &+ [b_{im,1} - n_{im,1}a_{re,1} - n_{re,2}a_{im,1} \\ &- m_{im,1}a_{re,1} - m_{re,2}a_{im,1}]z^{-1} + [c_{im,1} - n_{re,2}b_{im,1} \\ &- n_{im,1}m_{im,2}a_{im,1} - n_{im,1}b_{re,1} + n_{im,1}m_{re,1}a_{re,1} \\ &+ n_{re,2}m_{im,1}a_{re,1} + n_{re,2}m_{re,2}a_{im,1}]z^{-2},\end{aligned} \tag{12}$$

$$\begin{aligned}\varepsilon_Q[z] = 1 &- [n_{re,2} + m_{re,2}]z^{-1} + [n_{re,2}m_{re,2} \\ &- n_{im,1}m_{im,2}]z^{-2},\end{aligned} \tag{13}$$

$$\begin{aligned}\eta_Q[z] = [n_{im,1} &+ m_{im,1}]z^{-1} + [n_{im,1}m_{re,1} \\ &+ n_{re,2}m_{im,1}]z^{-2},\end{aligned} \tag{14}$$

$$\begin{aligned}\rho_Q[z] = [n_{re,2} &+ g_{re,2} + m_{re,2}]z^{-1} + [h_{re,2} + n_{im,1}g_{im,2} \\ &+ n_{im,1}m_{im,2} - n_{re,2}g_{re,2} - n_{re,2}m_{re,2}]z^{-2}\end{aligned} \tag{15}$$

$$\begin{aligned}\gamma_Q[z] = 1 &- [n_{im,1} + g_{im,1} + m_{im,1}]z^{-1} + [h_{im,1} \\ &- n_{im,1}g_{re,1} - n_{im,1}m_{re,1} - n_{re,2}g_{im,1} \\ &- n_{re,2}m_{im,1}]z^{-2}.\end{aligned} \tag{16}$$

Based on (3) and (10), omitting $[z]$ from the modulator coefficient variables of (4)–(9) and (11)–(16) for notational convenience, the final complex-valued output is given as

$$\begin{aligned}V[z] = \Bigg[&\frac{\gamma_Q\alpha_I + \gamma_I\alpha_Q - \rho_Q\beta_I - \rho_I\beta_Q}{2(\gamma_I\gamma_Q + \rho_I\rho_Q)} \\ &+ j\,\frac{\rho_I\alpha_Q + \rho_Q\alpha_I + \gamma_Q\beta_I + \gamma_I\beta_Q}{2(\gamma_I\gamma_Q + \rho_I\rho_Q)}\Bigg]U[z] \\ &+ \Bigg[\frac{\gamma_Q\alpha_I - \gamma_I\alpha_Q + \rho_Q\beta_I - \rho_I\beta_Q}{2(\gamma_I\gamma_Q + \rho_I\rho_Q)} \\ &+ j\,\frac{\rho_Q\alpha_I - \rho_I\alpha_Q + \gamma_I\beta_Q - \gamma_Q\beta_I}{2(\gamma_I\gamma_Q + \rho_I\rho_Q)}\Bigg]U^*[z^*] \\ &+ \Bigg[\frac{\gamma_Q\varepsilon_I + \gamma_I\varepsilon_Q + \rho_I\eta_Q + \rho_Q\eta_I}{2(\gamma_I\gamma_Q + \rho_I\rho_Q)} \\ &+ j\,\frac{\rho_I\varepsilon_Q + \rho_Q\varepsilon_I - \gamma_Q\eta_I - \gamma_I\eta_Q}{2(\gamma_I\gamma_Q + \rho_I\rho_Q)}\Bigg]E[z] \\ &+ \Bigg[\frac{\gamma_Q\varepsilon_I - \gamma_I\varepsilon_Q + \rho_I\eta_Q - \rho_Q\eta_I}{2(\gamma_I\gamma_Q + \rho_I\rho_Q)} \\ &+ j\,\frac{\gamma_Q\eta_I - \gamma_I\eta_Q + \rho_Q\varepsilon_I - \rho_I\varepsilon_Q}{2(\gamma_I\gamma_Q + \rho_I\rho_Q)}\Bigg]E^*[z^*].\end{aligned} \tag{17}$$

Now, the four transfer functions of the mismatched modulator (STF, ISTF, NTF and INTF) can be separated as multipliers of $U[z]$, $U^*[z^*]$, $E[z]$ and $E^*[z^*]$, respectively. In this way, the exact behavior of each transfer function can be solved analytically in different I/Q mismatch scenarios. These results will be highlighted in case of a second-order QΣΔM in Section IV with numerical examples.

IV. RESULTS ON TRANSFER FUNCTION ANALYSIS

Herein, the models derived in Section III are used to analytically calculate the transfer functions for a second-order QΣΔM under I/Q imbalance. The transfer functions are analyzed with randomly deviated real gain values (on I and Q rails) to model implementation inaccuracies. The deviation values are drawn from uniform distribution with maximum of ±1% relative to the ideal value. Thus, for example one realization of the real part of the mismatched modulator feedback gain is $g_{re,1} = (1 + \Delta_g)g_{re}$, where $g_{re,1}$ is the implementation value and g_{re} the ideal value. Five independent realizations of each transfer function, calculated with the described mismatches, are plotted to demonstrate effects of inaccuracies on the modulator response. In the plots, multi-band reception of two parallel information signals around relative center frequencies of 0.38 and -0.15 is assumed. These bands (bandwidth of 0.05 relative to the sampling frequency) are marked in the following figures with black solid lines.

The transfer functions used in the analysis are derived based on the information of the desired signal center frequencies and bandwidths. In case of mirror-frequency rejecting STF design, the STF notches are placed on the mirror frequencies of the desired signals. This design can be reconfigured based on the reception scenario at hand. Further details on the multi-band reception and transfer function parameterization can be found in [5].

The differing effects of separate I/Q imbalance sources are demonstrated by introducing mismatch first to the quantizer-feeding input branch (coefficient A in Fig. 2) and thereafter to

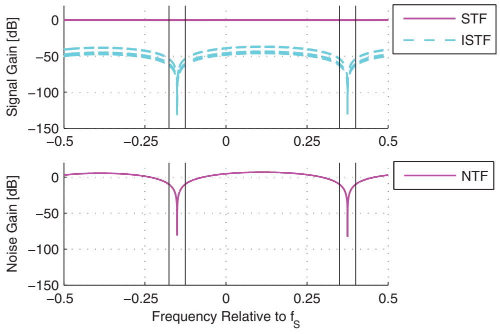

Fig. 4. Second-order single-stage QΣΔM STF, ISTF (above) and NTF (below). Five independent random variations in real gain values of input branch A and flat STF design.

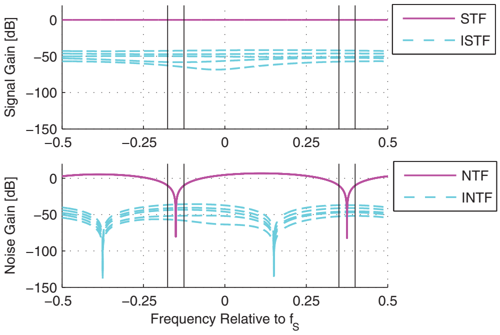

Fig. 5. Second-order single-stage QΣΔM STF, ISTF (above) and NTF (below). Five independent random variations in real gain values of both modulator feedback branches and frequency-flat STF design.

the feedback branches (coefficients G and H in Fig. 2). In Fig. 4, the results for the *input mismatch case with frequency-flat STF design* are shown. It is seen that the resulting ISTF is clearly notched on the assumed desired bands, having image gain at the level of -80 dB in all random realizations. This results in robust image rejection in this mismatch case. The INTF response does not exist because the quantization noise is not yet present in the input branch of the modulator.

Next, the transfer functions are presented in case of *feedback mismatches with frequency-flat STF design* in Fig. 5. The ISTF response averages at -50 dB level, varying between -40 dB and -60 dB, giving level of 30 dB less image rejection on the desired bands compared to the previous case with input mismatch. In addition, an INTF response is introduced, information band responses varying from -35 dB to -55 dB, exceeding the level of the original NTF (around 50 dB attenuation). However, when discussing noise responses, it should be noted that large power variations as in the input blocker scenario are improbable. Finally in Fig. 6, it is shown that *mirror-frequency-rejecting STF design*, introduced in [5], [6] for the first-order QΣΔM, can effectively improve image rejection in case of feedback branch mismatches also in second-order QΣΔM realizing multi-band conversion. The analysis confirms the ISTF notches on the desired signal center frequencies and shows 30 dB average improvements in image rejection over the desired signal bands (-80 dB ISTF response) compared to the frequency-flat STF design.

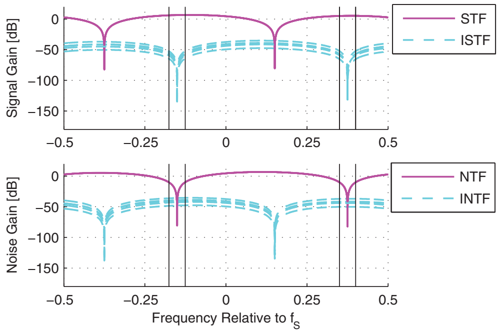

Fig. 6. Second-order single-stage QΣΔM STF, ISTF (above) and NTF (below). Five independent random variations in real gain values of both modulator feedback branches and mirror-frequency-rejecting STF design.

V. CONCLUSIONS

This paper provided an analytical model for I/Q imbalance effects in a second-order QΣΔM. Input branches, loop filters and feedback branches were modeled as potential mismatch sources. Mirror-frequency-rejecting STF design was proposed for single-stage and multi-stage QΣΔMs. Thereafter, based on the derived models, it was concluded that in single-stage case the mirror-frequency-rejecting STF design was able to improve the image rejection of the modulator by 30 dB when feedback branch I/Q mismatches were considered. This technique improves the image rejection of a QΣΔM without any additional electronics.

REFERENCES

[1] I. F. Akyildiz, W.-Y. Lee, M. C. Vuran and S. Mohanty, “NeXt generation/dynamic spectrum access/cognitive radio wireless networks: a survey,” *Computer Networks*, vol. 50, no. 13, pp. 2127–2159, Sep. 2006.

[2] P.-I. Mak, S.-P. U and R. P. Martins, “Transceiver architecture selection: review, state-of-the-art survey and case study,” *IEEE Circuits Syst. Mag.*, vol. 7, no. 2, pp. 6–25, 2007.

[3] B. Razavi, “Cognitive radio design challenges and techniques,” *IEEE J. Solid-State Circuits*, vol. 45, no. 8, pp. 1542–1553, Aug. 2010.

[4] S. Jantzi, K. Martin, and A. Sedra, “A quadrature bandpass delta-sigma modulator for digital radio,” *IEEE J. Solid-State Circuits*, vol. 32, no. 12, pp. 1935–1950, Dec. 1997.

[5] J. Marttila, M. Allén and M. Valkama, “Quadrature ΣΔ modulation for cognitive radio – I/Q imbalance analysis and complex multiband principle,” *Circuits, Syst. and Signal Process.*, vol. 30, no. 4, pp. 775–797, Aug. 2011.

[6] J. Marttila, M. Allén and M. Valkama, “I/Q imbalance effects in quadrature ΣΔ modulators – analysis and signal processing,” in *Proc. IEEE Int. Microwave Workshop Series RF Front-ends for Software Defined and Cognitive Radio Solutions*, Aveiro, Portugal, Feb. 2010.

[7] L. J. Breems, E. C. Dijkmans and J. H. Huijsing, “A quadrature data-dependent DEM algorithm to improve image rejection of a complex modulator,” *IEEE J. Solid-State Circuits*, vol. 36, no. 12, pp. 1879–1886, Dec. 2001.

[8] K.-P. Pun, C.-S. Choy, C.-F. Chan and J. E. da Franca, “An I/Q mismatch-free switched-capacitor complex sigma-delta modulator,” *IEEE Trans. Circuits and Syst. I: Express Briefs*, vol. 51, no. 5, May 2004.

[9] S. Reekmans, P. Rombouts and L. Weyten, “Mismatch insensitive double-sampling quadrature bandpass ΣΔ modulation,” *IEEE Trans. Circuits and Syst. I: Regular Papers*, vol. 54, no. 12, Dec. 2007.

[10] R. Schreier and G. C. Temes, *Understanding Delta-Sigma Data Converters*. Hoboken, NJ: Wiley, 2005.

PUBLICATION 3

Jaakko Marttila, Markus Allén and Mikko Valkama, “Quadrature sigma-delta modulators for cognitive radio - I/Q imbalance analysis and complex multiband principle,” *Circuits, Systems and Signal Processing*, volume 30, number 4, pages 775–797, August 2011.

Circuits Syst Signal Process
DOI 10.1007/s00034-011-9302-0

COGNITIVE RADIO-BASED WIRELESS COMMUNICATION DEVICES

Quadrature $\Sigma\Delta$ Modulators for Cognitive Radio—I/Q Imbalance Analysis and Complex Multiband Principle

Jaakko Marttila · Markus Allén · Mikko Valkama

Received: 31 December 2009 / Revised: 8 September 2010

Abstract This article discusses the applicability of quadrature $\Sigma\Delta$ modulator (Q$\Sigma\Delta$M) based analog-to-digital (A/D) conversion in cognitive radio (CR) receivers. First, unavoidable in-phase/quadrature (I/Q) mismatch effects, limiting the dynamic range, are analyzed in closed-form in the case of a first-order modulator. In addition, using the derived analytical converter model, it is shown that notching the signal transfer function (STF) of the modulator at the mirror frequencies of the desired signals will effectively cancel the I/Q imbalance induced mirror-frequency interference in case of the modulator feedback mismatch. In practice, such STF design is easy to implement within the existing converter circuitry, as will be demonstrated in this article. The latter part of the article proposes a novel complex multiband Q$\Sigma\Delta$M scheme, particularly aimed for the CR receivers. This multiband scheme allows parallel reception of scattered frequency chunks in the CR context and is stemming from the additional degrees of freedom in noise transfer function (NTF) design, provided by the Q$\Sigma\Delta$M principle. Here multiple noise shaping notches on distinct frequencies are effectively realized through proper design of complex NTF. The modulator structure also allows flexible reconfigurability of the notches with straightforward parameterization of the modulator transfer functions. When combined with the above mirror-frequency rejecting STF design, the concept is demonstrated and proved ef-

---

This work is supported by the Academy of Finland, the Finnish Funding Agency for Technology, Innovation (Tekes), Technology Industries of Finland Centennial Foundation, HPY Research Foundation and Nokia Foundation.

J. Marttila (✉) · M. Allén · M. Valkama
Department of Communications Engineering, Tampere University of Technology, Tampere, Finland
e-mail: jaakko.marttila@tut.fi

M. Allén
e-mail: markus.allen@tut.fi

M. Valkama
e-mail: mikko.e.valkama@tut.fi

fective and robust against I/Q imbalances using practical radio signal simulations in realistic received signal conditions.

Keywords A/D converter · Bandpass sigma–delta modulation · Cognitive radio receiver · Complex signals and systems · Image rejection · I/Q imbalance · Quadrature sigma–delta modulation

1 Introduction

The diverse and mobile nature of modern wireless communications calls for flexible radio transceivers. The biggest challenges are set on the mobile terminals, where the functionalities should be implemented in small size with low power consumption and low price for the mass-market. These demands have encouraged the drive toward increasing the role of digital signal processing in such systems. In this way, the analog front-end of the receiver can be simplified and made independent of the particular communication standard in use. Thus, designing complicated receivers with multiple radio frequency (RF) chains can basically be avoided. However, this sets very strict requirements for the A/D converter (ADC) in such systems, which is one of the biggest bottlenecks in the transition toward software-defined radio receivers [5, 9, 15, 16, 21, 30]. In addition, several RF standards being adopted to use, also the radio spectrum is a very scarce resource, demanding efficient allocation and utilization of the signal and system bands [1]. A practical example of such a system is the emerging cognitive radio (CR) principle [19, 20].

One of the most promising radio architectures in this context is the low-IF or wideband direct-conversion [7] multi-standard receiver principle with a bandpass (BP) $\Sigma\Delta$ ADC [9, 26]. The $\Sigma\Delta$ principle allows shaping the quantization noise away from the band of interest, thus enabling exploitation of the whole quantization precision at the desired signal [4, 8, 28]. In addition, the quadrature version of the converter allows designing complex noise and signal transfer functions (NTF and STF) not being restricted to be symmetric in respect of the zero-frequency (DC) [3, 4, 10, 12, 28]. This property can be put to use particularly in modern quadrature image rejecting receivers [10, 12]. At the same time, the Q$\Sigma\Delta$M has been shown to have several benefits, e.g., improved signal-to-noise ratio, over two parallel real BP $\Sigma\Delta$ modulators [14]. Such quadrature $\Sigma\Delta$ modulator based receiver principle, following [12], is demonstrated in Fig. 1, where the essential signal characteristics are also shown with principal spectra. After coarse RF filtering, the signal is in-phase/quadrature (I/Q) down-converted to the intermediate frequency, where A/D conversion is done. Thereafter, final filtering and mixing are done in digital domain. To limit the dynamic range and frequency content of the signal entering the ADC stage, a complex BP filter can be deployed prior to the Q$\Sigma\Delta$M. However, such filtering can also limit the flexibility of the receiver. The Q$\Sigma\Delta$M principle will be described in more detail in Sect. 2.

At the same time, the push toward cost-efficiency and lower-cost electronics gives also rise to various circuit nonidealities, such as nonlinearities [9, 23, 24], amplitude and phase mismatches of the I and Q rails [10–12, 23, 24, 29], timing jitter in the sampling circuit [29] and oscillator phase noise [9, 24]. This article will concentrate

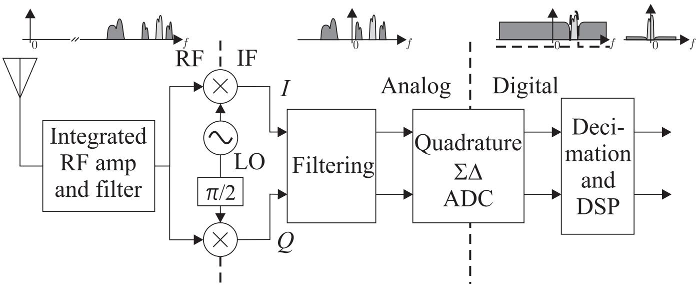

Fig. 1 A block diagram of a QΣΔM based low-IF quadrature receiver with principal spectra, where the *light grey signal* is the desired one, illustrating the essential signal characteristics at each stage

on the I/Q mismatch and resulting mirror-frequency interference (MFI) related to the aforementioned quadrature ΣΔ converter [6, 10–12, 22, 25, 32]. This is because complex or I/Q signal processing is obviously playing a key role in the QΣΔM principle, and is thus vulnerable to component mismatches. The mirror-frequency interference mechanisms due to I/Q mismatch in QΣΔM based receiver will be discussed in detail in Sect. 3. An analytic model for the imbalance effects, preliminary addressed by the authors in [17, 18], will be derived for a first-order QΣΔM. Based on this model, the effect of four distinct imbalance sources will be identified and analyzed in respective cases. In addition, mitigation of the MFI through sophisticated STF design will be addressed and identified. For reference, the properties of mirror-frequency rejecting NTF have been discussed already in [10–12, 32] and a brief analysis on the related STF phenomenon has been given earlier in [10, 12]. However, closed-form analysis of the imbalance phenomenon, presented in this article, gives more complete understanding on the generated interference, which in turn is essential in order to develop efficient mitigation methods. The STF—and input signal—related imbalance effects become of great interest especially when reducing analog selectivity of the receiver, which indeed is the goal when designing flexible receiver structures for CRs [31]. In this kind of solutions, it is essential to be able to deal with differing signal bandwidths, center frequencies, waveforms and presence of blocking signals [13]. In the literature, some quadrature ΣΔ specific analog I/Q mismatch mitigation methods [6, 22, 25] have also been presented. These solutions, however, demand alteration of the original modulator structure degrading the sampling properties [22] or adding supplementary analog electronics affecting the size and the power dissipation of the modulator [6, 25]. Thus, a technique for mitigating I/Q imbalance effects without having to modify the modulator structure would be of great value. In this article, the proposed sophisticated STF design is shown to do exactly that in case of modulator feedback mismatch.

Finally, the freedom that QΣΔM gives to the placement of the transfer function zeros and poles will be put to use by proposing a multiband converter setup having several separate noise notches. For simplicity, the concept is demonstrated with a second-order QΣΔM, which allows parallel reception of two distinct information signals on respective center frequencies. This will be particularly useful in the CR context, where information signals can be located on scattered center frequencies. The tuning of the notch frequencies is straightforwardly parameterized allowing simple reconfiguration of the received signal bands when necessary. Thus, the concept

Fig. 2 Discrete-time linearized model of a first-order quadrature ΣΔ modulator with complex-valued signals and coefficients

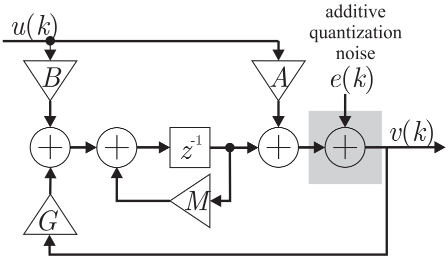

allows simple adaptation to varying demands set by the desired waveforms. In [2], similar kind of idea is realized with multiple parallel real ΣΔ modulators, but with QΣΔM no parallel branches are needed because of the available additional degrees of freedom in transfer function design. The need for development of multichannel ADCs for software-defined and cognitive radio solutions has been acknowledged, e.g., in [15, 30]. Multichannel systems with parallel ADCs, however, set additional burden for size, cost and power dissipation of the receiver implementation [15]. At the same time, quadrature ΣΔ noise shaping makes exploitation of whole quantization precision on the desired signal bands possible. Particularly, based on the comparison of real and complex ΣΔ modulators in [14], it can be concluded that the overall filter order can be reduced by applying QΣΔM in this kind of receiver. Thus, the complexity is decreased and the implementation size can be brought down.

Following notations are used throughout the article. Z-transform of discrete-time sequence $u(k)$ is denoted with $U[z]$ and complex conjugate of $u(k)$ is given as $u^*(k)$. In addition, quantity $U^*[z^*]$ is the Z-transform of complex conjugated sequence $u^*(k)$. Normalized frequency is defined as the actual frequency f (measured in Hz) divided by the sampling frequency f_S and is thus denoted with $\overline{f} = f/f_S$.

2 Quadrature ΣΔ Modulation for ADCs

QΣΔM extends the principle of lowpass and bandpass noise shaping employed in real modulators to allow also complex transfer functions [3, 10, 12, 28]. Thus, the output of the modulator is given essentially by $V[z] = \mathrm{STF}[z]U[z] + \mathrm{NTF}[z]E[z]$ where both transfer functions (STF and NTF) as well as input-, quantization noise- and output signals ($u(k)$, $e(k)$ and $v(k)$) are arbitrary complex-valued quantities. The complex transfer functions allow, e.g., frequency asymmetric noise shaping typical for QΣΔM. A QΣΔM can be implemented in practice with a complex input, loop filter, feedback and output [3, 10, 12, 28]. The complex loop filter can be realized as a complex integrator when considering the first-order modulator. Higher-order systems usually have multiple integrators included. Details of the modulator implementation are thoroughly discussed, e.g., in [10, 12], and thus only the main design principles will be highlighted in the following.

2.1 First-Order Modulator

The basic structure of the first-order ΣΔ modulator is presented in Fig. 2, where $u(k)$, $e(k)$ and $v(k)$ denote the complex input, the linearized complex quantization

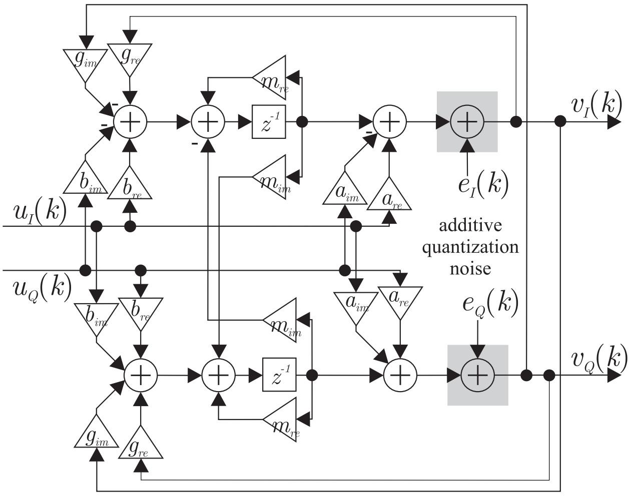

Fig. 3 Discrete-time linearized model of a QΣΔM with parallel real signals and coefficients with ideal matching of the I and Q branches

error and the complex output signals, respectively. The multipliers A, B and G are complex valued and affect the input signal fed straight to quantizer, the input signal fed to the loop filter (complex integrator with pole M) and the feedback signal from the output of the modulator, respectively.

This kind of complex-valued system can be implemented with parallel real-valued signals representing both the real and imaginary parts. In addition, complex multiplications can be realized with four real multiplications. Based on this, the implementation structure of the first-order QΣΔM is as shown in Fig. 3. The real and imaginary parts of the complex gains are denoted with subscripts re and im, respectively, i.e., $A = a_{\mathrm{re}} + ja_{\mathrm{im}}$, and so on. From the block diagram, e.g., multiple cross-connections between the branches are visible.

Based on the shown structure, the Z-domain transfer functions for input and quantization noise can be easily derived. Thus, the output $V[z]$ of the modulator can be expressed in terms of the input $U[z]$ and the quantization error $E[z]$ as

$$V[z] = \frac{A + (B - MA)z^{-1}}{1 - (G + M)z^{-1}} U[z] + \frac{1 - Mz^{-1}}{1 - (G + M)z^{-1}} E[z]. \tag{1}$$

The equation pronounces the significance of modulator coefficients, A, B, M and G, and defines the STF and NTF as

$$\mathrm{STF}[z] = \frac{A + (B - MA)z^{-1}}{1 - (G + M)z^{-1}}, \qquad \mathrm{NTF}[z] = \frac{1 - Mz^{-1}}{1 - (G + M)z^{-1}}. \tag{2}$$

In practice, the STF and NTF can be used to create selectivity for the modulator signal response and to shape the quantization noise away from the band (or bands) of the desired information signal.

Subsequently, based on (2), the zeros and the poles, which define the filtering properties of the transfer functions, are given as $z_{\mathrm{STF}} = (MA - B)/A$, $z_{\mathrm{NTF}} = M$ and $p_{\mathrm{common}} = G + M$, where z_{STF}, z_{NTF} and p_{common} denote the zero of the STF, the zero of the NTF and the common pole for both the transfer functions, respectively. In this

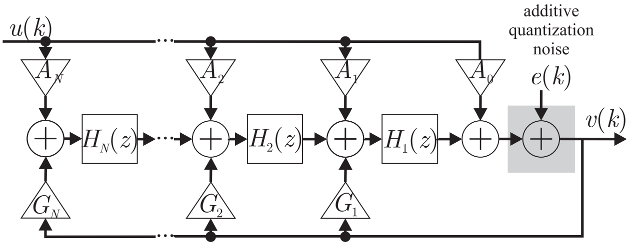

Fig. 4 Discrete-time linearized model of an Nth-order quadrature $\Sigma\Delta$ modulator with complex-valued signals and coefficients

way, straightforward reconfiguration of the overall modulator response is possible by tuning the complex gain values. As a practical example, setting z_{STF} and p_{common} to zero results in a unity STF while the NTF zero, defining the notch frequency, can be tuned independently. This unity signal transfer function design will be applied, and discussed in more detail, in Sect. 4.

2.2 Higher-Order Modulator

A more general model for an arbitrary-order Q$\Sigma\Delta$M can be derived by adding N loop filters [28] $H_1[z]$ to $H_N[z]$, and the corresponding input and feedback branches (coefficients A_0 to A_N and G_1 to G_N, respectively) to the structure. This is illustrated in Fig. 4. With Nth-order modulator, N zeros and poles can basically be used to shape the STF and NTF. Similar to above, the overall transfer function for input and quantization noise can again be derived. Fairly straightforward analysis, stemming from the structure in Fig. 4, yields the following form for the output $V[z]$:

$$V[z] = \frac{A_0 + \sum_{i=1}^{N} A_i \prod_{j=1}^{i} H_j[z]}{1 - \sum_{k=1}^{N} G_k \prod_{l=1}^{k} H_l[z]} U[z] + \frac{1}{1 - \sum_{k=1}^{N} G_k \prod_{l=1}^{k} H_l[z]} E[z]. \quad (3)$$

Based on above, the STF and NTF are of the form

$$\mathrm{STF}[z] = \frac{A_0 + \sum_{i=1}^{N} A_i \prod_{j=1}^{i} H_j[z]}{1 - \sum_{k=1}^{N} G_k \prod_{l=1}^{k} H_l[z]}, \quad \mathrm{NTF}[z] = \frac{1}{1 - \sum_{k=1}^{N} G_k \prod_{l=1}^{k} H_l[z]}. \quad (4)$$

3 I/Q Imbalance Model for Quadrature $\Sigma\Delta$ ADC

The main principle and impact of I/Q mismatch is quite extensively documented in the scientific literature [23, 24, 29, 32] in ordinary receiver context. In this section, the main objective is to obtain an analytical model for the imbalance effects in case of a quadrature $\Sigma\Delta$ modulator used in an ADC. The model was briefly introduced in [17] and the discussion and analysis are extended in more detail here. For illustration purposes and to simplify the notations, the mismatch effects will be studied here based on the model of the first-order system presented in Sect. 2.1.

The practical implementation structure (based on Fig. 3) with possible mismatches between the I and Q branches is presented in Fig. 5, where subscripts 1 and 2 denote

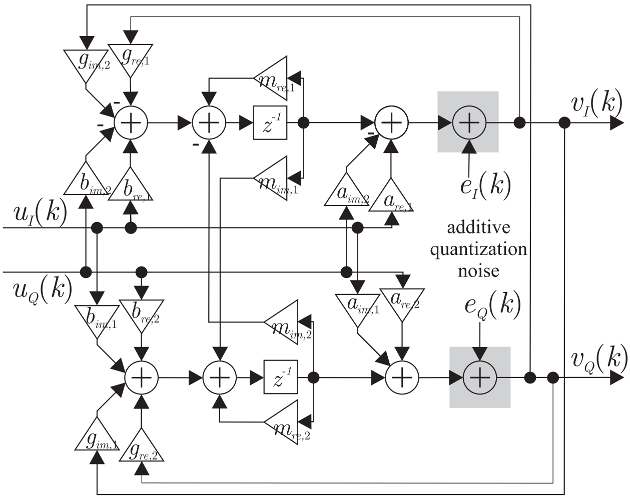

Fig. 5 Discrete-time linearized model of a QΣΔM with parallel real signals and coefficients taking possible mismatches into account

the possibly mismatched realizations of the ideally symmetric coefficients on each branch. The structure shows that mismatches are possible in either of the inputs, in the feedback of the loop filter or in the feedback of the modulator.

Traditionally, any mismatch in a complex multiplication causes mirror-frequency interference due to a conjugate response for the input signal [7, 23, 29]. This is the case also for the ΣΔ modulator [6, 10–12, 22, 25, 32]. On the other hand, the quantization noise, generated inside the modulator loop, has also an image response in case of the mismatch [6, 10–12, 22, 25, 32]. This results, in addition to the STF and the NTF, in two additional transfer functions, which are called an image signal transfer function (ISTF) and an image noise transfer function (INTF). Thus, the output of the mismatched modulator can generally be given in the form [11]

$$V[z] = \mathrm{STF}[z]U[z] + \mathrm{ISTF}[z]U^*[z^*] + \mathrm{NTF}[z]E[z] + \mathrm{INTF}[z]E^*[z^*]. \qquad (5)$$

These four transfer functions allow measuring image rejection ratios (IRR) of the signal and noise components as

$$\mathrm{IRR}_{\mathrm{STF}}\left[e^{j2\pi f T_S}\right] = 10\log_{10}\left(\left|\mathrm{STF}\left[e^{j2\pi f T_S}\right]\right|^2 / \left|\mathrm{ISTF}\left[e^{j2\pi f T_S}\right]\right|^2\right) \qquad (6)$$

and

$$\mathrm{IRR}_{\mathrm{NTF}}\left[e^{j2\pi f T_S}\right] = 10\log_{10}\left(\left|\mathrm{NTF}\left[e^{j2\pi f T_S}\right]\right|^2 / \left|\mathrm{INTF}\left[e^{j2\pi f T_S}\right]\right|^2\right), \qquad (7)$$

where actual frequency domain responses are attained with the substitution $z \leftarrow e^{j2\pi f T_S}$ to the above transfer functions. These IRR quantities describe the relation of the original input signal and noise energy to the respective mismatch induced MFI at the output signal. As an example, $\mathrm{IRR}_{\mathrm{NTF}}(e^{j2\pi f T_s}) = 20$ dB means that the power of the mismatch induced (mirrored) conjugate noise at a particular frequency f is 20 dB lower than the “original” quantization noise.

The feasible IRR range in practical quadrature receivers as a whole is typically reported to be around 20–40 dB [7, 23], which considering a gain mismatch between the real coefficients of the branches means values in the order of 1–10%. Because the IRR of a single receiver component should be higher than that of the whole receiver with multiple mirror-frequency interference sources, mismatches from 10^{-1} to 10^{-5} will be considered to cover the realistic range. It should also be emphasized that only the differential error is causing the mirroring effect. This means that the deviation from the nominal value is opposite in the two channels. If the error is common and parallel between the branches, the desired response (STF or NTF) is affected but no mirror-frequency interference is present [11].

Next, based on the principle and the modulator structure shown above, a closed-form expression for the mismatched first-order Q$\Sigma\Delta$M will be derived. Taking the possible mismatch into account, the real outputs of the modulator $V_I[z]$ and $V_Q[z]$ can be derived resulting, after fairly straightforward manipulations, in the following expressions:

$$\begin{aligned}
V_I[z] = {} & \frac{a_{\text{re1}} + (b_{\text{re1}} - m_{\text{re1}}a_{\text{re1}} + m_{\text{im2}}a_{\text{im1}})z^{-1}}{1-(g_{\text{re1}}+m_{\text{re1}})z^{-1}}U_I[z] \\
& - \frac{a_{\text{im2}} + (b_{\text{im1}} - m_{\text{re1}}a_{\text{im2}} - m_{\text{im2}}a_{\text{re2}})z^{-1}}{1-(g_{\text{re1}}+m_{\text{re1}})z^{-1}}U_Q[z] \\
& + \frac{1-m_{\text{re1}}z^{-1}}{1-(g_{\text{re1}}+m_{\text{re1}})z^{-1}}E_I[z] + \frac{m_{\text{im2}}z^{-1}}{1-(g_{\text{re1}}+m_{\text{re1}})z^{-1}}E_Q[z] \\
& - \frac{(g_{\text{im2}}+m_{\text{im2}})z^{-1}}{1-(g_{\text{re1}}+m_{\text{re1}})z^{-1}}V_Q[z]
\end{aligned} \tag{8}$$

and

$$\begin{aligned}
V_Q[z] = {} & \frac{a_{\text{im1}} + (b_{\text{im1}} - m_{\text{re2}}a_{\text{im1}} - m_{\text{im1}}a_{\text{re1}})z^{-1}}{1-(g_{\text{re2}}+m_{\text{re2}})z^{-1}}U_I[z] \\
& + \frac{a_{\text{re2}} + (b_{\text{re2}} - m_{\text{re2}}a_{\text{re2}} + m_{\text{im1}}a_{\text{im2}})z^{-1}}{1-(g_{\text{re2}}+m_{\text{re2}})z^{-1}}U_Q[z] \\
& - \frac{m_{\text{im1}}z^{-1}}{1-(g_{\text{re2}}+m_{\text{re2}})z^{-1}}E_I[z] + \frac{1-m_{\text{re2}}z^{-1}}{1-(g_{\text{re2}}+m_{\text{re2}})z^{-1}}E_Q[z] \\
& + \frac{(g_{\text{im1}}+m_{\text{im1}})z^{-1}}{1-(g_{\text{re2}}+m_{\text{re2}})z^{-1}}V_I[z].
\end{aligned} \tag{9}$$

Now, in order to obtain an expression for the complex-valued output $V[z] = V_I[z] + jV_Q[z]$ in the form given in (5), the following response variables are taken into use:

$$\begin{aligned}
\alpha_I[z] &= a_{\text{re1}} + (b_{\text{re1}} - m_{\text{re1}}a_{\text{re1}} + m_{\text{im2}}a_{\text{im1}})z^{-1}, \\
\beta_I[z] &= a_{\text{im2}} + (b_{\text{im1}} - m_{\text{re1}}a_{\text{im2}} - m_{\text{im2}}a_{\text{re2}})z^{-1}, \\
\varepsilon_I[z] &= 1 - m_{\text{re1}}z^{-1}, \\
\eta_I[z] &= m_{\text{im2}}z^{-1},
\end{aligned} \tag{10}$$

$$\begin{aligned}
\rho_I[z] &= (g_{\mathrm{im2}} + m_{\mathrm{im2}})z^{-1},\\
\gamma_I[z] &= 1 - (g_{\mathrm{re1}} + m_{\mathrm{re1}})z^{-1},
\end{aligned}$$

denoting the numerators and the common denominator of the terms multiplying the input, the error and the output signals in (8), respectively. Similar definitions are made for (9), meaning

$$\begin{aligned}
\alpha_Q[z] &= a_{\mathrm{re2}} + (b_{\mathrm{re2}} - m_{\mathrm{re2}}a_{\mathrm{re2}} + p_{\mathrm{im1}}a_{\mathrm{im2}})z^{-1},\\
\beta_Q[z] &= a_{\mathrm{im1}} + (b_{\mathrm{im1}} - m_{\mathrm{re2}}a_{\mathrm{im1}} - m_{\mathrm{im1}}a_{\mathrm{re1}})z^{-1},\\
\varepsilon_Q[z] &= 1 - m_{\mathrm{re2}}z^{-1},\\
\eta_Q[z] &= m_{\mathrm{im1}}z^{-1},\\
\rho_Q[z] &= (g_{\mathrm{im1}} + m_{\mathrm{im1}})z^{-1},\\
\gamma_Q[z] &= 1 - (g_{\mathrm{re2}} + m_{\mathrm{re2}})z^{-1}.
\end{aligned} \tag{11}$$

With these notations and some rearrangements, the complex output signal $V[z]$ can be written as

$$\begin{aligned}
V[z] = {} & \Bigg[\frac{\gamma_Q[z]\alpha_I[z] + \gamma_I[z]\alpha_Q[z] - \rho_Q[z]\beta_I[z] - \rho_I[z]\beta_Q[z]}{2(\gamma_I[z]\gamma_Q[z] + \rho_I[z]\rho_Q[z])}\\
& + j\frac{\rho_I[z]\alpha_Q[z] + \rho_Q[z]\alpha_I[z] + \gamma_Q[z]\beta_I[z] + \gamma_I[z]\beta_Q[z]}{2(\gamma_I[z]\gamma_Q[z] + \rho_I[z]\rho_Q[z])}\Bigg]U[z]\\
& + \Bigg[\frac{\gamma_Q[z]\alpha_I[z] - \gamma_I[z]\alpha_Q[z] + \rho_Q[z]\beta_I[z] - \rho_I[z]\beta_Q[z]}{2(\gamma_I[z]\gamma_Q[z] + \rho_I[z]\rho_Q[z])}\\
& + j\frac{\rho_Q[z]\alpha_I[z] - \rho_I[z]\alpha_Q[z] + \gamma_I[z]\beta_Q[z] - \gamma_Q[z]\beta_I[z]}{2(\gamma_I[z]\gamma_Q[z] + \rho_I[z]\rho_Q[z])}\Bigg]U^*[z^*]\\
& + \Bigg[\frac{\gamma_Q[z]\varepsilon_I[z] + \gamma_I[z]\varepsilon_Q[z] + \rho_I[z]\eta_Q[z] + \rho_Q[z]\eta_I[z]}{2(\gamma_I[z]\gamma_Q[z] + \rho_I[z]\rho_Q[z])}\\
& + j\frac{\rho_I[z]\varepsilon_Q[z] + \rho_Q[z]\varepsilon_I[z] - \gamma_Q[z]\eta_I[z] - \gamma_I[z]\eta_Q[z]}{2(\gamma_I[z]\gamma_Q[z] + \rho_I[z]\rho_Q[z])}\Bigg]E[z]\\
& + \Bigg[\frac{\gamma_Q[z]\varepsilon_I[z] - \gamma_I[z]\varepsilon_Q[z] + \rho_I[z]\eta_Q[z] - \rho_Q[z]\eta_I[z]}{2(\gamma_I[z]\gamma_Q[z] + \rho_I[z]\rho_Q[z])}\\
& + j\frac{\gamma_Q[z]\eta_I[z] - \gamma_I[z]\eta_Q[z] + \rho_Q[z]\varepsilon_I[z] - \rho_I[z]\varepsilon_Q[z]}{2(\gamma_I[z]\gamma_Q[z] + \rho_I[z]\rho_Q[z])}\Bigg]E^*[z^*],
\end{aligned} \tag{12}$$

which corresponds to (5). Based on this analogy, the STF, the ISTF, the NTF and the INTF can be separated as the multipliers of $U[z]$, $U^*[z^*]$, $V[z]$ and $V^*[z^*]$ in (12), respectively. Now, these expression can be used to calculate the signal and noise IRRs of the mismatched modulator, based on (6) and (7). These results will be analyzed and discussed next in Sects. 4 and 5 in more detail for the unity STF and the mirror-frequency notched STF designs, respectively. The effects of four distinct I/Q mismatch sources will be analyzed from both the signal and noise mirroring point of view.

4 IRR Analysis and Interpretations with Flat STF Design

In this section, IRRs of the first-order QΣΔM will be evaluated and analyzed in different mismatch scenarios based on the derived expressions (Sect. 3). Here we concentrate on the basic case where modulator has ideally a unity STF and a NTF notch on the desired signal band. Based on (1)–(2), the unity STF is achieved with following complex gain values: $A = 1$, $B = MA$ and $G = -M$. At the same time, M defines the zero of the NTF and can be modified to tune the notch frequency $\overline{f}_{\text{pass}}$, being $M = e^{j2\pi \overline{f}_{\text{pass}}}$. As a concrete example, we will consider the case where the desired signal is located at a center-frequency of 0.375 relative to the used sampling frequency. Mismatch effects will be examined from both the noise shaping effectiveness and signal distortion point of view. IRR values are given for the STF and the NTF when appropriate.

4.1 Effects of Input Mismatches

In the first-order QΣΔM, with two input branches (see Figs. 2 and 5), there are two separate mismatch sources (complex multipliers A and B). The mismatch Δ_A in the branch feeding the quantizer is defined as the opposite alteration of the circuit implementations of the real and imaginary parts of the complex multiplier on I and Q branches. Based on the notation in Fig. 5, this can be expressed as $a_{\text{re},1} = (1 + \Delta_A)a_{\text{re}}$ and $a_{\text{re},2} = (1 - \Delta_A)a_{\text{re}}$, where a_{re} is the ideal real part and $a_{\text{re},1}$ and $a_{\text{re},2}$ are the mismatched implementation values on the I and Q branches, respectively. Similar notation is maintained also in the following mismatch scenarios. In this particular case with flat STF, A is all real and thus no mismatch appears in the imaginary part. With mismatch Δ_B in the branch feeding the loop filter with complex gain B, the implementation values are as follows: $b_{\text{re},1} = (1 + \Delta_B)b_{\text{re}}$, $b_{\text{re},2} = (1 - \Delta_B)b_{\text{re}}$, $b_{\text{im},1} = (1 + \Delta_B)b_{\text{im}}$ and $b_{\text{im},2} = (1 - \Delta_B)b_{\text{im}}$. Symmetric mismatches $(1 \pm \Delta)$ in both real and imaginary parts were chosen for simplicity of analysis. This is because it was shown in [11] that only the relative difference between the branch values affects the mirror responses. In addition, it was confirmed in simulations that no significant differences appear between the transfer functions with symmetric and asymmetric mismatches.

With input coefficient mismatches only, INTF is all-zero. This is because the quantization noise is not processed in the input of the modulator. Thus, IRR values are given only for the STF. In case of imbalance in the multiplier (see Figs. 2 and 5) on the branch feeding the quantizer, the ISTF response has a notch exactly at the assumed desired signal band, which is marked with the solid black line in the IRR plots. This can be seen as an IRR peak at that frequency in the left plot of Fig. 6. Based on this observation, it can be concluded that the structure itself is mitigating the possible mirror-frequency interference, if the imbalance appears in the real-valued input multiplier.

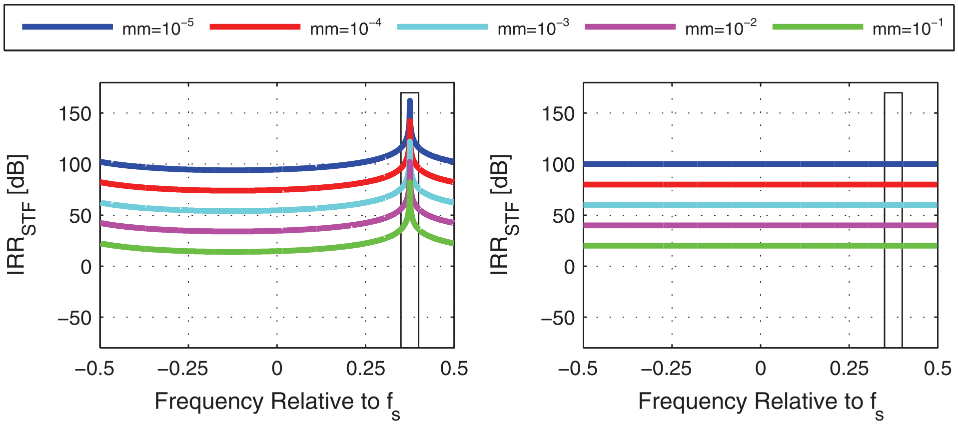

Fig. 6 Signal IRR as a function of frequency relative to f_S with mismatch in the input branch feeding the signal to the quantizer (*left*) and mismatch in the input branch feeding the signal to the loop filter (*right*), having frequency flat STF design in both cases. The assumed desired signal band is marked with a *solid black line*

On the other hand, if the mismatch takes place in the complex-valued multiplier of the branch feeding the quantizer (see again Figs. 2 and 5), the resulting signal IRR appears frequency flat as seen in the right side plot of Fig. 6. In both cases, the levels follow the traditional model where IRR is improved by 20 dB for every decade of improvement in matching of the branches.

4.2 Effect of Loop Filter Mismatch

For the loop filter, the mismatch source is assumed to be the complex multiplier M in the integrator feedback (see Figs. 2 and 5). Now, with the mismatch Δ_M, the implementation of the real and imaginary parts results in the following values: $m_{\mathrm{re},1} = (1 + \Delta_M)m_{\mathrm{re}}$, $m_{\mathrm{re},2} = (1 - \Delta_M)m_{\mathrm{re}}$, $m_{\mathrm{im},1} = (1 + \Delta_M)m_{\mathrm{im}}$ and $m_{\mathrm{im},2} = (1 - \Delta_M)m_{\mathrm{im}}$.

The main difference in a case of loop filter coefficient mismatch compared to the two cases of the input mismatches presented in the previous subsection is that no conjugate response of the input signal is generated. This holds for the unity STF design when the circuitry is considered otherwise ideal except for the mismatch in question. In this case, the resulting INTF is frequency flat meaning that the conjugated version of the noise is seen in the output of the modulator without any selectivity. Thus, with relatively high values of mismatch, the conjugate noise can be more significant on the desired signal band than the original nonconjugated noise, which is shaped by the NTF. Due to the flat INTF, the shape of the IRR curves in Fig. 7 is determined by the NTF and the amount of mismatch affects the level of the curve. With higher mismatch values, the IRR is even negative at the desired signal band, indicating clearly the dominance of the conjugate noise due to mismatch. As a practical example, assume 60 dB of noise attenuation for the original NTF notch and −20 dB noise IRR at the desired band, thus the conjugated quantization noise signal is attenuated by only $60 - 20 = 40$ dB defining the overall noise floor level in this case. In addition, it should be noted that 0 dB NTF IRR at the desired band indicates that the levels of

Fig. 7 Quantization noise IRR as a function of frequency relative to f_S with mismatch in the loop filter and frequency flat STF design. The assumed desired signal band is marked with a *solid black line*

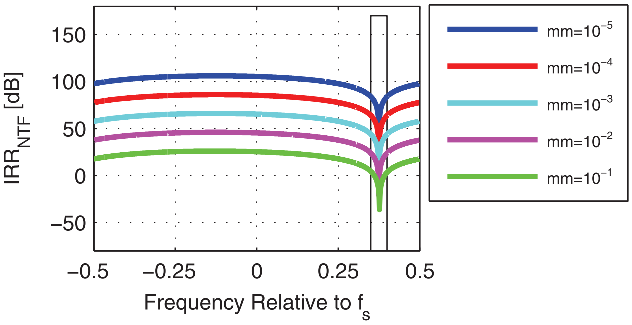

the original noise and the mirrored noise are similar, which, in case of efficient NTF, means that both are well attenuated.

Mismatch in the loop filter is also slightly disturbing the response of the original NTF. The notch frequency is shifted from its original location and, at the same time, the notch becomes shallower. However, the effect is mild with practical imbalance values and can be assumed negligible when compared to the mirror interference generated by the conjugate response of the noise.

4.3 Effect of Feedback Mismatch

For the modulator feedback (see Figs. 2 and 5), the mismatch source is assumed to be the complex multiplier G, wherein the mismatch Δ_G in the implementation of the real and imaginary parts results in the following: $g_{\mathrm{re},1} = (1 + \Delta_G)g_{\mathrm{re}}$, $g_{\mathrm{re},2} = (1 - \Delta_G)g_{\mathrm{re}}$, $g_{\mathrm{im},1} = (1 + \Delta_G)g_{\mathrm{im}}$ and $g_{\mathrm{im},2} = (1 - \Delta_G)g_{\mathrm{im}}$. Now, in the case of modulator feedback branch I/Q imbalance, both the input signal and the quantization noise are causing mirror-frequency interference. While having a frequency flat STF, also the ISTF appears frequency flat. These transfer functions result in frequency flat signal IRR behavior demonstrated on the left side of Fig. 8 following again 20 dB per matching decade rule.

The NTF notch at the positive frequencies and the opposite INTF notch at the negative band explain the noise IRR shape on the right side of Fig. 8. At the NTF notch band, the original nonconjugated noise is shaped away and when the INTF has no attenuation there, the IRR values are low or even negative. On the contrary, the NTF has no attenuation at negative frequencies and the INTF is notched leading to high IRR values. When compared to the previous case with the loop filter mismatch, the desired band NTF IRR values are lower, which results from the undistorted NTF response with the feedback mismatch. In addition to that, the noise mirroring principle in the previous subsection applies also here.

5 IRR Analysis and Interpretations with Mirror Band Rejecting STF Design

In this section, the image rejection behavior will be examined in a case of selective STF. The STF is designed such that there is a notch at the normalized frequency of −0.361, targeting to attenuate the energy of the desired signal's mirrorband. The

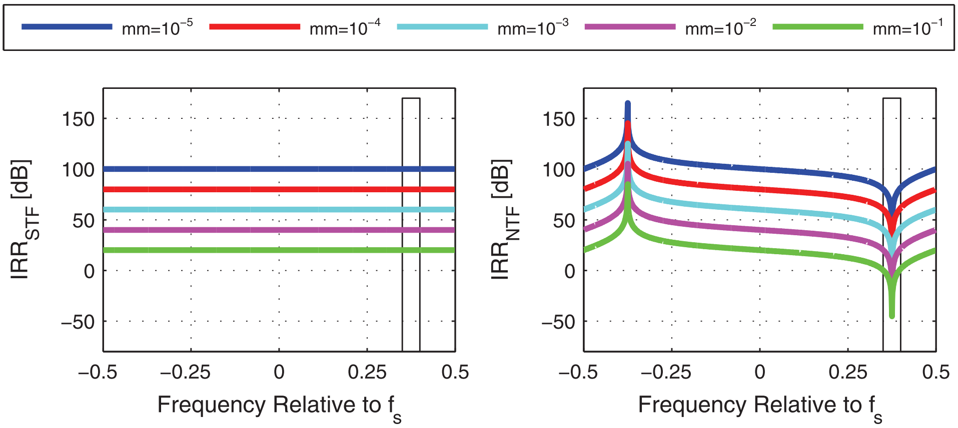

Fig. 8 Signal (*left*) and quantization noise (*right*) IRRs as a function of frequency relative to f_S with mismatch in the modulator feedback branch and frequency flat STF design. The assumed desired signal band is marked with *solid black line*

chosen notch frequency is intentionally shifted slightly off the exact mirror band of the desired signal (-0.375) for illustration purposes. In this way, the frequencies of the complex conjugate of the STF notch and the original NTF notch can be visually separated. The desired STF is achieved with following complex gains (see Fig. 2 and (1)–(2)): $A = 1$, $B = M + e^{j2\pi(0.5+\overline{f}_{\text{int}})}$ and $G = -M + e^{j2\pi\overline{f}_{\text{int}}}/2$, where $\overline{f}_{\text{int}} = -0.361$ is the assumed interference frequency at which the STF notch is designed. At the same time, M is again the desired NTF zero inside the unit-circle defined as $M = e^{j2\pi\overline{f}_{\text{pass}}}$ allowing simple tuning of the notch. In addition, definition of the STF zero (in Sect. 2.1) gives now $z_{\text{NTF}} = M + B = e^{j2\pi\overline{f}_{\text{int}}}$ confirming the STF notch at the normalized frequency $\overline{f}_{\text{int}}$.

The purpose of the study is to demonstrate that the mirror-frequency rejecting STF can be used to mitigate the I/Q imbalance effects in a Q$\Sigma\Delta$M. The resulting IRRs are presented in a similar manner as with the flat STF design in Sect. 4. In the following subsections, the modulator mismatches are also defined similarly as was done for the flat STF design in the Sects. 4.1–4.3.

5.1 Effects of Input Mismatches

With mismatch in the branch feeding the quantizer, the STF notch effect in the IRR can be seen on the left side in Fig. 9. The modest IRR values at the notch frequency band are due to the high attenuation of the input signal and the relatively low rejection of the conjugate signal. However, the frequencies around the desired signal center-frequency, being mostly of interest, have high IRR values because of the ISTF notch at the desired band. Even with as severe as 10% mismatch the IRR peaks at the level of 60 dB, which is usually considered adequate. From this point of view, the mismatch behavior is remarkably similar to the case of the flat STF, discussed in Sect. 4.1.

In case of mismatch in the branch feeding the loop filter, the resulting IRR curves are presented on the right in Fig. 9. The lower IRR values at the mirror band are due to the relatively flat ISTF and the STF notch, which is rejecting the original input.

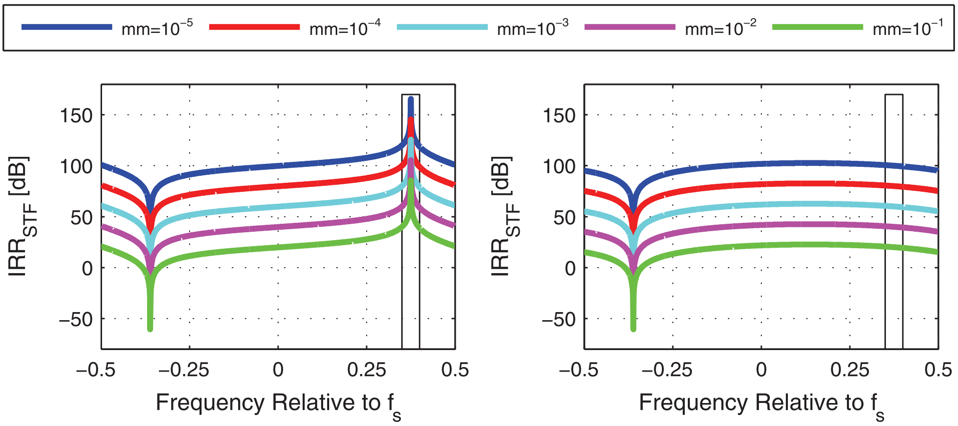

Fig. 9 Signal IRR as a function of frequency relative to f_S with mismatch in the input branch feeding the quantizer (*left*) and mismatch in the input branch feeding the loop filter (*right*), having mirror-frequency rejecting STF design in both cases. The assumed desired signal band is marked with *solid black line*

However, this is irrelevant from the desired signal point of view. At the desired signal band, the image rejection ratios seem to follow the 20-dB-per-decade rule of thumb nicely.

5.2 Effect of Loop Filter Mismatch

Designing the STF to reject the mirror frequencies affects the IRR behavior significantly in case of mismatch in the loop filter of the modulator. With the frequency flat STF in Sect. 4.2, the input signal did not suffer from mirror interference because the modulator feedback canceled the input to the loop filter. When considering the selective STF design, this is not the case and thus the mismatch in the filter is adding a conjugate response for the input signal as well.

In this case, because of the gently sloping behavior of both the image transfer functions, most of the IRR characteristics are defined by the STF and the NTF, as shown in Fig. 10. The IRR curves have notches at the frequencies of the original transfer function notches. The notches describe the rejection of the desired band quantization noise and the image band input signal power. Similarly as in the previous case of mismatch in the loop filter feeding branch, the output signal IRR is behaving quite smoothly at the desired signal band and giving image attenuation in the order of 20 dB per matching decade.

From the noise shaping point of view, the IRR results on the right side of Fig. 10 are similar to the ones achieved with flat STF in Fig. 7. This is of course intuitive, because the STF shape does not affect the noise response of the modulator. Thus, also the NTF IRR observations of Sect. 4.2 apply here.

5.3 Effect of Feedback Mismatch

The mirror-frequency rejecting STF has the most effect on the generated mirror-frequency distortion when considering the case of mismatched modulator feedback

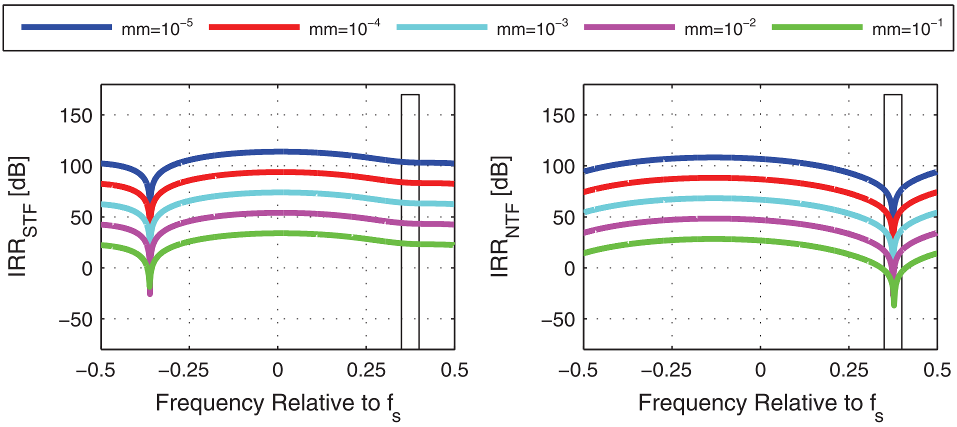

Fig. 10 Signal (*left*) and quantization noise (*right*) IRRs as a function of frequency relative to f_S with mismatch in the loop filter and mirror-frequency rejecting STF design. The assumed desired signal band is marked with *solid black line*

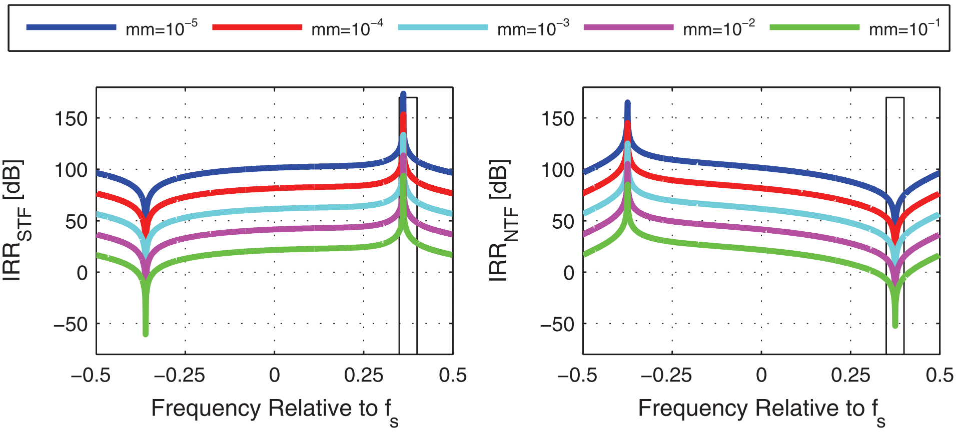

Fig. 11 Signal (*left*) and quantization noise (*right*) IRRs as a function of frequency relative to f_S with mismatch in the modulator feedback and mirror-frequency rejecting STF design. The assumed desired signal band is marked with *solid black line*

branch. This is illustrated in Fig. 11. The signal IRR peaks at the positive frequencies, seen in the left hand plot of the figure, are due to the ISTF notch there. This notch, and thus also peak IRR frequencies, can be tuned with the selection of the original STF notch frequency, because the STF and ISTF notches are at the opposite frequencies symmetrically around DC. The peak IRR values are in the order of 70 dB better than what was achieved with flat STF in Fig. 8.

Again, the quantization noise related IRR results on the right side of Fig. 11 are similar to the corresponding ones with flat STF. The IRR values are modest at the desired band, because the original nonconjugated noise is shaped with the NTF.

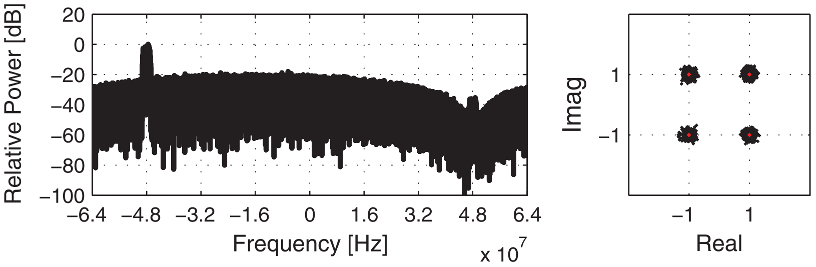

Fig. 12 Output spectrum of an ideal first-order quadrature modulator, consisting of desired QPSK signal around 48 MHz center-frequency and +35 dB Gaussian blocking signal on the mirror band, and the corresponding QPSK constellation after digital down conversion and filtering

6 Simulation Demonstration on I/Q Imbalance Analysis

To validate and demonstrate the results of the IRR analysis in the previous sections, a mismatched Q$\Sigma\Delta$M is simulated with corresponding mismatches. Different imbalance sources are tested separately with 1% mismatch level and the cases with both flat and mirror-frequency rejecting STF designs are demonstrated. The quantization noise source is assumed Gaussian, white, uncorrelated with the input and having a variance equal to 1-bit quantizer. The uncorrelatedness assumption was adopted also earlier in deriving the linearized model for the modulator. The spectrum of the modulator output signal, clarifying the composition used in the simulations is given on the left side of Fig. 12. The desired QPSK signal is located around +48 MHz having a band-limited Gaussian blocking signal with 35 dB higher power level at the mirror-frequency band. The bandwidth of both signals is around 3 MHz and the sampling frequency is 128 MHz. The constellation plot on the right side shows the obtained QPSK signal after digital down conversion and filtering, with perfect I/Q matching in the converter. This is used as the reference in evaluating the performance of the same setup but with I/Q mismatches included in the converter.

The obtained QPSK constellations with I/Q imbalances included and with the flat STF design are given in Fig. 13. The received symbols are plotted in black and the ideal constellation points in red color. Based on the plots, it is clear that the signals of the left side constellations have only marginal noise or interference and can thus be assumed practically free of MFI. These cases correspond to the mismatch in quantizer feeding branch (a) and loop filter (c). The earlier closed-form IRR analysis gave around 60 dB of signal IRR for the quantizer feeding branch with 1% mismatch, which is clearly enough to avoid any significant interference. At the same time, the loop filter imbalance was analyzed not to cause any input signal MFI in otherwise ideal setup. Thus, based on the constellation plots, it can be confirmed that neither the noise mirroring effect due to the loop filter mismatch nor the input signal mirroring is a concern in this scenario.

On the other hand, the other two constellations are heavily corrupted. This is due to frequency flat IRRs with mismatch in the loop filter feeding input branch and modulator feedback branch. In these cases, the signal IRR values are around 20 dB with the applied 1% mismatch. The 40 dB difference (compared to the earlier case) in image rejection is thus playing a great role in this scenario. At the same time, with

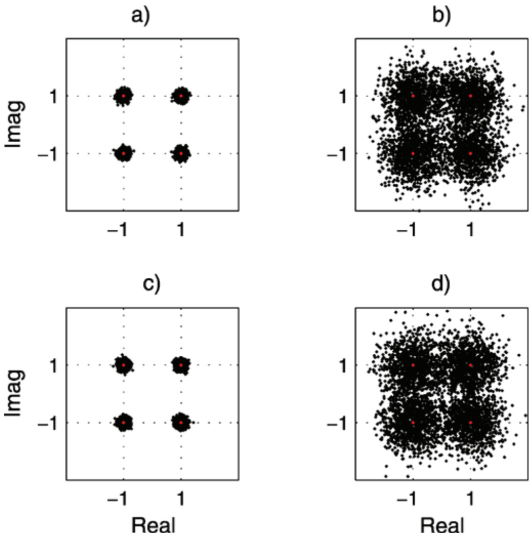

Fig. 13 Obtained desired signal constellations with frequency flat STF design and 1% mismatch in (**a**) quantizer feeding branch, (**b**) loop filter feeding branch, (**c**) loop filter feedback and (**d**) modulator feedback

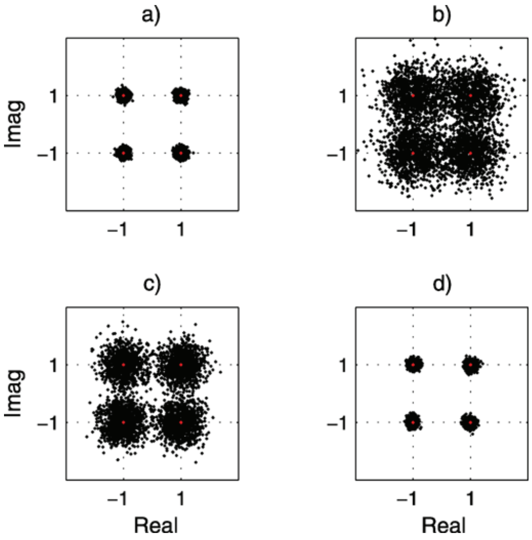

Fig. 14 Obtained desired signal constellations with mirror band rejecting STF design and 1% mismatch in (**a**) quantizer feeding branch, (**b**) loop filter feeding branch, (**c**) loop filter feedback and (**d**) modulator feedback

mirror-frequency rejecting STF design, the interference level with input mismatch remains at the same level as in the previous flat STF case. This can be seen from the top constellations (a) and (b) of Fig. 14. The analytical model also predicted this, because the noise conjugate does not appear and the signal IRR values are on the same level despite of the STF design.

With 1% mismatch in the loop filter and using mirror-frequency rejecting STF (constellation c in Fig. 14), the interference level is clearly increased when compared to the frequency flat STF results above. This is because with the selective STF, the input signal is actually entering the loop filter and thus suffers from the related mismatch. However, the interference is milder when compared to the mismatch in the loop filter input (constellation b in Fig. 14), because the errors on the forward branch of the modulator are shaped by the NTF.

Finally, the improvement attained with the STF notch on the mirror band is visible in the case of 1% mismatch in the feedback branch of the modulator. The interference, which was clearly visible with the flat STF (constellation d in Fig. 13) is well mitigated as can be seen from constellation d in Fig. 14. The result is close to the ideal constellation in Fig. 12 and thus ascertains the improved IRR predicted by the analytical model.

The simulation results are equivalent with the closed-form model and obtained results were clearly verified. In addition, the MFI mitigation properties of the notched STF design were confirmed in the case of modulator feedback mismatch. The loop filter mismatch performance was degraded with the nonunity STF design, which creates a design trade-off. However, it should be taken into account that forward branch errors are shaped by the NTF and the perfect cancellation of the input signal entering the loop filter might not be achieved in a circuit implementation even with the unity STF.

7 Complex Multiband Converter Design for Cognitive Radio

With emerging CR and spectrum-sensing based communication systems, it is essential to be able to adapt to varying waveforms, especially on the receiver side, in terms of the used radio spectrum. The Q$\Sigma\Delta$M offers a great possibility in this respect, especially in cases with scattered spectrum use, since the design of the transfer functions is not restricted to any symmetry with respect to zero frequency. With an Nth-order modulator structure, it is possible to design N separate notches in the NTF (as was noted in Sect. 2.2), allowing reception of signals on N separate frequency slices. On the other hand, if wideband waveforms (with overall bandwidth in the order of tens of MHz) are deployed, the NTF zeros can also be placed next to each other forming a wide uniform notch. This is actually the traditional way of exploiting higher-order modulators and has been discussed extensively in the literature, e.g., in [12, 27, 28]. Thus, we concentrate here on the complex multiband design approach. The principle is first introduced in more detail in the following and then the proposed concept is verified with computer simulations in Sect. 8.

The receiver principle is demonstrated with a block diagram in Fig. 15. In the principal spectra of different stages, the two light grey channels are the desired information signals. The front-end of the receiver is similar to the one described in Sect. 1 (see Fig. 1) but the A/D conversion is now done with a quadrature $\Sigma\Delta$ ADC making use of the multiband concept. Finally, digital filtering is done with a pair of complex BP filters, whereafter both the information signals are down-converted and detected separately.

For the sake of simplicity, the multiband quadrature $\Sigma\Delta$ modulator design is demonstrated here with a second-order quadrature modulator. One possible transfer function setup is illustrated graphically in Fig. 16, where the NTF notches are placed on the assumed desired signal frequencies (here 0.375 and -0.121 relative to sampling rate). The STF, in turn, is used to create selectivity for the overall modulator response. More specifically, the zeros of the signal transfer function are placed at the mirror frequencies of the desired signals (-0.375 and 0.121), applying the

Fig. 15 A block diagram of a $Q\Sigma\Delta M$ based *multiband* low-IF quadrature receiver with principal spectra, where the *two light grey signals* are the desired ones, illustrating the signal composition at each stage

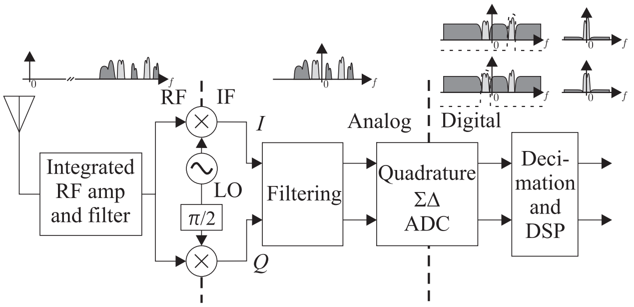

Fig. 16 Example multiband transfer functions with the desired signal spectrum slices at normalized frequencies of 0.375 and −0.121. NTF notches are placed at those frequencies and STF notches at the corresponding mirror frequencies

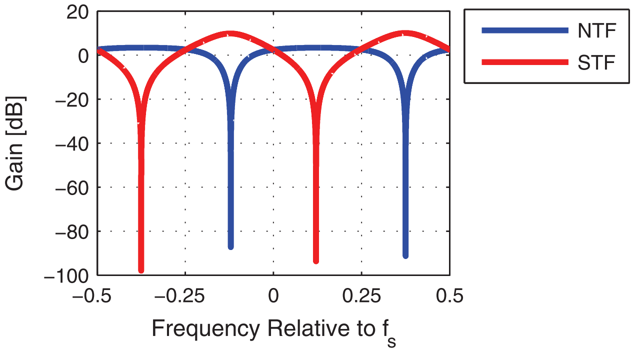

I/Q mismatch mitigation principle discussed in Sects. 3–6. Such a design principle was concluded earlier to be effective way to mitigate the mirror-frequency interference caused by the mismatches located in the modulator feedback branch. The poles of the transfer functions, in turn, are placed at the NTF notch frequencies in order to elevate the STF response at those bands. This particular second-order design (see Sect. 2.2) is achieved with the following complex gains on the input branches: $A_0 = 1$, $A_1 = M_2 + M_1 - (e^{j2\pi \overline{f}_{\text{int1}}} + e^{j2\pi \overline{f}_{\text{int2}}})$ and $A_2 = M_2 A_1 - M_1 M_2 + (e^{j2\pi \overline{f}_{\text{int1}}} + e^{j2\pi \overline{f}_{\text{int2}}})$, while the corresponding gains on the feedback branches have values $G_1 = -M_1 - M_2 + (0.6e^{j2\pi \overline{f}_{\text{pass1}}} + 0.6e^{j2\pi \overline{f}_{\text{pass2}}})$ and $G_2 = M_1 M_2 + M_2 G_1 - (0.6e^{j2\pi \overline{f}_{\text{pass1}}} + 0.6e^{j2\pi \overline{f}_{\text{pass2}}})$, where $\overline{f}_{\text{int1}} = -0.375$, $\overline{f}_{\text{int2}} = 0.121$, $\overline{f}_{\text{pass1}} = 0.375$ and $\overline{f}_{\text{pass2}} = -0.121$ denote the normalized frequencies of the two STF notches and the two NTF notches, respectively. The coefficients M_1 and M_2 are the complex-valued feedback gains of the two loop integrators ($H_1[z]$ and $H_2[z]$) giving the zeros of the NTF, being defined as $M = e^{j2\pi \overline{f}_{\text{pass1}}}$ and $M_2 = e^{j2\pi \overline{f}_{\text{pass2}}}$. At the same time, the terms $0.6e^{j2\pi \overline{f}_{\text{pass1}}}$ and $0.6e^{j2\pi \overline{f}_{\text{pass2}}}$ define the positions of the two common poles for the STF and the NTF.

All the NTF and the STF notches can be tuned independently of each other, giving the needed degree of freedom for the design of the receiver. In the second-order case, modifying the aforementioned frequency values ($\overline{f}_{\text{int1}}$, $\overline{f}_{\text{int2}}$, $\overline{f}_{\text{pass1}}$ and $\overline{f}_{\text{pass2}}$) based on the signal composition at hand (spectrum sensing), allows straightforward reconfigurability of the system. The principle was demonstrated in more detail for the first-order system, including the derivation the actual zeros and the poles, in Sect. 2.1. Thus in cognitive radio context, when the center-frequencies of the desired signal spectrum slices change, the NTF and STF designs are modified accordingly based on the information from a spectrum-sensing unit. Additionally, with STF design-based selectivity built in the modulator, the selectivity of the actual analog RF front-end can be reduced, improving the flexibility of the receiver.

8 Receiver Simulation Example on Complex Multiband Transfer Function Design

The receiver principle presented above is next simulated with true-like radio signals in order to verify the applicability. The spectrum of the signal composition used in the simulation is given in the top of Fig. 17 assuming intermediate frequency A/D conversion. The overall desired signal consists of two sub-waveforms, a 16-QAM signal around 48 MHz center-frequency with 6 MHz bandwidth and a QPSK signal around -15 MHz center-frequency with 8 MHz bandwidth. There are also two blocking signals consisting of band-limited Gaussian noise at center-frequencies 15 MHz and -48 MHz. The relative power levels of the 16-QAM desired signal, the blocker around $+15$MHz and the blocker around -48 MHz are $+5$ dB, $+15$ dB and $+25$ dB, respectively, when compared to the QPSK signal at -15 MHz. The quantization noise is assumed Gaussian, white, uncorrelated with the input and having a variance equal to 1-bit quantization error (as was the case in Sect. 6). In addition, I/Q mismatch of 1% is introduced in both the modulator feedback branches (complex gains G_1 and G_2). The mismatches are implemented in similar manner as was described for first-order Q$\Sigma\Delta$M with one feedback branch in Sect. 4.3. The signal and noise transfer functions of the Q$\Sigma\Delta$M are designed in such a way as shown in Fig. 16 to attenuate the mirror-frequency blocking signals and to shape the noise away from the desired signal bands, respectively.

The output spectrum of the Q$\Sigma\Delta$M is given in the bottom of Fig. 17, demonstrating clearly the filtering effect of the selective STF design described in Sect. 7. The blocking signals are pushed to the noise floor. The constellations of both the interesting signals are given in Fig. 18. The signals, despite being noisy, have less than 1% bit error ratios. In the spectrum plot, the weak QPSK signal appears to be buried in the noise but the applied noise shaping is pushing the noise level down exactly at that frequency band, thus enabling reliable enough detection of the signal.

Also the MFI is kept at minimum, despite the I/Q mismatches, due to proposed transfer function design.

Based on these findings, the complex multiband principle is found to be valid. In this way, it is possible to design a highly reconfigurable and efficient A/D stage with built-in selectivity and robustness against I/Q mismatches. The Q$\Sigma\Delta$M offers higher flexibility and degree of freedom when compared to real $\Sigma\Delta$ modulators and thus the multiband structure can be implemented more efficiently.

9 Conclusion

In this article, a closed-form model for the I/Q imbalanced first-order Q$\Sigma\Delta$M was first derived and then used to analyze the effects of distinct mismatch sources in two

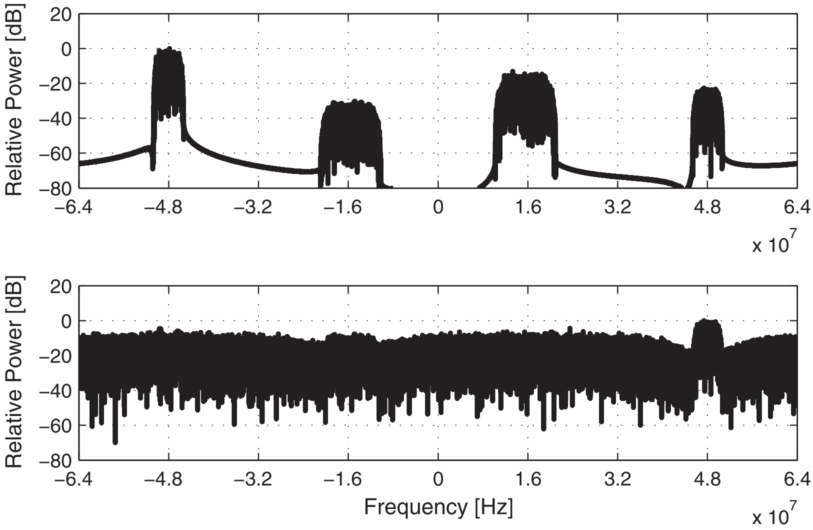

Fig. 17 Input (*top*) and output (*bottom*) spectra of the multiband quadrature modulator with mirror-frequency rejecting STF design, consisting of the desired 16-QAM signal (roughly 48 MHz center-frequency), the desired QPSK signal (roughly −15 MHz center-frequency) and the two Gaussian blocking signals at the mirror bands

Fig. 18 Received constellations in multiband setup for (**a**) 16-QAM signal around 48 MHz and (**b**) QPSK signal around −15 MHz

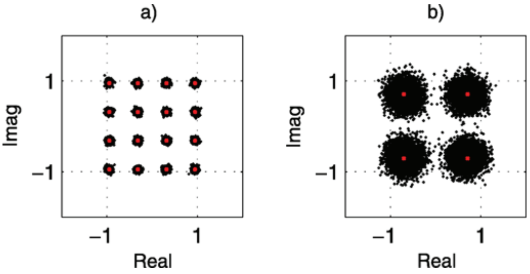

cases: flat STF and mirror-frequency rejecting STF designs. The two input branches, the loop filter and the modulator feedback branch were considered as possible mismatch sources. One of the main findings of this analysis was that the amount of mirror-frequency interference due to I/Q imbalances at the desired signal band is highly dependent on the *exact* location of the mismatch inside the modulator structure. At the same time, the mirror-frequency rejecting STF design was proven able to mitigate the mirror-frequency interference caused by the complex-conjugation of the modulator input signal, in case of the modulator feedback I/Q mismatch, giving close to ideal results. The latter part of the article proposed a novel complex multiband scheme for cognitive radio type receivers, where the NTF of the $\mathrm{Q}\Sigma\Delta\mathrm{M}$ is designed to have multiple scattered notches, thus allowing simultaneous reception of more than one distinct interesting information signals with a single modulator branch. The validity of the proposed concept was confirmed with a computer simulation, and the flexibility, achieved with the straightforward parametrization and reconfigurability, was pointed out.

References

1. D.D. Ariananda, M.K. Lakshmanan, H. Nikoo, A survey on spectrum sensing techniques for Cognitive Radio, in *Proc. 2nd Int. Workshop Cognitive Radio and Advanced Spectrum Manage* (2009), pp. 74–79
2. P.A. Aziz, H.V. Sorensen, J. Van der Spiegel, Multi band sigma delta analog to digital conversion, in *Proc. IEEE Int. Conf. Acoustics, Speech and Signal Process.* (1994), pp. III-249–III-252
3. P.A. Aziz, H.V. Sorensen, J. van der Spiegel, Performance of complex noise transfer functions in bandpass and multi band sigma delta systems, in *Proc. IEEE Int. Symp. Circuits and Syst.* (1995), pp. 641–644
4. P.A. Aziz, H.V. Sorensen, J. van der Spiegel, An overview of sigma-delta converters: how a 1-bit ADC achieves more than 16-bit resolution. IEEE Signal Process. Mag. **13**, 61–84 (1996)
5. R. Bagheri, A. Mirzaei, M.E. Heidari, S. Chehrazi, M. Lee, M. Mikhemar, W.K. Tang, A.A. Abidi, Software-defined radio receiver: dream to reality. IEEE Commun. Mag. **44**, 111–118 (2006)
6. L.J. Breems, E.C. Dijkmans, J.H. Huijsing, A quadrature data-dependent DEM algorithm to improve image rejection of a complex $\Sigma\Delta$ modulator. IEEE J. Solid-State Circuits **36**, 1879–1886 (2001)
7. J. Crols, M.S.J. Steyaert, Low-IF topologies for high-performance analog front ends of fully integrated receivers. IEEE Trans. Circuits Syst. II, Analog Digit. Signal Process. **45**, 269–282 (1998)
8. R.M. Gray, Quantization Noise in $\Delta\Sigma$ A/D Converters, in *Delta-Sigma Data Converters* (Wiley/IEEE Press, Hoboken, 1995), pp. 44–74, Chap. 2
9. M. Ismail, D. González (eds.), *Radio Design in Nanometer Technologies* (Springer, Dordrecht, 2006)
10. S. Jantzi, Quadrature bandpass delta-sigma modulation for digital radio. Ph.D. dissertation, Univ. Toronto, Toronto, Canada (1997)
11. S. Jantzi, K.W. Martin, A.S. Sedra, The effects of mismatch in complex bandpass $\Delta\Sigma$ modulators, in *Proc. IEEE Int. Symp. Circuits and Syst.* (1996), pp. 227–230
12. S. Jantzi, K.W. Martin, A.S. Sedra, Quadrature bandpass $\Delta\Sigma$ modulation for digital radio. IEEE J. Solid-State Circuits **32**, 1935–1950 (1997)
13. N. Jouida, C. Rebai, A. Ghazel, Built-in filtering for out-of-channel interferers in continuous-time quadrature bandpass delta sigma modulators, in *Proc. 14th IEEE Int. Conf. Electronics, Circuits and Syst* (2007), pp. 947–950
14. N. Jouida, C. Rebai, G. Ghazel, D. Dallet, Comparative study between continuous-time real and quadrature bandpass delta sigma modulator for multistandard radio receiver, in *Proc. Instrumentation and Measurement Technology Conf.* (2007), pp. 1–6
15. B. Le, T.W. Rondeau, J.H. Reed, C.W. Bostian, Analog-to-digital converters. IEEE Signal Process. Mag. **22**, 69–77 (2005)
16. P.-I. Mak, S.-P. U, R.P. Martins, Transceiver architecture selection: review, state-of-the-art survey and case study. IEEE Circuits Syst. Mag. **7**(2), 6–25 (2007)
17. J. Marttila, M. Allén, M. Valkama, I/Q imbalance effects in quadrature $\Sigma\Delta$ modulators—analysis and signal processing, in *Proc. IEEE Int. Microwave Workshop Series RF Front-ends for Software Defined and Cognitive Radio Solutions* (2010), pp. 1–4
18. J. Marttila, Quadrature sigma-delta ADCs: modeling and signal processing. M.Sc. Thesis, Tampere Univ. of Technol., Tampere, Finland (2010)
19. J. Mitola III, Cognitive radio—an integrated agent architecture for software defined radio. Ph.D. Dissertation, Royal Inst. of Technol., Stockholm, Sweden (2000)
20. J. Mitola, Cognitive radio architecture evolution. Proc. IEEE **97**, 626–641 (2009)
21. K. Muhammad, R.B. Staszewski, D. Leipold, Digital RF processing: toward low-cost reconfigurable radios. IEEE Commun. Mag. **43**, 105–113 (2005)
22. K.-P. Pun, C.-S. Choy, C.-F. Chan, J.E. da Franca, An I/Q mismatch-free switched-capacitor complex sigma–delta modulator. IEEE Trans. Circuits Syst. I, Express Briefs **51**, 254–256 (2004)
23. B. Razavi, Design considerations for direct-conversion receiver. IEEE Trans. Circuits Syst. II, Analog Digit. Signal Process. **44**, 428–435 (1997)
24. B. Razavi, *RF Microelectronics* (Prentice Hall, Upper Saddle River, 1998)
25. S. Reekmans, P. Rombouts, L. Weyten, Mismatch insensitive double-sampling quadrature bandpass $\Sigma\Delta$ modulation. IEEE Trans. Circuits Syst. I, Regul. Pap. **54**, 2599–2607 (2007)
26. A. Rusu, B. Dong, M. Ismail, Putting the "flex" in flexible mobile wireless radios. IEEE Circuits Devices Mag. **22**, 24–30 (2006)
27. R. Schreier, An empirical study of high-order single-bit delta-sigma modulators. IEEE Trans. Circuits Syst. II, Analog Digit. Signal Process. **40**, 461–466 (1993)

28. R. Schreier, G.C. Temes, *Understanding Delta-Sigma Data Converters* (Wiley, Hoboken, 2005)
29. M. Valkama, J. Pirskanen, M. Renfors, Signal processing challenges for applying software radio principles in future wireless terminals: an overview. Int. J. Commun. Syst. **15**, 741–769 (2002)
30. N. Vun, A.B. Premkumar, ADC systems for SDR digital front-end, in *Proc. 9th Int. Symp. Consumer Electronics* (2005), pp. 14–16
31. J. Yang, R.W. Brodersen, D. Tse, Addressing the dynamic range problem in cognitive radios, in *Proc. IEEE Int. Conf. Commun.* (2007), pp. 5183–5188
32. L. Yu, W.M. Snelgrove, A novel adaptive mismatch cancellation system for quadrature IF radio receivers. IEEE Trans. Circuits Syst. II, Analog Digit. Signal Process. **46**, 789–801 (1999)

PUBLICATION 4

Jaakko Marttila, Markus Allén and Mikko Valkama, “Multi-stage quadrature sigma-delta modulators for reconfigurable multi-band analog-digital interface in cognitive radio devices,” *EURASIP Journal on Wireless Communications and Networking*, volume 2011:130., 23 pages, October 2011.

Marttila *et al. EURASIP Journal on Wireless Communications and Networking* 2011, **2011**:130
http://jwcn.eurasipjournals.com/content/2011/1/130

EURASIP Journal on
Wireless Communications and Networking
a SpringerOpen Journal

RESEARCH **Open Access**

Multistage quadrature sigma-delta modulators for reconfigurable multi-band analog-digital interface in cognitive radio devices

Jaakko Marttila*, Markus Allén and Mikko Valkama

Abstract

This article addresses the design, analysis, and parameterization of reconfigurable multi-band noise and signal transfer functions (NTF and STF), realized with multistage quadrature $\Sigma\Delta$ modulator (Q$\Sigma\Delta$M) concept and complex-valued in-phase/quadrature (I/Q) signal processing. Such multi-band scheme was already proposed earlier by the authors at a preliminary level, and is here developed further toward flexible and reconfigurable A/D interface for cognitive radio (CR) receivers enabling efficient parallel reception of multiple noncontiguous frequency slices. Owing to straightforward parameterization, the NTF and the STF of the multistage Q$\Sigma\Delta$M can be adapted to input signal conditions based on spectrum-sensing information. It is also shown in the article through closed-form response analysis that the so-called mirror-frequency-rejecting STF design can offer additional operating robustness in challenging scenarios, such as the presence of strong mirror-frequency blocking signals under I/Q imbalance, which is an unavoidable practical problem with quadrature circuits. The mirror-frequency interference stemming from these blockers is analyzed with a novel analytic closed-form I/Q imbalance model for multistage Q$\Sigma\Delta$Ms with arbitrary number of stages. Concrete examples are given with three-stage Q$\Sigma\Delta$M, which gives valuable degrees of freedom for the transfer function design. High-order frequency asymmetric multi-band noise shaping is, in general, a valuable asset in CR context offering flexible and frequency agile adaptation capability to differing waveforms to be received and detected. As demonstrated by this article, multistage Q$\Sigma\Delta$Ms can indeed offer these properties together with robust operation without risking stability of the modulator.

1 Introduction

Nowadays, a growing number of parallel wireless communication standards, together with ever-increasing traffic amounts, create a widely acknowledged need for novel radio solutions, such as emerging cognitive radio (CR) paradigm [1, 2]. On the other hand, transceiver implementations, especially in mobile terminals, should be small-sized, power efficient, highly integrable, and cheap [3–7]. Thus, it would be valuable to avoid implementing parallel transceiver units for separate communication modes. However, operating band of this kind of software defined radio (SDR) should be extremely wide (even GHz range), and dynamic range of the receiver should be high (several tens of dBs) [5–10]. In addition, the transceiver should be able to adapt to numerous different transmission schemes and waveforms [4–8, 10]. The SDR concept is considered as a physical layer foundation for CR [1], but these demands create a big challenge for transceiver design, especially for mobile devices.

Particularly, the analog-to-digital (A/D) interface has been identified as a key performance-limiting bottleneck [1, 3, 4, 8, 10–12]. For example, GSM reception demands high dynamic range, and WLAN and LTE bandwidths, in turn, can be up to 20 MHz. Combining this kind of differing radio characteristics set massive demands for the A/D converter (ADC) in the receiver. Traditional Nyquist ADCs (possibly with oversampling) divide the conversion resolution equally on all the frequencies, and thus, if 14-bit

---

*Correspondence: jaakko.marttila@tut.fi
Department of Communications Engineering, Tampere University of Technology, P.O. Box 553, Tampere 33101, Finland

resolution is needed for one of the signals converted, then similar resolution is used over the whole band even if it would not be necessary [12]. At the same time, in wideband SDR receiver, the resolution demand might be even higher because of the increased dynamic range due to multiple waveforms with differing power levels entering the ADC. On the other hand, ΣΔ ADCs have inherent tradeoff between the sampling frequency and resolution [13]. With narrowband signals (such as GSM), e.g., 14-bit resolution can be achieved with 1-bit quantization because of high oversampling and digital filtering. At the same time, modulator structure can be reconfigured for reception of wideband waveforms to meet differing requirements set by, for example, WLAN or LTE standards [8, 14, 15].

Based on this, one promising solution for the receiver design in this kind of scenario is wideband direct-conversion or low-IF architecture [16] with a bandpass ΣΔ ADC [8, 14]. Additional degrees of freedom can be obtained by introducing quadrature ΣΔ modulator (QΣΔM) in the receiver, allowing efficient frequency asymmetric quantization noise shaping [17, 18]. Furthermore, a multi-band modulator aimed to CR receivers is preliminary proposed in [19] and illustrated with receiver block diagram and principal spectra in Figure 1. This kind of multi-band design for QΣΔM offers frequency agile flexibility and reconfigurability based on spectrum-sensing information [20] together with capability of receiving multiple parallel frequency bands [19], which are considered essential when realizing A/D interface for CR solutions [1]. In practice, multiple noise-shaping notches can be created on independent, noncontiguous signal bands. In addition, the center frequencies of these noise notches can be tuned based on the spectrum-sensing information obtained in the receiver.

Noise-shaping capabilities of a single-stage QΣΔM are limited by the order of the modulator [18]. However, the order of the overall noise transfer function (NTF) can be increased using cascaded multistage modulator [21–23]. Therein, the overall noise shaping is of the combined order of the stages. In a multistage QΣΔM, the noise notches of the stages can be placed independently, thus further increasing the flexibility of the ADC [21].

Unfortunately, implementing quadrature circuits brings always a challenge of matching the in-phase (I) and quadrature (Q) rails, which should ideally have symmetric component values. Inaccuracies in circuit implementation always shift the designed values, creating imbalance between the rails, known as I/Q imbalance [18, 24]. This mismatch induces image response of the input signal in addition to the original input, causing mirror-frequency interference (MFI) [18, 24]. This image response can be modeled mathematically with altered complex conjugate of the signal component. In QΣΔMs generally, the mismatches generate conjugate response for both the input signal and the quantization error [18, 19, 25], which is a clear difference to mirror-frequency problematics in more traditional receivers. Specifically, feedback branch mismatches have been highlighted as the most important MFI source [23, 26]. From the noise point of view, placing a NTF notch also on mirror frequency to cancel MFI was initially proposed in [18] and discussed further in [27]. This, however, wastes noise shaping performance from the preferred signal point of view and restricts design freedom, especially in multi-band scenario. In addition, this does not take the mirroring of the input signal into account. In wideband SDR quadrature receiver, the MFI stemming from the input of the receiver is a crucial viewpoint because of possible blocking signals. Furthermore, alterations to analog circuitry have been proposed in [26, 28, 29] to minimize the interference. Sharing the components between the branches, however, degrades sampling properties of the modulator [28,

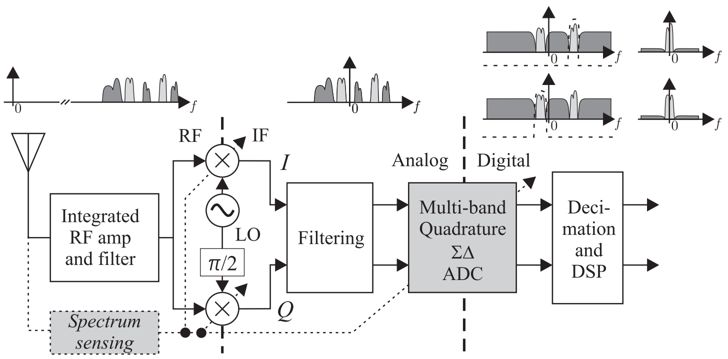

Figure 1 Block diagram of *multi-band* low-IF quadrature receiver, based on QΣΔM. Principal spectra, where the two light gray signals are the preferred ones, are illustrating the signal compositions at each stage.

29]. On the other hand, additional components add to the circuit area and power dissipation of the modulator [26]. In [19], the authors found that mirror-frequency-rejecting signal transfer function (STF) design mitigates the input signal-originating MFI in case of mismatch in the feedback branch of a first-order QΣΔM. In [21], this idea is extended to cover multi-band design of [19] with a simple two-stage QΣΔM. The feedback I/Q imbalance effects and related digital calibration in two-stage QΣΔM are addressed also in [23], where only a frequency-flat STF is considered. In addition, the mirror-frequency-rejecting STF design has a benefit of not demanding additional components to the original QΣΔM structure.

In this article, an analytic closed-form model for QΣΔM I/Q imbalance effects is derived covering multistage modulators with arbitrary number of stages, extending the preliminary analysis with two first-order stages in [21]. Herein, the I/Q imbalance model for second-order QΣΔM presented by the authors in [30] is used for each of the stages. Furthermore, design of the transfer functions (STF and NTF) of the stages in such multistage QΣΔM is addressed in detail with emphasis on robust operation under I/Q mismatches. In [31, 32], QΣΔM STF designs are proposed for reducing the dynamics of the receiver and to filter adjacent channel signals for lowpass and quadrature bandpass modulators, respectively. However, adapting the STF based on spectrum-sensing information is not covered in case of the QΣΔM in [31]. In addition, NTF adaptation to frequency handoffs or multi-band reception is not considered in either [31] or [32]. Herein, frequency agile design of the STF and the NTF of an I/Q mismatched multistage QΣΔM is discussed taking both the input signal and the quantization noise-oriented MFI into account during multi-band reception.

The push for development of multi-channel ADCs for SDR and CR solutions has been acknowledged, e.g., in [11]. A multi-channel system with parallel ADCs is one possible solution which, however, sets additional burden for size, cost, and power dissipation of the receiver implementation [11, 13]. On the other hand, quadrature ΣΔ noise shaping makes exploitation of whole quantization precision on the preferred signal bands possible. Three-stage lowpass ΣΔ modulators have traditionally been used only for applications demanding very high resolution [33], but like shown in this article, the QΣΔM variant allows noncontiguous placement of the NTF zeros, and thus the quantization precision can be divided on multiple parallel frequency bands. A reconfigurable three-stage converter using lowpass ΣΔ stages together with a pipeline ADC is proposed in [15] for mobile terminals. In comparison, a three-stage QΣΔM discussed in this article offers more efficient noise shaping and additional degrees of freedom for the receiver design. These are essential characteristics when heading toward a frequency agile-reconfigurable ADC for CR receivers. Thus, a multistage QΣΔM offers a competent platform for realizing flexible multi-band A/D conversion in CR devices.

The rest of the article is organized as follows. In Section 2, basics of quadrature ΣΔ modulation are reviewed, while Section 3 presents a closed-form model for I/Q imbalance effects in a second-order QΣΔM as a single stage of a multistage modulator and proposes a novel extension of the given model for multistage modulators with arbitrary number of stages. Parameterization and design of the modulator transfer functions in CR receivers in the presence of I/Q mismatches are discussed in Section 4. The receiver system level targets and QΣΔM performance are discussed in Section 5. Thereafter, Section 6 presents the results of the designs in the previous section with closed-form transfer function analysis and computer simulations. Finally, Section 7 concludes the article.

Short note on terminology and notations: term "order" refers in this article to the order of polynomial(s) in z-domain transfer functions, while term "stage" refers to individual QΣΔM block in a multistage converter where multiple QΣΔM blocks are interconnected. The z-domain representations of sequences $x(k)$ and $x^*(k)$ are denoted as $X[z]$ and $X^*[z^*]$, respectively, where superscript $(\cdot)^*$ denotes complex conjugation.

2 Basics of quadrature ΣΔ modulation

Quadrature variant of the ΣΔ modulator was originally presented in [18]. The concept is based on the modulator structure similar to the one used in real lowpass and bandpass modulators, but employing complex-valued input and output signals together with complex loop filters (integrators). This complex I/Q signal processing gives additional degree of freedom to response design, allowing for frequency-asymmetric STF and NTF. For analysis purposes, a linear model of the modulator is typically used. In other words, this means that quantization error is assumed to be additive and having no correlation with the input signal. Although not being exactly true, this allows analytic derivation of the transfer functions and has thus been applied widely, e.g., in [18, 33]. Now, the output of a single-stage QΣΔM, depicted in Figure 2, is defined as

$$V^{\text{ideal}}[z] = \text{STF}[z]U[z] + \text{NTF}[z]E[z], \tag{1}$$

where STF[z] and NTF[z] are generally complex-valued functions, and $U[z]$ and $E[z]$ denote z-transforms of the input signal and quantization noise, respectively.

The achievable NTF shaping and STF selectivity are defined by the order of the modulator. With Pth-order modulator, it is possible to place P zeros and poles in both transfer functions. This is confirmed by derivation of the transfer functions for the structure presented in Figure 2. The

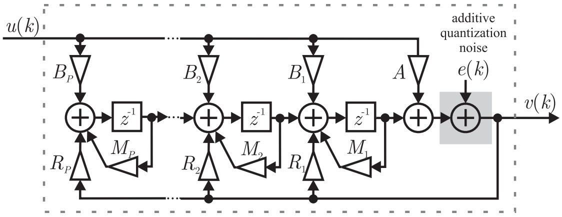

Figure 2 Discrete-time linearized model of a *P*th-order QΣΔM with complex-valued signals and coefficients.

NTF of the *P*th-order QΣΔM is given by

$$\mathrm{NTF}[z] = \frac{1}{1 - \sum_{p=1}^{P} R_p \prod_{i=1}^{p} \frac{1}{z-M_i}} \tag{2}$$

and, on the other hand, the corresponding STF is

$$\mathrm{STF}[z] = \frac{A + \sum_{p=1}^{P} B_p \prod_{i=1}^{p} \frac{1}{z-M_i}}{1 - \sum_{p=1}^{P} R_p \prod_{i=1}^{p} \frac{1}{z-M_i}}, \tag{3}$$

where $1/(z - M_i)$ terms are the transfer functions of the complex loop filters (integrators). Both transfer functions have common denominator and thus common poles. It can also be seen that in addition to the loop filters, only the feedback coefficients R_p (feeding the output to the loop filters) affect the noise shaping. Thus, input coefficients A (feeding the input to the quantizer) and B_p (feeding the input to the loop filters) can be used to tune the STF zeros independent of the NTF.

The NTF zeros are usually placed on the preferred signal band(s) to create the noise-shaping effect. At the same time, the STF zeros can be used to attenuate out-of-band frequencies and thus include some of the receiver selectivity in the QΣΔM. The transfer function design for CR is discussed in more detail in Section 4. In the following subsections, multi-band and multistage principles will be presented. These are important concepts, considering reconfigurability in the A/D interface and frequency agile conversion with high-enough resolution in CR devices.

2.1 Multi-band quadrature ΣΔ ADC for CR

With QΣΔM of higher than first order, it is possible to place multiple NTF zeros on the conversion band [18]. Traditional way of exploiting this property has been making the noise-shaping notch wider, thus improving the resolution of the interesting information signal over wider bandwidths [18]. However, in CR-based systems, it is desirable to be able to receive more than one detached frequency bands - and signals - in parallel [1]. The multi-band scheme offers transmission robustness, e.g., in case of appearance of a primary user when the CR user has to vacant that frequency band [1]. In that case, the transmissions can be continued on the other band(s) in use. In addition, if the CR traffic is divided on multiple bands, then lower power levels can be used, and thus the interference generated for primary users is decreased [1].

Multi-band noise shaping without restriction to frequency symmetry is able to respond to this need with noncontiguous NTF notches. This reception scheme is illustrated graphically in Figure 3. The possible number of

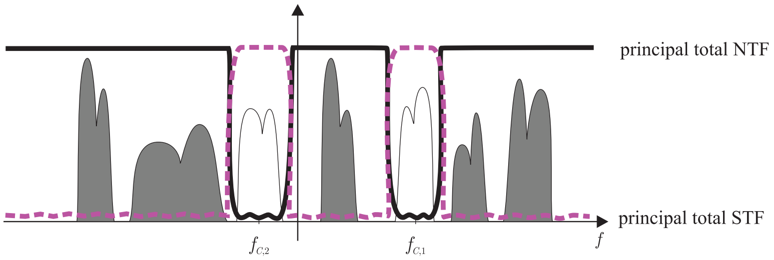

Figure 3 Principal illustration of complex multi-band QΣΔM scheme for cognitive radio devices. The *light gray* signals are assumed to be the preferred ones and principal total STF and NTF are illustrated with *magenta dotted* and *black solid lines*, respectively. Quantization noise is shaped away from preferred frequency bands and out-of-band signals are attenuated.

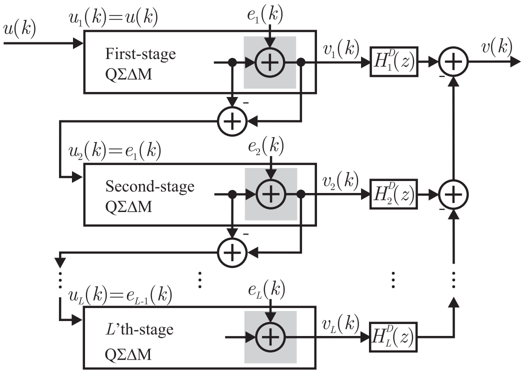

Figure 4 Multistage QΣΔM with arbitrary-order noise shaping in all the individual stages. Filters $H_1^{\text{D}}[z]$ to $H_L^{\text{D}}[z]$ are implemented digitally.

these notches is defined by the overall order of the modulator. With multistage QΣΔM this is the combined order of all the stages. In addition, the frequencies of the notches can be tuned straightforwardly, e.g., in case of frequency handoff. This tunability of the transfer functions allows also for adaptation to differing waveforms, center frequencies and bandwidths to be received. The resolution and bandwidth demands of the waveforms at hand can be taken into account and the response of the QΣΔM can be optimized for the scenario of the moment based on the spectrum-sensing information. Further details on design and parameterization of multi-band transfer functions are given in Section 4.

3 Multistage quadrature ΣΔ ADC

Multistage ΣΔ modulators have been introduced to improve resolution, e.g., in case of wideband information signal, when attainable oversampling is limited. This principle was first proposed with lowpass modulator [33], but has thereafter been extended to quadrature bandpass modulator [23, 26]. The block diagram of L-stage quadrature ΣΔ ADC is given in Figure 4, where all the stages are of arbitrary order. The inputs $u_l(k)$ of the L individual stages ($1 \le l \le L$, $l \in \mathbb{Z}$) are defined in the following manner. The input of the first-stage ($l = 1$) is the overall input of the whole structure, i.e., $u_1(k) = u(k)$, and for the latter stages, the (ideal) input is the quantization error of the previous stage; thus, $u_l(k) = e_{l-1}(k)$ when $2 \le l \le L$.

The main goal in multistage QΣΔM is to digitize quantization error of the previous stage with the next stage and thereafter subtract it from the output of that previous stage. Owing to the noise shaping in the stages, the digitized error estimate must be filtered in the same way, in order to achieve effective cancelation. Similarly, the output of the first stage must be filtered with digital equivalent of the second-stage STF (e.g., to match the delays). These filters are depicted in Figure 4 with $H_1^{\text{D}}[z]$ to $H_L^{\text{D}}[z]$. Now, assuming ideal implementation, the final output becomes

$$V^{\text{ideal}}[z] = \sum_{l=1}^{L}(-1)^{l+1}H_l^{\text{D}}[z]\,V_l^{\text{ideal}}[z], \tag{4}$$

where

$$\begin{aligned} V_l^{\text{ideal}}[z] &= \text{STF}_l^{\text{ideal}}[z]U_l[z] + \text{NTF}_l^{\text{ideal}}[z]E_l[z], \\ &\quad 1 \le l \le L, l \in \mathbb{Z}, \end{aligned} \tag{5}$$

and

$$H_l^{\text{D}}[z] = \frac{H_1^{\text{D}}[z]\prod_{l=1}^{L-1}\text{NTF}_l^{\text{ideal}}[z]}{\prod_{l=2}^{L}\text{STF}_l^{\text{ideal}}[z]}, \quad 1 \le l \le L, l \in \mathbb{Z}, \tag{6}$$

to match the analog transfer functions and the digital filters. It is usually chosen that $H_1^{\text{D}}[z] = \text{STF}_2[z]$, thus giving $H_2^{\text{D}}[z] = \text{NTF}_1[z]$ and $H_3^{\text{D}}[z] = \text{NTF}_1[z]\,\text{NTF}_2[z]/\,\text{STF}_3[z]$, etc. With these selections, the quantization errors of the earlier stages are canceled (assuming ideal circuitry), and the overall output of the L-stage QΣΔM becomes ($L \ge 2$)

$$\begin{aligned} V^{\text{ideal}}[z] &= \text{STF}_1^{\text{ideal}}[z]\,\text{STF}_2^{\text{D}}[z]U[z] \\ &\quad + \frac{\prod_{l=1}^{L}\text{NTF}_l^{\text{ideal}}[z]}{\prod_{l=3}^{L}\text{STF}_l^{\text{ideal}}[z]}E_L[z] \\ &= \text{STF}_{\text{TOT}}^{\text{ideal}}[z]U[z] + \text{NTF}_{\text{TOT}}^{\text{ideal}}[z]E_L[z], \end{aligned} \tag{7}$$

where only the quantization error of the last stage is present. It is observed that, if three or more stages are used, then special care should be taken in designing the STF of

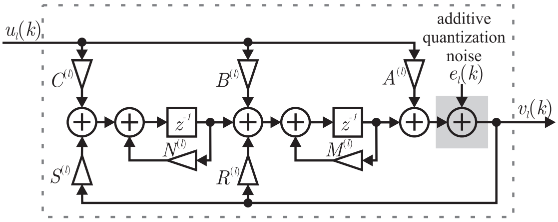

Figure 5 Discrete-time-linearized model of the *l*th second-order QΣΔM stage in a multistage QΣΔM with complex-valued signals and coefficients.

the third and the latter stages, which operate in the denominator of the noise-shaping term. However, the leakage of the quantization noise of the earlier stages might be limiting achievable resolution in practice because of nonideal matching of the digital filters [33]. One way to combat this phenomenon is to use adaptive filters [34, 35].

3.1 I/Q imbalance in multistage QΣΔMs

In this section, a closed-form transfer function analysis is carried out for a general multistage QΣΔM taking also the possible coefficient mismatches in complex I/Q signal processing into account. For mathematical tractability and notational convenience, second-order QΣΔM stages are assumed as individual building blocks (individual stages) in Figure 4, and the purpose is to derive a complete closed-form transfer function model for the overall multistage converter. Such analysis is missing from the existing state-of-the-art literature. For notational simplicity, the modulator coefficients are denoted in the following analysis as shown in the block diagram of Figure 5. With this structure, the ideal NTF for the lth stage is given by

$$\begin{aligned}\mathrm{NTF}_l[z] = {} & \left(1-(M^{(l)}+N^{(l)})z^{-1}+(M^{(l)}N^{(l)})z^{-2}\right)\\ & /\left(1-(M^{(l)}+N^{(l)}+R^{(l)})z^{-1}\right.\\ & \left.+(M^{(l)}N^{(l)}+N^{(l)}R^{(l)}-S^{(l)})z^{-2}\right).\end{aligned} \tag{8}$$

At the same time, the ideal STF for the lth stage is defined as

$$\begin{aligned}\mathrm{STF}_l[z] = {} & \left(A^{(l)}+(B^{(l)}-N^{(l)}A^{(l)}-M^{(l)}A^{(l)})z^{-1}\right.\\ & \left.+(C^{(l)}-N^{(l)}B^{(l)}+M^{(l)}N^{(l)}A^{(l)})z^{-2}\right)\\ & /\left(1-(M^{(l)}+N^{(l)}+R^{(l)})z^{-1}\right.\\ & \left.+(M^{(l)}N^{(l)}+N^{(l)}R^{(l)}-S^{(l)})z^{-2}\right).\end{aligned} \tag{9}$$

The transfer functions of (8) and (9) are valid when I and Q rails of the QΣΔM are matched perfectly. With this perfect matching, (1) and (4) give the outputs for single-stage and multistage modulators, respectively.

3.2 I/Q imbalance effects on individual QΣΔM stage

Quadrature signal processing is, in practice, implemented with parallel real signals and coefficients. In Figure 6, this is demonstrated in case of a single second-order QΣΔM stage (parallel real I and Q signal rails) and taking possible mismatches in the coefficients into account. Deviation between coefficient values of the rails, which should ideally be the same, results in MFI. This interference can be presented mathematically with conjugate response of the signal and the noise components. Thus, image signal transfer function (ISTF) and image noise transfer function (INTF) are introduced, in addition to the traditional STF and NTF, to describe the output under I/Q imbalance. In the following, an analytic model is presented, first for individual stages of a multistage QΣΔM, and then for I/Q mismatched multistage QΣΔM, having arbitrary number of stages, as a whole. Such analysis has not been presented in the literature earlier.

The I/Q imbalance analysis for a single stage is based on the block diagram given in Figure 6. In this figure, real and imaginary parts of the coefficients of Figure 5 are marked with subscripts re and im, whereas nonideal implementation values of the signal rails are separated with subscripts 1 and 2. The independent coefficients of the stages are denoted with superscript l. Thus, to obtain the complex outputs $V_l[z] = V_{\mathrm{I},l}[z] + jV_{\mathrm{Q},l}[z]$ of the stages ($l \in \{1, L\}$), the I branch outputs can be first shown to be

$$\begin{aligned}V_{\mathrm{I},l}[z] = {} & \frac{\alpha_{\mathrm{I}}^{(l)}[z]}{\gamma_{\mathrm{I}}^{(l)}[z]}U_{\mathrm{I},l}[z] - \frac{\beta_{\mathrm{I}}^{(l)}[z]}{\gamma_{\mathrm{I}}^{(l)}[z]}U_{\mathrm{Q},l}[z]\\ & + \frac{\varepsilon_{\mathrm{I}}^{(l)}[z]}{\gamma_{\mathrm{I}}^{(l)}[z]}E_{\mathrm{I},l}[z] + \frac{\eta_{\mathrm{I}}^{(l)}[z]}{\gamma_{\mathrm{I}}^{(l)}[z]}E_{\mathrm{Q},l}[z]\\ & - \frac{\rho_{\mathrm{I}}^{(l)}[z]}{\gamma_{\mathrm{I}}^{(l)}[z]}V_{\mathrm{Q},l}[z],\end{aligned} \tag{10}$$

where the auxiliary variables multiplying the signal components are defined by the coefficients (see Figure 6) in the

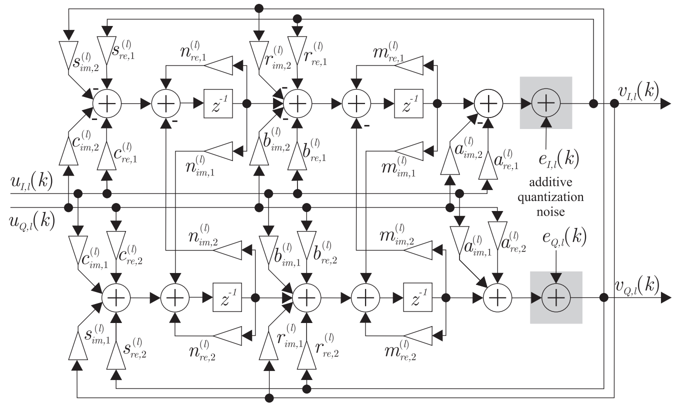

Figure 6 Implementation structure of the *l*th second-order QΣΔM stage in a multistage QΣΔM with parallel real signals and coefficients taking possible mismatches into account.

following manner:

$$\begin{aligned}\alpha_{\mathrm{I}}^{(l)}[z] = {} & a^{(l)}_{\mathrm{re},1} + [b^{(l)}_{\mathrm{re},1} - m^{(l)}_{\mathrm{re},1}a^{(l)}_{\mathrm{re},1} - n^{(l)}_{\mathrm{re},1}a^{(l)}_{\mathrm{re},1} \\ & + n^{(l)}_{\mathrm{im},2}a^{(l)}_{\mathrm{im},1} + m^{(l)}_{\mathrm{im},2}a^{(l)}_{\mathrm{im},1}]z^{-1} \\ & + [c^{(l)}_{\mathrm{re},1} - n^{(l)}_{\mathrm{re},1}b^{(l)}_{\mathrm{re},1} + n^{(l)}_{\mathrm{re},1}m^{(l)}_{\mathrm{re},1}a^{(l)}_{\mathrm{re},1} \\ & - n^{(l)}_{\mathrm{re},1}m^{(l)}_{\mathrm{im},2}a^{(l)}_{\mathrm{im},1} + n^{(l)}_{\mathrm{im},2}b^{(l)}_{\mathrm{im},1} \\ & - n^{(l)}_{\mathrm{im},2}m^{(l)}_{\mathrm{im},1}a^{(l)}_{\mathrm{re},1} - n^{(l)}_{\mathrm{im},2}m^{(l)}_{\mathrm{re},2}a^{(l)}_{\mathrm{im},1}]z^{-2},\end{aligned} \tag{11}$$

$$\begin{aligned}\beta_{\mathrm{I}}^{(l)}[z] = {} & a^{(l)}_{\mathrm{im},2} + [b^{(l)}_{\mathrm{im},2} - n^{(l)}_{\mathrm{re},1}a^{(l)}_{\mathrm{im},2} - n^{(l)}_{\mathrm{im},2}a^{(l)}_{\mathrm{re},2} \\ & - m^{(l)}_{\mathrm{re},1}a^{(l)}_{\mathrm{im},2} - m^{(l)}_{\mathrm{im},2}a^{(l)}_{\mathrm{re},2}]z^{-1} \\ & + [c^{(l)}_{\mathrm{im},2} - n^{(l)}_{\mathrm{re},1}b^{(l)}_{\mathrm{im},2} + n^{(l)}_{\mathrm{re},1}m^{(l)}_{\mathrm{re},1}a^{(l)}_{\mathrm{im},2} \\ & + n^{(l)}_{\mathrm{re},1}m^{(l)}_{\mathrm{im}2,}a^{(l)}_{\mathrm{re},2} - n^{(l)}_{\mathrm{im},2}b^{(l)}_{\mathrm{re},2} \\ & - n^{(l)}_{\mathrm{im},2}m^{(l)}_{\mathrm{im},1}a^{(l)}_{\mathrm{im},2} + n^{(l)}_{\mathrm{im},2}m^{(l)}_{\mathrm{re},2}a^{(l)}_{\mathrm{re},2}]z^{-2},\end{aligned} \tag{12}$$

$$\begin{aligned}\varepsilon_{\mathrm{I}}^{(l)}[z] = {} & 1 - [n^{(l)}_{\mathrm{re},1} + m^{(l)}_{\mathrm{re},1}]z^{-1} \\ & + [n^{(l)}_{\mathrm{re},1}m^{(l)}_{\mathrm{re},1} - n^{(l)}_{\mathrm{im},2}m^{(l)}_{\mathrm{im},1}]z^{-2},\end{aligned} \tag{13}$$

$$\begin{aligned}\eta_{\mathrm{I}}^{(l)}[z] = {} & [n^{(l)}_{\mathrm{im},2} + m^{(l)}_{\mathrm{im},2}]z^{-1} \\ & - [n^{(l)}_{\mathrm{re},1}m^{(l)}_{\mathrm{im},2} + n^{(l)}_{\mathrm{im},2}m^{(l)}_{\mathrm{re},2}]z^{-2},\end{aligned} \tag{14}$$

$$\begin{aligned}\rho_{\mathrm{I}}^{(l)}[z] = {} & [n^{(l)}_{\mathrm{im},2} + r^{(l)}_{\mathrm{im},2} + m^{(l)}_{\mathrm{im},2}]z^{-1} \\ & - [s^{(l)}_{\mathrm{im},2} - n^{(l)}_{\mathrm{re},1}r^{(l)}_{\mathrm{im},2} - n^{(l)}_{\mathrm{im},2}r^{(l)}_{\mathrm{re},2} \\ & - n^{(l)}_{\mathrm{re},1}m^{(l)}_{\mathrm{im},2} - n^{(l)}_{\mathrm{im},2}m^{(l)}_{\mathrm{re},2}]z^{-2},\end{aligned} \tag{15}$$

$$\begin{aligned}\gamma_{\mathrm{I}}^{(l)}[z] = {} & 1 - [n^{(l)}_{\mathrm{re},1} + r^{(l)}_{\mathrm{re},1} + m^{(l)}_{\mathrm{re},1}]z^{-1} \\ & + [s^{(l)}_{\mathrm{re},1} - n^{(l)}_{\mathrm{re},1}r^{(l)}_{\mathrm{re},1} + n^{(l)}_{\mathrm{im},2}r^{(l)}_{\mathrm{im},1} \\ & - n^{(l)}_{\mathrm{re},1}m^{(l)}_{\mathrm{re},1} + n^{(l)}_{\mathrm{im},2}m^{(l)}_{\mathrm{im},1}]z^{-2}.\end{aligned} \tag{16}$$

This follows directly from a step-by-step signal analysis of the implementation structure in Figure 6. Similarly, the real-valued Q branch outputs are given by

$$\begin{aligned}V_{\mathrm{Q},l}[z] = {} & \frac{\beta_{\mathrm{Q}}^{(l)}[z]}{\gamma_{\mathrm{Q}}^{(l)}[z]}U_{\mathrm{I},l}[z] + \frac{\alpha_{\mathrm{Q}}^{(l)}[z]}{\gamma_{\mathrm{Q}}^{(l)}[z]}U_{\mathrm{Q},l}[z] \\ & + \frac{\varepsilon_{\mathrm{Q}}^{(l)}[z]}{\gamma_{\mathrm{Q}}^{(l)}[z]}E_{\mathrm{Q},l}[z] - \frac{\eta_{\mathrm{Q}}^{(l)}[z]}{\gamma_{\mathrm{Q}}^{(l)}[z]}E_{\mathrm{I},l}[z] \\ & + \frac{\rho_{\mathrm{Q}}^{(l)}[z]}{\gamma_{\mathrm{Q}}^{(l)}[z]}V_{\mathrm{I},l}[z],\end{aligned} \tag{17}$$

where

$$\begin{aligned}\alpha_{\mathrm{Q}}^{(l)}[z] = {} & a^{(l)}_{\mathrm{re},2} + [b^{(l)}_{\mathrm{re},2} + n^{(l)}_{\mathrm{im},1}a^{(l)}_{\mathrm{im},2} - n^{(l)}_{\mathrm{re},2}a^{(l)}_{\mathrm{re},2} \\ & + m^{(l)}_{\mathrm{im},1}a^{(l)}_{\mathrm{im},2} - m^{(l)}_{\mathrm{re},2}a^{(l)}_{\mathrm{re},2}]z^{-1} \\ & + [c^{(l)}_{\mathrm{re},2} - n^{(l)}_{\mathrm{re},2}b^{(l)}_{\mathrm{re},2} - n^{(l)}_{\mathrm{im},1}m^{(l)}_{\mathrm{im},2}a^{(l)}_{\mathrm{re},2} \\ & + n^{(l)}_{\mathrm{im},1}b^{(l)}_{\mathrm{im},2} - n^{(l)}_{\mathrm{im},1}m^{(l)}_{\mathrm{re},1}a^{(l)}_{\mathrm{im},2} \\ & - n^{(l)}_{\mathrm{re},2}m^{(l)}_{\mathrm{im},1}a^{(l)}_{\mathrm{im},2} + n^{(l)}_{\mathrm{re},2}m^{(l)}_{\mathrm{re},2}a^{(l)}_{\mathrm{re},2}]z^{-2},\end{aligned} \tag{18}$$

$$\begin{aligned}\beta_{\mathrm{Q}}[z] = {} & a^{(l)}_{\mathrm{im},1} + [b^{(l)}_{\mathrm{im},1} - n^{(l)}_{\mathrm{im},1}a^{(l)}_{\mathrm{re},1} - n^{(l)}_{\mathrm{re},2}a^{(l)}_{\mathrm{im},1} \\ & - m^{(l)}_{\mathrm{im},1}a^{(l)}_{\mathrm{re},1} - m^{(l)}_{\mathrm{re},2}a^{(l)}_{\mathrm{im},1}]z^{-1} \\ & + [c^{(l)}_{\mathrm{im},1} - n^{(l)}_{\mathrm{re},2}b^{(l)}_{\mathrm{im},1} - n^{(l)}_{\mathrm{im},1}m^{(l)}_{\mathrm{im},2}a^{(l)}_{\mathrm{im},1} \\ & - n^{(l)}_{\mathrm{im},1}b^{(l)}_{\mathrm{re},1} + n^{(l)}_{\mathrm{im},1}m^{(l)}_{\mathrm{re},1}a^{(l)}_{\mathrm{re},1} \\ & + n^{(l)}_{\mathrm{re},2}m^{(l)}_{\mathrm{im},1}a^{(l)}_{\mathrm{re},1} + n^{(l)}_{\mathrm{re},2}m^{(l)}_{\mathrm{re},2}a^{(l)}_{\mathrm{im},1}]z^{-2},\end{aligned} \tag{19}$$

$$\begin{aligned}\varepsilon_{\mathrm{Q}}^{(l)}[z] = {} & 1 - [n^{(l)}_{\mathrm{re},2} + m^{(l)}_{\mathrm{re},2}]z^{-1} \\ & + [n^{(l)}_{\mathrm{re},2}m^{(l)}_{\mathrm{re},2} - n^{(l)}_{\mathrm{im},1}m^{(l)}_{\mathrm{im},2}]z^{-2},\end{aligned} \tag{20}$$

$$\eta_{\mathrm{Q}}^{(l)}[z] = [n_{\mathrm{im},1}^{(l)} + m_{\mathrm{im},1}^{(l)}]z^{-1} + [n_{\mathrm{im},1}^{(l)} m_{\mathrm{re},1}^{(l)} + n_{\mathrm{re},2}^{(l)} m_{\mathrm{im},1}^{(l)}]z^{-2}, \tag{21}$$

$$\begin{aligned}\rho_{\mathrm{Q}}^{(l)}[z] = {} & [n_{\mathrm{re},2}^{(l)} + r_{\mathrm{re},2}^{(l)} + m_{\mathrm{re},2}^{(l)}]z^{-1} \\ & + [s_{\mathrm{re},2}^{(l)} + n_{\mathrm{im},1}^{(l)} r_{\mathrm{im},2}^{(l)} - n_{\mathrm{re},2}^{(l)} r_{\mathrm{re},2}^{(l)} \\ & + n_{\mathrm{im},1}^{(l)} m_{\mathrm{im},2}^{(l)} - n_{\mathrm{re},2}^{(l)} m_{\mathrm{re},2}^{(l)}]z^{-2},\end{aligned} \tag{22}$$

$$\begin{aligned}\gamma_{\mathrm{Q}}^{(l)}[z] = {} & 1 - [n_{\mathrm{im},1}^{(l)} + r_{\mathrm{im},1}^{(l)} + m_{\mathrm{im},1}^{(l)}]z^{-1} \\ & + [s_{\mathrm{im},1}^{(l)} - n_{\mathrm{im},1}^{(l)} r_{\mathrm{re},1}^{(l)} - n_{\mathrm{re},2}^{(l)} r_{\mathrm{im},1}^{(l)} \\ & - n_{\mathrm{im},1}^{(l)} m_{\mathrm{re},1}^{(l)} - n_{\mathrm{re},2}^{(l)} m_{\mathrm{im},1}^{(l)}]z^{-2}.\end{aligned} \tag{23}$$

In this way, the complex-valued output and the exact behavior of each transfer function can be solved analytically in different I/Q mismatch scenarios. As a result, the complex output of an individual stage with nonideal matching of the I and Q branches becomes

$$\begin{aligned}V_l[z] &= V_{\mathrm{I},l}[z] + jV_{\mathrm{Q},l}[z] \\ &= \mathrm{STF}_l[z]U_l[z] + \mathrm{ISTF}_l[z]U_l^*[z^*] \\ &\quad + \mathrm{NTF}_l[z]E_l[z] + \mathrm{INTF}_l[z]E_l^*[z^*],\end{aligned} \tag{24}$$

where superscript asterisk (*) denotes complex conjugation, and the transfer functions are, based on (10) and (17) (omitting $[z]$ from the modulator coefficient variables of (11)-(16) and (18)-(23) for notational convenience), given by

$$\begin{aligned}\mathrm{STF}_l[z] = {} & \frac{\gamma_{\mathrm{Q}}^{(l)}\alpha_{\mathrm{I}}^{(l)} + \gamma_{\mathrm{I}}^{(l)}\alpha_{\mathrm{Q}}^{(l)} - \rho_{\mathrm{Q}}^{(l)}\beta_{\mathrm{I}}^{(l)} - \rho_{\mathrm{I}}^{(l)}\beta_{\mathrm{Q}}^{(l)}}{2(\gamma_{\mathrm{I}}^{(l)}\gamma_{\mathrm{Q}}^{(l)} + \rho_{\mathrm{I}}^{(l)}\rho_{\mathrm{Q}}^{(l)})} \\ & + j\frac{\rho_{\mathrm{I}}^{(l)}\alpha_{\mathrm{Q}}^{(l)} + \rho_{\mathrm{Q}}^{(l)}\alpha_{\mathrm{I}}^{(l)} + \gamma_{\mathrm{Q}}^{(l)}\beta_{\mathrm{I}}^{(l)} + \gamma_{\mathrm{I}}^{(l)}\beta_{\mathrm{Q}}^{(l)}}{2(\gamma_{\mathrm{I}}^{(l)}\gamma_{\mathrm{Q}}^{(l)} + \rho_{\mathrm{I}}^{(l)}\rho_{\mathrm{Q}}^{(l)})},\end{aligned} \tag{25}$$

$$\begin{aligned}\mathrm{ISTF}_l[z] = {} & \frac{\gamma_Q^{(l)}\alpha_I^{(l)} - \gamma_I^{(l)}\alpha_Q^{(l)} + \rho_Q^{(l)}\beta_I^{(l)} - \rho_I^{(l)}\beta_Q^{(l)}}{2(\gamma_I^{(l)}\gamma_Q^{(l)} + \rho_I^{(l)}\rho_Q^{(l)})} \\ & + j\frac{\rho_Q^{(l)}\alpha_I^{(l)} - \rho_I^{(l)}\alpha_Q^{(l)} + \gamma_I^{(l)}\beta_Q^{(l)} - \gamma_Q^{(l)}\beta_I^{(l)}}{2(\gamma_I^{(l)}\gamma_Q^{(l)} + \rho_I^{(l)}\rho_Q^{(l)})},\end{aligned} \tag{26}$$

$$\begin{aligned}\mathrm{NTF}_l[z] = {} & \frac{\gamma_Q^{(l)}\varepsilon_I^{(l)} + \gamma_I^{(l)}\varepsilon_Q^{(l)} + \rho_I^{(l)}\eta_Q^{(l)} + \rho_Q^{(l)}\eta_I^{(l)}}{2(\gamma_I^{(l)}\gamma_Q^{(l)} + \rho_I^{(l)}\rho_Q^{(l)})} \\ & + j\frac{\rho_I^{(l)}\varepsilon_Q^{(l)} + \rho_Q^{(l)}\varepsilon_I^{(l)} - \gamma_Q^{(l)}\eta_I^{(l)} - \gamma_I^{(l)}\eta_Q^{(l)}}{2(\gamma_I^{(l)}\gamma_Q^{(l)} + \rho_I^{(l)}\rho_Q^{(l)})},\end{aligned} \tag{27}$$

$$\begin{aligned}\mathrm{INTF}_l[z] = {} & \frac{\gamma_Q^{(l)}\varepsilon_I^{(l)} - \gamma_I^{(l)}\varepsilon_Q^{(l)} + \rho_I^{(l)}\eta_Q^{(l)} - \rho_Q^{(l)}\eta_I^{(l)}}{2(\gamma_I^{(l)}\gamma_Q^{(l)} + \rho_I^{(l)}\rho_Q^{(l)})} \\ & + j\frac{\gamma_Q^{(l)}\eta_I^{(l)} - \gamma_I^{(l)}\eta_Q^{(l)} + \rho_Q^{(l)}\varepsilon_I^{(l)} - \rho_I^{(l)}\varepsilon_Q^{(l)}}{2(\gamma_I^{(l)}\gamma_Q^{(l)} + \rho_I^{(l)}\rho_Q^{(l)})}.\end{aligned} \tag{28}$$

In Section 3.2, the above analysis for the individual stages $l \in \{1, L\}$ is combined to complete the closed-form overall model for the multistage Q$\Sigma\Delta$M.

Based on (24), the converter output consists of not only the (filtered) input signal and quantization noise but also their complex conjugates, which, in frequency domain, corresponds to spectral mirroring or imaging. Thus, based on (24), the so-called image rejection ratios (IRRs) of the lth stage are

$$\begin{aligned}\mathrm{IRR}_{\mathrm{STF}}^{(l)}[e^{j2\pi fT_{\mathrm{S}}}] \\ = 10\log_{10}\left(\left|\mathrm{STF}_l[e^{j2\pi fT_{\mathrm{S}}}]\right|^2 / \left|\mathrm{ISTF}_l[e^{j2\pi fT_{\mathrm{S}}}]\right|^2\right)\end{aligned} \tag{29}$$

and

$$\begin{aligned}\mathrm{IRR}_{\mathrm{NTF}}^{(l)}[e^{j2\pi fT_{\mathrm{S}}}] \\ = 10\log_{10}\left(\left|\mathrm{NTF}_l[e^{j2\pi fT_{\mathrm{S}}}]\right|^2 / \left|\mathrm{INTF}_l[e^{j2\pi fT_{\mathrm{S}}}]\right|^2\right),\end{aligned} \tag{30}$$

where actual frequency-domain responses are attained with the substitution $z \leftarrow e^{j2\pi fT_{\mathrm{S}}}$ to the earlier transfer functions, where f is the frequency measured in Hertz and T_{S} is the sampling time. These IRR quantities describe the relation of the direct input signal and noise energy to the respective mismatch-induced MFI at the output signal. As an example, $\mathrm{IRR}_{\mathrm{STF}}^{(1)}(e^{j2\pi f_0 T_{\mathrm{S}}}) = 20$ dB means that the power of the mismatch-induced (mirrored) conjugate input signal is 20 dB lower than the direct input signal at the frequency f_0. Similarly, $\mathrm{IRR}_{\mathrm{NTF}}^{(1)}(e^{j2\pi f_0 T_{\mathrm{S}}}) = 20$ dB indicates that the nonconjugated quantization error level is 20 dB above the mirror image of the quantization error at the frequency f_0. Notice also that, in general, both IRRs are frequency-dependent functions.

3.3 Combined I/Q imbalance effects of the stages in multistage Q$\Sigma\Delta$M

For multistage Q$\Sigma\Delta$M, as illustrated in Figure 4, the final output signal is defined as a difference of digitally filtered output signals of the stages [33]. Furthermore, like shortly discussed already, the first-stage input $U_1[z] = U[z]$ while for $l > 1$, $U_l[z] = E_{l-1}[z]$. The output of the first stage, given by (24) with $l = 1$, is filtered with digital filter $H_1^{\mathrm{D}}[z]$ (usually matched to the STF of the second stage) and the output of the second stage, similarly given by (24) with $l = 2$, is filtered with $H_2^{\mathrm{D}}[z]$ (usually matched to the NTF of the first stage), and so on for $l \in \{1, L\}$. Thus, the final output in case of I/Q mismatches in all the stages can now be expressed as

$$V[z] = \sum_{l=1}^{L} (-1)^{l+1} H_l^{\mathrm{D}}[z] V_l[z]. \tag{31}$$

Replacing $V_l[z]$ in (31) with (24) for $l \in \{1, L\}$ gives now an expression for the overall output as

$$\begin{aligned} V[z] = \sum_{l=1}^{L} (-1)^{l+1} H_l^{\mathrm{D}}[z] (&\mathrm{STF}_l[z] U_l[z] \\ &+ \mathrm{ISTF}_l[z] U_l^*[z^*] + \mathrm{NTF}_l\, E_l[z] \\ &+ \mathrm{INTF}_l E_l^*[z^*]), \end{aligned} \tag{32}$$

where the transfer functions are as defined in (25)-(28). Again, the digital filters are assumed matched to the analog transfer functions according to (6). As a concrete example, (32) can be evaluated for a three-stage ($L = 3$) Q$\Sigma\Delta$M, giving

$$\begin{aligned} V[z] = {} & H_1^{\mathrm{D}}[z] (\mathrm{STF}_1[z] U[z] + \mathrm{ISTF}_1[z] U^*[z^*] \\ & + \mathrm{NTF}_1\, E_1[z] + \mathrm{INTF}_1 E_1^*[z^*]) \\ & - H_2^{\mathrm{D}}[z] (\mathrm{STF}_2[z] E_1[z] + \mathrm{ISTF}_2[z] E_1^*[z^*] \\ & + \mathrm{NTF}_2\, E_2[z] + \mathrm{INTF}_2 E_2^*[z^*]) \\ & + H_3^{\mathrm{D}}[z] (\mathrm{STF}_3[z] E_2[z] + \mathrm{ISTF}_3[z] E_2^*[z^*] \\ & + \mathrm{NTF}_3\, E_3[z] + \mathrm{INTF}_3 E_3^*[z^*]) \\ = {} & \mathrm{STF}_2^{\mathrm{D}}\, \mathrm{STF}_1[z] U[z] \\ & + \mathrm{STF}_2^{\mathrm{D}}\, \mathrm{ISTF}_1[z] U^*[z^*] \\ & + (\mathrm{STF}_2^{\mathrm{D}}[z]\, \mathrm{NTF}_1[z] \\ & - \mathrm{NTF}_1^{\mathrm{D}}[z]\, \mathrm{STF}_2[z]) E_1[z] \\ & + (\mathrm{STF}_2^{\mathrm{D}}[z] \mathrm{INTF}_1[z] \\ & + \mathrm{NTF}_1^{\mathrm{D}}[z] \mathrm{ISTF}_2[z]) E_1^*[z^*] \\ & + \big(-\mathrm{NTF}_1^{\mathrm{D}}[z]\, \mathrm{NTF}_2[z] \\ & + (\mathrm{NTF}_1^{\mathrm{D}}[z]\, \mathrm{NTF}_2^{\mathrm{D}}[z] \\ & / \, \mathrm{STF}_3^{\mathrm{D}}[z])\, \mathrm{STF}_3[z]\big) E_2[z] \\ & + \big(-\mathrm{NTF}_1^{\mathrm{D}}[z] \mathrm{INTF}_2[z] \\ & + (\mathrm{NTF}_1^{\mathrm{D}}[z]\, \mathrm{NTF}_2^{\mathrm{D}}[z] \\ & / \, \mathrm{STF}_3^{\mathrm{D}}[z]) \mathrm{ISTF}_3[z]\big) E_2^*[z^*] \\ & + (\mathrm{NTF}_1^{\mathrm{D}}[z]\, \mathrm{NTF}_2^{\mathrm{D}}[z]\, \mathrm{NTF}_3[z] \\ & / \, \mathrm{STF}_3^{\mathrm{D}}[z]) E_3[z] \\ & + (\mathrm{NTF}_1^{\mathrm{D}}[z]\, \mathrm{NTF}_2^{\mathrm{D}}[z] \mathrm{INTF}_3[z] \\ & / \, \mathrm{STF}_3^{\mathrm{D}}[z]) E_3^*[z^*] \\ = {} & \mathrm{STF}_{\mathrm{TOT}}[z] U[z] + \mathrm{ISTF}_{\mathrm{TOT}}[z] U^*[z^*] \\ & + \mathrm{NTF}_{\mathrm{TOT},1}[z] E_1[z] + \mathrm{INTF}_{\mathrm{TOT},1}[z] E_1^*[z^*] \\ & + \mathrm{NTF}_{\mathrm{TOT},2}[z] E_2[z] + \mathrm{INTF}_{\mathrm{TOT},2}[z] E_2^*[z^*] \\ & + \mathrm{NTF}_{\mathrm{TOT},3}[z] E_3[z] + \mathrm{INTF}_{\mathrm{TOT},3}[z] E_3^*[z^*] \end{aligned} \tag{33}$$

with digital filters $H_1^{\mathrm{D}}[z] = \mathrm{STF}_2^{\mathrm{D}}[z]$, $H_2^{\mathrm{D}}[z] = \mathrm{NTF}_1^{\mathrm{D}}[z]$, and $H_3^{\mathrm{D}}[z] = \mathrm{NTF}_1^{\mathrm{D}}[z]\, \mathrm{NTF}_2^{\mathrm{D}}[z] / \mathrm{STF}_3^{\mathrm{D}}[z]$. It should be noted that $\mathrm{STF}_{\mathrm{TOT}}[z] U[z]$ and $\mathrm{NTF}_{\mathrm{TOT},3}[z] E_3[z]$ correspond structurally to the ideal output given in (7). However, the responses of $\mathrm{STF}_{\mathrm{TOT}}[z]$ and $\mathrm{NTF}_{\mathrm{TOT},3}[z]$ can be altered when compared to $\mathrm{STF}_{\mathrm{TOT}}^{\mathrm{ideal}}[z]$ and $\mathrm{NTF}_{\mathrm{TOT}}^{\mathrm{ideal}}[z]$ because of possible common-mode errors in the modulator coefficients [25]. Consequently, the six additional terms in (33) are considered as mismatch-induced interference, which includes the leakage of the first- and second-stage noises and the corresponding MFI (conjugate) components. It should also be noticed that the first-stage quantization error terms $\mathrm{STF}_2^{\mathrm{D}}[z]\, \mathrm{NTF}_1[z] E_1[z]$ and $\mathrm{NTF}_1^{\mathrm{D}}[z]\, \mathrm{STF}_2[z] E_1[z]$ do not reduce to zero because of noncommutativity of the complex transfer functions under I/Q imbalance [23]. On the other hand, second-stage quantization error vanishes if $\mathrm{NTF}_1^{\mathrm{D}}[z]\, \mathrm{NTF}_2[z]$ and $(\mathrm{NTF}_1^{\mathrm{D}}[z]\, \mathrm{NTF}_2^{\mathrm{D}}[z] / \mathrm{STF}_3^{\mathrm{D}}[z])\, \mathrm{STF}_3[z]$ are equal. This means that $\mathrm{NTF}_2^{\mathrm{D}}[z]$ and $\mathrm{STF}_3^{\mathrm{D}}[z]$ should be equal to their analog counterparts, which can realized with, e.g., adaptive digital filters [34, 35]. The matching can also be made more robust by designing the third stage to have unity signal response ($\mathrm{STF}_3[z] = 1$).

Now, based on (33), it is clear that filtered versions of the original and conjugate components of the input, the first-stage, the second-stage, and the third-stage quantization errors all contribute to the final output. In order to inspect the overall IRR of the complete multistage structure, the transfer functions of the original signals (the input and the errors) and their conjugate counterparts should be compared. Based on (33), this gives the following formulas for the three-stage case considered herein:

$$\begin{aligned} \mathrm{IRR}_{\mathrm{STF}_{\mathrm{TOT}}}[e^{j2\pi f T_{\mathrm{S}}}] = 10 \log_{10} \big(&|\mathrm{STF}_{\mathrm{TOT}}[e^{j2\pi f T_{\mathrm{S}}}]|^2 \\ & / |\mathrm{ISTF}_{\mathrm{TOT}}[e^{j2\pi f T_{\mathrm{S}}}]|^2 \big), \end{aligned} \tag{34}$$

$$\begin{aligned} &\mathrm{IRR}_{\mathrm{NTF}_{\mathrm{TOT},1}}[e^{j2\pi f T_{\mathrm{S}}}] \\ &\quad = 10 \log_{10} \big(|\mathrm{NTF}_{\mathrm{TOT},1}[e^{j2\pi f T_{\mathrm{S}}}]|^2 \\ &\qquad / |\mathrm{INTF}_{\mathrm{TOT},1}[e^{j2\pi f T_{\mathrm{S}}}]|^2 \big), \end{aligned} \tag{35}$$

$$\begin{aligned} &\mathrm{IRR}_{\mathrm{NTF}_{\mathrm{TOT},2}}[e^{j2\pi f T_{\mathrm{S}}}] \\ &\quad = 10 \log_{10} \big(|\mathrm{NTF}_{\mathrm{TOT},2}[e^{j2\pi f T_{\mathrm{S}}}]|^2 \\ &\qquad / |\mathrm{INTF}_{\mathrm{TOT},2}[e^{j2\pi f T_{\mathrm{S}}}]|^2 \big), \end{aligned} \tag{36}$$

$$\begin{aligned} &\mathrm{IRR}_{\mathrm{NTF}_{\mathrm{TOT},3}}[e^{j2\pi f T_{\mathrm{S}}}] \\ &\quad = 10 \log_{10} \big(|\mathrm{NTF}_{\mathrm{TOT},3}[e^{j2\pi f T_{\mathrm{S}}}]|^2 \\ &\qquad / |\mathrm{INTF}_{\mathrm{TOT},3}[e^{j2\pi f T_{\mathrm{S}}}]|^2 \big). \end{aligned} \tag{37}$$

In addition to the above IRRs, the performance of a non-ideal Q$\Sigma\Delta$M can be measured by the amount of total additional interference stemming from the implementation nonidealities. This can be expressed with interference rejection ratio Γ. In case of a three-stage Q$\Sigma\Delta$M, following from (33), the signal component (interference-free output) is defined as

$$\sigma(k) = \mathrm{STF}_{\mathrm{TOT}}(k) * u(k) + \mathrm{NTF}_{\mathrm{TOT},3}(k) * e_3(k), \tag{38}$$

where impulse responses of the STF and third-stage NTF are convolving the overall input and third-stage quantization error, respectively. At the same time, the total interference component (total additional interference caused by the nonidealities) is defined as

$$\begin{aligned}\tau(k) = {} & \mathrm{ISTF}_{\mathrm{TOT}}(k) * u^*(k) + \mathrm{NTF}_{\mathrm{TOT},1}(k) * e_1(k) \\ & + \mathrm{INTF}_{\mathrm{TOT},1}(k) * e_1^*(k) \\ & + \mathrm{NTF}_{\mathrm{TOT},2}(k) * e_2(k) \\ & + \mathrm{INTF}_{\mathrm{TOT},2}(k) * e_2^*(k) \\ & + \mathrm{INTF}_{\mathrm{TOT},3}(k) * e_3^*(k),\end{aligned} \tag{39}$$

where time-domain signal components are again convolved by respective transfer function impulseresponses. It should be noted that, in case of ideal three-stage Q$\Sigma\Delta$M, (39) reduces to zero. Now, interference rejection ratio at any given useful signal band is given by the integrals of spectral densities $G_\sigma(e^{j2\pi fT_S})$ and $G_\tau(e^{j2\pi fT_S})$ of the above random signals $\sigma(k)$ and $\tau(k)$, i.e.,

$$\Gamma_1 = \frac{\int_{f\in\Omega_{C,1}} G_\sigma(e^{j2\pi fT_S})\,df}{\int_{f\in\Omega_{C,1}} G_\tau(e^{j2\pi fT_S})\,df}, \tag{40}$$

where integration is done over the preferred signal band, defined as $\Omega_{C,1} = \{f_{C,1} - W_1/2, \ldots, f_{C,1} + W_1/2\}$ (where W_1 is the bandwidth of the signal). If there are two parallel signals (two-band scenario), the interference rejection ratio of the second signal is calculated in similar manner:

$$\Gamma_2 = \frac{\int_{f\in\Omega_{C,2}} G_\sigma(e^{j2\pi fT_S})\,df}{\int_{f\in\Omega_{C,2}} G_\tau(e^{j2\pi fT_S})\,df}, \tag{41}$$

where $\Omega_{C,2} = \{f_{C,2} - W_2/2, \ldots, f_{C,2} + W_2/2\}$.

An example of interference rejection ratio analysis in receiver-dimensioning context is given in Section 5. In addition, the roles of the separate signal components are further illustrated with numerical results in Section 6.

4 Q$\Sigma\Delta$M transfer function parametrization and design for CR under I/Q imbalance

In CR-type wideband receiver, signal dynamics can be tens of (even 50-60) dBs [5, 6]. With such signal composition, controlling linearity and image rejection of the receiver components is essential [5, 6, 9]. In this section, we concentrate on Q$\Sigma\Delta$M transfer function design under I/Q imbalance, having minimization of input signal oriented MFI as the goal.

4.1 Transfer function parametrization for reconfigurable CR receivers

The NTF and STF of a Q$\Sigma\Delta$M can be designed by placing transfer function zeros and poles, parameterized and tuned (allowing reconfigurability) by the Q$\Sigma\Delta$M coefficients, inside the unit circle [18]. In the following, the design process is described for a second-order Q$\Sigma\Delta$M as a single-stage converter or an individual stage l of a multistage converter. This is then extended to multistage converters in Section 4.2.

Based on the numerator of (8), the NTF zeros of the second-order Q$\Sigma\Delta$M are defined by the loop-filter feedback coefficients, i.e.,

$$\varphi_{\mathrm{NTF},1}^{(l)} = M^{(l)} = \lambda_{\mathrm{NTF},1}^{(l)} e^{j2\pi f_{\mathrm{NTF},1}^{(l)} T_S}, \tag{42}$$

$$\varphi_{\mathrm{NTF},2}^{(l)} = N^{(l)} = \lambda_{\mathrm{NTF},2}^{(l)} e^{j2\pi f_{\mathrm{NTF},2}^{(l)} T_S}, \tag{43}$$

where $\lambda_{\mathrm{NTF},1}^{(l)} = |\varphi_{\mathrm{NTF},1}^{(l)}|$ and $\lambda_{\mathrm{NTF},2}^{(l)} = |\varphi_{\mathrm{NTF},2}^{(l)}|$, being usually set to unity for the zero-placement on the unit circle, and $f_{\mathrm{NTF},1}^{(l)}$ and $f_{\mathrm{NTF},2}^{(l)}$ are the frequencies of the two NTF notches. Thus, designing these complex gains tunable allows straightforward reconfigurability for NTF notch frequencies based on the spectrum-sensing information about the preferred information signals. Common choice is to place NTF zeros on the preferred signal band or in case of multi-band reception on those bands, generating the preferred noise-shaping effect. At the same time, the poles, which are common to the NTF and the STF, are solved based on the denominator of either (8) or (9), giving

$$\begin{aligned}\psi_{\mathrm{common},1}^{(l)} = {} & \big(R^{(l)} + M^{(l)} + N^{(l)} + (R^{(l)^2} + M^{(l)^2} \\ & + N^{(l)^2} + 2R^{(l)}N^{(l)} - 2R^{(l)}M^{(l)} \\ & - 2M^{(l)}N^{(l)} + 4S^{(l)})^{1/2}\big)/2 \\ = {} & \lambda_{\mathrm{pole},1}^{(l)} e^{j2\pi f_{\mathrm{pole},1}^{(l)} T_S},\end{aligned} \tag{44}$$

$$\begin{aligned}\psi_{\mathrm{common},2}^{(l)} = {} & \big(R^{(l)} + M^{(l)} + N^{(l)} - (R^{(l)^2} + M^{(l)^2} \\ & + N^{(l)^2} + 2R^{(l)}N^{(l)} \\ & - 2R^{(l)}M^{(l)} - 2M^{(l)}N^{(l)} + 4S^{(l)})^{1/2}\big)/2 \\ = {} & \lambda_{\mathrm{pole},2}^{(l)} e^{j2\pi f_{\mathrm{pole},2}^{(l)} T_S},\end{aligned} \tag{45}$$

where $\lambda_{\mathrm{pole},1}^{(l)} = |\psi_{\mathrm{common},1}^{(l)}|$ and $\lambda_{\mathrm{pole},2}^{(l)} = |\psi_{\mathrm{common},2}^{(l)}|$, which can be used to tune the magnitude of the poles and $f_{\mathrm{pole},1}^{(l)}$

and $f^{(l)}_{\mathrm{pole},2}$, are the frequencies of the poles. The coefficients $M^{(l)}$ and $N^{(l)}$ are already fixed according to (42), leaving $R^{(l)}$ and $S^{(l)}$ free to tune the pole placement. The poles can, e.g., be placed on the frequency bands of the preferred signals to elevate the STF response and thus give gain for the preferred signals. However, the pole placement elevates also the STF response, and thus this kind of design is always a tradeoff between the noise-shaping and STF selectivity efficiencies.

On the other hand, the loop-filter coefficients ($M^{(l)}$ and $N^{(l)}$) have also their effects on the STF zeros, which, however, can be further tuned with the input coefficients ($A^{(l)}$, $B^{(l)}$, and $C^{(l)}$) of the modulator. This is illustrated in case of second-order QΣΔM, based on (9), by the expressions

$$\begin{aligned}\varphi^{(l)}_{\mathrm{STF},1} &= (1/2A^{(l)})(A^{(l)}M^{(l)} + A^{(l)}N^{(l)} - B^{(l)})\\ &\quad + (1/2A^{(l)})(B^{(l)^2} + A^{(l)^2}M^{(l)^2} + A^{(l)^2}N^{(l)^2}\\ &\quad + 2A^{(l)}B^{(l)}M^{(l)} - 2A^{(l)}B^{(l)}N^{(l)}\\ &\quad - 2A^{(l)}M^{(l)}N^{(l)} - 4A^{(l)}C^{(l)})^{1/2}\\ &= \lambda^{(l)}_{\mathrm{STF},1}e^{j2\pi f^{(l)}_{\mathrm{STF},1}T_{\mathrm{S}}},\end{aligned} \tag{46}$$

$$\begin{aligned}\varphi^{(l)}_{\mathrm{STF},2} &= (1/2A^{(l)})(A^{(l)}M^{(l)} + A^{(l)}N^{(l)} - B^{(l)})\\ &\quad - (1/2A^{(l)})(B^{(l)^2} + A^{(l)^2}M^{(l)^2} + A^{(l)^2}N^{(l)^2}\\ &\quad + 2A^{(l)}B^{(l)}M^{(l)} - 2A^{(l)}B^{(l)}N^{(l)}\\ &\quad - 2A^{(l)}M^{(l)}N^{(l)} - 4A^{(l)}C^{(l)})^{1/2}\\ &= \lambda^{(l)}_{\mathrm{STF},2}e^{j2\pi f^{(l)}_{\mathrm{STF},2}T_{\mathrm{S}}},\end{aligned} \tag{47}$$

where $\lambda^{(l)}_{\mathrm{STF},1} = |\varphi^{(l)}_{\mathrm{STF},1}|$ and $\lambda^{(l)}_{\mathrm{STF},2} = |\varphi^{(l)}_{\mathrm{STF},2}|$. Thus, (46)-(47) clearly show that $A^{(l)}$, $B^{(l)}$, and $C^{(l)}$ allow independent placement of the STF zeros. In proportion to the NTF zero analysis above, $f^{(l)}_{\mathrm{STF},1}$ and $f^{(l)}_{\mathrm{STF},2}$ are the frequencies of the two STF notches. The proposed way to design the STF includes setting $f^{(l)}_{\mathrm{STF},1}$ and $f^{(l)}_{\mathrm{STF},2}$ to be the mirror frequencies of the preferred information signals (based on the spectrum-sensing information) to attenuate possible blockers on those critical frequency bands. More generally, these frequencies, and thus the STF zero locations, can be tuned to give preferred frequency-selective response for the STF. On the other hand, if frequency-flat STF design is preferred, then the zeros can be set to the origin by setting $\lambda^{(l)}_{\mathrm{STF},1}$ and $\lambda^{(l)}_{\mathrm{STF},2}$ to zero.

Usually, the first step in the QΣΔM NTF and STF design is to obtain the placements of the zeros and the poles as already discussed above. Thereafter, the modulator coefficient values realizing those zeros and poles should be found out. In the following, this procedure is explained for a second-order QΣΔM as the lth stage of a multistage QΣΔM. Practically, the goal is to find values for the input coefficients ($A^{(l)}$, $B^{(l)}$, and $C^{(l)}$), the loop-filter coefficients ($M^{(l)}$ and $N^{(l)}$) and the feedback coefficients ($R^{(l)}$ and $S^{(l)}$) that realize the STF zeros ($\varphi^{(l)}_{\mathrm{STF},1}$ and $\varphi^{(l)}_{\mathrm{STF},2}$), the NTF zeros ($\varphi^{(l)}_{\mathrm{NTF},1}$ and $\varphi^{(l)}_{\mathrm{NTF},2}$), and the common poles ($\psi^{(l)}_{\mathrm{common},1}$ and $\psi^{(l)}_{\mathrm{common},2}$) fixed above based on the transfer function characteristics.

The numerator of the NTF, the numerator of the STF, and the denominator of both transfer functions are used to solve the coefficient values. To begin with, the loop-filter feedback coefficients $M^{(l)}$ and $N^{(l)}$, the numerator of the NTF can be expressed with the modulator coefficients of the respective stage, as in (8), or with the help of the respective zeros $\varphi^{(l)}_{\mathrm{NTF},1}$ and $\varphi^{(l)}_{\mathrm{NTF},2}$. Setting these expressions equal, i.e.,

$$\begin{aligned}&1 - (M^{(l)} + N^{(l)})z^{-1} + (M^{(l)}N^{(l)})z^{-2}\\ &\quad = 1 - (\varphi^{(l)}_{\mathrm{NTF},1} + \varphi^{(l)}_{\mathrm{NTF},2})z^{-1} + (\varphi^{(l)}_{\mathrm{NTF},1}\varphi^{(l)}_{\mathrm{NTF},2})z^{-2},\end{aligned} \tag{48}$$

allows for solving the coefficient values of the lth stage based on the zeros by setting the terms with similar delays equal. Thus,

$$M^{(l)} + N^{(l)} = \varphi^{(l)}_{\mathrm{NTF},1} + \varphi^{(l)}_{\mathrm{NTF},2}, \tag{49}$$

$$M^{(l)}N^{(l)} = \varphi^{(l)}_{\mathrm{NTF},1}\varphi^{(l)}_{\mathrm{NTF},2}, \tag{50}$$

giving

$$M^{(l)} = \varphi^{(l)}_{\mathrm{NTF},1}, \tag{51}$$

$$N^{(l)} = \varphi^{(l)}_{\mathrm{NTF},2}. \tag{52}$$

This result confirms that the NTF zeros are set by the complex-valued feedback gains of the loop integrators.

The input coefficients $A^{(l)}$, $B^{(l)}$, and $C^{(l)}$ of the lth stage can be solved in similar manner, based on the STF numerator given in (9). Next, the numerator of (9) is set equal to the STF numerator presented with the respective zeros $\varphi^{(l)}_{\mathrm{STF},1}$ and $\varphi^{(l)}_{\mathrm{STF},2}$, i.e.,

$$\begin{aligned}&A^{(l)} + (B^{(l)} - N^{(l)}A^{(l)} - M^{(l)}A^{(l)})z^{-1}\\ &\quad + (C^{(l)} - N^{(l)}B^{(l)} + M^{(l)}N^{(l)}A^{(l)})z^{-2}\\ &\qquad = 1 - (\varphi^{(l)}_{\mathrm{STF},1} + \varphi^{(l)}_{\mathrm{STF.2}})z^{-1} + (\varphi^{(l)}_{\mathrm{STF},1}\varphi^{(l)}_{\mathrm{STF},2})z^{-2}.\end{aligned} \tag{53}$$

Now, $A^{(l)}$, $B^{(l)}$, and $C^{(l)}$ can be solved setting the separate delay components equal. This gives

$$A^{(l)} = 1, \tag{54}$$

$$B^{(l)} = N^{(l)}A^{(l)} + M^{(l)}A^{(l)} - (\varphi^{(l)}_{\mathrm{STF},1} + \varphi^{(l)}_{\mathrm{STF},2}), \tag{55}$$

$$C^{(l)} = N^{(l)}B^{(l)} - M^{(l)}N^{(l)}A^{(l)} + \varphi^{(l)}_{\mathrm{STF},1}\varphi^{(l)}_{\mathrm{STF},2}, \tag{56}$$

pronouncing that these coefficient can be used to tune the STF response. However, the NTF zeros should also be taken indirectly into account because they define the values of $M^{(l)}$ and $N^{(l)}$, as found out in (51)-(52).

At this point, only the feedback coefficients $R^{(l)}$ and $S^{(l)}$ of the lth stage remain unknown. Those can be solved using the common denominator of the NTF and the STF in (8) and (9). Again, the denominator of (8) and (9) is set equal to the denominator presented with the common poles of the transfer functions $\psi^{(l)}_{\text{common},1}$ and $\psi^{(l)}_{\text{common},2}$. In other words,

$$\begin{aligned} 1 - (M^{(l)} + N^{(l)} + R^{(l)})z^{-1} \\ +(M^{(l)}N^{(l)} + N^{(l)}R^{(l)} - S^{(l)})z^{-2} \\ = 1 - (\psi^{(l)}_{\text{common},1} + \psi^{(l)}_{\text{common},2})z^{-1} \\ + (\psi^{(l)}_{\text{common},1}\psi^{(l)}_{\text{common},2})z^{-2}. \end{aligned} \tag{57}$$

Again, setting the separate delay components equal gives solutions for the feedback coefficients:

$$R^{(l)} = -M^{(l)} - N^{(l)} + \psi^{(l)}_{\text{common},1} + \psi^{(l)}_{\text{common},2}, \tag{58}$$

$$S^{(l)} = M^{(l)}N^{(l)} + N^{(l)}R^{(l)} - \psi^{(l)}_{\text{common},1}\psi^{(l)}_{\text{common},2}. \tag{59}$$

Thus, the feedback gains are affected by the NTF zeros (again via $M^{(l)}$ and $N^{(l)}$) but finally defined by the poles of both the transfer functions.

Based on this parametrization, tuning the modulator response in frequency agile way is straightforward. The spectrum-sensing information is used to extract the information about the frequency bands preferred to be received, and NTF zeros are placed on these frequencies ($f^{(l)}_{\text{NTF},1}$ and $f^{(l)}_{\text{NTF},2}$ in second-order case) with unity magnitude ($\lambda^{(l)}_{\text{NTF},1} = 1$ and $\lambda^{(l)}_{\text{NTF},2} = 1$ in second-order case). In addition, the most harmful blockers can be identified based on the spectrum sensing. Thus, the STF zeros can be set on the unit circle ($\lambda^{(l)}_{\text{STF},1} = 1$ and $\lambda^{(l)}_{\text{STF},2} = 1$ in second-order case) on the frequencies of those blocker signals ($f^{(l)}_{\text{STF},1}$ and $f^{(l)}_{\text{STF},2}$ in second-order case). The poles can be used to tune both the transfer functions, being common though. Usually, the frequencies that are attenuated in the NTF design are supposed not to be attenuated in the STF and vice versa. This sets an optimization problem for the pole placement. Pole placement in the origin is of course a neutral choice. The authors have chosen poles on the preferred signal center frequencies, i.e., $f^{(l)}_{\text{pole},1} = f^{(l)}_{\text{NTF},1}$ and $f^{(l)}_{\text{pole},2} = f^{(l)}_{\text{NTF},2}$, to highlight STF selectivity with gain on the preferred signal bands. The magnitudes of the poles are chosen to be $\lambda^{(l)}_{\text{pole},1} = 0.5$ and $\lambda^{(l)}_{\text{pole},2} = 0.5$, thus pulling the poles half way off the unit circle to maintain efficient quantization noise shaping. A summary table of the overall design flow will be presented, after discussing the design aspects under I/Q imbalance, at the end of the following subchapter.

4.2 Multistage QΣΔM transfer function design under I/Q imbalance

In QΣΔMs, the modulator feedback branch mismatches have been considered most crucial [23, 26, 28]. Exactly this problem can be fought against with mirror-frequency-rejecting STF design in a single-stage QΣΔM [19] or in the first stage of multistage QΣΔM [21]. The signal fed to the feedback branch of the modulator is the same as in the output, so the STF and NTF effects are seen therein in full extent. Considering this together with potential blocking signal energy on the mirror band, mirror-frequency-rejecting STF design is a recommended choice for feedback branch-mismatched QΣΔMs based on the analysis in [19, 21].

The main difference in this design compared to the one proposed in [18] is deeper notching of the mirror-band(s) to attenuate possible input blocker(s) as effectively as possible. This is attained by setting the STF zeros on the unit-circle at the mirror-frequencies of the preferred information signals, meaning in second-order case that $\varphi^{(1)}_{\text{STF},1} = \lambda^{(1)}_{\text{STF},1}e^{j2\pi f^{(1)}_{\text{STF},1}T_S} = e^{-j2\pi f^{(1)}_{\text{NTF},1}T_S}$ and $\varphi^{(1)}_{\text{STF},2} = \lambda^{(1)}_{\text{STF},2}e^{j2\pi f^{(1)}_{\text{STF},2}T_S} = e^{-j2\pi f^{(1)}_{\text{NTF},2}T_S}$, while the NTF zeros are located on the unit-circle ($\lambda^{(1)}_{\text{NTF},1} = 1$ and $\lambda^{(1)}_{\text{NTF},1} = 1$) at $\varphi^{(1)}_{\text{NTF},1} = e^{j2\pi f^{(1)}_{\text{NTF},1}T_S}$ and $\varphi^{(1)}_{\text{NTF},2} = e^{j2\pi f^{(1)}_{\text{NTF},2}T_S}$. The poles are placed on the preferred signal center frequencies, as described above, to elevate the STF response, i.e., $\psi^{(1)}_{\text{common},1} = 0.5e^{j2\pi f^{(1)}_{\text{NTF},1}T_S}$ and $\psi^{(1)}_{\text{common},2} = 0.5e^{j2\pi f^{(1)}_{\text{NTF},2}T_S}$ (with $\lambda^{(1)}_{\text{pole},1} = 0.5$ and $\lambda^{(1)}_{\text{pole},2} = 0.5$).

In multistage QΣΔMs, the latter stages process only the quantization error of the preceding stage, and thus the STFs of these stages do not contribute to the overall input–output STF. This can be seen also in (7), where the overall STF is a product of the first-stage STF and the following digital $H^{\text{D}}_1[z]$ filter matched to the STF of the second stage. From the signal-component point of view, the role of the first stage is emphasized because of the possible blockers in the input. The input of the latter stage(s) is the error of the previous stage and thus likely having less power variations along frequency axis. Albeit the overall STF is a product of the first two stage STFs, only the first-stage STF can offer robustness against input signal originating MFI stemming from the mismatches in the feedback branch of the first stage. Thus, design of the first-stage STF should be considered carefully in the presence of I/Q mismatches. With second-order first stage, it is possible to place two zeros in the related (first-stage) STF and thus the design is constrained to rejection of two frequency bands from the MFI mitigation point of view. At the same time, the overall noise-shaping order is of the combined order of all the L stages. Thus, the order of the first stage is limiting the capabilities to implement the mirror-frequency-rejecting STF design, e.g., in multi-band reception. The benefits of mirror-frequency-rejecting STF design will be demonstrated graphically and numerically in Section 6 using the earlier closed-form response analysis results and computer simulations.

Considering the NTF design of the stages under I/Q imbalance (a three-stage Q$\Sigma\Delta$M used as an example), the role of the digital second-stage filter $H_2^{\mathrm{D}}[z] = \mathrm{NTF}_1^{\mathrm{D}}[z]$ is emphasized. In ideal case, the overall noise present at the output should be the noise of the last stage shaped by the product of all the stage NTFs. Thus, notching of each of the preferred signal frequency bands could be done in any of the stages having similar overall effect. However, under I/Q imbalance, quantization errors of the stages have also image response components, e.g., $\mathrm{NTF}_1^{\mathrm{D}}[z]\mathrm{ISTF}_2[z]$ for $E_1^*[z]$ and $-\mathrm{NTF}_1^{\mathrm{D}}[z]\mathrm{INTF}_2[z]$ for $E_2^*[z]$ (see (33)). Naturally, these terms are preferred to be minimized on all the interesting frequency bands. Thus, it is proposed to place the NTF zeros of the first stage at the center frequencies of the preferred information signals, i.e., $\varphi_{\mathrm{NTF},1}^{(1)} = e^{j2\pi f_{\mathrm{C},1}T_{\mathrm{S}}}$ and $\varphi_{\mathrm{NTF},2}^{(1)} = e^{j2\pi f_{\mathrm{C},2}T_{\mathrm{S}}}$, where $f_{\mathrm{C},1}$ and $f_{\mathrm{C},2}$ are the center frequencies of the two signals to be received. With the latter stage(s), the noise notches can widened by placing the respective NTF zeros around the ones of the first-stage NTF. This means that, e.g., in three-stage scenarios, the second-stage zeros are $\varphi_{\mathrm{NTF},1}^{(2)} = e^{j2\pi(f_{\mathrm{C},1}\pm f_{\mathrm{offset},1})T_{\mathrm{S}}}$ and $\varphi_{\mathrm{NTF},2}^{(2)} = e^{j2\pi(f_{\mathrm{C},2}\pm f_{\mathrm{offset},2})T_{\mathrm{S}}}$ and for the third stage $\varphi_{\mathrm{NTF},1}^{(3)} = e^{j2\pi(f_{\mathrm{C},1}\mp f_{\mathrm{offset},1})T_{\mathrm{S}}}$ and $\varphi_{\mathrm{NTF},2}^{(3)} = e^{j2\pi(f_{\mathrm{C},2}\mp f_{\mathrm{offset},2})T_{\mathrm{S}}}$, where $f_{\mathrm{offset},1} = \sqrt{3/20}W_1$ and $f_{\mathrm{offset},2} = \sqrt{3/20}W_2$ (W_1 and W_2 being the respective signal bandwidths) for optimal zero placements [36]. The signs in the exponent terms are opposite for the second- and the third-stage zeros. The ideal model would allow also for such NTF design that the noise shaping of the interesting frequency bands would be done separately in different stages, meaning, e.g., that the first-stage NTF would notch the frequencies of certain signal and the second-stage NTF the frequencies of the other one. However, this kind of approach would allow the underlying I/Q imbalance-induced image components to leak more heavily on the latter signal band. The above-mentioned NTF design is proposed to avoid this scenario. This overall design flow, starting with spectrum-sensing information in terms of preferred signal center frequencies and blocker center frequencies, is illustrated as a whole in Table 1.

5 Receiver system level considerations

In this section, system level parameters are considered to define realistic target values for the needed interference rejection ratio introduced in Section 3. The proposed Q$\Sigma\Delta$M performance is illustrated in a realistic multi-band

Table 1 Overall design flow of a three-stage two-band Q$\Sigma\Delta$M.

Preliminary spectrum information

1. Obtain the center frequencies ($f_{\mathrm{C},1}$ and $f_{\mathrm{C},2}$) and the suitable frequency offsets ($f_{\mathrm{offset},1}$ and $f_{\mathrm{offset},2}$) based on the bandwidths of the desired signals, e.g., from [36]
2. Based on the spectrum sensing information, find the most harmful blockers ($f_{\mathrm{int},1}$ and $f_{\mathrm{int},2}$)
   - In case of mirror-frequency rejecting STF design $f_{\mathrm{int},1} = -f_{\mathrm{C},1}$ and $f_{\mathrm{int},2} = -f_{\mathrm{C},2}$

Design of a three-stage two-band Q$\Sigma\Delta$M with mirror-frequency rejecting first-stage STF

Transfer function design for the first-stage (two-band NTF and mirror-frequency rejecting STF)

1. Place the NTF zeros: $\varphi_{\mathrm{NTF},1}^{(1)} = e^{j2\pi f_{\mathrm{C},1}T_{\mathrm{S}}}$, $\varphi_{\mathrm{NTF},2}^{(1)} = e^{j2\pi f_{\mathrm{C},2}T_{\mathrm{S}}}$
2. Place the STF zeros: $\varphi_{\mathrm{STF},1}^{(1)} = e^{j2\pi f_{\mathrm{int},1}T_{\mathrm{S}}}$, $\varphi_{\mathrm{NTF},2}^{(1)} = e^{j2\pi f_{\mathrm{int},2}T_{\mathrm{S}}}$
3. Place the common poles: $\psi_{\mathrm{common},1}^{(1)} = 0.5e^{j2\pi f_{\mathrm{C},1}T_{\mathrm{S}}}$ and $\psi_{\mathrm{common},2}^{(1)} = 0.5e^{j2\pi f_{\mathrm{C},2}T_{\mathrm{S}}}$
4. Solve the modulator coefficients $M^{(1)}$ and $N^{(1)}$ using (51)-(52); $A^{(1)}$, $B^{(1)}$ and $C^{(1)}$ using (54)-(56); and $R^{(1)}$ and $S^{(1)}$ using (58)-(59).

Transfer function design for the second-stage (two-band NTF and frequency-flat STF)

5. Place the NTF zeros: $\varphi_{\mathrm{NTF},1}^{(2)} = e^{j2\pi(f_{\mathrm{C},1}+f_{\mathrm{offset},1})T_{\mathrm{S}}}$, $\varphi_{\mathrm{NTF},2}^{(2)} = e^{j2\pi(f_{\mathrm{C},2}+f_{\mathrm{offset},2})T_{\mathrm{S}}}$
6. Place the STF zeros: $\varphi_{\mathrm{STF},1}^{(2)} = 0$, $\varphi_{\mathrm{NTF},2}^{(2)} = 0$
7. Place the common poles: $\psi_{\mathrm{common},1}^{(2)} = 0$ and $\psi_{\mathrm{common},2}^{(2)} = 0$
8. Solve the modulator coefficients $M^{(2)}$ and $N^{(2)}$ using (51)-(52); $A^{(2)}$, $B^{(2)}$ and $C^{(2)}$ using (54)-(56); and $R^{(2)}$ and $S^{(2)}$ using (58)-(59).

Transfer function design for the third-stage (two-band NTF and frequency-flat STF)

9. Place the NTF zeros: $\varphi_{\mathrm{NTF},1}^{(3)} = e^{j2\pi(f_{\mathrm{C},1}-f_{\mathrm{offset},1})T_{\mathrm{S}}}$, $\varphi_{\mathrm{NTF},1}^{(3)} = e^{j2\pi(f_{\mathrm{C},2}-f_{\mathrm{offset},2})T_{\mathrm{S}}}$
10. Place the STF zeros: $\varphi_{\mathrm{STF},1}^{(3)} = 0$, $\varphi_{\mathrm{NTF},2}^{(3)} = 0$
11. Place the common poles: $\psi_{\mathrm{common},1}^{(3)} = 0$ and $\psi_{\mathrm{common},2}^{(3)} = 0$
12. Solve the modulator coefficients $M^{(3)}$ and $N^{(3)}$ using (51)-(52); $A^{(3)}$, $B^{(3)}$ and $C^{(3)}$ using (54)-(56); and $R^{(3)}$ and $S^{(3)}$ using (58)-(59).

reception scheme, assuming the sampling frequency f_S = 128 MHz.

The detection of a 16-QAM waveform on intermediate frequency $f_{C,16\text{-QAM}} = 36.74$ MHz with bandwidth of $W_{16\text{-QAM}} = 10$ MHz is considered as a practical example. The received preferred signal power is assumed to be −84 dBm (sensitivity level), remaining 20 dB above the thermal noise floor at −104 dBm. Taking typical receiver overall noise figure of 7 dB into account, this gives signal-to-noise ratio (SNR) of 13 dB at the input of the ADC ($\text{SNR}_{\text{PRE}} = 13$ dB). Thus, with digital signal-to-interference and noise ratio (SINR) target of say 10 dB ($\text{SINR}_{\text{target}} = 10$ dB) for detection, implementation margin of 3 dB is allowed.

Different combinations of QΣΔM parameters are considered to highlight the flexibility of the structure, namely first-, third-, and sixth-order, noise shaping ($P_{16\text{-QAM}} = \{1, 3, 6\}$) is applied for the preferred signal band in 1- and 3-bit quantization schemes ($b_Q = \{1, 3\}$). The noise-shaping order $P_{16\text{-QAM}}$ describes the combined noise-shaping effects of all the QΣΔM stages on that frequency band according to the discussion in Sections 2 and 4, assuming an ideal QΣΔM. The related zero-optimization gains for each noise-shaping order ($\text{ZOG}_{\text{dB}} = \{0, 8, 23\}$) are obtained from [36] and represent the SNR gain of the optimal zero placements compared to the case where all the zeros are on the center frequency of the preferred signal.

The Crest factors in the range of 4 to 6 dB were found in simulations with realistic power levels for a number of out-of-band signals in addition to the preferred one, depending on the exact power distribution (the simulation setup will be further discussed in Section 6). Thus, Crest factor of $\text{CF}_{\text{dB}} = 5$ dB is assumed in the following analysis for the sake of simplicity. The full-band signal power to the preferred signal power ratio is assumed to range from 0 dB (only the preferred signal) up to +140 dB. Such a high maximum value is chosen to illustrate also the performance of the sixth-order efficient noise shaping. The properties defined above are summarized in Table 2.

Based on the given parameters, signal-to-quantization noise ratio (SQNR) of the QΣΔM, yet without implementation nonidealities, can be solved in different scenarios by varying the amount of quantization bits and noise-shaping order. The SQNR equations derived for real lowpass modulators [13] of corresponding order can be adopted to use also in quadrature bandpass case because the noise-shaping efficiency is maintained with only asymmetric shift of the NTF notch center frequency. Thus, the inband SQNR for a single-frequency channel (assuming an ideal QΣΔM), taking also receiver out-of-band signal content into account, is defined as

$$\begin{aligned}\text{SQNR} = {} & 6.02b_Q + 4.76 - \text{CF}_{\text{dB}} \\ & - 10\log_{10}\left(\frac{\pi^{2P_{16\text{-QAM}}}}{2P_{16\text{-QAM}}+1}\right) \\ & + (20P_{16\text{-QAM}}+10)\log_{10}\left(\frac{f_S}{W_{16\text{-QAM}}}\right) \\ & + \text{ZOG}_{\text{dB}} - 10\log_{10}\left(\frac{S_{\text{full-band}}}{S_{16\text{-QAM}}}\right),\end{aligned} \tag{60}$$

where, in addition to the values given in Table 2, $S_{\text{full-band}}$ is the power of the whole ADC input signal, and $S_{16\text{-QAM}}$ is the power of the preferred 16-QAM waveform. Increasing full-band signal power compared to the preferred signal power decreases the SQNR because with large values of this ratio, the out-of-band signal content dominates the dynamics of the overall signal. In this kind of scenario, the weak preferred signal is effectively scaled down at the ADC input. Now, the total SNR after the A/D conversion (SNR_{TOT}) is the ratio of signal power $S_{16\text{-QAM}}$ to the combined inband thermal noise power N_{PRE} and inband quantization noise power N_Q ($N_{\text{TOT}} = N_{\text{PRE}} + N_Q$). Furthermore, this ratio can be defined with SNR_{PRE} and SQNR, giving

$$\begin{aligned}\text{SNR}_{\text{TOT}} &= 10\log_{10}\left(\frac{S_{16\text{-QAM}}}{N_{\text{TOT}}}\right) \\ &= 10\log_{10}\left(\frac{S_{16\text{-QAM}}}{N_{\text{PRE}}+N_Q}\right) \\ &= 10\log_{10}\left(\frac{1}{10^{-\text{SNR}_{\text{PRE}}/10}+10^{-\text{SQNR}/10}}\right).\end{aligned} \tag{61}$$

In addition, $\text{SINR}_{\text{target}}$ set for the detection defines also the maximum level of additional inband interference com-

Table 2 A summary of receiver system level and A/D interface properties used in the interference rejection example.

System properties	Value	A/D interface properties	Value
Desired signal waveform	16-QAM	Sampling frequency f_S	128 MHz
Intermediate frequency $f_{C,16\text{-QAM}}$	36.74 MHz	Quantization bits b_Q	$\{1, 3\}$
Desired signal bandwidth $W_{16\text{-QAM}}$	10 MHz	Noise-shaping order $P_{16\text{-QAM}}$	$\{1, 3, 6\}$
Received preferred signal power	−84 dBm	Zero-optimization gain ZOG_{dB}	$\{0, 8, 23\}$ dB
Thermal noise $kTW_{16\text{-QAM}}$	−104 dBm	SNR_{PRE} at the ADC input	13 dB
Receiver overall noise figure	7 dB	Full-band Crest-factor CF_{dB}	5 dB (4…6 dB)
Implementation margin	3 dB	Full-band signal power relative to the desired signal power	0 to 140 dB
$\text{SINR}_{\text{target}}$ for detection	10 dB		

ponents other than thermal and quantization noises, such as MFI and noise leakage, generated by the $\Sigma\Delta$ modulator nonidealities, discussed in Section 3. In that section, interference rejection ratio Γ was defined to measure the amount of this interference relative to the ideal modulator output inband power. Now, the maximum tolerable amount of additional inband interference I_{MAX}, compared to the preferred signal, the inband thermal noise and the inband quantization noise powers ($S_{16\text{-QAM}} + N_{\mathrm{TOT}}$), defines the needed interference rejection ratio demanded to fulfill the set $\mathrm{SINR}_{\mathrm{target}}$. Thus, interference rejection ratio is given by

$$\begin{aligned}\Gamma_{\mathrm{demand}} &= 10\log_{10}\left(\frac{S_{16\text{-QAM}} + N_{\mathrm{TOT}}}{I_{\mathrm{MAX}}}\right)\\ &= 10\log_{10}\left(\frac{1+10^{-\mathrm{SNR}_{\mathrm{TOT}}/10}}{10^{-\mathrm{SINR}_{\mathrm{target}}/10} - 10^{-\mathrm{SNR}_{\mathrm{TOT}}/10}}\right),\\ &\mathrm{SNR}_{\mathrm{TOT}} > \mathrm{SINR}_{\mathrm{target}}.\end{aligned} \quad (62)$$

If $\mathrm{SNR}_{\mathrm{TOT}}$ is below $\mathrm{SINR}_{\mathrm{target}}$, achieving the set SINR is obviously not possible and a logarithm of a negative number results in a complex-valued Γ_{demand} (hence the condition $\mathrm{SNR}_{\mathrm{TOT}} > \mathrm{SINR}_{\mathrm{target}}$).

This interference rejection demand is plotted in Figure 7 as a function of the full-band signal power compared to the preferred inband signal power. The increasing power ratio on the x-axis limits the performance of the ADC because of the decreasing SQNR according to (60). Subsequently, from (62) it is clear that, if $\mathrm{SNR}_{\mathrm{TOT}}$ approaches $\mathrm{SINR}_{\mathrm{target}}$, then the denominator goes to zero and thus Γ_{demand} goes to infinity, indicating that no additional interference is allowed. The flooring at approximately 13 dB happens because, this is, together with the thermal noise SNR of 13 dB, the minimum level of interference rejection ratio with any SQNR to achieve the SINR target of 10 dB. The six Q$\Sigma\Delta$M scenarios with 1- or 3-bit quantization and differing noise-shaping orders on the preferred signal band defined above are illustrated in Figure 7 as examples. The most straightforward case for multi-band reception of parallel signals with the bandwidths in megahertz-range is third-order noise shaping with 1- or 3-bit quantization, allowing two signal bands to be converted efficiently. These results are plotted with dashed lines and show tolerance of the full-band power to signal power ratios up to the range of 50 to 70 dB, depending on the quantization scheme. The first- and sixth-order noise shapings are applicable for the conversion of narrow- and wideband signals, respectively. However, the results given in Figure 7 are applicable only with given exemplary set of parameters (see Table 2), such as 10-MHz bandwidth. The derived interference rejection ratio demands are compared to the simulated achievable figures of the proposed Q$\Sigma\Delta$M design in Section 6.

6 Results and illustrations

In this section, the models derived in Section 3 and the design principles in Section 4 are used to analytically calculate and illustrate the transfer functions for a three-stage Q$\Sigma\Delta$M under I/Q imbalance (Section 6.1). Finally, the Q$\Sigma\Delta$M behavior under I/Q imbalance is simulated to illustrate the interference rejection performance of the modulator (Section 6.2) for which the target values were derived in Section 5.

In general, multi-band IF reception [19] of two parallel information signals around center frequencies of

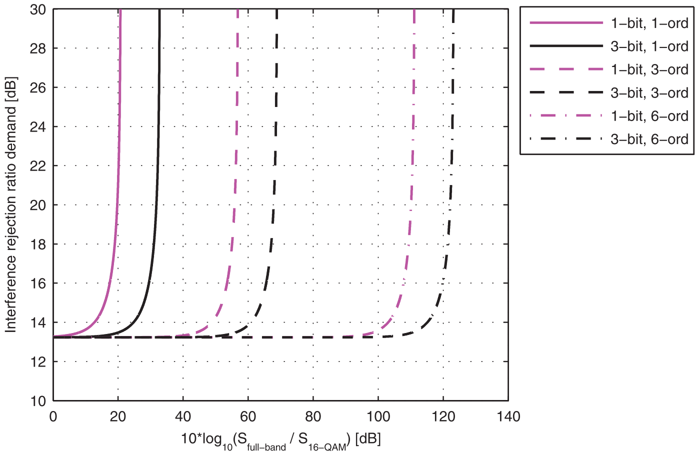

Figure 7 Demanded interference rejection ratio with different Q$\Sigma\Delta$M setups as a function full-band signal power relative to the preferred signal power. $\mathrm{SNR}_{\mathrm{PRE}}$ at the ADC input and $\mathrm{SINR}_{\mathrm{target}}$ for detection are assumed 13 and 10 dB, respectively, giving implementation margin of 3 dB.

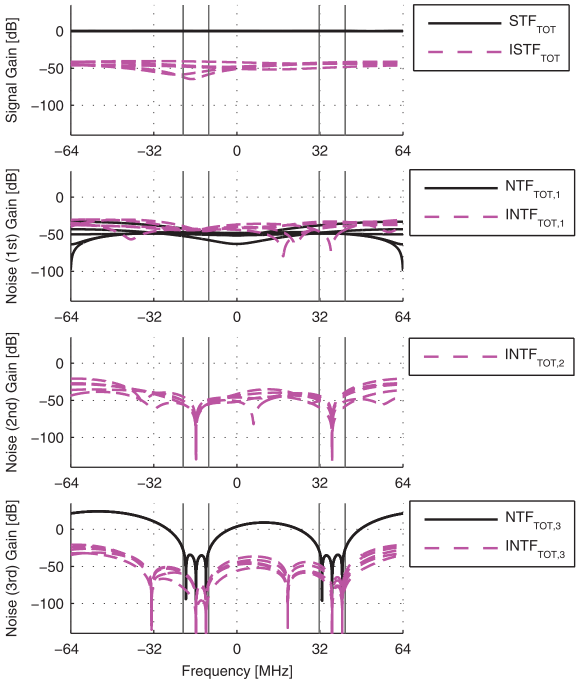

Figure 8 Three-stage QΣΔM STF and ISTF (*top*) together with NTF and INTF for first-, second-, and third-stage quantization noises. Five independent random realizations in real gain values of feedback branches of both stages and *flat STF design in all the stages*. Multi-band reception of two information signals with center frequencies of 36.74 and −15.74 MHz is assumed. These bands are marked with *gray solid lines* in the plots.

$f_{C,1} = 36.74$ MHz and $f_{C,2} = -15.74$ MHz is assumed with sampling frequency of $f_S = 128$ MHz (giving $T_S = 1/f_S = 7.8125$ ns). These bands, with bandwidth of $W_1 = W_2 = 10$ MHz, are marked in Figures 8 and 9 with vertical gray lines. The frequency offsets from the center frequencies for the outermost NTF zeros are $f_{\text{offset},1} = f_{\text{offset},2} = \sqrt{3/20} * 10$ MHz $= 3.87$ MHz, setting those zeros close to the interesting band edges.

The transfer functions of the stages are designed in the following manner, based on the above-described scenario and the discussion on design flow in Section 4. Third-order noise shaping is designed for both the signal bands, allowed by the overall NTF order of six. The first-stage NTF has unit-circle zeros on the center frequencies of the two signals, thus $\varphi^{(1)}_{\text{NTF},1} = e^{j2\pi f_{C,1}T_S} = e^{j2\pi 0.287}$ and $\varphi^{(1)}_{\text{NTF},2} = e^{j2\pi f_{C,2}T_S} = e^{-j2\pi 0.123}$. The second-stage zeros, $\varphi^{(2)}_{\text{NTF},1} = e^{j2\pi(f_{C,1}+f_{\text{offset},1})T_S} = e^{j2\pi 0.317}$ and $\varphi^{(2)}_{\text{NTF},2} = e^{j2\pi(f_{C,2}+f_{\text{offset},2})T_S} = e^{-j2\pi 0.093}$, are used to widen the noise-shaping notches toward higher frequencies. The lower frequencies of the interesting bands are notched by the third-stage NTF zeros $\varphi^{(3)}_{\text{NTF},1} = e^{j2\pi(f_{C,1}-f_{\text{offset},1})T_S} = e^{j2\pi 0.257}$ and $\varphi^{(3)}_{\text{NTF},2} = e^{j2\pi(f_{C,2}-f_{\text{offset},2})T_S} = e^{-j2\pi 0.153}$. With frequency-flat STF designs, the STF zeros and the common poles are placed in the origin. In the mirror-frequency-rejecting STF design considered for the first stage, the zeros of the first-stage STF are placed on respective mirror frequencies, giving $\varphi^{(1)}_{\text{STF},1} = e^{-j2\pi 0.287}$ and $\varphi^{(1)}_{\text{STF},2} = e^{j2\pi 0.123}$. At the same time, the common poles of the first-stage transfer functions are placed on the signal center frequencies, i.e., $\psi^{(1)}_{\text{common},1} = 0.5e^{j2\pi 0.287}$ and $\psi^{(1)}_{\text{common},2} = 0.5e^{-j2\pi 0.123}$, to highlight the STF selectivity and to maintain efficient noise shaping. Based on this design, the modulator coefficients are solved separately for each second-order stage as discussed above (see (48)-(59)). The digital filters $H_1^D[z], H_2^D[z]$, and $H_3^D[z]$ are assumed to be matched perfectly to the analog transfer functions as described above.

6.1 Transfer function analysis

The transfer functions are evaluated and analyzed with randomly deviated real gain values (on I and Q rails) to model implementation inaccuracies. The deviation values are drawn from uniform distribution with maximum of ±1% relative to the ideal value. Thus, for example, one

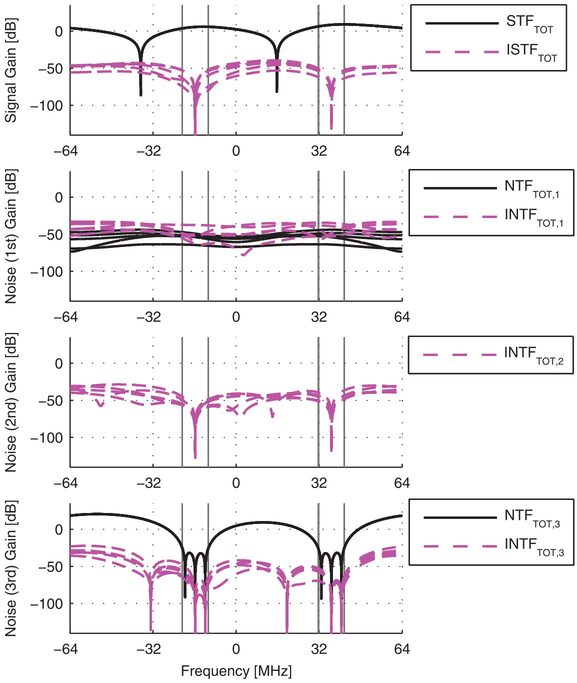

Figure 9 Three-stage QΣΔM STF and ISTF (*top*) together with NTF and INTF for first-, second-, and third-stage quantization noises. Five independent random realizations in real gain values of feedback branches of both stages and *mirror-frequency-rejecting STF design in first stage.* Multi-band reception of two information signals with center frequencies of 36.74 and −15.74 MHz is assumed. These bands are marked with *gray solid lines* in the plots.

realization of the real part of the mismatched first-stage modulator feedback gain becomes $r_{\text{re},1}^{(1)} = (1 + \Delta_{r_{\text{re},1}^{(1)}})r_{\text{re}}^{(1)}$, where $r_{\text{re},1}^{(1)}$ is the implementation value and $r_{\text{re}}^{(1)}$ the ideal value. First, the transfer functions are analyzed and illustrated in a case of second-order three-stage QΣΔM with flat STF design in all the stages. The effects of I/Q imbalance are demonstrated by introducing mismatch to the feedback branches (coefficients $R^{(l)}$ and $S^{(l)}$ in Figure 5) of the stages. Five independent realizations of each transfer function, calculated with described mismatches, are plotted to demonstrate effects of inaccuracies on modulator response. The resulting transfer functions are shown in Figure 8. The overall ISTF response averages at −50 dB level, varying between −40 and −60 dB over the frequency. While the overall STF has 0 dB response, this results in averagely 50 dB image rejection for the input signal. The three latter plots in Figure 8 present the responses for the first-, second-, and third-stage quantization errors, respectively. The noise responses show that third-stage error is well shaped showing all six notches of the stages. Also the third-stage conjugate-noise (MFI stemming from the quantization error) is well attenuated, e.g., due to the digital filter $H_3^{\text{D}}[z] = \text{NTF}_1^{\text{D}}[z]\,\text{NTF}_2^{\text{D}}[z]/\,\text{STF}_3^{\text{D}}[z]$, which gives nice attenuation on the interesting frequency bands. First-stage error is leaking to the output due to noncommutativity of mismatched complex transfer functions. However, attenuation on the preferred signal bands is still on average at the level of −50 dB for the first-stage quantization error and −40 dB for the conjugate component. However, when discussing noise responses, it should be remembered that large power variations as in the input blocker scenario are improbable. The second-stage nonconjugate noise is effectively canceled, but the conjugate version is visible at the output. This second-stage mirror-noise is, however, shaped by the NTF of the first stage, as mentioned in Section 4, and thus nicely attenuated on the preferred signal bands.

Finally, in Figure 9, it is shown that *mirror-frequency-rejecting STF design*, proposed and discussed in Sections 3 and 4, can effectively improve input image rejection in case of *feedback branch mismatches* also in a multi-stage modulator realizing multi-band conversion. This was shown in

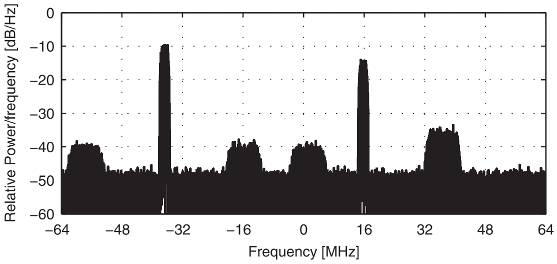

Figure 10 An example power spectral density of input signal used in the simulations. The preferred information signals are located around center frequencies of 36.74 and −15.74 MHz with 16-QAM and QPSK waveforms, respectively. Two strongest signals are located on the mirror frequencies of the preferred signals.

[19] and [30] for single-stage $Q\Sigma\Delta$Ms and in [21] preliminarily for a two-stage modulator. Now, the closed-form analysis having arbitrary number of stages clearly confirms this. Specifically, in the three-stage example at hand, 20 dB average improvements in image rejection are seen over the information bands (−70 dB average ISTF response) compared to the frequency-flat STF. From Figure 9, it is seen that the ISTF notch is fairly narrow compared to the assumed bandwidth of the signal, stemming from the use of second-order $Q\Sigma\Delta$M block which limits the number of the first-stage notches to two. However, MFI mitigation efficiency is more dependent on the bandwidth and power level of the blocking signal. For example, a narrow-band blocker at the mirror frequency of the preferred signal center frequency would be attenuated by over 80 dB. In addition, it can be concluded, based on (7) and (33), that the characteristics of the third (or any subsequent) stage do not affect the processing of the original input signal or its image signal (conjugate response). On the other hand, increasing the order of the first stage would allow for more efficient STF design, resulting, e.g., in parallel notches in the ISTF at the interesting frequency band and thus improving the IRR even further.

6.2 Computer simulations

The conclusions of the transfer function analysis are confirmed herein with computer simulations and achievable interference rejection ratios are demonstrated. The multiband reception is simulated with an assumption of 16-QAM and QPSK waveforms to be received on the center frequencies of $f_{C,1} = 36.74$ MHz and $f_{C,2} = -15.74$ MHz, respectively. Raised-cosine filters with roll-off of 0.25 are used for the pulse shaping, which together with symbol rate of 8 MHz, gives 10-MHz waveform bandwidth. The QPSK band is received at 5 dB lower power level compared to 16-QAM band. Together with these preferred information signals, the overall input consists of four additional waveforms, of which two are located on the mirror frequencies of the signals of interest acting as blocking signals. In addition, a thermal input noise floor is present, limiting the 16-QAM and QPSK input SNRs to 13 and 8 dB, respectively. An example of input spectrum is shown in Figure 10 including mirror-frequency blockers with +20 dB power level compared to the preferred signals. The noninteresting signals consist of band-filtered white Gaussian noise with bandwidths of 3 MHz for the mirror-frequency blockers and 10 MHz for the other two. Interference rejection ratio results are simulated with varying power levels for the two blockers.

In the interference rejection ratio simulations, true quantizers are used inside the modulator loop for the I and Q rails to confirm the validity of the analytic model derived with the additive noise assumption. For generality, cases with 1-, 3-, and 8-bit quantizers are simulated and compared. In addition, frequency-flat and mirror-frequency-rejecting STF designs are simulated with 1% I/Q mismatches in the feedback branches of the stages (coefficients $R^{(l)}$ and $S^{(l)}$ in Figure 5). These correspond to the maximum deviations used in the analytic transfer function analysis in Section 6.1. The mismatches are assigned randomly for the real and imaginary parts of each of the complex-valued coefficients, i.e., the real I-rail coefficients can be 1% smaller or larger than the ideal values, and the corresponding real Q-rail coefficients are deviated in the opposite direction. Thus, two examples (presenting the real part of the complex-valued $R^{(1)}$) of possible mismatched values of I-rail coefficients are $r_{\mathrm{re},1}^{(1)} = (1 + 0.01)r_{\mathrm{re}}^{(1)}$ and $r_{\mathrm{re},1}^{(1)} = (1 - 0.01)r_{\mathrm{re}}^{(1)}$. In these cases, the respective Q-rail real coefficient values are $r_{\mathrm{re},2}^{(1)} = (1 - 0.01)r_{\mathrm{re}}^{(1)}$ and $r_{\mathrm{re},2}^{(1)} = (1 + 0.01)r_{\mathrm{re}}^{(1)}$. The mismatches in each of the complex coefficients are independent of each other. The interference rejection ratio Γ values are averaged over 25 independent random realizations of the mismatches. A single realization has input signal length of 2^{19} samples. The interference rejection ratio values are evaluated by subtract-

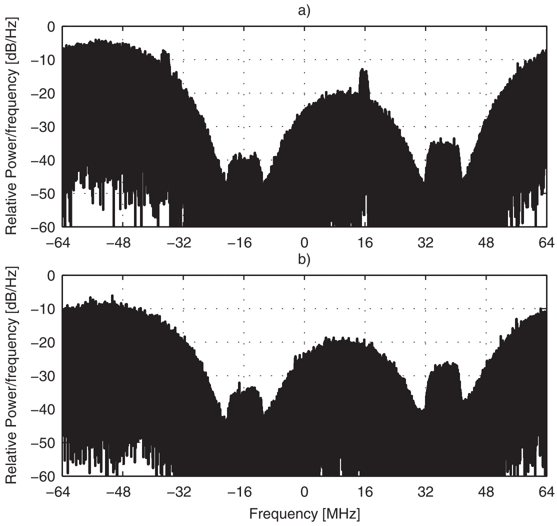

Figure 11 Example power spectral densities of output signals used in simulations: **(a)** with frequency-flat STF design, **(b)** with mirror-frequency-rejecting STF design. The preferred information signals are located around center frequencies of 36.74 and –15.74 MHz with 16-QAM and QPSK waveforms, respectively. 3-bit quantizers are used in all the three stages.

ing the output of an ideal $Q\Sigma\Delta M$ from the output of a mismatched $Q\Sigma\Delta M$, obtaining thus an estimate of distortion component. The interference rejection ratio itself is given as a ratio of the ideal output power on the preferred signal band and the distortion power estimate on the same band (see (38)-(41)). The presented power spectral densities are calculated with FFT-length of 2^{19} samples. The amplitudes of the real and imaginary parts of the overall received input signal are limited by the receiver automatic gain control mechanism to be equal to or less than 0.7 to avoid quantizer clipping (quantizer full scale range from –1 to 1), i.e., $|u_{I,1}(k)| \leq 0.7$ and $|u_{Q,1}(k)| \leq 0.7$ for all k. This limitation is maintained also when increasing the blocking signal power levels, which means that with increasing blocker input power, the useful signals are scaling down and become more and more sensitive to, e.g., quantization noise. For the sake of clarity, the output power spectral densities of the $Q\Sigma\Delta M$ are illustrated with frequency-flat and mirror-frequency-rejecting STF designs in Figure 11. From the plot (b), it is visible that, with the mirror-frequency-rejecting STF, the blockers around –36 and 16 MHz are filtered out, and the preferred signals are more clearly above the noise compared to the case with flat STF design in the plot (a), thus indicating improved SINR. Further, Figure 12 shows the output power spectral densities of the two transfer function designs when 16-QAM waveform is disabled. Thus, it is possible to see the difference at the emerging MFI, originating from the blocker. In this scenario, the power spectral density of the frequency-flat STF design case shows interference peak on the assumed preferred signal band and mirror-frequency-rejecting STF design is able to push the MFI component below the noise floor.

Next, Figure 13 illustrates the interference rejection ratio results with 1-bit quantizers applied in the stages of a three-stage multi-band $Q\Sigma\Delta M$. The interference rejection ratios are calculated separately for the two received signals, separated with colors in the figures. In addition, frequency-flat and mirror-frequency-rejecting STF designs are compared. From Figure 13, it is clear that mirror-frequency-rejecting STF design improves the interference rejection ratio of both the signals. The gain given by the STF design remains at 6 dB for the 16-QAM signal until relative blocker powers of +20 dB. For the QPSK signal, the corresponding gain is around 3 dB. However, with the highest simulated blocking signal powers (+40 to 60 dB compared to the QPSK signal) the interference rejection ratio floors at the same level, independent of the STF design. These limited gain values of the mirror-frequency-rejecting STF design and similar flooring level between the designs originate from the distortion components other than the complex conjugate of the input signal. Thus, the signal quality is decreasing despite the input signal originating MFI being mitigated. For example, the leakage of the first-stage quantization error, already discussed in Section 6.1, has a considerable role with 1-bit quantization,

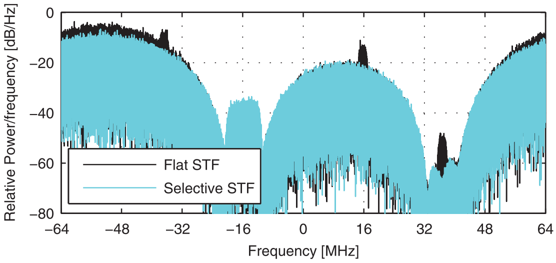

Figure 12 Example power spectral densities of output signals used in simulations with frequency-flat and mirror-frequency-rejecting STF designs with 16-QAM information signal around center frequency of 36.74 MHz disabled to highlight image rejection properties. 3-bit quantizers are used in all the three stages.

nonshaped quantization error having significant power on the preferred signal bands. With increasing blocking signal powers, also the level of first-stage quantization error is increasing compared to the preferred signals, and this decreases the interference rejection ratio values regardless of the STF design.

Overall, the achievable interference rejection ratios are well in line with demands derived in Section 5. From 16-QAM signal point of view, the demanded rejection (see Figure 7) is fulfilled with selective STF up to the relative blocker power of 20 dB. At this point, the full-band power to the 16-QAM signal power ratio can be approximated to be 23 dB, neglecting the minor effect of other out-of-band signals than the two mirror-frequency blockers. At this point, the achieved interference rejection ratio of 15 dB fulfills the demand of 13 dB with 3-bit quantization (see Figure 7).

The results with 3-bit quantizers, given in Figure 14, support the above conclusions. When the levels of the error components are decreased due to additional quantization bits, the gain given by the mirror-frequency-rejecting STF design is more pronounced. The gain increases when the blocking signal power cross the 0 dB level, due to the increasing amount of MFI stemming from the input signal. This gain remains around 15 dB for the 16-QAM signal and 10 dB for the QPSK signal at the relative blocker power ranging from +10 to +60 dB. This is because of the decreased levels of the quantization error components. Especially in wideband CR receivers operating in challenging radio conditions with strong out-of-band signal dynamics,

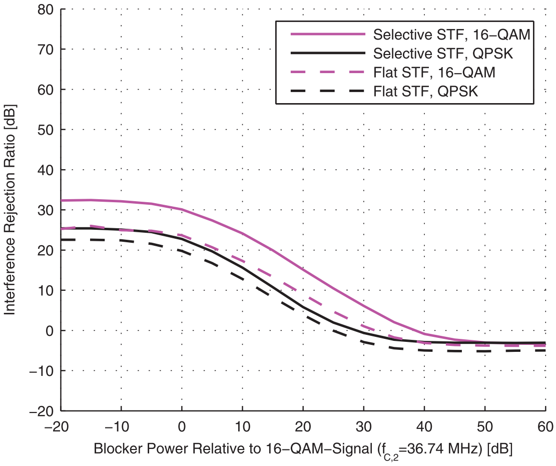

Figure 13 Interference rejection ratios for preferred signals with three-stage QΣΔM, using 1-bit quantizers at each stage, as a function of blocker signal power. Frequency-flat ("Flat STF") and mirror-frequency-rejecting STF ("Selective STF") designs are simulated.

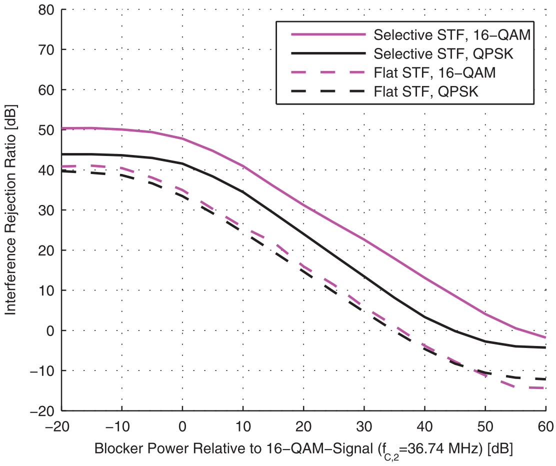

Figure 14 Interference rejection ratios for preferred signals with three-stage QΣΔM, using 3-bit quantizers at each stage, as a function of blocker signal power. Frequency-flat ("Flat STF") and mirror-frequency-rejecting STF ("Selective STF") designs are simulated.

the shown 10–15 dB gains are very valuable, improving the robustness of the receiver significantly.

Comparing these results to the set demand for the interference rejection ratio, it can be seen that 16-QAM with selective STF fulfills the demand up to the relative blocker levels of +40 dB. In this scenario, full-band power to the 16-QAM power ratio is approximately 43 dB, which gives interference rejection ratio demand of 13 dB with 3-bit quantization (see Figure 7) matching to the 13 dB result seen in Figure 14.

Finally, Figure 15 provides the results with 8-bit quantizers used in the stages (mainly for reference, without interference rejection target). In this scenario, the quantization error levels are pushed even further down, and the MFI from the input remains as a dominant error source. The interference rejection ratio values in Figure 15 pronounce

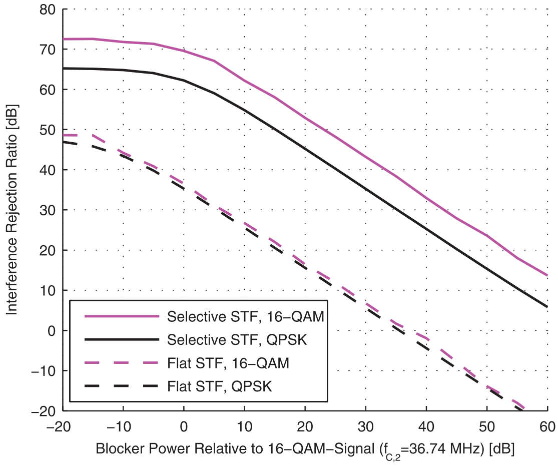

Figure 15 Interference rejection ratios for preferred signals with three-stage QΣΔM, using 8-bit quantizers at each stage, as a function of blocker signal power. Frequency-flat ("Flat STF") and mirror-frequency-rejecting STF ("Selective STF") designs are simulated.

the efficiency of the mirror-frequency-rejecting STF design in mitigating this distortion. The gains achieved with this design remain at the levels of 40 and 30 dB for the 16-QAM and QPSK signals, respectively, with the relative blocker levels above +10 dB. Again, these findings support the capability of the mirror-frequency STF design in input signal-originating MFI mitigation. However, with limited quantization precisions (such as the 1-bit case), the role of the other distortion sources is also significant.

7 Conclusions

This article provided an analytic transfer function model for I/Q imbalance effects in a second-order multistage $Q\Sigma\Delta M$ with arbitrary number of stages. For each of the stages, input branches, loop filters, and feedback branches were modeled as potential mismatch sources. Mirror-frequency-rejecting STF design was proposed for the first stage of multistage $Q\Sigma\Delta M$s as an efficient tool against MFI due to feedback mismatches. Thereafter, based on the derived model, it was concluded that in three-stage $Q\Sigma\Delta M$ the mirror-frequency-rejecting STF design in the first stage was able to improve the image rejection of the modulator by 20 dB, when feedback branch I/Q mismatches were considered. This technique improves the image rejection of a multistage $Q\Sigma\Delta M$ without any additional electronics. The MFI mitigation capability of the mirror-frequency-rejecting STF design was also confirmed with computer simulation-based interference rejection ratio calculations. Based on the simulations, it was concluded that this STF design is able to significantly reduce the MFI on the preferred signal bands. However, with limited quantization precision, the quantization error-based additional distortion components restrict the achievable interference rejection ratio.

In general, multi-band design aimed toward CR receivers was discussed, and the three-stage $Q\Sigma\Delta M$ was found to offer valuable degrees of freedom in transfer function design to receive scattered frequency slices efficiently. This multi-band reception scheme is a promising possibility for frequency agile A/D conversion for CR. The transfer functions of a multistage $Q\Sigma\Delta M$ can be reconfigured straightforwardly based on the spectrum-sensing information. This was shown with parameterization of the zeros and the poles of the stage NTFs and STFs. The proposed design principles and flow can be realized with information about the center frequencies and the bandwidths of the signals to be received.

While the mirror-frequency-rejecting STF design was shown to be effective against input blocker mirroring, the closed-form analysis also showed that first-stage quantization noise leakage due to noncommutativity of the complex transfer functions under I/Q imbalance is a problem in multistage $Q\Sigma\Delta M$s. This problem was confronted also in interference rejection ratio simulations. Developing ways to mitigate the noise leakage would increase the resolution of the ADC and increase the role of the proposed mirror-frequency-rejecting STF design even further. This will be addressed in future research.

Acknowledgement
This study was supported by the Academy of Finland (under the project entitled "Digitally-enhanced RF for cognitive radio devices"), the Finnish Funding Agency for Technology and Innovation (Tekes, under the projects entitled "Advanced techniques for RF impairment mitigation in future wireless radio systems" and "Enabling methods for dynamic spectrum access and cognitive radio"), Austrian Center of Competence in Mechatronics (ACCM, under the project entitled "Wireless communication technologies"), Tampere University of Technology Graduate School, HPY Research Foundation, and Nokia Foundation.

Competing interests
The authors declare that they have no competing interests.

Received: 30 April 2011 Accepted: 12 October 2011 Published: 12 October 2011

References

1. IF Akyildiz, W-Y Lee, MC Vuran, S Mohanty, NeXt generation/dynamic spectrum access/cognitive radio wireless networks: a survey. Comput. Networks **50**, 2127–2159 (2006)
2. M Mueck, A Piipponen, K Kalliojärvi, G Dimitrakopoulos, K Tsagkaris, P Demestichas, F Casadevall, J Perez-Romero, O Sallent, G Baldini, S Filin, H Harada, M Debbah, T Haustein, J Gebert, B Deschamps, P Bender, M Street, S Kandeepan, J Lota, A Hayar, ETSI reconfigurable radio systems: status and future directions on software defined radio and cognitive radio standards. IEEE Commun. Mag. **48**, 78–86 (2010)
3. P-I Mak, S-P U, RP Martins, Transceiver architecture selection: review, state-of-the-art survey and case study. IEEE Circuits Syst. Mag. **7**, 6–25 (2007)
4. R Bagheri, A Mirzaei, ME Heidari, S Chehrazi, M Lee, M Mikhemar, WK Tang, AA Abidi, Software-defined radio receiver: dream to reality. IEEE Commun. Mag. **44**, 111–118 (2006)
5. Z Ru, NA Moseley, E Klumperink, B Nauta, Digitally enhanced software-defined radio receiver robust to out-of-band interference. IEEE J. Solid-State Circuits **44**, 3359–3375 (2009)
6. B Razavi, Cognitive radio design challenges and techniques. IEEE J. Solid-State Circuits **45**, 1542–1553 (2010)
7. PB Kenington, L Astier, Power consumption of A/D converters for software radio applications. IEEE Trans. Veh. Technol. **49**, 643–650 (2000)
8. M Ismail, D Rodríguez de Llera González (eds.), *Radio Design in Nano-meter Technologies* (Springer, Dordrecht, 2006)
9. J Yang, RW Brodersen, D Tse, Addressing the dynamic range problem in cognitive radios, in *Proceedings of the IEEE International Conference on Communications*, Glasgow, Scotland, 24-28 June 2007
10. AA Abidi, The path to the software-defined radio receiver. IEEE J. Solid-State Circuits **42**, 954–966 (2007)
11. B Le, TW Rondeau, JH Reed, CW Bostian, Analog-to-digital converters. IEEE Signal Process. Mag. **22**, 69–77 (2005)
12. N Vun, AB Premkumar, ADC systems for SDR digital front-end, in *Proceedings of the 9th International Symposium on Consumer Electronics*, Macau, Hong Kong, 14-16 June 2005
13. PA Aziz, HV Sorensen, J van der Spiegel, An overview of sigma-delta converters: how a 1-bit ADC achieves more than 16-bit resolution. IEEE Signal Process. Mag. **13**, 61–84 (1996)
14. A Rusu, B Dong, M Ismail, Putting the "flex" in flexible mobile wireless radios. IEEE Circuits Devices Mag. **22**, 24–30 (2006)
15. A Silva, J Guilherme, N Horta, Reconfigurable multi-mode sigma-delta modulator for 4G mobile terminals. Integration. The VLSI J. **42**, 34–46 (2009)
16. J Crols, MSJ Steyaert, Low-IF topologies for high-performance analog front ends of fully integrated receivers. IEEE Trans. Circuits Syst. II Analog Digit. Signal Process. **45**, 269–282 (1998)

17. N Jouida, C Rebai, G Ghazel, D Dallet, Comparative study between continuous-time real and quadrature bandpass delta sigma modulator for mul-tistandard radio receiver, in *Proceedings of the Instrumentation Measurement Technology Conference*, Warsaw, Poland, 1-3 May 2007
18. S Jantzi, K Martin, A Sedra, A quadrature bandpass delta-sigma modulator for digital radio. IEEE J. Solid-State Circuits. **32**, 1935–1950 (1997)
19. J Marttila, M Allén, M Valkama, Quadrature $\Sigma\Delta$ modulation for cognitive radio - I/Q imbalance analysis and complex multiband principle. Circuits, Syst. and Signal Process. **30**, 775–797, (2011)
20. DD Ariananda, MK Lakshmanan, H Nikoo, A survey on spectrum sensing techniques for cognitive radio, in *Proceedings of the 2nd International Workshop on Cognitive Radio and Advanced Spectrum Management*, Aalborg, Denmark, 18-20 May 2009
21. J Marttila, M Allén, M Valkama, Design and analysis of multi-stage quadrature sigma-delta A/D converter for cognitive radio receivers, in *Proceedings of the 16th IEEE International Workshop on Computer-Aided Modeling Analysis and Design of Communication Links and Networks*, Kyoto, Japan, 10-11 June 2011
22. YBN Kumar, S Talay, F Maloberti, Complex cascaded bandpass $\Sigma\Delta$ ADC design, in *Proceedings of the IEEE International Symposium on Circuits and Systems*, Taipei, Taiwan, 24-27 May 2009
23. Y Tang, K-W Cheng, S Gupta, J Paramesh, DJ Allstot, Cascaded complex ADCs with adaptive digital calibration for I/Q mismatch. IEEE Trans. Circuits Syst. I Reg. Papers **55**, 817–827 (2008)
24. M Valkama, J Pirskanen, M Renfors, Signal processing challenges for applying software radio principles in future wireless terminals: an overview. Int. J. Commun. Syst. **15**, 741–769 (2002)
25. S Jantzi, KW Martin, AS Sedra, The effects of mismatch in complex bandpass $\Delta\Sigma$ modulators, in *Proceedings of the IEEE International Symposium on Circuits and Systems*, Atlanta, GA, 12-15 May 1996
26. LJ Breems, EC Dijkmans, JH Huijsing, A quadrature data-dependent DEM algorithm to improve image rejection of a complex modulator. IEEE J. Solid-State Circuits **36**, 1879–1886 (2001)
27. L Yu, WM Snelgrove, A novel adaptive mismatch cancellation system for quadrature IF radio receivers. IEEE Trans. Circuits Syst. II Analog Digit. Signal Process. **46**, 789–801 (1999)
28. K-P Pun, C-S Choy, C-F Chan, JE da Franca, An I/Q mismatch-free switched-capacitor complex sigma-delta modulator. IEEE Trans. Circuits Syst. I Express Briefs **51**, 254–256 (2004)
29. S Reekmans, P Rombouts, L Weyten, Mismatch insensitive double-sampling quadrature bandpass $\Sigma\Delta$ modulation. IEEE Trans. Circuits Syst. I Regular Papers **54**, 2599–2607 (2007)
30. J Marttila, M Allén, M Valkama, Response analysis and design of second-order quadrature $\Sigma\Delta$ modulators with applications in cognitive radio devices, in *54th IEEE International Midwest Symposium on Circuits and Systems*, Seoul, South-Korea, 7-10 August 2011 (invited paper)
31. N Jouida, C Rebai, G Ghazel, Built-in filtering for out-of-channel interferers in continuous-time quadrature bandpass delta sigma modulators, in *Proceedings of the 14th IEEE International Conference on Electronics, Circuits Systems*, Marrakech, Morocco, 11-14 December 2007
32. K Hyungseok, L Junghan, T Copani, S Bazarjani, S Kiaei, B Bakkaloglu, Adaptive blocker rejection continuous-time $\Sigma\Delta$ ADC for mobile WiMAX applications. IEEE J. Solid-State Circuits **44**, 2766–2779 (2009)
33. R Schreier, GC Temes, *Understanding Delta-Sigma Data Converters* (Wiley, Hoboken, 2005)
34. P Kiss, Adaptive digital compensation of analog circuit imperfections for cascaded delta-sigma analog-to-digital converters, Dissertation, "Politehnica" Univ. Timisoara, Romania, 1999
35. G Cauwenberghs, GC Temes, Adaptive digital correction of analog errors in MASH ADCs. I. Off-line and blind on-line calibration. IEEE Trans. Circuits Syst. II Analog Digit. Signal Process. **47**, 621–628 (2000)
36. R Schreier, An empirical study of high-order single-bit delta-sigma modulators. IEEE Trans. Circuits Syst. II Analog Digit. Signal Process. **40**, 461–466 (1993)

doi:10.1186/1687-1499-2011-130
Cite this article as: Marttila *et al.*: **Multistage quadrature sigma-delta modulators for reconfigurable multi-band analog-digital interface in cognitive radio devices.** *EURASIP Journal on Wireless Communications and Networking* 2011 **2011**:130.

PUBLICATION 5

Jaakko Marttila, Markus Allén and Mikko Valkama, “Digital mirror-frequency interference compensation for multiband quadrature sigma-delta ADC based cognitive radio receivers,” in *Proceedings of the 55th IEEE International Midwest Symposium on Circuits and Systems*, Boise, ID, August 2012.

Digital Mirror-frequency Interference Compensation for Multiband Quadrature Sigma-Delta ADC based Cognitive Radio Receivers

Jaakko Marttila, Markus Allén and Mikko Valkama
Department of Communications Engineering
Tampere University of Technology
P.O. Box 553, FI-33101, Tampere, Finland
jaakko.marttila@tut.fi, markus.allen@tut.fi, mikko.e.valkama@tut.fi

Abstract — **This article proposes a novel frequency-agile transfer function design for quadrature ΣΔ modulators (QΣΔMs), allowing digital post-compensation of mirror-frequency interference generated by the mismatches between the receiver I and Q branches. In addition to mitigating the interference created inside the QΣΔM, doing the compensation in digital domain allows taking into account the implementation inaccuracies of the preceding receiver front-end components, such as a quadrature mixer. This is made possible by using the signal and noise transfer functions to maintain the mirror-band signal information in the digital domain with sufficient signal-to-noise ratio. The performance of the transfer function design and digital compensation are illustrated in a multi-band scenario aimed for cognitive radio reception. Practical examples are given with eighth order noise shaping, allowed by a two-stage QΣΔM, having stage-orders of four.**

I. INTRODUCTION

Lately, increasing mobile data traffic volume has created novel challenges for the usage of available radio spectrum, being a limited and shared resource [1]. This is why the efficiency of spectrum utilization has become a major research problem, resulting in the introduction of dynamic spectrum access and cognitive radio (CR) paradigms [1]-[3]. In parallel, the radio circuits should be small-sized, cheap and power efficient [2]. The widely acknowledged trend in answering to these demands has been to move most of the receiver functionalities into digital domain, i.e., pushing the analog-to-digital interface towards the antenna [3]. This, however, sets high demands for the analog-to-digital converter (ADC), operating in challenging signal conditions [2], [3].

This kind of software defined radio receiver, using wideband direct-conversion or intermediate frequency digitization, has been proposed as a viable solution for the CR physical layer [4]. For the A/D interface, bandpass ΣΔ modulators have been proposed, shaping the quantization noise away from the desired signal band [4]. In addition, quadrature ΣΔ modulators (QΣΔMs) have been proven to have several benefits over the real counterparts [5], [6], making this a very interesting choice for development of future CR receivers.

However, exploiting complex signal processing with quadrature circuits brings the problem of matching in-phase (I) and quadrature (Q) rails [5]. These mismatches are known as I/Q imbalance and generate mirror-frequency interference (MFI) via spectral mirroring of the signal content. In the case of QΣΔM, where the quantization noise is processed inside the modulator, also the noise has a mirror response [5]-[6]. This article proposes a novel transfer function (TF) design for QΣΔMs, combined with digital post-compensation of exactly this interference, taking the MFI originating from both the input signal and the quantization noise into account.

Moreover, designs mitigating the MFI generated inside the QΣΔM are proposed in [5], [6]-[9]. However, none of these is able to mitigate MFI appearing before the actual QΣΔM (e.g., the I/Q mixer as an error source) [5], [6] or to avoid inserting calibration signals [7], additional analog circuitry, [8] or impairing the sampling properties [9]. In demonstrating the overall receiver concept and performance, the blind MFI suppression algorithm published originally in [10] is deployed. This frequency-independent algorithm is chosen based on the inherent oversampling present in the ΣΔ conversion (assuming mild frequency selectivity inside a single subband) and the simplicity of the blockwise compensator.

The rest of this article is organized as follows. In Section II, QΣΔM basics are reviewed. The TF design facilitating the digital post-compensation of MFI, independent of the interference source, and the compensation itself, are proposed in Sections III and IV, respectively. Thereafter, Section V presents the results of the design and compensation scheme. Finally, Section VI concludes the article.

II. QUADRATURE ΣΔ MODULATION

The analytical transfer function presentation of a QΣΔM is based on [5]. The *P*th order QΣΔM used in the following analysis, employing complex-valued input $u(k)$, quantization noise $e(k)$ and output $v(k)$ is presented in Fig. 1. This quadrature structure allows the use of frequency asymmetric (complex) noise and signal transfer functions (NTF and STF). The output of an ideal ΣΔ modulator is given (by adopting a linear model of the modulator [5]) in z-domain by

$$V^{ideal}[z] = STF[z]U[z] + NTF[z]E[z]. \tag{1}$$

The linearity assumption is not exactly accurate, the quantization noise being correlated with the quantizer input, but it is widely adopted because of simplifying the design and analysis of ΣΔ modulators [11].

This work was supported by the Academy of Finland, the Finnish Funding Agency for Technology and Innovation (Tekes), Austrian Center of Competence in Mechatronics (ACCM), Tampere University of Technology Graduate School, HPY Research Foundation and Nokia Foundation.

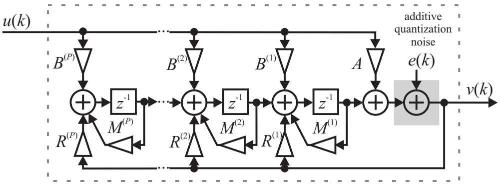

Fig. 1. Discrete-time linearized model of a *P*th-order QΣΔM with complex-valued signals and coefficients.

The *P*th order structure of Fig. 1 allows placing P NTF and STF zeros on the conversion band, together with P poles common to both of the TFs. Moreover, the NTF is given by

$$NTF[z] = \frac{1}{1 - \sum_{p=1}^{P} R^{(p)} \prod_{i=1}^{p} \frac{z^{-1}}{1 - M^{(i)} z^{-1}}} \tag{2}$$

and the corresponding STF is defined as

$$STF[z] = \frac{A + \sum_{p=1}^{P} B^{(p)} \prod_{i=1}^{p} \frac{z^{-1}}{1 - M^{(i)} z^{-1}}}{1 - \sum_{p=1}^{P} R^{(p)} \prod_{i=1}^{p} \frac{z^{-1}}{1 - M^{(i)} z^{-1}}}, \tag{3}$$

where the $z^{-1} / (1 - M^{(i)} z^{-1})$ terms are the TFs of the complex loop filters [6]. It should be noted that the denominators of both transfer functions are equal, meaning that the poles are common. More detailed description of a multi-stage QΣΔM used in the following examples can be found, e.g., from [6].

III. FREQUENCY-AGILE TRANSFER FUNCTION DESIGN

This section proposes a novel TF design, allowing the digital post compensation of the overall MFI generated at the receiver front-end (FE) and inside the QΣΔM itself. This design extends the mirror-band NTF zero placement of [5] to the multiband concept of [6]. In addition, the STF passbands are created on the desired signal mirror-bands in order to maintain the information about possible blocker signals appearing therein for post-compensation purposes. The actual QΣΔM coefficients are derived in similar manner as in [6], maintaining the straightforward reconfigurability, e.g., in case of frequency handoff. This frequency-agile operation is enabled by the information of desired signals' center frequencies and bandwidths, defining the coefficient values.

The design is demonstrated in a practical reception scenario of multiple desired signals on scattered center frequencies. The overall noise shaping order in this case is eight, allowed by a two-stage QΣΔM having both the stage of fourth order. The high noise shaping order maintains the flexible reconfiguration of the noise shaping bands discussed in [6]. A contiguous placement of the NTF zeros allows reception of a wideband waveform (such as LTE 20 MHz), while multiple distinct narrowband signals can be handled with a noncontiguous NTF design.

In the following, a concrete TF design example is given, having the NTF zeros divided for the simultaneous reception of two desired signals on noncontiguous frequency bands by placing three NTF zeros on both bands. The remaining two zeros are placed on the mirror-bands of those signals to improve the signal-to-noise ratio (SNR) of the blockers possibly appearing therein. At the same time, the main principle in the STF design is to allow the desired signals and their mirror-band signals to be converted with reasonable resolution. In simplest, this means STF being equal to unity. However, the STF zeros of the first stage can be used to filter out other non-interesting signal content possibly limiting the dynamics of the converter. It is important to notice that the TFs can be straightforwardly reconfigured using information about the transmission center frequencies, bandwidths, resolution demands and the spectrum sensing information.

The placements of the NTF zeros inside the desired signal band is based on [12]. Since the noise shaping order per desired signal band is three, the four first stage zeros are placed on the edges of the two bands, i.e., $\varphi_{NTF,1}^{(1)} = e^{j2\pi(f_{\mathrm{C},1} + f_{\mathrm{offset},1})T}$, $\varphi_{NTF,2}^{(1)} = e^{j2\pi(f_{\mathrm{C},1} - f_{\mathrm{offset},1})T}$, $\varphi_{NTF,3}^{(1)} = e^{j2\pi(f_{\mathrm{C},2} + f_{\mathrm{offset},2})T}$ and $\varphi_{NTF,4}^{(1)} = e^{j2\pi(f_{\mathrm{C},2} - f_{\mathrm{offset},2})T}$, where $f_{\mathrm{C},1}$ and $f_{\mathrm{C},2}$ are the desired signal center frequencies and $f_{\mathrm{offset},1} = B_1 \sqrt{3 / 5} / 2$ and $f_{\mathrm{offset},2} = B_2 \sqrt{3 / 5} / 2$ (following [12]), with B_1 and B_2 being the bandwidths of the desired signals in Hertz. The second stage NTF zeros are placed in the middle of the desired signal bands and on the mirror frequencies, giving $\varphi_{NTF,1}^{(2)} = e^{j2\pi f_{\mathrm{C},1} T}$, $\varphi_{NTF,2}^{(2)} = e^{j2\pi f_{\mathrm{C},2} T}$, $\varphi_{NTF,3}^{(2)} = e^{-j2\pi f_{\mathrm{C},1} T}$ and $\varphi_{NTF,4}^{(2)} = e^{-j2\pi f_{\mathrm{C},2} T}$.

The poles of the stages are placed in Butterworth positions in order to secure the stability of the modulators [5]. This limits the NTF out-of-band gain, which is an important factor in the stability aspect [11]. The STF zeros of the first stage are placed on the center frequencies of the possible additional, noninteresting, signals in order to reduce the signal dynamics at the quantizer input.

IV. DIGITAL MFI POST-COMPENSATION

The MFI experienced by the desired signals is generated in the receiver radio FE and the quadrature ΣΔ ADC, because of the inherent implementation inaccuracies therein. In the radio FE, the imbalance source can be, e.g., an I/Q mixer. Thus, the input signal $U[z]$ fed to the QΣΔM is already a combination of the ideal signal $T[z]$ and its complex conjugate $T^*[z^*]$, scaled by certain, generally frequency-selective, gains, i.e.,

$$U[z] = STF_{\mathrm{FE}}[z] T[z] + ISTF_{\mathrm{FE}}[z] T^*[z^*], \tag{4}$$

where $STF_{\mathrm{FE}}[z]$ and $ISTF_{\mathrm{FE}}[z]$ are the signal and image signal transfer functions of the receiver FE.

When this nonideal signal is used as an input for the I/Q mismatched QΣΔM, both the components experience the STF and image STF (ISTF) of the QΣΔM. In addition, the noise and image noise components are added, shaped by the NTF and image NTF (INTF), respectively. In this scenario, the final output of a single-stage QΣΔM is given by

$$\begin{aligned} V[z] = {} & STF_{\mathrm{TOT}}[z] T[z] + ISTF_{\mathrm{TOT}}[z] T^*[z^*] \\ & + NTF[z] E[z] + INTF[z] E^*[z^*], \end{aligned} \tag{5}$$

where $STF_{\mathrm{TOT}}[z]$ and $ISTF_{\mathrm{TOT}}[z]$ are the combined STF and ISTF of the FE and the QΣΔM, respectively.

Now, having a two-stage QΣΔM as an practical example, the interference rejection ratio is calculated with the signal components ideally present at the output, using impulse responses and time-domain signals,

$$\tilde{\alpha}(k) = h_{\mathrm{STF}}^{\mathrm{TOT}}(k) * t(k) + h_{\mathrm{NTF}}^{\mathrm{TOT},2}(k) * e_2(k) \tag{6}$$

and the I/Q imbalance induced interference components

$$\begin{aligned}\tilde{\beta}(k) = {}& h_{\mathrm{ISTF}}^{\mathrm{TOT}}(k) * t^*(k) + h_{\mathrm{NTF}}^{\mathrm{TOT},1}(k) * e_1(k) \\ & + h_{\mathrm{INTF}}^{\mathrm{TOT},1}(k) * e_1^*(k) + h_{\mathrm{INTF}}^{\mathrm{TOT},2} * e_2^*(k),\end{aligned} \tag{7}$$

where the STF and the ISTF components include the contribution of the whole receiver, and $e_1(k)$ and $e_2(k)$ are the quantization noise components of the first and the second stage, respectively [6]. Thus, the interference rejection ratio [6] of the whole receiver, for the signal band s, is given by

$$\tilde{\Gamma}_{\mathrm{s}} = \frac{\displaystyle\int_{f\in\Omega_{\mathrm{s}}} G_{\tilde{\alpha}}(e^{j2\pi fT})df}{\displaystyle\int_{f\in\Omega_{\mathrm{s}}} G_{\tilde{\beta}}(e^{j2\pi fT})df}. \tag{8}$$

In Section V, this measure $\tilde{\Gamma}_{\mathrm{s}}$ is used to verify the efficiency of the digital MFI post-compensation.

In case of the ΣΔ modulation, the frequency-selective behavior of the generated interference can be assumed mild inside a single signal subband because of the high oversampling inherently present. Thus, a simple frequency-independent compensation algorithm [10] can be used to demonstrate the efficiency of digital post-compensation, facilitated by the discussed TF designs. Possible deviations at the level of the interference between the signal bands are taken into account by doing the compensation separately for each of the desired signal bands, as illustrated in Fig. 2.

With this narrowband assumption, the output signals $w_{\mathrm{s}}(k)$, depicted in Fig. 2, are given by

$$\begin{aligned} w_{\mathrm{s}}(k) &= \overline{v}_{\mathrm{s}}(k) + \varphi_{\mathrm{s}}\overline{v}_{\mathrm{s}}^{\,*}(k) \\ &\approx L_{\overline{t}_{\mathrm{s}},1}\overline{t}_{\mathrm{s}}(k) + L_{\overline{e}_{\mathrm{s}},1}\overline{e}_{\mathrm{s}}(k) + L_{\overline{t}_{\mathrm{s}},2}\overline{t}_{\mathrm{s}}^{\,*}(k) \\ &\quad + L_{\overline{e}_{\mathrm{s}},2}\overline{e}_{\mathrm{s}}^{\,*}(k) + \varphi_{\mathrm{s}}[L_{\overline{t}_{\mathrm{s}},1}\overline{t}_{\mathrm{s}}^{\,*}(k) + L_{\overline{e}_{\mathrm{s}},1}\overline{e}_{\mathrm{s}}^{\,*}(k) \\ &\quad + L_{\overline{t}_{\mathrm{s}},2}\overline{t}_{\mathrm{s}}(k) + L_{\overline{e}_{\mathrm{s}},2}\overline{e}_{\mathrm{s}}(k)], \end{aligned} \tag{9}$$

where the signal components with the bar are the inband signals after the filters $n_{\mathrm{s}}(k)$ for the desired signal bands and $n_{\mathrm{s}}^*(k)$ for the image bands, the noise components $\overline{e}_{\mathrm{s}}(k)$ and $\overline{e}_{\mathrm{s}}^{\,*}(k)$ including the total quantization noise after the two ΣΔ stages. In addition, the L coefficients are the approximate inband scaling factors for the signal components, defined as

$$\begin{aligned} L_{\overline{t}_{\mathrm{s}},1} &\approx STF_{\mathrm{TOT}}[e^{j2\pi f_{\mathrm{C,s}}T_{\mathrm{sample}}}], \\ L_{\overline{t}_{\mathrm{s}},2} &\approx ISTF_{\mathrm{TOT}}[e^{j2\pi f_{\mathrm{C,s}}T_{\mathrm{sample}}}], \\ L_{\overline{e}_{\mathrm{s}},1} &\approx NTF_{\mathrm{TOT,2}}[e^{j2\pi f_{\mathrm{C,s}}T_{\mathrm{sample}}}], \\ L_{\overline{e}_{\mathrm{s}},2} &\approx NTF_{\mathrm{TOT,1}}[e^{j2\pi f_{\mathrm{C,s}}T_{\mathrm{sample}}}] + INTF_{\mathrm{TOT,1}}[e^{j2\pi f_{\mathrm{C,s}}T_{\mathrm{sample}}}] \\ &\quad + NTF_{\mathrm{TOT,2}}[e^{j2\pi f_{\mathrm{C,s}}T_{\mathrm{sample}}}], \end{aligned} \tag{10}$$

where the TFs are evaluated at the desired signal center frequencies and T_{sample} is the sampling time in seconds. Further, by assuming practical (clearly above 0 dB) inband SNR and thus neglecting the lower power noise components, (9) can be simplified to take form

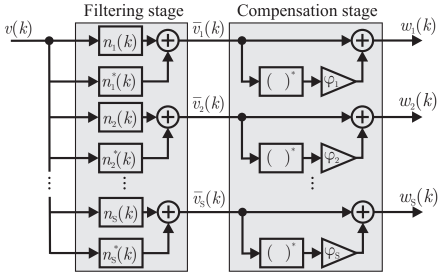

Fig. 2. Digital MFI post-compensation structure for S parallel signals to be received. The compensation algorithm used per branch is published in [10].

$$\begin{aligned} w_{\mathrm{s}}(k) \approx {}& L_{\overline{t}_{\mathrm{s}},1}\overline{t}_{\mathrm{s}}(k) + L_{\overline{t}_{\mathrm{s}},2}\overline{t}_{\mathrm{s}}^{\,*}(k) \\ & + \varphi_{\mathrm{s}}[L_{\overline{t}_{\mathrm{s}},1}\overline{t}_{\mathrm{s}}^{\,*}(k) + L_{\overline{t}_{\mathrm{s}},2}\overline{t}_{\mathrm{s}}(k)], \end{aligned} \tag{11}$$

This approximation simplifies finding the MFI compensator coefficients φ_{s} significantly.

The compensator coefficients φ_{s} are estimated based on the circularity restoring MFI compensation principle proposed in [10], where the circularity is defined as the complementary autocorrelation function $c_{\overline{t}_{\mathrm{s}}}(\tau)$ of $\overline{t}_{\mathrm{s}}(k)$ being zero at zero lag, i.e., $c_{\overline{t}_{\mathrm{s}}}(0) = E[\overline{t}_{\mathrm{s}}(k)^2] = 0$, meaning that real and imaginary parts of the compensated outputs are equally powerful and instantaneously mutually uncorrelated. This is defined as $c_{\overline{t}_{\mathrm{s}}} = c_{\overline{t}_{\mathrm{s}}}(0) = \mathrm{E}[\overline{t}_{\mathrm{s}}(k)^2]$ [10]. Similarly, autocorrelation function $\gamma_{\overline{t}_{\mathrm{s}}}(\tau)$ at zero lag is given by $\gamma_{\overline{t}_{\mathrm{s}}} = \gamma_{\overline{t}_{\mathrm{s}}}(0) = \mathrm{E}[\left|\overline{t}_{\mathrm{s}}(k)\right|^2]$ [10]. In practice, $c_{\overline{t}_{\mathrm{s}}}$ and $\gamma_{\overline{t}_{\mathrm{s}}}$ are estimated with sample averages. Now, the optimal compensator coefficients are given by [10]

$$\varphi_{\mathrm{s}} = -c_{\overline{t}_{\mathrm{s}}} \Big/ \left(\gamma_{\overline{t}_{\mathrm{s}}} + \sqrt{\gamma_{\overline{t}_{\mathrm{s}}}^2 - \left|c_{\overline{t}_{\mathrm{s}}}^2\right|}\right) \tag{12}$$

having $\mathrm{s} \in \{1,2\}$ for two-band reception. In the following, the sample estimates of $c_{\overline{t}_{\mathrm{s}}}$ and $\gamma_{\overline{t}_{\mathrm{s}}}$ are calculated from $\overline{v}_{\mathrm{s}}(k)$.

V. RESULTS

Herein, the QΣΔM design and MFI compensation of Sections III and IV are simulated using realistic communication waveforms to be received. For simplicity, the mirror-frequency blocking signals are complex-valued exponential tones. The quantization noise is shaped with the two-stage QΣΔM discussed in Section III. The MFI source is assumed to be the preceding receiver chain having 30 dB image rejection ratio and nonideal matching of all the QΣΔM coefficients. The realized real-valued coefficient values are drawn from a uniform distribution ±1% around the ideal value. The sampling frequency of the ADC is assumed to be 128 MHz.

An example of the assumed input signal in the computer simulations is illustrated Fig. 3, together with the ideal overall TFs. In addition to the signal content, a noise floor is included at the receiver input, giving 18 dB SNR for the 16-QAM waveform around $f_{\mathrm{C,1}} = 40.28\ \mathrm{MHz}$ and 10 dBs for the QPSK waveform around $f_{\mathrm{C,2}} = -14.49\ \mathrm{MHz}$, having 8 dB lower power level. The mirror-frequency blocking tones are simulated on the relative power level from 0 dB to +60 dB compared to the respective desired signals. A true 3-bit quantizer is simulated in both the QΣΔM stages (separately for the I and Q branches).

In the simulations, 100 independent realizations of the QΣΔM coefficients are drawn from the described distributions. The Interference Rejection Ratio $\tilde{\Gamma}_s$ values are evaluated for each realization by subtracting the output of an ideal QΣΔM from the output of a mismatched QΣΔM, obtaining thus an estimate of the interference component.

In addition to the proposed STF design, the frequency flat and mirror-frequency rejecting [6] STF designs are simulated for reference. In Fig. 4 (top plot), the results are given for the 16-QAM waveform. The gain achieved with the digital post-compensation is clearly visible, the compensated interference ratio exceeding the noncompensated one by 5–7 dB with the proposed STF and 9–10 dB with frequency flat STF designs with relative blocker powers higher than 30 dB. At the same time, the proposed STF design exceeds the frequency flat one with relative blocker powers up to 40 dB. The achieved gain reduces slightly with decreasing power difference for the signals. The mirror-frequency rejecting STF design of [6] shows no improvement with post-compensation because the information about the mirror-frequency signal is lost in the converter. On the other hand, with relatively low blocker powers, this design is performing well, being close to the proposed STF with post-compensation. One aspect explaining the degrading performance of the mirror-frequency rejecting STF design is the lack of the mirror-band NTF zeros, allowing high noise levels therein to be mirrored as significant interference on the desired signal band.

The results for the QPSK signal in Fig. 4 (bottom plot) show also compensation gain of 5–6 dB with the proposed STF design. Again, the proposed STF design performance exceeds the frequency flat one up to relative blocker power of 40 dB. The smaller performance benefit is because the QPSK signal has a lower SNR compared to the 16-QAM signal, making the input noise components more pronounced error sources in addition to the input signal originating MFI.

VI. CONCLUSION

In this article, a novel frequency agile multiband transfer function design for single- and multistage QΣΔMs was proposed and combined with digital post-compensation of MFI originating from implementation inaccuracies of the radio front-end and the QΣΔM itself. This allows the compensation to be done independently of the location of the actual error source in the receiver chain. The computer simulations showed significant interference rejection ratio gain, proving the digital post-compensation approach to be feasible. The following step is to study the applicability in more realistic simulation and measurement scenarios.

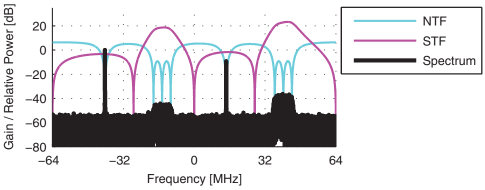

Fig. 3. An example spectrum of input signal together with the ideal designed transfer functions (overall response). The desired information signals are located around center frequencies of 40.28 MHz and -14.49 MHz.

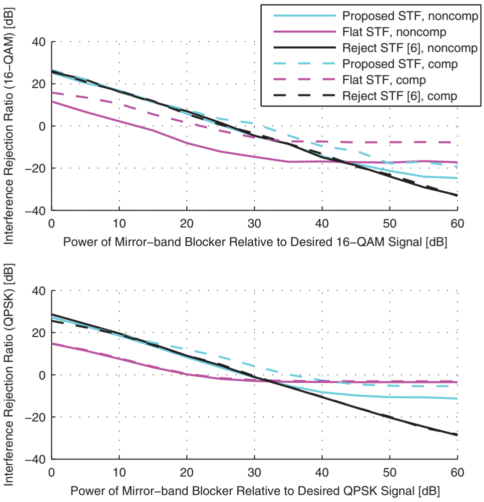

Fig. 4. Interference rejection ratios for a 16-QAM (top) and QPSK (bottom) signals as a function of relative blocker signal power. The proposed STF, frequency-flat STF ("Flat STF") and mirror-frequency rejecting STF [6] ("Reject STF") designs are simulated.

REFERENCES

[1] I. F. Akyildiz, W.-Y. Lee, M. C. Vuran and S. Mohanty, "NeXt generation/dynamic spectrum access/cognitive radio wireless networks: a survey," *Computer Networks*, vol. 50, no. 13, pp. 2127–2159, Sep. 2006.

[2] P.-I. Mak, S.-P. U and R. P. Martins, "Transceiver architecture selection: review, state-of-the-art survey and case study," *IEEE Circuits Syst. Mag.*, vol. 7, no. 2, pp. 6–25, 2007.

[3] B. Razavi, "Cognitive radio design challenges and techniques," *IEEE J. Solid-State Circuits*, vol. 45, no. 8, pp. 1542–1553, Aug. 2010.

[4] M. Ismail and D. Rodríguez de Llera González (eds.), Radio Design in Nano-meter Technologies (Springer, Dordrecht, Netherlands, 2006)

[5] S. Jantzi, K. Martin, and A. Sedra, "A quadrature bandpass delta-sigma modulator for digital radio," *IEEE J. Solid-State Circuits*, vol. 32, no. 12, pp. 1935–1950, Dec. 1997.

[6] J. Marttila, M. Allén and M. Valkama, "Multi-stage quadrature sigma-delta modulators for reconfigurable multi-band analog-to-digital interface in cognitive radio devices," *EURASIP J. Wirel. Commun. Netw.*, vol. 2011, no. 1, pp. 1–23, Oct. 2011.

[7] L. Yu and W. M. Snelgrove, "A novel adaptive mismatch cancellation system for quadrature IF radio receivers," *IEEE Trans. Circuits Syst. II, Analog Digit. Signal Process.*, vol. 46, no. 6, pp. 789–801, June 1999.

[8] S. Reekmans, P. Rombouts and L. Weyten, "Mismatch insensitive double-sampling quadrature bandpass ΣΔ modulation," *IEEE Trans. Circuits and Syst. I: Regular Papers*, vol. 54, no. 12, Dec. 2007.

[9] K.-P. Pun, C.-S. Choy, C.-F. Chan and J. E. da Franca, "An I/Q mismatch-free switched-capacitor complex sigma-delta modulator," *IEEE Trans. Circuits and Syst. I: Express Briefs*, vol. 51, no. 5, May 2004.

[10] L. Anttila, M. Valkama and M. Renfors, "Blind moment estimation techniques for I/Q imbalance compensation in quadrature receivers," in Proc. 17th Annu. *IEEE Int. Symp. Personal, Indoor and Mobile Radio Commun.*, Helsinki, Finland, 11–14, Sept. 2006.

[11] R. Schreier and G. C. Temes, Understanding Delta-Sigma Data Converters. Hoboken, NJ: Wiley, 2005.

[12] R. Schreier, "An empirical study of high-order single-bit delta-sigma modulators," *IEEE Trans. Circuits Syst. II, Analog Digit. Signal Process.*, vol. 40, no. 8, pp. 461–466, Aug. 1993.

PUBLICATION 6

Markus Allén, Jaakko Marttila and Mikko Valkama, “Wideband quadrature sigma-delta A/D conversion for cognitive radio - reconfigurable design and digital mirror-frequency suppression,” in *Proceedings of the 78th IEEE Vehicular Technology Conference*, Las Vegas, NV, September 2013.

Wideband Quadrature $\Sigma\Delta$ A/D Conversion for Cognitive Radio – Reconfigurable Design and Digital Mirror-Frequency Suppression

Markus Allén, Jaakko Marttila, Mikko Valkama
Dept. of Electronics and Communications Engineering, Tampere University of Technology
P.O. Box 553, FI-33101 Tampere, Finland
markus.allen@tut.fi, jaakko.marttila@tut.fi, mikko.e.valkama@tut.fi

***Abstract*—This article proposes a reconfigurable wideband transfer function design for quadrature $\Sigma\Delta$ A/D converters combined with digital post-compensation of frequency-selective mirror-frequency interference (MFI) induced by the inherent mismatches between the in-phase (I) and quadrature (Q) rails of the receiver. When receiving wideband waveforms, e.g., similar to LTE signals, it is crucial for the compensation performance to be able to consider also frequency variations in the image rejection. In addition to compensating the MFI originating from inside the quadrature $\Sigma\Delta$ modulator (Q$\Sigma\Delta$M), the digital compensation considers also the interference generated at the preceding receiver front-end components, such as an I/Q mixer. The performance of this approach is illustrated with a 20 MHz reception bandwidth, being a practical example of requirements for modern communications waveforms. This concrete example is given with a two-stage Q$\Sigma\Delta$M giving eighth order noise-shaping.**

***Index Terms*—Analog-to-digital conversion, cognitive radio, interference cancellation, I/Q imbalance, mirror-frequency interference**

I. INTRODUCTION

For realization of a cognitive radio (CR), it is of high importance to design flexible receivers, being able to operate on varying center frequencies and waveforms [1]. Especially, a wideband direct-conversion receivers have gathered considerable amount of attention in this perspective [2]. For digitization, e.g., lowpass, bandpass and quadrature bandpass $\Sigma\Delta$ A/D converters (ADCs) have been considered [2]–[4]. $\Sigma\Delta$ modulators have several benefits exactly in this kind of scenario, being, e.g., power efficient and able to include part of the receiver selectivity inside the ADC [3].

One downfall of $\Sigma\Delta$ ADCs has been applicability mainly for narrowband signals [5]. However, this can be overcome by employing higher-order modulator, multi-bit quantizer or multi-stage structure [5], [6]. Especially, a quadrature $\Sigma\Delta$ modulator (Q$\Sigma\Delta$M) based ADC has valuable flexibility, allowing frequency-asymmetric quantization noise shaping and signal filtering by complex-valued noise and signal transfer functions (NTF and STF, respectively) [3]. Particularly, this capability can be exploited by designing the modulator response for reception of multiple noncontiguous frequency bands or a single, wider, band. In addition, the transfer functions can be straightforwardly reconfigured, making the Q$\Sigma\Delta$M a very appealing solution for CR hardware platforms [4], [7], [8].

Exploiting complex signal processing, however, introduces also mismatches between in-phase (I) and quadrature (Q) rails of the receiver because of inherent implementation inaccuracies [3]. This I/Q imbalance creates mirror-frequency interference (MFI), which can be also frequency-selective [9]. Especially, a Q$\Sigma\Delta$M including signal selectivity can induce frequency-selective MFI stemming from the input signal, being an crucial aspect when receiving wideband waveforms, like, e.g., 20 MHz LTE signals. This article proposes a combination of reconfigurable transfer function design and digital post-compensation being able to tackle exactly this problem.

It is important to notice that MFI is generated both at the receiver front-end and inside the Q$\Sigma\Delta$M. This is why the mitigation schemes making the Q$\Sigma\Delta$M more robust, such as [4], [10]–[12], are taking care only of one part of the problem. By doing the compensation in digital domain it is possible to take also the MFI created by, e.g., the down-converting I/Q mixer into account. The blind frequency-selective MFI suppression algorithm published in [9] is used in this article, doing without additional analog circuitry [10], impairing the sampling properties [11] or adding calibration signals [13]. The narrowband compensation of Q$\Sigma\Delta$M MFI has been discussed earlier in [7], [8]. Herein, the analysis is extended to cover the frequency-selective characteristics of the MFI which are significant when receiving wideband signals.

The rest of this article is organized as follows. In Section II, Q$\Sigma\Delta$M basics and applicability for reconfigurable wideband CR receiver is discussed. The frequency-selective MFI compensation, taking the whole receiver into account, is discussed in Section III. Thereafter, Section IV presents the results of the computer simulations and Section V concludes the article.

This work was supported by the Finnish Funding Agency for Technology and Innovation (Tekes) under the project "Enabling Methods for Dynamic Spectrum Access and Cognitive Radio," the Academy of Finland under the project 251138 "Digitally-Enhanced RF for Cognitive Radio Devices," Austrian Competence Center in Mechatronics (ACCM), Tampere University of Technology Graduate School, Nokia Foundation and HPY Research Foundation.

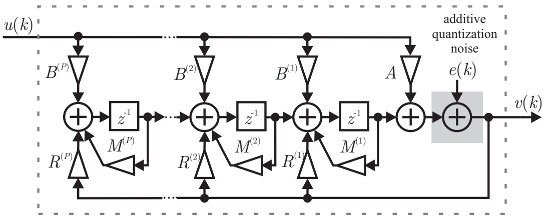

Fig. 1. Discrete-time linearized model of a Pth-order QΣΔM with complex-valued signals and coefficients. A single modulator stage is depicted.

II. QUADRATURE ΣΔ A/D CONVERSION FOR COGNITIVE RADIO

A. Basics of Quadrature ΣΔ Modulation

The analytical presentation of a QΣΔM is based on [3]. Herein, a L-stage QΣΔM is used, having arbitrary stage orders of P, for generality. Later, concrete examples are given with two-stage QΣΔM having stage orders of four. The structure of a single stage, employing complex-valued input $u(k)$, quantization noise $e(k)$ and output $v(k)$ is presented in Fig. 1. The ΣΔ modulator architecture considered in this article is a complex-valued version of cascaded integrators with distributed feedback and input [3], [14]. This allows the use of frequency-asymmetric transfer functions (NTF and STF). By adopting a linear model of the modulator [3], the output of an ideal modulator (without implementation inaccuracies) is given in z-domain by

$$V^{\mathrm{id}}[z] = STF[z]U[z] + NTF[z]E[z]. \tag{1}$$

The Pth-order structure of Fig. 1 allows placing P NTF and STF zeros on the conversion band, together with P poles common to both of the transfer functions. The NTF of the QΣΔM is given by

$$NTF[z] = \frac{1}{1 - \sum\limits_{p=1}^{P} R^{(p)} \prod\limits_{i=1}^{p} \frac{z^{-1}}{1-M^{(i)}z^{-1}}} \tag{2}$$

and the corresponding STF is defined as

$$STF[z] = \frac{A + \sum\limits_{p=1}^{P} B^{(p)} \prod\limits_{i=1}^{p} \frac{z^{-1}}{1-M^{(i)}z^{-1}}}{1 - \sum\limits_{p=1}^{P} R^{(p)} \prod\limits_{i=1}^{p} \frac{z^{-1}}{1-M^{(i)}z^{-1}}}, \tag{3}$$

where the $z^{-1}/(1-M^{(i)}z^{-1})$ terms are the transfer functions of the complex loop filters (integrators).

Moreover, the output of an ideal L-stage QΣΔM, depicted in Fig. 2, is given by

$$V^{\mathrm{id}}[z] = \sum_{l=1}^{L} (-1)^{l+1} H_l^D[z] V_l^{\mathrm{id}}[z], \tag{4}$$

where

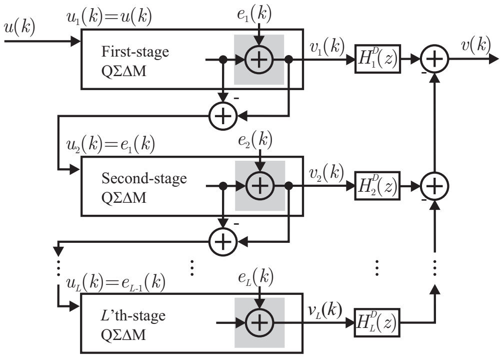

Fig. 2. L-stage QΣΔM with arbitrary-order noise shaping in individual stages. Filters from $H_1^D[z]$ to $H_L^D[z]$ are implemented digitally.

$$V_l^{\mathrm{id}}[z] = STF_l^{\mathrm{id}}[z]U_l[z] + NTF_l^{\mathrm{id}}[z]E_l[z] \tag{5}$$

and

$$H_l^D[z] = \frac{H_1^D[z] \prod\limits_{l=1}^{L-1} NTF_l^{\mathrm{id}}[z]}{\prod\limits_{l=2}^{L} STF_l^{\mathrm{id}}[z]}. \tag{6}$$

The digital filters $H_l^D[z]$ are used to match the nonshaped digital noise estimate to the NTF-shaped noise at the output of the previous stage.

B. Reconfigurable Wideband A/D Interface for Cognitive Radio

The first big goal set for CR is to improve spectrum efficiency by dynamic spectrum access, i.e., by exploiting temporarily and spatially unused frequency bands for secondary transmissions [1]. For this purpose, the transceivers must be capable of switching the operation bands in agile manner. For mobile receiver, one of the biggest challenges is to design an A/D interface fit for such operation. However, covering wide frequency band with a static wideband ADC has a downfall of increased power consumption. This is something that can be avoided with reconfigurable A/D solutions. Herein, a reconfigurable QΣΔM transfer function design fit for such purpose is proposed.

A popular way to provide higher bit rates for consumer applications, has lately been to increase the transmission bandwidths [2]. For discrete-time ΣΔ modulators, wideband signals have traditionally been problematic because of limited available oversampling ratio. However, with multi-bit quantization and multi-stage implementation, the necessary resolution can be achieved also with lower sampling rates, without increasing the power consumption exceedingly [6]. This has made reconfigurable ΣΔ modulators very interesting option for CR receivers [2].

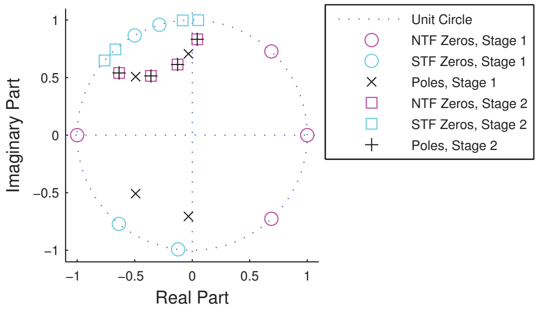

Fig. 3. Zero-pole plot of the STF and NTFs of a two-stage QΣΔM having fourth order stages (overall noise shaping order of eight). The main reception band is assumed around center-frequency of 40 MHz with 20 MHz (0.315 and 0.156 in relative frequency) bandwidth, having sampling-rate of 128 MHz.

Furthermore, with the knowledge of transmission frequency and bandwidth the QΣΔM STF and NTF can be straightforwardly reconfigured for dynamic spectrum access [4], [8]. At the same time, these complex-valued transfer functions can be designed to exploit noncontiguos frequency bands, making it posssible to divide the transmissions between multiple available spectrum holes [4], [8]. Thus, giving valuable flexibility for the CR platform. A concrete example of a two-stage QΣΔM with stage-orders of four is used in Fig. 3, where the NTF and STF of both the stages are illustrated with a zero-pole plot, assuming reception of a 20 MHz waveform around center-frequency of 40 Mhz (having sampling rate of 128 MHz), being a practical example of modern communication signals. The NTF zero positions are optimized according to [15] and the poles are placed in Butterworth positions [3]. The stability analysis of the first modulator stage, being most crucial because of dynamic signal conditions typical for CR, gives $\max_k |u(k)| = M_{\text{step},1} + 2 - \sum_k^{\infty} |h_{\text{NTF},1}(k)| = 5.35$ and thus 67 % stable input range [14]. For both the stages, 3-bit quantization is used and thus $M_{\text{step},1} = 8$. It should be also noted that the implementation inaccuracies affect the stability properties and thus the final stability is ensured with simulations and limiting the input amplitude accordingly.

III. DIGITAL COMPENSATION OF FREQUENCY-SELECTIVE MIRROR-FREQUENCY INTERFERENCE

In this section, the transfer function design properties that allow digital post-compensation of MFI are highlighted. Thereafter, actual compensation algorithm is described. The chosen frequency-selective algorithm is published earlier in [9]. This blind block-based algorithm was chosen because of its simplicity and being independent of any calibration signals.

As described in [7], [8], the digital MFI compensation needs information of the mirror-band signal content. Herein, this is made possible by designing a STF passband also on the mirror frequency of the actual desired information signal. This can be seen from Fig. 3 as two first-stage poles around the mirror-frequency of -40 MHz. In addition, two of the NTF zeros are placed on the mirror-band in order maintain reasonable signal-to-noise ratio (SNR).

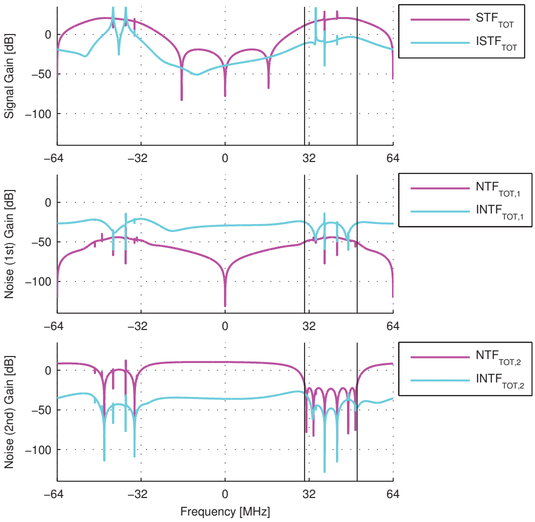

Fig. 4. An example of two-stage QΣΔM total STF and ISTF (above) and the total NTF and INTF for the first-stage quantization noise (middle) and the second-stage quantization noise (below). All the QΣΔM coefficients in both the stages are assumed to have 1 % I/Q mismatches.

At the same time, Fig. 4 shows clearly the frequency-selective characteristics of the image signal transfer function (ISTF). This makes also the generated MFI frequency-selective over, e.g., 20 MHz band, which is considered as the bandwidth of the desired signal, located around the center frequency of 40 MHz. In practice, the I/Q imbalance in the QΣΔM produces MFI, which is the complex-conjugate of the QΣΔM input filtered by the ISTF. At the same time, also the quantization noise creates MFI, being conjugated and shaped by the image noise transfer function (INTF).

In this section, the compensator coefficients are derived in a multi-band reception case, where S noncontiguous signal bands are received and detected, for generality. Thereafter, in the following computer simulations the single-band case (having $S = 1$) is applied. Now, the final QΣΔM output, including the MFI created by the receiver front-end, e.g., because of the nonideal I/Q mixers, and the QΣΔM itself, is given by

$$\begin{aligned} V[z] =& STF_{\text{TOT}}[z]X[z] + ISTF_{\text{TOT}}[z]X^*[z^*] \\ &+ NTF[z]E[z] + INTF[z]E^*[z^*], \end{aligned} \tag{7}$$

where $STF_{\text{TOT}}[z]$ and $ISTF_{\text{TOT}}[z]$ include the total contribution of both the front-end and the QΣΔM. It should be noted that, these are frequency-selective functions, having notable dynamics over frequency when a wide signal band is considered. In addition, $X[z]$ is the ideally down-converted MFI-free baseband signal.

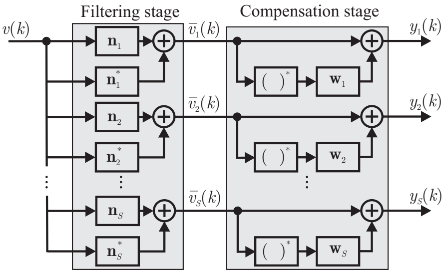

Fig. 5. Digital frequency-selective MFI post-compensation structure for general multi-band reception, processing S parallel information signals to be received and detected. The filters $\mathbf{n}_1$ to $\mathbf{n}_S$ and $\mathbf{n}_1^*$ to $\mathbf{n}_S^*$ are used to pick the desired signals and the related mirror-bands, respectively.

Now, the interference rejection ratio is calculated with the signal components ideally present at the output, using impulse responses and time-domain signals,

$$\tilde{\alpha}(k) = \mathbf{h}_{\text{STF}}^{\text{TOT}} * x(k) + \mathbf{h}_{\text{NTF}}^{\text{TOT,2}} * e_2(k) \tag{8}$$

and the I/Q imbalance induced MFI components

$$\begin{aligned}\tilde{\beta}(k) =& \mathbf{h}_{\text{ISTF}}^{\text{TOT}} * x^*(k) + \mathbf{h}_{\text{NTF}}^{\text{TOT,1}} * e_1(k) \\ &+ \mathbf{h}_{\text{INTF}}^{\text{TOT,1}} * e_1^*(k) + \mathbf{h}_{\text{INTF}}^{\text{TOT,2}} * e_2^*(k),\end{aligned} \tag{9}$$

where the STF and ISTF components include the contribution of the whole receiver, $e_1(k)$ and $e_2(k)$ being the quantization errors of the first and the second stage, respectively. With these quantities the interference rejection ratio of the whole receiver, inside the desired signal band Ω_s, is defined as

$$\tilde{\Phi}_s = \frac{\int\limits_{f\in\Omega_s} G_{\tilde{\alpha}}(e^{j2\pi fT})\mathrm{d}f}{\int\limits_{f\in\Omega_s} G_{\tilde{\beta}}(e^{j2\pi fT})\mathrm{d}f}, \tag{10}$$

where the subscript s is the band number in general multi-band reception. In the following simulations, reception of a single wideband waveform is assumed and thus $\tilde{\Phi}_1$ is evaluated.

By assuming practical (clearly above 0 dB) inband SNR and thus neglecting the lower power noise components, the compensated output signals $y_s(k)$, shown in Fig. 5, are given by

$$\begin{aligned}y_s(k) \approx& \mathbf{h}_{\text{STF},\bar{x}_s}^{\text{TOT}} * \bar{x}_s(k) + \mathbf{h}_{\text{ISTF},\bar{x}_s}^{\text{TOT}} * \bar{x}_s^*(k) \\ &+ \mathbf{w}_s * [\mathbf{h}_{\text{ISTF},\bar{x}_s}^{\text{TOT}} * \bar{x}_s^*(k) + \mathbf{h}_{\text{STF},\bar{x}_s}^{\text{TOT}} * \bar{x}_s(k),\end{aligned} \tag{11}$$

where the STF and ISTF impulse-responses contain the inband contribution of the S desired reception bands.

The N-tap compensation vectors $\mathbf{w}_s$ are estimated using the frequency-selective circularity restoring MFI compensation algorithm published in [9]. Therein, the circularity is defined as the complementary autocorrelation function c_{y_s} of $y_s(k)$ being zero, i.e., $c_{y_s}(\tau) = \mathrm{E}\left[y_s(k)y_s(k-\tau)\right] = 0$, meaning that real and imaginary parts of the compensated outputs are equally powerful and instantaneously mutually uncorrelated. Similarly, the traditional autocorrelation function γ_{y_s} is given by $\gamma_{y_s} = \mathrm{E}[y_s(k)y_s^*(k-\tau)]$. Now, the compensator coefficients $\mathbf{w}_s$, restoring the circularity of the compensated signal, can be solved by using the observed subband signal second order statistics $c_{\bar{v}_s}(\tau) = \mathrm{E}\left[\bar{v}_s(k)\bar{v}_s(k-\tau)\right]$ and $\gamma_{\bar{v}_s}(\tau) = \mathrm{E}[\bar{v}_s(k)\bar{v}_s^*(k-\tau)]$. The complementary autocorrelation values are placed in a column-vector

$$\mathbf{c}_{\bar{v}_s} = \mathrm{E}\left[\bar{\mathbf{v}}_s(k)\bar{v}_s(k)\right] = \left[c_{\bar{v}_s}(0), c_{\bar{v}_s}(1), ..., c_{\bar{v}_s}(N-1)\right]^T, \tag{12}$$

where

$$\bar{\mathbf{v}}_s(k) = \left[\bar{v}_s(k), \bar{v}_s(k-1), ..., \bar{v}_s(k-N+1)\right]^T, \tag{13}$$

having the length of N. In parallel, the autocorrelation function values are used to create the matrices

$$\mathbf{\Gamma}_{\bar{v}_s} = \begin{bmatrix} \gamma_{\bar{v}_s}(0) & \gamma_{\bar{v}_s}(1) & \cdots & \gamma_{\bar{v}_s}\bar{v}_s(N-1) \\ \gamma_{\bar{v}_s}^*(1) & \gamma_{\bar{v}_s}(0) & \cdots & \gamma_{\bar{v}_s}(N-2) \\ \vdots & \vdots & \ddots & \vdots \\ \gamma_{\bar{v}_s}^*(N-1) & \gamma_{\bar{v}_s}^*(N-2) & \cdots & \gamma_{\bar{v}_s}(0) \end{bmatrix}, \tag{14}$$

and

$$\mathbf{\Gamma}'_{\bar{v}_s} = \begin{bmatrix} \gamma_{\bar{v}_s}(0) & \gamma_{\bar{v}_s}(1) & \cdots & \gamma_{\bar{v}_s}(N-1) \\ \gamma_{\bar{v}_s}(1) & \gamma_{\bar{v}_s}(0) & \cdots & \gamma_{\bar{v}_s}(N-2) \\ \vdots & \vdots & \ddots & \vdots \\ \gamma_{\bar{v}_s}(N-1) & \gamma_{\bar{v}_s}(N-2) & \cdots & \gamma_{\bar{v}_s}(0) \end{bmatrix}. \tag{15}$$

Finally, the approximately optimal compensator coefficients are given by

$$\mathbf{w}_s = -(\mathbf{\Gamma}_{\bar{v}_s} + \mathbf{\Gamma'}_{\bar{v}_s})^{-1}\mathbf{c}_{\bar{v}_s} \tag{16}$$

In above, $s = 1$ for single-band reception and generally $s \in \{1, ..., S\}$ for reception of S signal bands. In practice, sample estimates of the second-order statistics $c_{\bar{v}_s}(\tau)$ and $\gamma_{\bar{v}_s}(\tau)$ are used and calculated over a block of received data signals.

IV. SIMULATION RESULTS FOR COMPENSATION PERFORMANCE

Herein, the transfer function design and digital MFI compensation, discussed in Sections II and III, respectively, are simulated using realistic reception scenario. It is assumed that there is a mirror-band signal present with varied power level in order verify the performance with differing levels of the MFI. The receiver front-end is assumed to have image rejection ratio of 30 dB. In addition, the real gain values in all the modulator coefficients are randomly deviated in order to model the implementation inaccuracies and evaluate their effects. These gains are drawn from a uniform distribution of ±1 % around the ideal value. In other words, when, e.g., $R^{(1)} = r_{\text{re}}^{(1)} + jr_{\text{im}}^{(1)}$, the realized value $\hat{r}_{\text{re},1}^{(1)}$ is uniformly distributed between $0.99r_{\text{re},1}^{(1)}$ and $1.01r_{\text{re},1}^{(1)}$ and similarly for

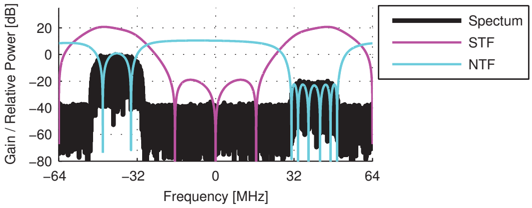

Fig. 6. An example spectrum of input signal together with the ideal designed transfer functions (overall response). The desired 16-QAM signal is located around the center-frequency of 40 MHz.

the other coefficients. 200 random realizations are used for the final results. It should be noted that because of these mismatches, e.g., the ISTF is clearly frequency-selective also inside the signal band to be received, as shown in Fig. 4. The sampling frequency is assumed to be 128 MHz.

A 16-QAM waveform around center-frequency of 40 MHz is used as a receiver input signal with 18 dB SNR. The mirror-frequency signal, being a major source of the MFI, is simulated on the relative power level from -20 dB to +60 dB compared to the desired signal. True 3-bit I/Q quantizers are simulated in both the QΣΔM stages. The input scenario is illustrated in Fig. 6 together with the ideal transfer functions.

Fig. 7 shows clearly that employing multi-tap compensation gives significant interference rejection gain in this wideband signal scenario. For example, at the rejection level of 10 dB, single-tap compensation extends the blocker tolerance only by 3 dB while two-tap compensation gives further 7 dB of additional tolerance. Thus in the latter case, the tolerance is improved by 10 dB compared to no-compensation case. Overall, it is clear that two-tap compensation results in significantly improved performance over the whole practical blocker level range. With relative blocker powers below 0 dB, the blocker signal starts get buried in the noise while, also the experienced MFI level drops, which can be seen from the good rejection level even without compensation. With this compensation performance the whole receiver can be made more robust against mirror-band blockers, which can easily appear at the challenging conditions typical for CR.

V. CONCLUSION

This article proposed a reconfigurable QΣΔM transfer function design fit for reception and detection of communications waveforms with 20 MHz bandwidth. In addition, the design considers the inherent problem of I/Q imbalance in the preceding receiver stages and the QΣΔM itself, creating unavoidable MFI. It was shown that by digital post-compensation the interference rejection can be significantly improved considering also the frequency-selective characteristics that are unavoidable when dealing with wideband signals.

REFERENCES

[1] I. F. Akyildiz, W.-Y. L. Lee, M. C. Vuran, and S. Mohanty, "NeXt generation/dynamic spectrum access/cognitive radio wireless networks: a survey," *Computer Networks*, vol. 50, pp. 2127–2159, 2006.

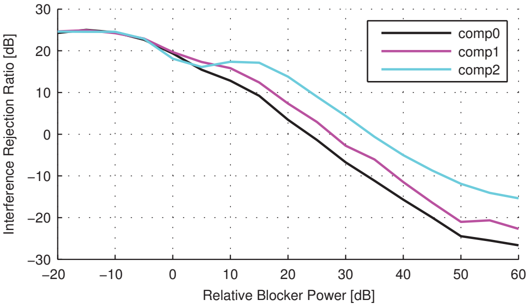

Fig. 7. Interference rejection ratios for the 16-QAM signal as a function of relative blocker signal power. No compensation, single-tap compensation [7] and two-tap compensation cases are simulated

[2] M. Ismail and D. Rodríguez de Llera González, Eds., *Radio Design in Nano-meter Technologies*. Dordrecht, Netherlands: Springer, 2006.
[3] S. Jantzi, K. Martin, and A. Sedra, "A quadrature bandpass delta-sigma modulator for digital radio," *IEEE J. Solid-State Circuits*, vol. 32, no. 12, pp. 1935–1950, Dec. 1997.
[4] J. Marttila, M. Allén, and M. Valkama, "Multi-stage quadrature sigma-delta modulators for reconfigurable multi-band analog-to-digital interface in cognitive radio devices," *EURASIP J. Wirel. Commun. Netw.*, vol. 2011, no. 1, pp. 1–23, Oct. 2011.
[5] P. Aziz, H. Sorensen, and J. van der Spiegel, "An overview of sigma-delta converters: how a 1-bit ADC achieves more than 16-bit resolution," *IEEE Signal Processing Mag.*, vol. 13, no. 1, pp. 61–84, Sept. 1996.
[6] A. Morgado, J. Gerardo Garcia, S. Asghar, L. Guerrero, R. del Río, and J. de la Rosa, "A power-scalable concurrent cascade 2-2-2 SC ΣΔ modulator for software defined radio," in *Proc. IEEE Int. Symp. Circuits and Syst.*, Seoul, South Korea, 20-23 May 2012.
[7] J. Marttila, M. Allén, and M. Valkama, "Digital mirror-frequency interference compensation for multiband quadrature sigma-delta ADC based cognitive radio receivers," in *Proc. 55th IEEE Int. Midwest Symp. Circuits and Syst.*, Boise, ID, 5-8 Aug. 2012, (invited paper).
[8] ——, "Frequency-agile multiband quadrature sigma-delta modulator for cognitive radio: Analysis, design and digital post-processing," *IEEE J. Sel. Areas in Commun.*, vol. 31, no. 11, Nov. 2013.
[9] L. Anttila, M. Valkama, and M. Renfors, "Circularity based I/Q imbalance compensation in wideband direct-conversion receivers," *IEEE Trans. Veh. Technol.*, vol. 57, no. 3, pp. 2099–2113, July 2008.
[10] S. Reekmans, P. Rombouts, and L. Weyten, "Mismatch insensitive double-sampling quadrature bandpass ΣΔ modulation," *IEEE Trans. Circuits and Syst. I, Reg. Papers*, vol. 54, no. 12, pp. 2599–2607, Dec. 2007.
[11] K.-P. Pun, C.-S. Choy, C.-F. Chan, and J. da Franca, "An I/Q mismatch-free switched-capacitor complex sigma-delta modulator," *IEEE Trans. Circuits and Syst. I, Express Briefs*, vol. 51, no. 5, pp. 254–256, May 2004.
[12] Y. Kumar, E. Bonizzoni, A. Patra, and F. Maloberti, "Interference rejection in delay line based quadrature band-pass ΣΔ modulators," in *Proc. IEEE Int. Symp. Circuits and Syst.*, Seoul, South Korea, 20-23 May 2012.
[13] L. Yu and W. Snelgrove, "A novel adaptive mismatch cancellation system for quadrature IF radio receivers," *IEEE Trans. Circuits Syst. II, Analog Digit. Signal Process.*, vol. 46, no. 6, pp. 789–801, June 1999.
[14] R. Schreier and G. Temes, *Understanding Delta-Sigma Data Converters*. Hoboken, NJ: Wiley, 2005.
[15] R. Schreier, "An empirical study of high-order single-bit delta-sigma modulators," *IEEE Trans. Circuits Syst. II, Analog Digit. Signal Process.*, vol. 40, no. 8, pp. 461–466, Aug. 1993.

PUBLICATION 7

Jaakko Marttila, Markus Allén and Mikko Valkama, “Frequency-agile multi-band quadrature sigma-delta modulator for cognitive radio: analysis, design and digital post-processing,” *IEEE Journal on Selected Areas in Communications*, volume 31, number 11, pages 2222–2236, November 2013.

Frequency-Agile Multiband Quadrature Sigma-Delta Modulator for Cognitive Radio: Analysis, Design and Digital Post-Processing

Jaakko Marttila, Markus Allén and Mikko Valkama

Abstract – **A quadrature ΣΔ analog-to-digital converter (ADC) is a promising solution for intermediate frequency digitizing software defined cognitive radio (CR) receivers because of, e.g., multiband capability and power efficiency. However, inherent coefficient mismatches between the in-phase and quadrature rails can severely damage the performance of such receiver by creating mirror-frequency interference (MFI). In this article, a novel frequency-agile and reconfigurable transfer function design, allowing digital post-compensation of the MFI, is proposed. The design is based on a novel closed-form transfer function model for higher-order quadrature ΣΔ modulators (QΣΔMs) under implementation inaccuracies, proposed herein. By doing the compensation in digital domain, it is possible to take into account all error-sources of the receiver chain, including, e.g., a quadrature mixer before the ADC, at once. This capability is obtained by preserving the mirror-band signal information and using the noise transfer function of a QΣΔM to remove quantization noise from therein. This is demonstrated in a multiband scenario aimed for CR receivers, where a number of frequency channels can be received and detected in parallel. Practical examples of the transfer function analysis under implementation inaccuracies and the post-compensation performance are given with a two-stage QΣΔM, having stage-orders of four, allowing eighth order noise shaping.**

Index Terms – **Analog-to-digital conversion, complex filters, cognitive radio, digital radio, I/Q imbalance, mirror-frequency interference, radio receivers, sigma-delta modulation**

I. INTRODUCTION

A. Research Motivation

A rapid growth in the number of mobile devices accessing the internet, together with an increase in data connection speeds per device, has created novel challenges for radio spectrum usage [1]. Thus, it is nowadays very important to utilize the available spectrum as efficiently as possible. This has led to the introduction of dynamic spectrum access and cognitive radio (CR) concepts [1], [2]. At the same time, the transceivers should be small-sized, power efficient, highly integrable and cheap [3]–[7]. This is why the trend in the recent years has been to move towards software defined radio (SDR) solutions, where most of the functionalities

---

Manuscript received April 13, 2012 and revised August 31, 2012. This work was supported by the Academy of Finland (under the project entitled "Digitally-enhanced RF for cognitive radio devices"), the Finnish Funding Agency for Technology and Innovation (Tekes, under the projects entitled "Advanced techniques for RF impairment mitigation in future wireless radio systems" and "Enabling methods for dynamic spectrum access and cognitive radio"), Austrian Center of Competence in Mechatronics (ACCM, under the project entitled "Wireless communication technologies"), Tampere University of Technology Graduate School, HPY Research Foundation and Nokia Foundation.

The authors are with the Department of Communications Engineering, Tampere University of Technology, P.O. Box 553, FI-33101 Tampere, Finland (e-mail: jaakko.marttila@tut.fi; markus.allen@tut.fi; mikko.e.valkama@tut.fi).

are implemented in digital domain [5]–[10]. This also facilitates efficient post-compensation of interference and distortion generated by the remaining analog radio components, easing the demand for near-perfect circuit implementations [11]. However, the scheme sets high demands for the A/D interface of the receiver [2], [8], [10], [12], [13].

The SDR based on direct-conversion or wideband intermediate frequency (IF) digitization has been proposed as a solution for the CR physical layer [8], [14]–[16] . Therein, analog-to-digital converters (ADCs) using bandpass ΣΔ modulator have received considerable attention [8], [14], [16]. Furthermore, quadrature ΣΔ modulators (QΣΔMs) have been proven to have several performance benefits over the real counterparts [17], [18], making this a very interesting choice for development of future CR receivers [19]. This receiver principle is illustrated in Fig. 1, where the components of focus in this article are highlighted with grey background.

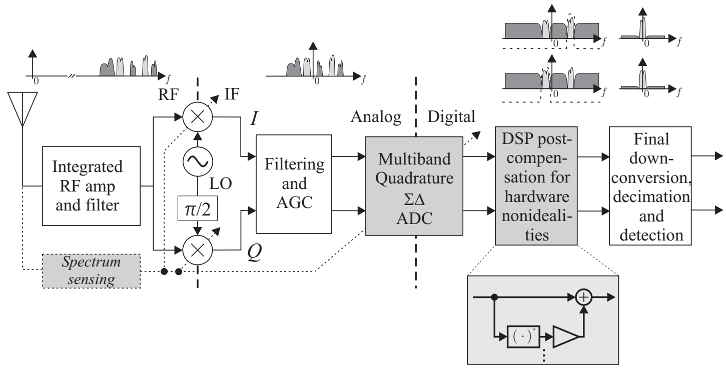

Fig. 1. Block diagram of a *multiband* low-IF quadrature receiver, based on frequency-agile QΣΔM. Principal spectra, where the two light grey signals are the desired ones, are illustrating the signal compositions at each stage. Post-compensation scheme is illustrated in simplified format.

Traditional Nyquist ADCs (possibly with oversampling) divide the conversion precision equally on all the frequencies and thus, similar resolution is used over the whole band even if unnecessary. Furthermore, in wideband SDR receiver the resolution demand might be even higher because of the increased dynamic range due to numerous waveforms with differing power levels entering the ADC [9]. Opposed to Nyquist converters, ΣΔ converters have different noise transfer function (NTF) and signal transfer function (STF) and inherent tradeoff between the sampling frequency and resolution [18], [20], allowing sophisticated allocation of the quantization precision. Thus, also the power used for sampling and quantizing can be optimized, when only the interesting frequency bands are cleared of the quantization noise. With multiband QΣΔM, this reconfigurability has even more degrees-of-freedom, allowing frequency-agile reception of multiple narrowband signals or few wideband waveforms in parallel [19].

Unfortunately, exploiting complex-valued signal processing with quadrature circuits brings the problem of matching in-phase (I) and quadrature (Q) rails [18], [21]. This is usually known as I/Q imbalance and generates mirror-frequency interference (MFI) via spectral mirroring. Especially under challenging signal conditions typical for SDR and CR receivers, the MFI can degrade the quality of the received signals significantly [6], [10], [19]. Specific to the QΣΔM, also the quantization noise generated inside the modulator experiences spectral mirroring [18], [21]. This article proposes a novel transfer function design for QΣΔMs combined with digital post-compensation of exactly this interference, taking the mirror-frequency interference originating from both the input signal and from the quantization noise into account. The compensation block is shown at principal level also in Fig. 1. Other possible error-sources, such as sampling jitter or modulator nonlinearity are not considered in this work.

B. State-of-the-Art in Quadrature ΣΔ Modulator Design and Mirror-frequency Interference Compensation

A single-stage quadrature ΣΔ converter for single-band IF digitization was proposed in [18]. Therein, the STF is used to attenuate out-of-band signal content in the input of the QΣΔM. In addition, one NTF zero is used to create a noise shaping notch on the mirror-band, in order to reduce the MFI originating from the quantization noise therein. However, this does not take into account the mirroring of the input signal in any way. This is very important because in a CR-like system, the power level of the mirror-band signal can be tens of dBs higher compared to the desired signal to be detected [6]. The MFI might be originating from either the analog radio front-end or the QΣΔM itself. If the error source, such as a quadrature mixer, is located early in the receiver chain, the filtering before the A/D stage cannot mitigate this problem. Thus, it is desirable to compensate the interference of the whole receiver in the digital domain.

For the digital interference compensation as such, there are multiple solutions in the literature, e.g., [22]–[26]. In general, it is common for the digital compensation that some information of the original interference sources should be available in the digital domain. Precisely this information is lost if the mirror-frequency signals are filtered out in the analog domain. In this article, a multiband STF design preserving the mirror-band information, preliminarily proposed by the authors in [27], is further developed and analyzed in realistic conditions. This is done with the help of a novel transfer function analysis method under implementation inaccuracies proposed in Section III. The analysis method is one of the key contributions of this article and allows derivation of the NTF and the STF, giving also the image noise transfer function (INTF) and the image signal transfer function (ISTF) of an I/Q mismatched general multistage QΣΔM having arbitrary number of stages of arbitrary order. The multiband design of QΣΔM transfer functions has been discussed in [19], [28], [35] and [36]. In [35], the basic multiband concept was proposed, being then developed further for CR devices in [19], [28]. Moreover, in addition to [18], designs mitigating the MFI generated inside the QΣΔM are proposed in [19], [28], [29]–[34]. However, none of these designs is able to mitigate MFI appearing before the actual ΣΔ modulator (e.g., the I/Q mixer as an error source) [19], [28], [29], [33] or to avoid inserting calibration signals [29], additional analog circuitry [31], [32] or impairing the sampling properties by sharing the capacitors [34]. These limitations are overcome by the proposed QΣΔM solutions in this article.

In demonstrating the overall receiver concept and performance, the blind MFI suppression algorithm published originally in [22] is deployed. This frequency-independent algorithm is chosen based on the inherent oversampling present in the ΣΔ conversion (assuming mild frequency selectivity inside a single subband) and the simplicity of the blockwise compensator.

The rest of this article is organized as follows. In Section II, QΣΔM basics are reviewed whereas Section III proposes a novel transfer function analysis method for an I/Q mismatched multistage QΣΔM. The transfer function design facilitating the digital post-compensation of MFI, independent of the interference source, and the compensation itself, are proposed in Section IV. Thereafter, Section V presents the results of the design and compensation scheme discussed in the previous section using both closed-form transfer function analysis and computer simulations. Finally, Section VI concludes the article.

II. QUADRATURE ΣΔ MODULATION FOR COGNITIVE RADIO

A. Basics of Quadrature ΣΔ Modulation

The analytical presentation of a QΣΔM is based on [18]. The structure of a *P*th order QΣΔM, employing complex-valued input $u(k)$, quantization noise $e(k)$ and output $v(k)$ is presented in Fig. 2. The ΣΔ modulator architecture considered in this paper is a complex-valued version of cascaded integrators with distributed feedback and input [18], [37]. This allows the use of frequency asymmetric transfer functions (NTF and STF). By adopting a linear model of the modulator [18], the output of an ideal modulator (without implementation inaccuracies) is given in z-domain by

$$V^{ideal}[z] = STF[z]U[z] + NTF[z]E[z]. \tag{1}$$

Although not exactly accurate, because the quantization noise is actually correlated with the quantizer input, this model for the ΣΔ modulators is widely adopted because of its applicability for the modulator design and analysis [37].

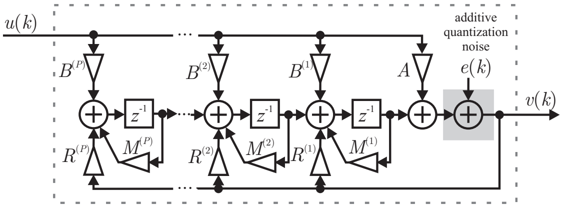

Fig. 2. Discrete-time linearized model of a *P*th-order QΣΔM with complex-valued signals and coefficients.

The *P*th order structure of Fig. 2 allows placing *P* NTF and STF zeros on the conversion band, together with *P* poles common to both of the transfer functions. The main idea in the design process is to use feedback gains $M^{(1)}$ to $M^{(P)}$ of the complex integrators to shift the NTF zeros away from the zero frequency. Thereafter, the feedback gains of the whole modulator ($R^{(1)}$ to $R^{(P)}$) are used to define the locations of the poles of both transfer functions. Finally, the input coefficients, A and $B^{(1)}$ to $B^{(P)}$, are used to set the zeros of the STF. Thus, the NTF of the QΣΔM is given by

$$NTF[z] = \frac{1}{1 - \sum_{p=1}^{P} R^{(p)} \prod_{i=1}^{p} \frac{z^{-1}}{1 - M^{(i)} z^{-1}}} \tag{2}$$

and the corresponding STF is defined as

$$STF[z] = \frac{A + \sum_{p=1}^{P} B^{(p)} \prod_{i=1}^{p} \frac{z^{-1}}{1 - M^{(i)} z^{-1}}}{1 - \sum_{p=1}^{P} R^{(p)} \prod_{i=1}^{p} \frac{z^{-1}}{1 - M^{(i)} z^{-1}}}, \tag{3}$$

where the $z^{-1} \, / \, (1 - M^{(i)} z^{-1})$ terms are the transfer functions of the complex loop filters (integrators). It should be noted that the denominators of both transfer functions are equal, indicating the presence of common poles, as mentioned above.

It is a common choice to place the NTF zeros on the desired signal band, in order to shape the noise towards out-of-band frequencies [18]. At the same time, the STF response can be used to implement part of the receiver selectivity filtering inside the QΣΔM [18], [19], [28]. The exact locations of the common poles are, on the other hand, a question of design optimization. One well-documented choice for the poles is to use Butterworth positions around the NTF zeros [18]. The transfer function design aspects will be further discussed in Section IV, taking the effects of the implementation inaccuracies and related compensation schemes into account in CR receivers.

B. *Multiband Transfer Function Design*

A multiband transfer function design for QΣΔM was originally introduced in [35] and targeted for CR devices in [28] with further discussions in [19] and [36]. It is an efficient tool aiming towards a flexible and reconfigurable A/D interface for CR devices. Herein, the basics of the concept are reviewed shortly and further details can be checked from, e.g., [19], [28].

Adopting a Pth order QΣΔM allows to place P NTF zeros on the conversion band, as already discussed above. In addition, these zeros do not need to be contiguous. Fig. 3 shows a principal example of a multiband reception scheme, where two noncontiguous frequency bands and information signals (with center frequencies of $f_{C,1}$ and $f_{C,2}$) are to be received. The NTF zeros are used to remove the noise from those bands and, at the same time, the STF is used to attenuate the out-of-band signal content.

The transfer function design principle of Fig. 3 would be suitable for an ideal receiver. However, the effects of implementation inaccuracies in the receiver hardware set additional challenges, which should also be taken into account in the transfer function design. The novel multiband reception combined with digital post-compensation of interference induced by the preceding radio front-end or the QΣΔM itself is discussed further in Section IV.

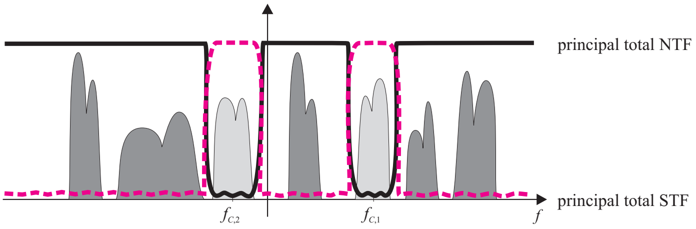

Fig. 3. Principal illustration of a complex multiband QΣΔM scheme for cognitive radio devices. The light grey signals are assumed to be the desired ones and the principal total STF and NTF are illustrated with dotted and solid lines, respectively.

C. Multistage Quadrature ΣΔ Modulation

Multistage ΣΔ modulation is an efficient way to improve the noise shaping efficiency of a ΣΔ ADC without impractical increase in the order of a single modulator stage. For example, the stability analysis for a single modulator stage of very high order becomes cumbersome [37]. The multistage principle was first introduced with lowpass ΣΔ modulators [37], but has been thereafter extended to cover also quadrature bandpass modulators [19], [29], [38], [39]. In [19], a general transfer function model for an ideal QΣΔM having L stages was introduced. This is reviewed herein, as a basis for the following analysis, taking also implementation inaccuracies of the arbitrary order stages into account (Section III).

The output of an ideal L-stage QΣΔM, depicted in Fig. 4, is given by

$$V^{ideal}[z] = \sum_{l=1}^{L} (-1)^{l+1} H_l^D[z] V_l^{ideal}[z],\ 1 \le l \le L,\ l \in \mathbb{Z} \tag{4}$$

where

$$V_l^{ideal}[z] = STF_l^{ideal}[z] U_l[z] + NTF_l^{ideal}[z] E_l[z],\ 1 \le l \le L,\ l \in \mathbb{Z} \tag{5}$$

and

$$H_l^D[z] = \frac{H_1^D[z] \prod_{l=1}^{L-1} NTF_l^{ideal}[z]}{\prod_{l=2}^{L} STF_l^{ideal}[z]},\ 1 \le l \le L,\ l \in \mathbb{Z}. \tag{6}$$

The digital filters $H_l^D[z]$ are used to match the nonshaped digital noise estimate to the NTF-shaped noise at the output of the previous stage. In addition, (4) can be rewritten as

$$V^{ideal}[z] = STF_1^{ideal}[z] STF_2^D[z] U[z] + \frac{\prod_{l=1}^{L} NTF_l^{ideal}[z]}{\prod_{l=3}^{L} STF_l^{ideal}[z]} E_L[z] = STF_{\text{TOT}}^{ideal}[z] U[z] + NTF_{\text{TOT}}^{ideal}[z] E_L[z], \tag{7}$$

from where it is clearly visible that the STF of the first stage is shaping the signal component, being thereafter filtered with the STF of the second stage and on top of this appears the quantization noise of the last stage shaped by the product of all the stage NTFs (assuming the STFs for stages $l \ge 3$ to be unity). However, complete cancellation of the noise of the earlier stages demands accurate matching of the analog transfer functions and the digital filters, by using, e.g., adaptive filters [40], [41].

III. CLOSED-FORM TRANSFER FUNCTION ANALYSIS FOR ARBITRARY-ORDER MULTISTAGE QΣΔM UNDER IMPLEMENTATION INACCURACIES

In this section, a novel matrix algebraic method is proposed for transfer function analysis of I/Q mismatched multistage quadrature ΣΔ modulators. Such analysis is missing in the current state-of-the-art literature. The proposed analysis method has the advantage of being easily applicable to cover arbitrary-order QΣΔMs. Herein this is demonstrated by deriving the four transfer

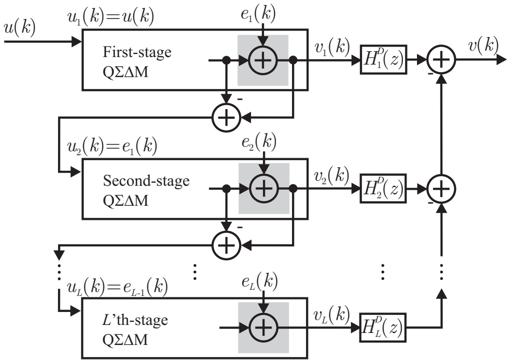

Fig. 4. Multistage QΣΔM with arbitrary-order noise shaping in all the individual stages. Filters $H_1^D[z]$ to $H_L^D[z]$ are implemented digitally.

functions (STF, ISTF, NTF and INTF) for a *P*th order modulator. First, the matrix representation of an I/Q mismatched complex multiplication and division are introduced, forming the basis for the transfer function analysis, proposed in the following.

A. Matrix Representation of Mismatched Complex Multiplication and Division

Realizing a complex multiplication is an essential part of the QΣΔM implementation. This is because the input of the modulator is a complex-valued signal and modulator coefficients are complex-valued (see Fig. 2). Thus, the *P*th order QΣΔM of Fig. 2 has generally $3P+1$ complex multiplications ($P+1$ inputs, P loop filters and P feedbacks). The matrix representation of a complex number [42], [43] is used here to describe those multiplications, as discussed in the following.

A complex multiplication is implemented with four real multiplications as shown in Fig. 5. Mathematically this is formulated as

$$v(k)=v_{\mathrm{I}}(k)+jv_{\mathrm{Q}}(k)=Au(k)=(a_{\mathrm{re}}+ja_{\mathrm{im}})(u_{\mathrm{I}}(k)+ju_{\mathrm{Q}}(k))=a_{\mathrm{re}}u_{\mathrm{I}}(k)-a_{\mathrm{im}}u_{\mathrm{Q}}(k)+ja_{\mathrm{im}}u_{\mathrm{I}}(k)+ja_{\mathrm{re}}u_{\mathrm{Q}}(k), \qquad (8)$$

assuming ideal matching of the real-valued coefficients ($a_{\mathrm{re},1}=a_{\mathrm{re},2}=a_{\mathrm{re}}$ and $a_{\mathrm{im},1}=a_{\mathrm{im},2}=a_{\mathrm{im}}$). Introducing mismatches to the multiplying coefficients, due to inherent implementation inaccuracies, (see Fig. 5) gives

$$v_{\mathrm{mm}}(k)=a_{\mathrm{re},1}u_{\mathrm{I}}(k)-a_{\mathrm{im},2}u_{\mathrm{Q}}(k)+ja_{\mathrm{im},1}u_{\mathrm{I}}(k)+ja_{\mathrm{re},2}u_{\mathrm{Q}}(k). \qquad (9)$$

From (9), the real and imaginary parts of the result can be solved to be $v_{\mathrm{I,mm}}(k)=a_{\mathrm{re},1}u_{\mathrm{I}}(k)-a_{\mathrm{im},2}u_{\mathrm{Q}}(k)$ and $v_{\mathrm{Q,mm}}(k)=a_{\mathrm{im},1}u_{\mathrm{I}}(k)+a_{\mathrm{re},2}u_{\mathrm{Q}}(k)$.

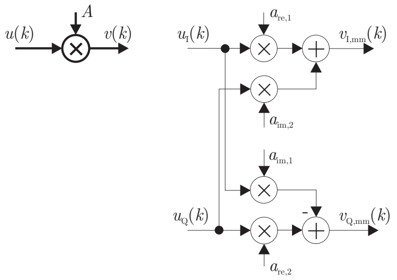

Fig. 5. Complex multiplication $v(k)=Au(k)$ implemented with ideal complex-valued (left) and nonideal real-valued (right) signal processing.

Now, according to basic matrix algebra, a 1×2 vector consisting of the real valued outputs ($v_{\mathrm{I,mm}}(k)$ and $v_{\mathrm{Q,mm}}(k)$) of the mismatched complex multiplication can be solved by single matrix multiplication. This holds when the multiplier coefficients ($a_{\mathrm{re},1}$, $a_{\mathrm{im},1}$, $a_{\mathrm{im},2}$ and $a_{\mathrm{re},2}$) are used to form a matrix $\mathbf{A}_{\mathrm{mat}}$. This $\mathbf{A}_{\mathrm{mat}}$ is used to multiply a 1×2 vector consisting of the real valued inputs ($u_{\mathrm{I}}(k)$ and $u_{\mathrm{Q}}(k)$) to give the outputs, i.e.,

$$\begin{aligned}\begin{bmatrix} v_{\mathrm{I,mm}}(k) & v_{\mathrm{Q,mm}}(k) \end{bmatrix} = \begin{bmatrix} u_{\mathrm{I}}(k) & u_{\mathrm{Q}}(k) \end{bmatrix} \mathbf{A}_{\mathrm{mat}} &= \begin{bmatrix} u_{\mathrm{I}}(k) & u_{\mathrm{Q}}(k) \end{bmatrix} \begin{bmatrix} a_{\mathrm{re},1} & a_{\mathrm{im},1} \\ -a_{\mathrm{im},2} & a_{\mathrm{re},2} \end{bmatrix} \\ &= \begin{bmatrix} a_{\mathrm{re},1} u_{\mathrm{I}}(k) - a_{\mathrm{im},2} u_{\mathrm{Q}}(k) & a_{\mathrm{im},1} u_{\mathrm{I}}(k) + a_{\mathrm{re},2} u_{\mathrm{Q}}(k) \end{bmatrix}.\end{aligned} \tag{10}$$

Now, by comparing (9) to (10), it is evident that the results are equal.

Furthermore, a division of two complex-valued coefficients $A = a_{\mathrm{re}} + j a_{\mathrm{im}}$ and $B = b_{\mathrm{re}} + j b_{\mathrm{im}}$, being ideally defined as

$$\frac{A}{B} = \frac{AB^*}{|B|^2} = \frac{a_{\mathrm{re}} b_{\mathrm{re}} + a_{\mathrm{im}} b_{\mathrm{im}} + j(a_{\mathrm{re}} b_{\mathrm{im}} - a_{\mathrm{im}} b_{\mathrm{re}})}{b_{\mathrm{re}}^2 + b_{\mathrm{im}}^2}, \tag{11}$$

can also be represented in matrix format, taking inherent coefficient mismatches into account. This is done by right-multiplying $\mathbf{A}_{\mathrm{mat}}$, defined above, with the inverse of the matrix $\mathbf{B}_{\mathrm{mat}}$, defined similar to $\mathbf{A}_{\mathrm{mat}}$. This is justified by assuming the coefficient matrices invertible because of the 2-by-2 structure where the real part (diagonal) elements share the same sign and the imaginary part (cross diagonal) elements have opposite signs, making the determinant nonzero in practical cases. This results in

$$\mathbf{A}_{\mathrm{mat}} \mathbf{B}_{\mathrm{mat}}^{-1} = \begin{bmatrix} a_{\mathrm{re},1} & a_{\mathrm{im},1} \\ -a_{\mathrm{im},2} & a_{\mathrm{re},2} \end{bmatrix} \begin{bmatrix} b_{\mathrm{re},1} & b_{\mathrm{im},1} \\ -b_{\mathrm{im},2} & b_{\mathrm{re},2} \end{bmatrix}^{-1} = \frac{1}{b_{\mathrm{re},1} b_{\mathrm{re},2} + b_{\mathrm{im},1} b_{\mathrm{im},2}} \begin{bmatrix} a_{\mathrm{re},1} b_{\mathrm{re},2} + a_{\mathrm{im},1} b_{\mathrm{im},2} & -a_{\mathrm{re},1} b_{\mathrm{im},1} + a_{\mathrm{im},1} b_{\mathrm{re},1} \\ -\left(-a_{\mathrm{re},2} b_{\mathrm{im},2} + a_{\mathrm{im},2} b_{\mathrm{re},2}\right) & a_{\mathrm{re},2} b_{\mathrm{re},2} + a_{\mathrm{im},2} b_{\mathrm{im},1} \end{bmatrix}, \tag{12}$$

giving the real and imaginary parts giving the real and imaginary parts of the mismatched scalar complex division, opposed to (11) where ideal coefficients are assumed.

Although the complex division operation is not specifically implemented in ΣΔ structure, it is an essential part of the transfer function analysis for such system. A simple example of this is the transfer function of a single loop-filter, $H[z] = 1 / (z - M)$. Now, the four transfer function components induced by the implementation inaccuracies [21] can be verified to be

$$\begin{aligned}\begin{bmatrix} H_{\mathrm{re},1}[z] & H_{\mathrm{im},1}[z] \\ -H_{\mathrm{im},2}[z] & H_{\mathrm{re},2}[z] \end{bmatrix} &= \left(\mathbf{I}z - \mathbf{M}_{\mathrm{mat}}\right)^{-1} \\ &= \begin{bmatrix} z - m_{\mathrm{re},1} & -m_{\mathrm{im},1} \\ m_{\mathrm{im},2} & z - m_{\mathrm{re},2} \end{bmatrix}^{-1} = \frac{1}{(z - m_{\mathrm{re},1})(z - m_{\mathrm{re},2}) + m_{\mathrm{im},1} m_{\mathrm{im},2}} \begin{bmatrix} z - m_{\mathrm{re},2} & m_{\mathrm{im},1} \\ -m_{\mathrm{im},2} & z - m_{\mathrm{re},1} \end{bmatrix},\end{aligned} \tag{13}$$

where $\mathbf{M}_{\mathrm{mat}}$ is defined in a corresponding manner to $\mathbf{A}_{\mathrm{mat}}$ and $\mathbf{B}_{\mathrm{mat}}$ above and $\mathbf{I}$ is a 2-by-2 identity matrix. Assuming ideal matching of the real coefficients, this simplifies to

$$\begin{bmatrix} H_{\mathrm{re}}[z] & H_{\mathrm{im}}[z] \\ -H_{\mathrm{im}}[z] & H_{\mathrm{re}}[z] \end{bmatrix} = \begin{bmatrix} \dfrac{z - m_{\mathrm{re}}}{(z - m_{\mathrm{re}})^2 + m_{im}^2} & \dfrac{m_{\mathrm{im}}}{(z - m_{\mathrm{re}})^2 + m_{im}^2} \\ \dfrac{-m_{\mathrm{im}}}{(z - m_{\mathrm{re}})^2 + m_{im}^2} & \dfrac{z - m_{\mathrm{re}}}{(z - m_{\mathrm{re}})^2 + m_{im}^2} \end{bmatrix}, \tag{14}$$

giving finally

$$H[z] = H_{\mathrm{re}}[z] + jH_{\mathrm{im}}[z] = \frac{1}{z - m_{\mathrm{re}} - jm_{\mathrm{im}}} = \frac{1}{z - M}. \tag{15}$$

From the above analysis, it can be concluded that by replacing the ideal complex multipliers by the matrix multiplication of (10), the effects of implementation inaccuracies can be included in a straightforward manner. In addition, the right-multiplication with the inverse of the coefficient matrix can be used to replace the complex division in the transfer function analysis, as shown in (13)–(15). This gives the advantage of being able to include the implementation inaccuracies in the overall QΣΔM response analysis in an efficient manner. The application of this technique in the transfer function analysis of an arbitrary-order I/Q mismatched QΣΔM is introduced in the following subsection.

B. Arbitrary-order Multistage QΣΔM Transfer Function Analysis with Matrix Representation

Herein, the matrix representation of a complex multiplication is used to derive the output and the transfer functions of I/Q mismatched arbitrary-order (order P) multistage (L stages) QΣΔM. The derivation is based on the ideal transfer functions introduced in Section II. The scalar multiplications in these equations ((1)–(3) and (4)–(7)) are replaced by matrix multiplications applying the possibly mismatched real-valued modulator coefficients. These coefficients are illustrated in Fig. 6 for the lth stage of a multistage QΣΔM, having order P. In this way, the work of manually analyzing individual signal paths of such a complicated structure can be avoided.

To start with, the coefficient matrices are defined in the following manner. The input coefficients in the branch feeding the quantizer of the lth stage are defined by

$$\mathbf{A}_{\mathrm{mat}}^{(l)} = \begin{bmatrix} a_{\mathrm{re},1}^{(l)} & a_{\mathrm{im},1}^{(l)} \\ -a_{\mathrm{im},2}^{(l)} & a_{\mathrm{re},2}^{(l)} \end{bmatrix}. \tag{16}$$

In a similar manner, the rest of the input coefficients of the lth stage are defined by

$$\mathbf{B}_{\mathrm{mat}}^{(p,l)} = \begin{bmatrix} b_{\mathrm{re},1}^{(p,l)} & b_{\mathrm{im},1}^{(p,l)} \\ -b_{\mathrm{im},2}^{(p,l)} & b_{\mathrm{re},2}^{(p,l)} \end{bmatrix}, \tag{17}$$

where $p \in \{1, 2, ..., P\}$, going through the branches. Likewise, the loop filter and feedback coefficients are defined by

$$\mathbf{M}_{\mathrm{mat}}^{(p,l)} = \begin{bmatrix} m_{\mathrm{re},1}^{(p,l)} & m_{\mathrm{im},1}^{(p,l)} \\ -m_{\mathrm{im},2}^{(p,l)} & m_{\mathrm{re},2}^{(p,l)} \end{bmatrix} \tag{18}$$

and

$$\mathbf{R}_{\mathrm{mat}}^{(p,l)} = \begin{bmatrix} r_{\mathrm{re},1}^{(p,l)} & r_{\mathrm{im},1}^{(p,l)} \\ -r_{\mathrm{im},2}^{(p,l)} & r_{\mathrm{re},2}^{(p,l)} \end{bmatrix}, \tag{19}$$

having $p \in \{1, 2, ..., P\}$ again.

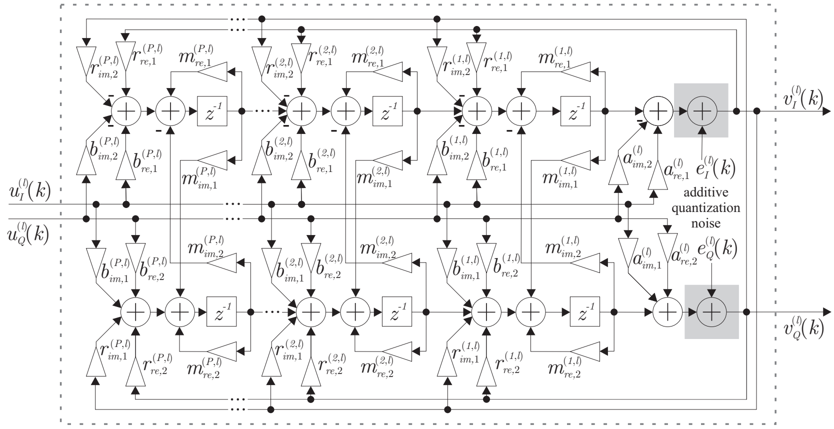

Fig. 6. Implementation structure of the lth QΣΔM stage of order P in a multistage QΣΔM with parallel real signals and coefficients taking possible mismatches into account.

Now, inserting these matrices into (2) in place of the (ideal) scalar coefficients results in

$$\begin{bmatrix} NTF_{\mathrm{re},1}^{(l)}[z] & NTF_{\mathrm{im},1}^{(l)}[z] \\ -NTF_{\mathrm{im},2}^{(l)}[z] & NTF_{\mathrm{re},2}^{(l)}[z] \end{bmatrix} = \left(\mathbf{I} - \sum_{p=1}^{P} \mathbf{R}_{\mathrm{mat}}^{(p,l)} \prod_{i=1}^{p} \mathbf{I} z^{-1} \left(\mathbf{I} - \mathbf{M}_{\mathrm{mat}}^{(i,l)} z^{-1} \right)^{-1} \right)^{-1}, \tag{20}$$

where $NTF_{\mathrm{re},1}^{(l)}[z]$, $NTF_{\mathrm{im},1}^{(l)}[z]$, $NTF_{\mathrm{im},2}^{(l)}[z]$ and $NTF_{\mathrm{re},2}^{(l)}[z]$ are the parallel real components of the widely-linear I/Q mismatched lth stage noise transfer function $NTF^{(l)}[z]$. The actual lth stage complex NTF and INTF can be solved [21] by

$$NTF_l[z] = \frac{NTF_{\mathrm{re},1}^{(l)}[z] + NTF_{\mathrm{re},2}^{(l)}[z]}{2} + j\frac{NTF_{\mathrm{im},1}^{(l)}[z] + NTF_{\mathrm{im},2}^{(l)}[z]}{2} \tag{21}$$

and

$$INTF_l[z] = \frac{NTF_{\mathrm{re},1}^{(l)}[z] - NTF_{\mathrm{re},2}^{(l)}[z]}{2} + j\frac{NTF_{\mathrm{im},1}^{(l)}[z] - NTF_{\mathrm{im},2}^{(l)}[z]}{2}, \tag{22}$$

respectively.

In parallel, the STF and the ISTF of the lth stage can be solved by replacing the scalar coefficients of (3) with the matrices of (16)–(19). This results in the real valued STF components given by

$$\begin{bmatrix} STF_{\mathrm{re},1}^{(l)}[z] & STF_{\mathrm{im},1}^{(l)}[z] \\ -STF_{\mathrm{im},2}^{(l)}[z] & STF_{\mathrm{re},2}^{(l)}[z] \end{bmatrix} = \left(\mathbf{A}_{\mathrm{mat}}^{(l)} + \sum_{p=1}^{P} \mathbf{B}_{\mathrm{mat}}^{(p,l)} \prod_{i=1}^{p} \mathbf{I} z^{-1} \left(\mathbf{I} - \mathbf{M}_{\mathrm{mat}}^{(i,l)} z^{-1} \right)^{-1} \right) \left(\mathbf{I} - \sum_{p=1}^{P} \mathbf{R}_{\mathrm{mat}}^{(p,l)} \prod_{i=1}^{p} \mathbf{I} z^{-1} \left(\mathbf{I} - \mathbf{M}_{\mathrm{mat}}^{(i,l)} z^{-1} \right)^{-1} \right)^{-1}. \tag{23}$$

Now, the STF and the ISTF can be solved [21] by

$$STF_l[z] = \frac{STF_{\mathrm{re},1}^{(l)}[z] + STF_{\mathrm{re},2}^{(l)}[z]}{2} + j\frac{STF_{\mathrm{im},1}^{(l)}[z] + STF_{\mathrm{im},2}^{(l)}[z]}{2} \tag{24}$$

and

$$ISTF_l[z] = \frac{STF^{(l)}_{\mathrm{re},1}[z] - STF^{(l)}_{\mathrm{re},2}[z]}{2} + j\frac{STF^{(l)}_{\mathrm{im},1}[z] - STF^{(l)}_{\mathrm{im},2}[z]}{2}, \tag{25}$$

respectively.

The actual output of the lth stage can be derived either using real-valued $V^{(l)}_{\mathrm{I}}[z]$ and $V^{(l)}_{\mathrm{Q}}[z]$ or going for the complex-valued output signal $V_l[z]$. The real valued output signals are obtained using the transfer function matrices of (20) and (23) to multiply the in-phase and quadrature components of the quantization noise and the input signal as 1×2 vectors, respectively. This gives

$$\begin{bmatrix} V^{(l)}_{\mathrm{I}}[z] & V^{(l)}_{\mathrm{Q}}[z] \end{bmatrix} = \begin{bmatrix} U^{(l)}_{\mathrm{I}}[z] & U^{(l)}_{\mathrm{Q}}[z] \end{bmatrix} \begin{bmatrix} STF^{(l)}_{\mathrm{re},1}[z] & STF^{(l)}_{\mathrm{im},1}[z] \\ -STF^{(l)}_{\mathrm{im},2}[z] & STF^{(l)}_{\mathrm{re},2}[z] \end{bmatrix} + \begin{bmatrix} E^{(l)}_{\mathrm{I}}[z] & E^{(l)}_{\mathrm{Q}}[z] \end{bmatrix} \begin{bmatrix} NTF^{(l)}_{\mathrm{re},1}[z] & NTF^{(l)}_{\mathrm{im},1}[z] \\ -NTF^{(l)}_{\mathrm{im},2}[z] & NTF^{(l)}_{\mathrm{re},2}[z] \end{bmatrix}. \tag{26}$$

On the other hand, the four complex-valued transfer functions, given by (21), (22), (24) and (25), can be used to analyze the filtering of the quantization noise $E_l[z]$, the complex conjugate of the quantization noise $E_l^*[z^*]$, the input signal $U_l[z]$ and the complex conjugate of the input signal $U_l^*[z^*]$, resulting in

$$V_l[z] = STF_l[z]U[z] + ISTF_l[z]U_l^*[z^*] + NTF_l[z]E_l[z] + INTF_l[z]E_l^*[z^*]. \tag{27}$$

Finally, the overall output of the multistage QΣΔM is given by

$$V[z] = \sum_{l=1}^{L} (-1)^{l+1} H_l^D[z] V_l[z], \tag{28}$$

which can be written, using the quantization noise of the previous stage as an input for the following one, as

$$\begin{aligned} V[z] = {} & H_1^D[z](STF_1[z]U[z] + ISTF_1[z]U^*[z^*] + NTF_1E_1[z] + INTF_1E_1^*[z^*]) \\ & + \sum_{l=2}^{L} (-1)^{l+1} H_l^D[z](STF_{l-1}[z]E_{l-1}[z] + ISTF_{l-1}[z]E_{l-1}^*[z^*] + NTF_lE_l[z] + INTF_lE_l^*[z^*]). \end{aligned} \tag{29}$$

From (29), it is finally possible to deduce the overall transfer functions for the input signal and the quantization noise of all L stages, and respective conjugate components. These are given as

$$\begin{aligned} STF_{\mathrm{TOT}}[z] &= H_1^D[z]STF_1[z], \\ ISTF_{\mathrm{TOT}}[z] &= H_1^D[z]ISTF_1[z], \\ NTF_{\mathrm{TOT},l}[z] &= H_l^D[z]NTF_l[z] - H_{l+1}^D STF_{l+1}[z],\ 1 \le l \le L-1,\ l \in \mathbb{Z}, \\ INTF_{\mathrm{TOT},l}[z] &= H_l^D INTF[z] + H_{l+1}^D ISTF_{l+1}[z],\ 1 \le l \le L-1,\ l \in \mathbb{Z} \\ NTF_{\mathrm{TOT},L}[z] &= H_L^D[z]NTF_L[z], \\ INTF_{\mathrm{TOT},L}[z] &= H_L^D[z]INTF_L[z]. \end{aligned} \tag{30}$$

Considering now a practical example of two-stage QΣΔM with $L = 2$, application of (29) gives

$$\begin{aligned}V[z] &= H_1^D[z](STF_1[z]U[z] + ISTF_l[z]U^*[z^*] + NTF_1E_1[z] + INTF_1E_1^*[z^*]) \\ &\quad -H_2^D[z](STF_2[z]E_1[z] + ISTF_2[z]E_1^*[z^*] + NTF_2E_2[z] + INTF_2E_2^*[z^*]) \\ &= STF_2^D STF_1[z]U[z] + STF_2^D ISTF_1[z]U^*[z^*] + (STF_2^D[z]NTF_1[z] - NTF_1^D[z]STF_2[z])E_1[z] \\ &\quad +(STF_2^D[z]INTF_1[z] + NTF_1^D[z]ISTF_2[z])E_1^*[z^*] - NTF_1^D[z]NTF_2[z]E_2[z] - NTF_1^D[z]INTF_2[z]E_2^*[z^*] \\ &= STF_{\mathrm{TOT}}[z]U[z] + ISTF_{\mathrm{TOT}}[z]U^*[z^*] + NTF_{\mathrm{TOT},1}[z]E_1[z] + INTF_{\mathrm{TOT},1}[z]E_1^*[z^*] \\ &\quad +NTF_{\mathrm{TOT},2}[z]E_2[z] + INTF_{\mathrm{TOT},2}[z]E_2^*[z^*],\end{aligned} \tag{31}$$

with digital filters $H_1^D[z] = STF_2^D[z]$, $H_2^D[z] = NTF_1^D[z]$. It should be noted that $STF_{\mathrm{TOT}}[z]U[z]$ and $NTF_{\mathrm{TOT},2}[z]E_2[z]$ correspond structurally to the ideal output given in (7). However, the responses of $STF_{\mathrm{TOT}}[z]$ and $NTF_{\mathrm{TOT},2}[z]$ can differ from $STF_{\mathrm{TOT}}^{ideal}[z]$ and $NTF_{\mathrm{TOT}}^{ideal}[z]$ due to possible common-mode errors in the modulator coefficients [33]. Furthermore, the four additional terms in (31) are identified as mismatch induced interference, which includes the MFI (conjugate) component of the input signal, the leakage of the first-stage noise and its conjugate component and the conjugate of the second-stage noise.

Now, the interference rejection ratio introduced in [19] can be used to measure the power of the I/Q imbalance induced interference components in relation to the power of the ideal output for the signal band Ω_{s} in multiband scenario consisting of a total of S signals to be received. This is given as

$$\Gamma_{\mathrm{s}} = \frac{\int\limits_{f\in\Omega_{\mathrm{s}}} G_\sigma(e^{j2\pi fT})df}{\int\limits_{f\in\Omega_{\mathrm{s}}} G_\tau(e^{j2\pi fT})df}, \tag{32}$$

where $G_\sigma(e^{j2\pi fT})$ and $G_\tau(e^{j2\pi fT})$ are the spectral densities of the ideal output signal and the I/Q imbalance induced interference (f being the frequency measured in Hertz and T the sampling interval of the ADC), respectively, given by

$$\sigma(k) = h_{\mathrm{STF}}^{\mathrm{TOT}}(k) * u(k) + h_{\mathrm{NTF}}^{\mathrm{TOT,L}}(k) * e_L(k) \tag{33}$$

and

$$\tau(k) = h_{\mathrm{TOT}}^{\mathrm{ISTF}}(k) * u^*(k) + h_{\mathrm{INTF}}^{\mathrm{TOT},L}(k) * e_L^*(k) + \sum_{l=1}^{L-1}\Big(h_{\mathrm{NTF}}^{\mathrm{TOT},l}(k) * e_l(k) + h_{\mathrm{INTF}}^{\mathrm{TOT}.l} * e_l^*(k)\Big). \tag{34}$$

Here, the impulse responses correspond to inverse z-transforms of the total transfer functions defined in (30). The integration is done over the bandwidth of the signal s, given by $\Omega_{\mathrm{s}} = \left\{f_{\mathrm{C,s}} - W_{\mathrm{s}} / 2, \ldots, f_{\mathrm{C,s}} + W_{\mathrm{s}} / 2\right\}$, where W_{s} is the bandwidth of the respective signal band.

IV. TRANSFER FUNCTION DESIGN AND DIGITAL POST-COMPENSATION FOR MIRROR-FREQUENCY INTERFERENCE IN QΣΔM BASED MULTICHANNEL COGNITIVE RADIO RECEIVERS

First, in this section, post-compensation challenges specific for receivers utilizing QΣΔM are discussed. Thereafter, designing the transfer functions (STF and NTF) of the modulator, to facilitate the digital interference compensation and to combat the mentioned challenges, is proposed. For example, for mirror-frequency interference compensation, it is essential to maintain information about the mirror-band content through the receiver front-end and A/D interface to digital domain.

A. QΣΔM Related Challenges in Post-Compensation

The traditional way of designing QΣΔM transfer functions has been to shape the quantization noise away from the desired signal band (place the NTF zeros on the band) and to either use simple frequency-flat signal transfer function or filter the out-of-band signal content partially away [18]. Combining this kind of noise shaping and STF filtering is an efficient solution when considering an ideal receiver having quantization noise as the dominant error source. However, the distortion and interference generated by the implementation inaccuracies of both the preceding radio front-end and the QΣΔM itself must be taken into account when considering true circuits. Such treatment is lacking in the current literature.

Lately, there have been significant advances in digital compensation of these, so called dirty-RF, impairments, such as the mirror-frequency interference originating from the mismatches of quadrature circuits [6], [11], [44], [45]. These compensation algorithms typically need access to the original interference sources in the digital domain. Thus, in the case of I/Q imbalance considered in this article, the mirror-band signal being the source of mirror-frequency interference should be converted into the digital domain with reasonable precision. This is where the above-described traditional NTF design (possibly combined with the STF filtering) becomes unsuitable. If all the NTF zeros are placed on the desired signal band, the noise load of the mirror-band is potentially very high, resulting in a very low signal-to-noise ratio (SNR). This is, of course, even more emphasized if the STF is attenuating the mirror-band. In [18], a mirror-band NTF notch was proposed to avoid mirroring of the high noise levels. However, the STF was used to filter the mirror-band input signal content away, impeding the actual post-compensation of input signal originating mirror-frequency interference.

The mirror-frequency interference inside the QΣΔM (the feedback branch I/Q mismatches being most crucial) can be controlled by mirror-frequency rejecting STF design [19], [28]. However, problems arise when the I/Q mismatches of the preceding receiver components (and other QΣΔM coefficients) are taken into account. For example, when the I/Q mixer used to bring the desired signal down to IF creates mirror-frequency interference and the original mirror-band signal is filtered out inside the QΣΔM, the interference remains on top of the desired signal but the information of the interference source is removed, making post-compensation a troublesome task. The signal and noise transfer function designs solving this problem are proposed in the following subsection.

B. Transfer Function Design to Facilitate Post-Compensation and Frequency Agile Operation

Herein, a transfer function design targeted to be combined with digital post-compensation of the overall mirror-frequency interference induced by the receiver front-end and the QΣΔM is proposed. The design is based on a single-band NTF design with one mirror-band NTF zero of [18], being extended to the multiband concept of [19], [28]. Now, the possible mirror-band blockers are preserved, emphasizing the usability of such information for digital compensation purposes, by creating STF passbands also on the mirror bands. Although allowing the mirror band signals to enter the modulator increases the input dynamics, it brings a significant benefit for compensation of the mirror-frequency interference generated in the receiver front-end. Without the knowledge about these signals, the compensation task of such interference becomes very challenging (or even impossible). In addition, in the highly dynamic conditions typical for cognitive radio (considering both power levels and operating frequencies), avoiding mirror-frequency interference in the receiver front-end becomes nearly impossible, because it is very challenging or practically impossible to design RF filters that would have sufficient tunability and selectivity to get rid of the other signal content. The QΣΔM coefficients are derived in similar manner as in [19] and the straightforward reconfigurability, e.g., in case of frequency hand-off, discussed in Section II and [19] is maintained. Thus, the easy implementation of all the QΣΔM coefficients as functions of the desired signals' center frequencies enables efficient frequency-agile operation.

This design is demonstrated in a practical scenario with a two-stage QΣΔM having both the stages of fourth order. Thus, the overall NTF order, being the combined order of the stages, is eight, allowing eight noise notches to be placed on the conversion band. This capability allows flexible reconfiguration of the frequency bands to be received and detected, in a similar manner as discussed in [19] in case of a three-stage QΣΔM. On one hand, the NTF zeros can be placed inside one contiguous band for reception of wideband waveforms (such as LTE with 20 MHz bandwidth), or on the other hand, noncontiguous NTF design allows reception of multiple distinct information signals on separate frequency bands. Tuning of the QΣΔM coefficients is in practice implemented with digital control, having 6-8 bit resolution, resulting in sufficient dynamics and coefficient accuracy when operating on, for example, TV white spaces, where channel spacing and center frequency resolution is 8 MHz. The actual implementation details of the control are, however, not in scope of this paper, but remain as an important future work topic.

In the following, a concrete transfer function design example is given, having the NTF zeros divided for the simultaneous reception of two desired signals on noncontiguous frequency bands by placing three NTF zeros on both bands. The remaining two zeros are placed on the mirror-bands of the desired signals to improve the signal-to-noise ratio of the signals possibly appearing therein. On the other hand, the main principle in the STF design is to allow the desired signals and their mirror-band signals to be converted with reasonable resolution. In simplest, this means STF being equal to unity. However, the STF zeros of the first stage can be used to filter out other noninteresting signal content possibly limiting the dynamics of the converter. The second-stage STF is designed to be frequency flat. The frequency-flat design is chosen because of its minimal delay and because the second stage processes only the quantization error of the first stage, not the signal itself. Different design options for the second-stage STF are discussed further in [38] by the authors. It is important to notice that both transfer functions can be straightforwardly reconfigured using information available about the transmission center frequencies, bandwidths, resolution demands and spectrum sensing information about the strongest blocking signals possibly present within the overall conversion band.

The exact placement of the NTF zeros inside the desired signal band is based on [46]. This is because the analysis for lowpass ΣΔ modulators can be exploited for QΣΔMs also, the noise shaping differing only by the translation of the center frequency to an

IF. Thus, since the noise shaping order per one desired signal band is three, as described above, the four first stage zeros are placed on the edges of the bands, i.e., $\varphi^{(1)}_{NTF,1} = e^{j2\pi(f_{\mathrm{C},1}+f_{\mathrm{offset},1})T}$, $\varphi^{(1)}_{NTF,2} = e^{j2\pi(f_{\mathrm{C},1}-f_{\mathrm{offset},1})T}$, $\varphi^{(1)}_{NTF,3} = e^{j2\pi(f_{\mathrm{C},2}+f_{\mathrm{offset},2})T}$ and $\varphi^{(1)}_{NTF,3} = e^{j2\pi(f_{\mathrm{C},2}-f_{\mathrm{offset},2})T}$, where $f_{\mathrm{C},1}$ and $f_{\mathrm{C},2}$ are the desired signal center frequencies and $f_{\mathrm{offset},1} = W_1\sqrt{3/5}/2$ and $f_{\mathrm{offset},2} = W_2\sqrt{3/5}/2$ (following [46]), with W_1 and W_2 being the bandwidths of the desired signals in Hertz. The second stage NTF zeros are placed in the middle of the desired signal bands and on the mirror frequencies, giving $\varphi^{(2)}_{NTF,1} = e^{j2\pi f_{\mathrm{C},1}T}$, $\varphi^{(2)}_{NTF,2} = e^{j2\pi f_{\mathrm{C},2}T}$, $\varphi^{(2)}_{NTF,3} = e^{-j2\pi f_{\mathrm{C},1}T}$ and $\varphi^{(2)}_{NTF,3} = e^{-j2\pi f_{\mathrm{C},2}T}$.

The poles of the stages are placed in Butterworth positions around the NTF zeros in order to secure the stability of the modulators [18], as shown in Fig. 7 in the example case of $f_{\mathrm{C},1} = 40.28$ MHz, $f_{\mathrm{C},2} = -14.49$ MHz and $W_1 = W_2 = 10$ MHz (assuming sampling frequency of 128 MHz). The stability is improved by limiting the out-of-band gain of the NTF, which is one of the most important factors in this aspect [37]. The STF zeros of the first stage are placed on the center frequencies of the possible additional, noninteresting, signals in order to reduce the overall signal dynamics at the quantizer input. In the example of Fig. 7, these zero locations are $\varphi^{(1)}_{STF,1} = e^{j2\pi f_{\mathrm{int},1}T} = 1$, $\varphi^{(1)}_{STF,2} = e^{j2\pi f_{\mathrm{int},2}T} = -1$, $\varphi^{(1)}_{STF,3} = e^{j2\pi f_{\mathrm{int},3}T} = e^{j2\pi 0.2139}$ and $\varphi^{(1)}_{STF,4} = e^{j2\pi f_{\mathrm{int},4}T} = e^{-j2\pi 0.2139}$. The second-stage STF is designed as frequency-flat, resulting in the zero locations overlapping with the Butterworth poles of the second-stage NTF, as illustrated in Fig. 7. Overall, by tuning the locations of these zeros and poles, it is straightforward to reconfigure the QΣΔM response, thus allowing frequency-agile operation.

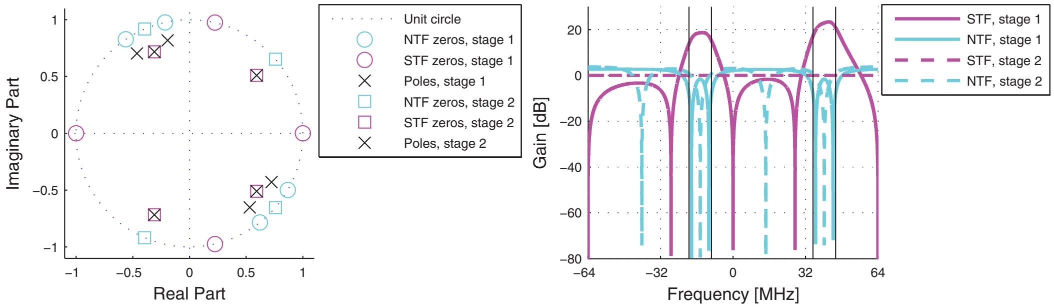

Fig. 7. Zero-pole plot (left) of the overall NTF and STF of a two-stage QΣΔM having fourth order individual stages (overall noise shaping order of eight) and frequency responses of the transfer functions of the stages (right). Multiband reception of two information signals with center frequencies of 40.28 MHz and -14.49 MHz is assumed. These bands to be detected are marked with vertical black lines in the right plot.

For the stability of the modulator, [37] gives two criteria; for single-bit modulators is required that $\max_{\omega}\left|NTF(e^{j\omega})\right| < 1.5$ (being, however, neither necessary nor sufficient) and for multi-bit modulators $\max_{n}\left|u(n)\right| \leq M_{\mathrm{step}} + 2 - \sum_{n}^{\infty}\left|h_{\mathrm{NTF}}(n)\right|$ (sufficient), where M_{step} is the number of quantizer steps. For the design at hand, $\max_{\omega}\left|NTF_1(e^{j\omega})\right| = 1.89$ and $\max_{\omega}\left|NTF_2(e^{j\omega})\right| = 2.36$ and thus 1-bit implementation cannot be expected to be fully stable. On the other hand, if 3-bit quantizers are chosen, the latter criterion gives $\max_{n}\left|u(n)\right| = M_{\mathrm{step},1} + 2 - \sum_{n}^{\infty}\left|h_{\mathrm{NTF},1}(n)\right| = 5.28$, making stable operation guaranteed with 66 % of the quantizer full-scale range. For the second stage of the design, the corresponding figures, with 3-bit quantizer, are

$\max_n \left| u_2(n) \right| = M_{\text{step},2} + 2 - \sum_n^{\infty} \left| h_{\text{NTF},2}(n) \right| = 6.07$ and 76 % of the full-scale range. Thus, 3-bit quantizers and feedback digital-to-analog converters (DACs) are chosen for both the stages.

Based on the above design, it is noted that the second stage NTF is actually symmetric (the zeros are complex conjugate pairs) and thus real valued and could be realized with a real bandpass ΣΔ modulator stage. However, this is only a special case with exactly two distinct signals to be received. In the challenging and dynamic conditions, typical for the cognitive radio solutions, the flexibility of the quadrature (complex) modulator is appreciated for its frequency agile operation and degrees-of-freedom and thus maintained in the general design. With QΣΔM stages at hand, the NTF can be configured for the reception of one to four separate signal bands. This valuable capability would be partly lost with a real bandpass ΣΔ modulator as the second stage.

C. *Removing Mirror-Frequency Interference with Digital Post-Processing*

The mirror-frequency interference experienced by the desired signals is generated in both the receiver radio front-end and the QΣΔM considered for the A/D conversion, because of the inherent implementation inaccuracies resulting in I/Q imbalance between the I and Q signal branches. In the radio front-end, the imbalance source can be, e.g., a quadrature mixer having imperfect phase and amplitude matching. Thus, the input signal (in z-domain $U[z]$) fed to the QΣΔM is already a combination of the ideal signal, say $X[z]$, and it's complex conjugate $X^*[z^*]$, scaled by certain, generally frequency selective, gains or responses, i.e.,

$$U[z] = STF_{\text{FE}}[z]X[z] + ISTF_{\text{FE}}[z]X^*[z^*], \tag{35}$$

where $STF_{\text{FE}}[z]$ and $ISTF_{\text{FE}}[z]$ denote the signal transfer function and image signal transfer functions of the receiver front-end, which are assumed to be unknown.

When this nonideal signal (including the conjugate term) is used as an input for the I/Q mismatched QΣΔM, both components experience the STF and the ISTF of the modulator. In addition, the noise and image noise components are added, shaped by the NTF and the INTF, respectively. In this scenario, the final output of a single-stage QΣΔM is given by

$$\begin{aligned} V[z] &= STF_{\text{SD}}[z]U[z] + ISTF_{\text{SD}}[z]U^*[z] + NTF[z]E[z] + INTF[z]E^*[z^*] \\ &= STF_{\text{SD}}[z](STF_{\text{FE}}[z]X[z] + ISTF_{\text{FE}}[z]X^*[z^*]) \\ &\quad + ISTF_{\text{SD}}[z](ISTF_{\text{FE}}[z]X[z] + STF_{\text{FE}}[z]X^*[z^*]) + NTF[z]E[z] + INTF[z]E^*[z^*] \\ &= (STF_{\text{SD}}[z]STF_{\text{FE}}[z] + ISTF_{\text{SD}}[z]ISTF_{\text{M}}[z])X[z] \\ &\quad + (STF_{\text{SD}}[z]ISTF_{\text{FE}}[z] + ISTF_{\text{SD}}[z]STF_{\text{FE}}[z])X^*[z^*] + NTF[z]E[z] + INTF[z]E^*[z^*] \\ &= STF_{\text{FE+SD}}[z]X[z] + ISTF_{\text{FE+SD}}[z]X^*[z^*] + NTF[z]E[z] + INTF[z]E^*[z^*], \end{aligned} \tag{36}$$

where $STF_{\text{FE+SD}}$ and $ISTF_{\text{FE+SD}}$ are the combined signal transfer function and the image signal transfer function of the front-end and the QΣΔM, respectively. For a multistage QΣΔM, having L stages, the corresponding output is given by

$$\begin{aligned} V[z] &= H_1^D[z](STF_{\text{FE+SD1}}[z]X[z] + ISTF_{\text{FE+SD1}}[z]X^*[z^*] + NTF_1E_1[z] + INTF_1E_1^*[z^*]) \\ &+ \sum_{l=2}^{L}(-1)^{l-1}H_l^D[z](STF_l[z]E_{l-1}[z] + ISTF_l[z]E_{l-1}^*[z^*] + NTF_lE_l[z] + INTF_lE_l^*[z^*]), \end{aligned} \tag{37}$$

where $STF_{\text{FE+SD1}}[z]$ and $ISTF_{\text{FE+SD1}}[z]$ are the combined STF and ISTF of the receiver front-end and the first ΣΔ stage. Similarly as in (30), the total effective signal transfer functions, including now the effects of both the analog radio front-end and the QΣΔM converter structure, can be written as

$$\begin{aligned} STF_{\text{TOT, FE+SD1}}[z] &= H_1^D[z]STF_{\text{FE+SD1}}[z] \\ ISTF_{\text{TOT,FE+SD1}}[z] &= H_1^D[z]ISTF_{\text{FE+SD1}}[z]. \end{aligned} \tag{38}$$

The noise transfer functions, in turn, are not dependent on the analog radio front-end, and are thus identical to those in (30).

Now, in the case of two-stage QΣΔM as a practical example, the overall interference rejection ratio of (32) is calculated using the signal components ideally present at the output

$$\tilde{\sigma}(k) = h_{\text{STF}}^{\text{TOT,FE+SD1}}(k) * x(k) + h_{\text{NTF}}^{\text{TOT},2}(k) * e_2(k) \tag{39}$$

and the I/Q imbalance induced interference components

$$\tilde{\tau}(k) = h_{\text{ISTF}}^{\text{TOT,FE+SD1}}(k) * x^*(k) + h_{\text{NTF}}^{\text{TOT},1}(k) * e_1(k) + h_{\text{INTF}}^{\text{TOT},1}(k) * e_1^*(k) + h_{\text{INTF}}^{\text{TOT},2}(k) * e_2^*(k), \tag{40}$$

where the STF and the ISTF components include now the contribution of the whole receiver. Thus, the interference rejection ratio of the whole receiver, for the signal band s, is given by

$$\tilde{\Gamma}_{\text{s}} = \frac{\int\limits_{f \in \Omega_{\text{s}}} G_{\tilde{\sigma}}(e^{j2\pi fT})df}{\int\limits_{f \in \Omega_{\text{s}}} G_{\tilde{\tau}}(e^{j2\pi fT})df}. \tag{41}$$

In the special case of an ideal receiver before the QΣΔM, (41) reduces to (32) because then $\tilde{\sigma}(k) = \sigma(k)$ and $\tilde{\tau}(k) = \tau(k)$. In Section V, this measure $\tilde{\Gamma}_{\text{s}}$ is used to verify, quantify and analyze the efficiency of the digital MFI post-compensation discussed in the following.

In case of the ΣΔ modulation, the frequency-selective behavior of the signal transfer functions can be assumed mild inside a single signal subband because of the high oversampling inherently present. Thus, a simple frequency-independent compensation algorithm [22], per subband, can be used to demonstrate the efficiency of digital post-compensation, facilitated by the above discussed transfer function designs. Possible deviations at the level of the interference between separate signals and respective frequency bands are taken into account by doing the compensation separately for each of the desired information signals, i.e., separately for the subbands, as illustrated in Fig. 8. At the same time, the transfer function design would also allow use of more sophisticated, e.g., frequency-selective digital post-compensation algorithms, such as [26]. This option should be considered especially for reception of very wideband waveforms, when there might be significant frequency-selective behavior also inside the individual subbands, because of, e.g., the I/Q mismatch properties of the analog front-end. This is interesting topic for future work.

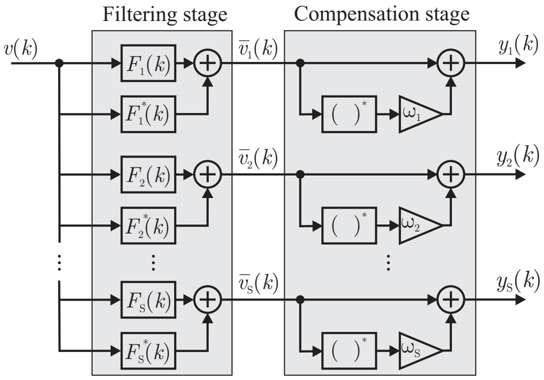

Fig. 8. Digital MFI post-compensation structure for multiband reception, processing S parallel information signals to be received and detected. The compensation algorithm used per signal band is published in [22]. The filters $F_1(k)$ to $F_S(k)$ and $F_1^*(k)$ to $F_S^*(k)$ are used to pick the desired signals and the related mirror-bands, respectively.

With the previous narrowband assumption and assuming a two-stage QΣΔM again as a practical example, the compensator output signals $y_\mathrm{s}(k)$, depicted in Fig. 8, are given by

$$\begin{aligned} y_\mathrm{s}(k) &= \overline{v}_\mathrm{s}(k) + \omega_\mathrm{s}\overline{v}_\mathrm{s}^{\,*}(k) \\ &\approx K_{1,\overline{x}_\mathrm{s}}\overline{x}_\mathrm{s}(k) + K_{2,\overline{x}_\mathrm{s}}\overline{x}_\mathrm{s}^{\,*}(k) + K_{1,\overline{e}_{1,\mathrm{s}}}\overline{e}_{1,\mathrm{s}}(k) + K_{2,\overline{e}_{1,\mathrm{s}}}\overline{e}_{1,\mathrm{s}}^{*}(k) + K_{1,\overline{e}_{2,\mathrm{s}}}\overline{e}_{2,\mathrm{s}}(k) + K_{2,\overline{e}_{2,\mathrm{s}}}\overline{e}_{2,\mathrm{s}}^{*}(k) \\ &\quad +\omega_\mathrm{s}[K_{1,\overline{x}_\mathrm{s}}^{*}\overline{x}_\mathrm{s}^{*}(k) + K_{2,\overline{x}_\mathrm{s}}^{*}\overline{x}_\mathrm{s}(k) + K_{1,\overline{e}_{1,\mathrm{s}}}^{*}\overline{e}_{1,\mathrm{s}}^{*}(k) + K_{2,\overline{e}_{1,\mathrm{s}}}^{*}\overline{e}_{1,\mathrm{s}}(k) + K_{1,\overline{e}_{2,\mathrm{s}}}^{*}\overline{e}_{2,\mathrm{s}}^{*}(k) + K_{2,\overline{e}_{2,\mathrm{s}}}^{*}\overline{e}_{2,\mathrm{s}}(k)], \end{aligned} \tag{42}$$

where the signal and noise variables with the bar and the subscript s are the corresponding inband components after the subband filters $F_\mathrm{s}(k)$ for the desired signal bands and $F_\mathrm{s}^*(k)$ for the image bands, respectively. In addition, the model coefficients are the complex scaling factors for the signal and noise components, defined as

$$\begin{aligned} K_{1,\overline{x}_\mathrm{s}} &\approx STF_{\mathrm{TOT,\ FE+SD1}}[e^{j2\pi f_{\mathrm{C,s}}T}], \\ K_{2,\overline{x}_\mathrm{s}} &\approx ISTF_{\mathrm{TOT,FE+SD1}}[e^{j2\pi f_{\mathrm{C,s}}T}], \\ K_{1,\overline{e}_{1,\mathrm{s}}} &\approx NTF_{\mathrm{TOT,1}}[e^{j2\pi f_{\mathrm{C,s}}T}], \\ K_{2,\overline{e}_{1,\mathrm{s}}} &\approx INTF_{\mathrm{TOT,1}}[e^{j2\pi f_{\mathrm{C,s}}T}], \\ K_{1,\overline{e}_{2,\mathrm{s}}} &\approx NTF_{\mathrm{TOT,2}}[e^{j2\pi f_{\mathrm{C,s}}T}], \\ K_{2,\overline{e}_{2,\mathrm{s}}} &\approx INTF_{\mathrm{TOT,2}}[e^{j2\pi f_{\mathrm{C,s}}T}], \end{aligned} \tag{43}$$

where the transfer functions are evaluated at the desired signal center frequencies and T is the sampling interval in seconds. Further, by assuming practical (clearly above 0 dB) inband signal-to-quantization noise ratio and thus neglecting the lower power noise components (also the conjugate noise component is assumed to be controlled by the mirror-band NTF notch), (42) can be simplified as

$$y_\mathrm{s}(k) \approx K_{1,\overline{x}_\mathrm{s}}\overline{x}_\mathrm{s}(k) + K_{2,\overline{x}_\mathrm{s}}\overline{x}_\mathrm{s}^{\,*}(k) + \omega_\mathrm{s}[K_{1,\overline{x}_\mathrm{s}}^{\ *}\overline{x}_\mathrm{s}^{\,*}(k) + K_{2,\overline{x}_\mathrm{s}}^{\ *}\overline{x}_\mathrm{s}(k)]. \tag{44}$$

This approximation simplifies finding the mirror-frequency compensator coefficients ω_s significantly.

Stemming from the signal model structure in (44), the compensator coefficients ω_s can be estimated based on the circularity restoring mirror-frequency compensation principle proposed in [22]. In [22], the circularity is defined as the complementary autocorrelation function $c_{y_\mathrm{s}}(\tau)$ of $y_\mathrm{s}(k)$ being zero at zero lag, i.e., $c_{y_\mathrm{s}}(0) = c_{y_\mathrm{s}} = E\left[y_\mathrm{s}(k)^2\right] = 0$, meaning that real and imaginary parts of the compensated outputs are equally powerful and instantaneously mutually uncorrelated. Similarly, traditional autocorrelation function $\gamma_{y_\mathrm{s}}\left(\tau\right)$ at zero lag is given by $\gamma_{y_\mathrm{s}}(0) = \gamma_{y_\mathrm{s}} = \mathrm{E}\left[\left|y_\mathrm{s}(k)\right|^2\right]$ [22]. Now, as shown in [22], the optimal compensator coefficient for signal subband s, restoring the circularity of the compensated signal, can be written as a function of the observed subband signal second-order statistics, $c_{\overline{v}_\mathrm{s}}$ and $\gamma_{\overline{v}_\mathrm{s}}$, as

$$\omega_\mathrm{s} = -\frac{c_{\overline{v}_\mathrm{s}}}{\gamma_{\overline{v}_\mathrm{s}} + \sqrt{\gamma^2_{\overline{v}_\mathrm{s}} - \left|c^2_{\overline{v}_\mathrm{s}}\right|}}. \qquad (45)$$

In above, $\mathrm{s} \in \left\{1,2\right\}$ for two-band reception and generally $\mathrm{s} \in \left\{1,\ldots,\mathrm{S}\right\}$ for S signal bands to be received and detected. In practice, sample estimates of the second-order statistics, $c_{\overline{v}_\mathrm{s}}$ and $\gamma_{\overline{v}_\mathrm{s}}$, are used, calculated over a block of received data. This estimation-compensation approach is deployed in the following computer simulations. The results are illustrated in Section V.

V. RESULTS OF TRANSFER FUNCTION OPTIMIZATION AND POST-COMPENSATION

A. Closed-form Two-Stage Quadrature ΣΔ Modulator Transfer Function Analysis

In this section, the transfer function model proposed in Section III is used to calculate the four transfer functions of the two-band QΣΔM design discussed in Section IV. Two detached frequency channels are assumed for the desired information signals, with center frequencies of $f_{\mathrm{C},1} = 40.28\ \mathrm{MHz}$, $f_{\mathrm{C},2} = -14.49\ \mathrm{MHz}$ and bandwidths $W_1 = W_2 = 10\ \mathrm{MHz}$. The sampling frequency is 128 MHz, giving $T = 1 / f_\mathrm{S} = 7.8125\,\mathrm{ns}$. The transfer functions of the QΣΔM are designed according to the proposed design flow of Section IV. The overall noise shaping order is eight and two zeros are placed on the mirror-bands of the desired signals, leaving three zeros per signal band to be used for the actual noise shaping. The digital filters $H_1^D[z]$ and $H_2^D[z]$ are assumed to be matched to the ideal analog transfer functions.

The transfer functions are evaluated with randomly deviated real gain values in the modulator coefficients in order to model the implementation inaccuracies and evaluate their effects. The gain values are drawn from a uniform distribution of $\pm 1\%$ around the ideal value. In other words, the realized value $\hat{r}_{\mathrm{re},1}^{(1,1)}$ of ideal $r_{\mathrm{re},1}^{(1,1)}$ is uniformly distributed between $0.99 r_{\mathrm{re},1}^{(1,1)}$ and $1.01 r_{\mathrm{re},1}^{(1,1)}$ and similarly for the other coefficients.

First, the case of QΣΔM feedback mismatch is considered, being mentioned as the most crucial MFI source inside the modulator [31]. This is because the feedback errors are not shaped by the NTF as the forward branch errors [31]. In Fig. 9, the results for 50 independent draws from the above described distribution for the feedback coefficients are illustrated. The results show the image rejection of the input signal (STF response of 10 dB versus the ISTF response of -40 dB) to be around 50 dB on the frequency channel around -14.49 MHz and 40 dB (STF response of 10 dB versus the ISTF response of -40 dB) around

40.28 MHz. The second stage quantization noise (being ideally the only quantization noise present) is attenuated between 15 dB and 30 dB inside the desired signal bands and the related conjugate response ($INTF_{\mathrm{TOT},2}[z]$) has more than 50 dB attenuation, remaining clearly below the nonconjugate response. The mirror band zeros push the noise levels down also on those frequencies. From the middle plot of Fig. 9, it is clearly visible that the quantization error of the first stage is not cancelled completely. This is because of the noncommutativity of the complex transfer functions under I/Q imbalance [33]. The conjugate component of the first-stage noise ($INTF_{\mathrm{TOT},1}[z]$) has 30 to 40 dBs of attenuation on the negative frequency channel and 15 to 35 dBs on the positive frequency channel. The nonconjugate noise ($NTF_{\mathrm{TOT},1}[z]$) is attenuated on average by 40 dB on both the channels. This confirms that the transfer functions work as designed in case of the modulator feedback coefficient mismatch. However, there remains the potential risk of heavy MFI if strong mirror-band signals are present at the input signal. The post-compensation of this interference is demonstrated in the following subsection.

In addition, Fig. 10 gives the transfer function analysis results assuming implementation inaccuracies in all the QΣΔM coefficients in both the stages of the previously described two-stage modulator used as a practical example. The findings in Fig. 10 have certain significant differences to the ones in Fig. 9. For example, the ISTF maximum response has risen by 10 (positive frequency channel) to 20 (positive frequency channel) dBs. In addition, out-of-band peaking is clearly visible in the ISTFs. At the

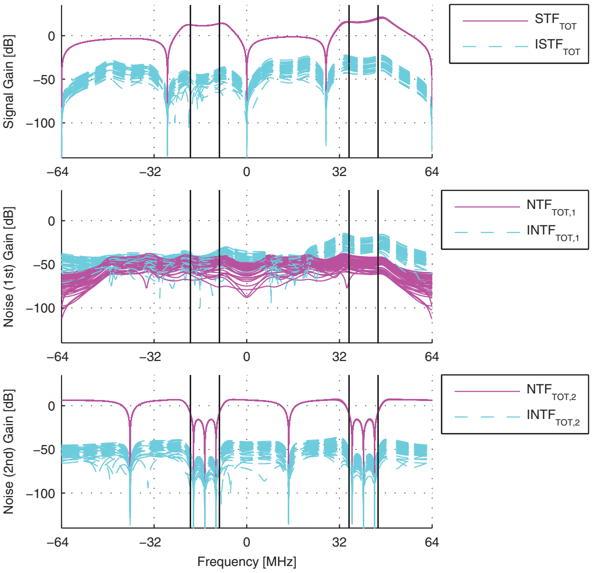

Fig. 9. Two-stage QΣΔM STF and ISTF (top) together with NTF and INTF for first- (middle) and second-stage (bottom) quantization noise. 50 independent random realizations in real gain values of feedback branches of both stages are considered and multiband reception of two information signals with center frequencies of 40.28 MHz and -14.49 MHz is assumed. These bands to be detected are marked with vertical black lines in the plots.

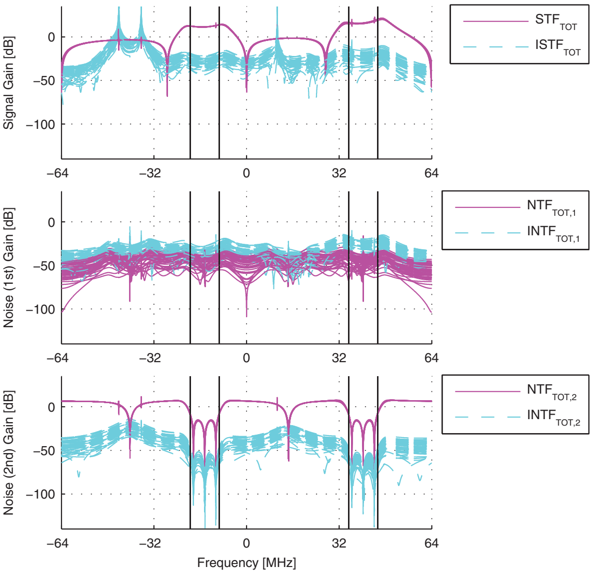

Fig. 10. Two-stage QΣΔM STF and ISTF (top) together with NTF and INTF for first- (middle) and second-stage (bottom) quantization noise. 50 independent random realizations in real gain values of all the coefficients of both stages are considered and multiband reception of two information signals with center frequencies of 40.28 MHz and -14.49 MHz is assumed. These bands to be detected are marked with vertical black lines in the plots.

same time, the second stage noise behavior on the desired bands remains similar. However, the conjugate response is elevated on the mirror-bands, having still around 20 dB attenuation. From the first stage noise point-of-view, the most visible difference is that conjugate attenuation on the negative frequency channel has decreased by around 10 dB. Overall, the results indicate that, while the feedback mismatches might be the most important error source, the mismatches of the feed-forward coefficients cannot be excluded either and have a pronounced effect on the image rejection of the whole QΣΔM.

B. Verification Simulations on Digital Post-Compensation of Mirror-frequency Interference

Herein, the QΣΔM design and MFI compensation of Section IV are simulated using realistic communication waveforms to be received (16-QAM and QPSK modulated desired information signals), together with mirror-frequency blocking signals as interference sources. Two separate scenarios are presented in the following. In the first case, QΣΔM feedback I/Q mismatches are assumed to be the only implementation inaccuracy. The latter case, on the other hand, assumes all the QΣΔM coefficients to be nonideally implemented and, in addition, the frequency independent image rejection ratio of the preceding receiver chain (mainly I/Q mixer) is assumed to be 30 dB. When nonideally implemented QΣΔM coefficients are considered, the realized real-valued coefficient values are drawn from a uniform distribution of $\pm 1\%$ around the ideal value as described also in the above case of transfer function analysis.

An example of the assumed input signal in the computer simulations is illustrated Fig. 11. In addition, the ideal overall transfer functions are included in the figure, in order to illustrate the noise shaping and the STF passbands. In addition to the signal content, a white noise floor is included at the receiver input, giving 18 dB signal-to-noise ratio for the 16-QAM waveform around $f_{\mathrm{C},1} = 40.28\ \mathrm{MHz}$ and 10 dBs for the QPSK waveform around $f_{\mathrm{C},2} = -14.49\ \mathrm{MHz}$. The difference is due to an 8 dB higher power level for the 16-QAM signal. The mirror-frequency blockers consist of band-limited Gaussian noise, with a bandwidth of 3 MHz, and are simulated on the relative power level from 0 dB to +60 dB compared to the respective desired signal. In this way, with the highest blocker level, the mirror-band signal across the 16-QAM signal is 68 dB stronger than the weaker QPSK waveform, representing an extremely challenging scenario. A true 3-bit quantizer is simulated in both the QΣΔM stages (and separately for the I and Q branches) for feasible quantization noise levels. The DACs of the stages are assumed ideal.

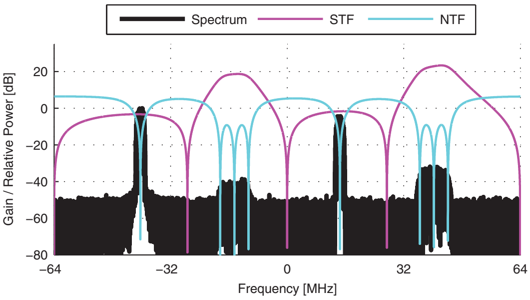

Fig. 11. An example spectrum of input signal used in the simulations together with the ideal designed transfer functions (overall response). The desired information signals are located around center frequencies of 40.28 MHz and -14.49 MHz with 16-QAM and QPSK waveforms, respectively. The blocking signals are located on the mirror frequencies of the desired signals.

In both simulation cases, 150 independent realizations of the QΣΔM coefficients are drawn from the described distributions. The Interference Rejection Ratio $\tilde{\Gamma}_{\mathrm{s}}$ values are evaluated for each realization of the modulator coefficients by subtracting the output of an ideal QΣΔM from the output of a mismatched QΣΔM, obtaining thus an estimate of distortion component. The signal length used is 2^{18} samples and the blockwise post-compensation (when applicable) is done using these samples. The optimization of the compensation block-length is not considered herein. The interference rejection ratio itself is given as a ratio of the ideal output power on the desired signal band and the distortion power estimate on the same band. The amplitudes of the real and imaginary parts of the overall received input signal are limited by the receiver automatic gain control mechanism to be equal to or less than 0.7 in order to avoid quantizer clipping (quantizer full scale range from -1 to 1), i.e., $\left|u_{\mathrm{I},1}(k)\right| \leq 0.7$ and $\left|u_{\mathrm{Q},1}(k)\right| \leq 0.7$ for all k. This limitation is maintained also when increasing the blocking signal power levels, which means that with increasing blocker input power, the useful signals are scaling down and become more and more sensitive to, e.g., quantization noise. The stability of the modulator within the amplitude range has been confirmed by extensive simulations.

The interference rejection ratio simulation results are illustrated in the following figures. In addition to the proposed STF design, also frequency flat and mirror-frequency rejecting [19] STF designs are simulated for reference. In Fig. 12, the results are given for the 16-QAM waveform, considering first I/Q mismatches only in the feedbacks of the QΣΔM stages. The gain achieved with the digital post-compensation is clearly visible, the compensated interference ratio reaching up to 3 dB with both frequency flat and the proposed STF designs with higher relative blocker powers. However, it is clear that in this special case, the mirror-frequency rejecting STF design of [19] has better performance than either the proposed or the flat STF designs combined with digital post-compensation, exceeding the results of the proposed design and compensation by around 5 dB. This is because the mirror-frequency rejecting STF design combats exactly the effects of the feedback branch I/Q mismatches. The digital compensation does not bring additional improvement with this mirror-frequency rejecting STF design because the mirror-band information is lost before the conversion. However, one should note that this first simulation scenario is unrealistic since only feedback branch I/Q mismatches are considered while the other coefficients of the ΣΔ modulator as well as the preceding radio receiver I/Q matching are assumed ideal.

In Fig. 13, similar results are given for the QPSK signal and feedback branch I/Q mismatches only. The biggest difference therein is the drop in the post-compensation gain. This happens because the QPSK signal has a lower power level compared to the 16-QAM signal and thus smaller SNR making the input noise components dominant error sources over the input signal originating MFI. The good performance of the mirror-frequency rejecting STF is again clearly visible, exceeding the other simulated options by up to 20 dB at relative blocker level of +20 to +30 dB.

Fig. 14 and Fig. 15 illustrate then the corresponding results of a much more realistic scenario with I/Q mismatches in all the QΣΔM coefficients and also 30 dB image rejection ratio for the preceding receiver chain for 16-QAM and QPSK waveforms, respectively. This is indeed the realistic scenario for which the proposed transfer function design was developed and combined with the digital post-compensation of the MFI of the whole receiver. As expected, there is significant difference between the results in Fig. 14 (16-QAM and mismatches in the whole receiver) and Fig. 12 (16-QAM and only feedback mismatches). The performance of the mirror-frequency rejecting STF design has dropped by more than 20 dB when considering the relative blocker level range up from +20 dB. At the same time, while significant additional error-sources have been introduced compared to the

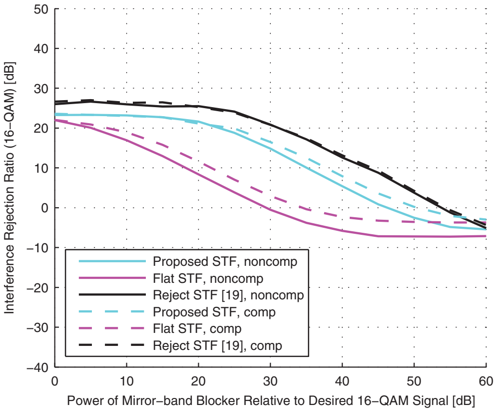

Fig. 12. Interference rejection ratios for a 16-QAM signal with two-stage QΣΔM, using 3-bit quantizers at each stage, as a function of blocker signal power. The proposed STF, frequency-flat ("Flat STF") and mirror-frequency rejecting STF [19] ("Reject STF") designs are simulated. Implementation inaccuracies are considered only in the feedback branch coefficients of both the stages.

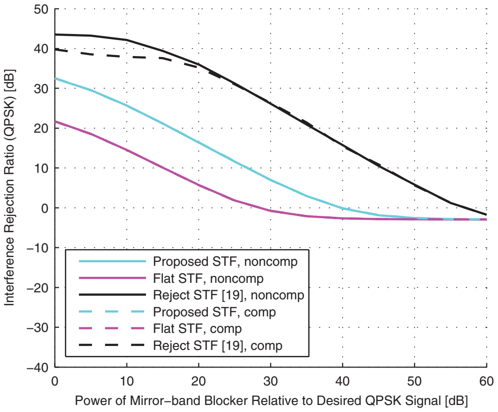

Fig. 13. Interference rejection ratios for a QPSK signal with two-stage QΣΔM, using 3-bit quantizers at each stage, as a function of blocker signal power. The proposed STF, frequency-flat ("Flat STF") and mirror-frequency rejecting STF [19] ("Reject STF") designs are simulated. Implementation inaccuracies are considered only in the feedback branch coefficients of both the stages.

previous scenario, the performance of the proposed STF design combined with the digital post-compensation has dropped by only 3 dB. This is because the post-compensation, when combined with proposed transfer function optimization, is able to mitigate the MFI independent of the exact location of the error-source. The gain achieved by this post-compensation with the proposed STF design is from 6 to 14 dB on the relative blocker level range from +20 to +50dB. In parallel, also the frequency-flat STF design has around 6 dB gain as a result of the post-compensation. With the highest blocker power levels, the quantization noise and its conjugate component become eventually the dominating error-source because of the effective down-scaling of the desired waveforms. The digital compensation applied is not able to mitigate this interference as efficiently as the input signal originating MFI. Overall, it is anyway clear that the combination of the proposed STF design and the digital compensation algorithm has the best performance in this realistic and challenging scenario considering the whole simulated blocker level range.

The results for the QPSK signal in Fig. 15 show similar characteristics compared to the 16-QAM results. The clear drop in the performance of the mirror-frequency rejecting STF design is visible as well as increased post-compensation gain for the proposed STF design due to the increased role of the input signal originating MFI because of the additional mismatches and nonideal image rejection of the receiver front-end. The achieved gain is now between 4 dB and 6 dB, the latter being with higher blocker powers. These results support the conclusion that in this more realistic scenario, considering practical error sources, the proposed STF design combined with the digital post-compensation outperforms the earlier solutions, taking the whole simulated relative blocker power range into account.

Overall, when considering the practical simulation scenario with mismatches in the whole receiver, the results show significant increase in the interference rejection ratio with the proposed transfer function design complemented with the digital MFI post-compensation discussed herein. The gains are most evident in good SNR conditions. With low SNR the noise components

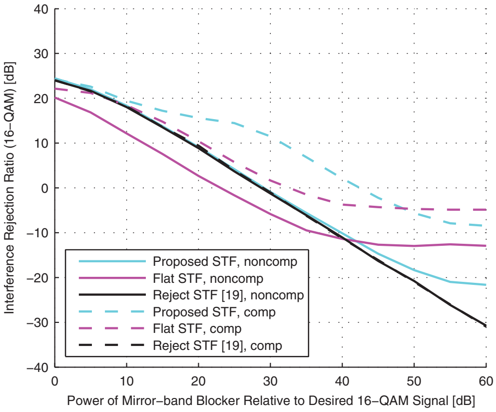

Fig. 14. Interference rejection ratios for a 16-QAM signal with two-stage QΣΔM, using 3-bit quantizers at each stage, as a function of blocker signal power. The proposed STF, frequency-flat ("Flat STF") and mirror-frequency rejecting STF [19] ("Reject STF") designs are simulated. Implementation inaccuracies are considered in all the coefficients of both the stages together with image rejection ratio of 30 dB for the preceding receiver chain.

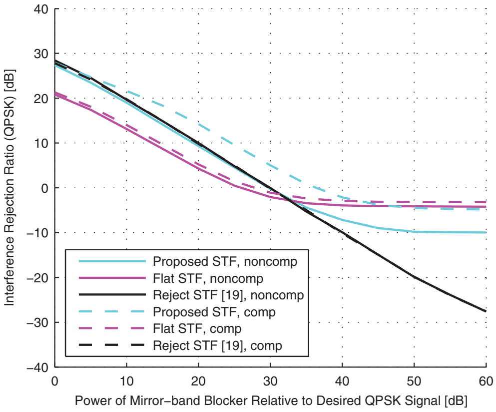

Fig. 15. Interference rejection ratios for a QPSK signal with two-stage QΣΔM, using 3-bit quantizers at each stage, as a function of blocker signal power. The proposed STF, frequency-flat ("Flat STF") and mirror-frequency rejecting STF [19] ("Reject STF") designs are simulated. Implementation inaccuracies are considered in all the coefficients of both the stages together with image rejection ratio of 30 dB for the preceding receiver chain.

(nonconjugated and conjugated) become the dominant error source. Although the mirror-frequency rejecting STF design copes well with the feedback branch mismatches, its performance drops significantly, e.g., by 20 dB in the previous 16-QAM example, when also other mismatches are introduced. In parallel, this drop for the proposed STF design combined with digital compensation was only few dBs, showing particular robustness in the realistic reception scenario. This gain in received signal quality, achieved by the suppression of input signal originating MFI by means of the digital post-compensation, is of significant importance in challenging radio conditions typical for CR receivers. The results confirm that the proposed STF and NTF designs facilitate such gain via preserving mirror-band signal information to be exploited in the post-compensation algorithm. Thus, also the interference generated at the receiver front-end circuitry can be mitigated, easing the requirements for those components.

VI. CONCLUSIONS

In this article, a novel frequency-agile multiband transfer function design for single- and multistage QΣΔMs was proposed, combined with digital post-compensation of MFI originating from implementation inaccuracies of the preceding radio front-end and the QΣΔM itself. This allows the compensation to be done independently of the location of the actual error source in the receiver chain. This is essential for practical implementations of such a receiver, especially in challenging signal conditions typical for CR systems. The computer simulations showed significant interference rejection gain, achieved by simple post-compensation algorithm presented in the literature, proving the digital post-compensation approach to be feasible also with QΣΔM (in addition to the traditional ADCs without noise shaping). This is an important step towards robust receiver implementations using quadrature ΣΔ ADC, allowing the promising multiband and reconfigurability properties to be exploited in practice. The proposed design can be implemented without additional analog components and is straightforwardly reconfigurable in dynamic conditions, e.g., in case of frequency handoff because of a primary user appearance. In addition, facilitating the digital post-compensation of the receiver front-end originating interference eases the demands for the implementation and matching of these circuits.

In addition, a novel closed-form transfer function analysis method was presented, based on the matrix-representation of I/Q mismatched QΣΔM coefficients. In this way, the four transfer functions (NTF, STF, INTF and ISTF) of the QΣΔM can be solved for any modulator order or number of stages. Furthermore, a closed-form equation for the output of such modulator under coefficient mismatches was presented. This allows the designers to examine the effects of inherent implementation inaccuracies in more detail already before measuring the actual implementation.

REFERENCES

[1] M. Mueck, et. al., “ETSI reconfigurable radio systems: status and future directions on software defined radio and cognitive radio standards,” *IEEE Comm. Mag.*, vol. 48, no. 4, pp. 78-86, Sept. 2010.

[2] I. F. Akyildiz, W.-Y. Lee, M. C. Vuran and S. Mohanty, “NeXt generation/dynamic spectrum access/cognitive radio wireless networks: a survey,” *Computer Networks*, vol. 50, pp. 2127–2159, 2006.

[3] P.-I. Mak, S.-P. U and R. P. Martins, “Transceiver architecture selection: review, state-of-the-art survey and case study,” *IEEE Circuits Syst. Mag.*, vol. 7, no. 2, pp. 6–25, 2nd quarter 2007.

[4] R. Bagheri, A. Mirzaei, M. E. Heidari, S. Chehrazi, M. Lee, M. Mikhemar, W. K. Tang and A. A. Abidi, “Software-defined radio receiver: dream to reality,” IEEE *Commun. Mag.*, vol. 44, no. 8, pp. 111–118, Aug. 2006.

[5] Z. Ru, N.A. Moseley, E. Klumperink and B. Nauta, B. “Digitally enhanced software-defined radio receiver robust to out-of-band interference,” *IEEE J. Solid-State Circuits*, vol. 44, no. 12, pp. 3359-3375, Dec. 2009.

[6] B. Razavi, “Cognitive radio design challenges and techniques,” *IEEE J. Solid-State Circuits*, vol. 45, no. 8, pp. 1542–1553, Aug. 2010.

[7] P. B. Kenington, and L. Astier, “Power consumption of A/D converters for software radio applications,” *IEEE Trans. Veh. Technology*, vol. 49, no. 2, pp. 643-650, March 2000.

[8] M. Ismail and D. Rodríguez de Llera González (eds.), Radio Design in Nano-meter Technologies (Springer, Dordrecht, Netherlands, 2006)

[9] J. Yang, R. W. Brodersen and D. Tse, “Addressing the dynamic range problem in cognitive radios,” in *Proc. IEEE Int. Conf. Commun.*, Glasgow, Scotland, 24-28 June 2007.

[10] A.A. Abidi, “The path to the software-defined radio receiver,” *IEEE J. Solid-State Circuits*, vol. 42, no. 5, pp. 954–966, May 2007.

[11] M. Valkama, J. Pirskanen, and M. Renfors, ”Signal processing challenges for applying software radio principles in future wireless terminals: An overview.” *Int. J. Commun. Syst.*, vol. 15, pp. 741–769, 2002.

[12] B. Le, T. W. Rondeau, J. H. Reed and C. W. Bostian, “Analog-to-digital converters,” *IEEE Signal Processing Mag.*, vol. 22, no. 6, pp. 69-77, Nov. 2005.

[13] N. Vun, A. B. Premkumar, “ADC systems for SDR digital front-end,” in *Proc. 9th Int. Symp. Consumer Electronics*, Macau, Hong Kong, 14-16 June 2005.

[14] A. Rusu, B. Dong and M. Ismail, “Putting the “flex” in flexible mobile wireless radios,” *IEEE Circuits Devices Mag.*, vol. 22, no. 6, pp. 24-30, Nov.–Dec. 2006.

[15] A. Silva, J. Guilherme and N. Horta, “Reconfigurable multi-mode sigma–delta modulator for 4G mobile terminals,” *Integration, The VLSI J.*, vol. 42, no. 1, pp. 34-46, Jan. 2009.

[16] A. Morgado, J. Gerardo Garcia, S. Asghar, L. I. Guerrero, R. del Río, and J. M. de la Rosa, “A power-scalable concurrent cascade 2-2-2 SC ΣΔ modulator for Software Defined Radio,” *IEEE Int. Symp. Circuits and Syst.*, Seoul, South-Korea, 20-23 May 2012.

[17] N. Jouida, C. Rebai, G. Ghazel and D. Dallet, “Comparative study between continuous-time real and quadrature bandpass delta sigma modulator for mul-tistandard radio receiver,” in *Proc. Instrumentation Measurement Technology Conf.*, Warsaw, Poland, 1-3 May 2007.

[18] S. Jantzi, K. Martin, and A. Sedra, “A quadrature bandpass delta-sigma modulator for digital radio,” *IEEE J. Solid-State Circuits.*, vol. 32, no. 12, pp. 1935–1950, Dec. 1997.

[19] J. Marttila, M. Allén and M. Valkama, ”Multi-stage quadrature sigma-delta modulators for reconfigurable multi-band analog-to-digital interface in cognitive radio devices,” *EURASIP J. Wirel. Commun. Netw.*, vol. 2011, no. 1, pp. 1-23, Oct. 2011.

[20] P. A. Aziz, H. V. Sorensen and J. van der Spiegel, “An overview of sigma-delta converters: how a 1-bit ADC achieves more than 16-bit resolution,” *IEEE Signal Processing Mag*, vol. 13, no. 1, pp. 61–84, Sep. 1996.

[21] S. Jantzi, K. W. Martin and A. S. Sedra, “The effects of mismatch in complex bandpass ΔΣ modulators,” in *Proc. IEEE Int. Symp. Circuits Syst.*, Atlanta, GA, 12-15 May 1996.

[22] L. Anttila, M. Valkama and M. Renfors, ”Blind moment estimation techniques for I/Q imbalance compensation in quadrature receivers,” in *Proc. 17th Annu. IEEE Int. Symp. Personal, Indoor and Mobile Radio Commun.*, Helsinki, Finland, 11-14 Sept. 2006.

[23] G.-T. Gil, “Nondata-aided I/Q mismatch and DC offset compensation for direct conversion receivers,” *IEEE Trans. Signal Process.*, vol. 56, no. 7, pp. 2662-2668, July 2008.

[24] F. Harris, “Digital filter equalization on analog gain and phase mismatch in I-Q receivers,” in *Proc. 5th IEEE Int. Conf. Univeral Personal Commun.*, Cambridge, MA, Sept. 29-Oct 2, 1996.

[25] K. P. Pun, J. E. Franca, C. Azeredo-Leme, C F. Chan and C. S. Choy, “Correction of frequency dependent I/Q mismatches in quadrature receivers,” *Electronics Letters*, vol. 37, no. 23, pp. 1415-1417, Nov. 2001.

[26] L. Anttila, M. Valkama and M. Renfors, ”Circularity based I/Q imbalance compensation in wideband direct-conversion receivers,” *IEEE Trans. Veh. Technol.*, vol. 57, no. 3, pp. 2099-2113, July 2008.

[27] J. Marttila, M. Allén and M. Valkama, “Digital mirror-frequency interference compensation for multiband quadrature sigma-delta ADC based cognitive radio receivers,” in *Proc. 55th IEEE Int. Midwest Symp. Circuits and Syst.*, Boise, ID, Aug. 2012 (invited paper).

[28] J. Marttila, M. Allén and M. Valkama, “Quadrature ΣΔ modulation for cognitive radio – I/Q imbalance analysis and complex multiband principle,” *Circuits, Syst. and Signal Process*. vol. 30, no. 4, pp. 775–797, Aug. 2011.

[29] Y. B. N. Kumar, E. Bonizzoni, A. Patra, F. Maloberti, “Interference rejection in delay line based quadrature band-pass ΣΔ modulators,” *IEEE Int. Symp. Circuits and Syst.*, Seoul, South-Korea, 20-23 May 2012.

[30] L. Yu and W. M. Snelgrove, “A novel adaptive mismatch cancellation system for quadrature IF radio receivers,” *IEEE Trans. Circuits Syst. II, Analog Digit. Signal Process.*, vol. 46, no. 6, pp. 789–801, June 1999.

[31] L. J. Breems, E. C. Dijkmans and J. H. Huijsing, “A quadrature data-dependent DEM algorithm to improve image rejection of a complex modulator,” *IEEE J. Solid-State Circuits*, vol. 36, no. 12, pp. 1879–1886, Dec. 2001.

[32] S. Reekmans, P. Rombouts and L. Weyten, “Mismatch insensitive double-sampling quadrature bandpass ΣΔ modulation,” *IEEE Trans. Circuits and Syst. I: Regular Papers*, vol. 54, no. 12, pp.2599-2607, Dec. 2007.

[33] Y. Tang, K.-W. Cheng, S. Gupta, J. Paramesh and D. J. Allstot, “Cascaded complex ADCs with adaptive digital calibration for I/Q mismatch,” *IEEE Trans. Circuits Syst. I, Reg. Papers*, vol. 55, no. 3, pp. 817–827, April 2008.

[34] K.-P. Pun, C.-S. Choy, C.-F. Chan and J. E. da Franca, “An I/Q mismatch-free switched-capacitor complex sigma-delta modulator,” *IEEE Trans. Circuits and Syst. I: Express Briefs*, vol. 51, no. 5, pp. 254-256, May 2004.

[35] P.M. Aziz, “Multi-band Oversampled noise shaping analog to digital conversion,” Ph.D. dissertation, Dept. Elect. and Systems Eng., Univ. Pennsylvania, Philadelphia, PA, 1996.

[36] Y. B. N. Kumar, A. Patra and F. Maloberti, “Reconfigurable multi-band quadrature ΣΔ modulators,” in *Proc. 7th Conf. Ph.D. Research Microelectronics and Electronics*, Tirento, Italy, 3-7 July 2011.

[37] R. Schreier and G. C. Temes, Understanding Delta-Sigma Data Converters. (Wiley, Hoboken, NJ, 2005).

[38] J. Marttila, M. Allén and M. Valkama, “Design and analysis of multi-stage quadrature sigma-delta A/D converter for cognitive radio receivers,” in *Proc. 16th IEEE Int. Workshop Comput.-Aided Modeling Anal. and Design of Commun. Links and Networks*, Kyoto, Japan, 10-11 June 2011.

[39] Y. B. N. Kumar, S. Talay and F. Maloberti, “Complex cascaded bandpass ΣΔ ADC design,” in *Proc. IEEE Int. Symp. Circuits and Syst.*, Taipei, Taiwan, 24-27 May 2009.

[40] P. Kiss, “Adaptive digital compensation of analog circuit imperfections for cascaded delta-sigma analog-to-digital converters,” Ph.D. dissertation, “Politehnica” Univ. Timisoara, Romania, 1999.

[41] G. Cauwenberghs and G. C. Temes, “Adaptive digital correction of analog errors in MASH ADCs. I. off-line and blind on-line calibration,” *IEEE Trans. Circuits Syst. II, Analog Digit. Signal Process.*, vol. 47, no. 7, pp. 621-628, July 2000.

[42] K. R. Matthews, *Elementary Linear Algebra*, Brisbane, Australia, Univ. Queensland, 2012. [E-book]. Available: http://www.numbertheory.org/ [Accessed: 11 Apr. 2012]

[43] T. Adah, P. J. Schreier and L. L. Scharf, “Complex-valued signal processing: the proper way to deal with impropriety,” *IEEE Trans. Signal Process.*, vol. 59, no. 11, pp.5101-5125, Nov. 2011.

[44] G. Fettweis, M. Lohning, D. Petrovic, M. Windisch, P. Zillmann and W. Rave, “Dirty RF: a new paradigm,” *in Proc. 16th Annu. IEEE Int. Symp. Personal, Indoor and Mobile Radio Commun.*, Berlin, Germany, 11-14 Sept. 2005.

[45] Z. Ru, N. A. Moseley, M. Klumpernik and B. Nauta, “Digitally enhanced software-defined radio receiver robust to out-of-band interferers,” IEEE J. Solid-State Circuits, vol. 44. no. 12, pp. 3359–3375, Dec. 2009.

[46] R. Schreier, “An empirical study of high-order single-bit delta-sigma modulators,” *IEEE Trans. Circuits Syst. II, Analog Digit. Signal Process.*, vol. 40, no. 8, pp. 461-466, Aug. 1993.

[47] L. Anttila, M. Valkama and M. Renfors, ” Circularity-based I/Q imbalance compensation in wideband direct-conversion receivers,” *IEEE Trans. Veh. Technol.*, vol. 57, no. 4, pp. 2099–2113, July 2008.

Tampereen teknillinen yliopisto
PL 527
33101 Tampere

Tampere University of Technology
P.O.B. 527
FI-33101 Tampere, Finland

ISBN 978-952-15-3408-9
ISSN 1459-2045